KU LEUVEN

ARENBERG DOCTORAL SCHOOL
Faculty of Engineering Science

Joint Kalman-based input/parameter/state estimation for structural applications

Roberta Cumbo

Dissertation presented in partial fulfillment of the requirements for the degree of Doctor of Engineering Science (PhD): Mechanical Engineering

— 2024

Joint Kalman-based input/parameter/state estimation for structural applications

Roberta CUMBO

Examination committee:
Prof. dr. ir. P. Wambacq, chair
Prof. dr. ir. F. Naets, supervisor
Dr. ir. D. De Gregoriis, supervisor
(Siemens Digital Industries Software)
Prof. dr. ir. M. Vanierschot
Prof. dr. ir. D. Chronopoulos
Dr. ir. T. Tamarozzi (Raidyn)
Dr. ir. A. Kumar (Leonardo S.p.A.)
Prof. dr. ir. P. Masarati (Politecnico di Milano)

Prof. dr. ir. E. Cross (University of Sheffield)

Dissertation presented in partial fulfillment of the requirements for the degree of Doctor in Engineering

— 2024

© 2024 KU Leuven – Faculty of Engineering Science
Uitgegeven in eigen beheer, Roberta Cumbo, Celestijnenlaan 200A box 2402, B-3001 Leuven (Belgium)

Alle rechten voorbehouden. Niets uit deze uitgave mag worden vermenigvuldigd en/of openbaar gemaakt worden door middel van druk, fotokopie, microfilm, elektronisch of op welke andere wijze ook zonder voorafgaande schriftelijke toestemming van de uitgever.

All rights reserved. No part of the publication may be reproduced in any form by print, photoprint, microfilm, electronic or any other means without written permission from the publisher.

I did not use generative AI assistance tools during the research/writing process of my thesis, except for mere language assistance to improve text quality in the Part I, *Executive Summary*, of the thesis. The text/code/images in this thesis are my own and generative AI has only been used in accordance with the KU Leuven guidelines and appropriate references have been added. I have reviewed and edited the content as needed and I take full responsibility for the content of the thesis.

Preface

This thesis represents an important chapter of my career that began in 2019. If someone had asked me a year ago if I had ever managed to finish it, I would have answered no. After two years of PhD, I decided to interrupt this path that I felt did not belong to me and I followed another career path in Italy. I realize that this milestone is not like for those who have put passion and determination in the PhD and I am not proud to have taken a long time, but for me it is an important piece of my career and a small personal achievement. If I could complete it today and reach the position I am in now, I owe it to all the people I have met along my career path who have supported, encouraged and guided me. Results in research, as well as many professional and personal achievements, are not achieved solely thanks to the commitment of the individual but above all thanks to the people we meet and interact with every day.

First, I thank Tommaso Tamarozzi, who was my supervisor at Siemens but who contributed throughout the duration of my PhD. The milestones I reached in my first job experience are thanks to his guidance, and I learned a lot from him. When I decided to interrupt the PhD, he supported me in continuing it despite all the difficulties. Similarly, Wim Desmet and Frank Naets, supervisors at KU Leuven. I thank Frank for immediately making himself available to support me in completing the PhD even remotely and for enriching my technical knowledge. I thank Daniel De Gregoriis for his patience, support, and availability, making it possible to finalize this work. Pierangelo Masarati and colleagues from the Department of Aerospace Science and Technology at the Polytechnic University of Milan with whom I had the opportunity to work for two secondments in the early period. Stefano Corvaglia, Antonio Baroni, and Alessandro Massa from Leonardo who gave me the opportunity to finish the PhD started at Siemens, giving me trust and encouragement.

Completing this PhD was possible thanks to the collaboration between many people belonging to different entities, and it was a great honor for me to have you as a guide during this journey. I then thank all the other members of the

committee, the R&D team of the Simulation Division and Test Division at Siemens, and the colleagues of Leonardo Labs.

Thanks also go to all my friends from Belgium who made my time in Leuven an unforgettable experience and made me feel at home even when I missed Italy. Here I have had many experiences and in all my best memories, you are there. A special thanks goes to Sara, Claudio, Giampiero, Adriano, Vincenzo, Maria, Silvia, Elena, Emilio, Caterina, Enrico, and Fabio. You all represented an important part of this journey.

To my family, Mamma, Papà, Cristina, Valentina, Fabio, and Susanna, who have always been there for me in all moments of difficulty and whom I have always been able to count on. To my grandmother whom I would have liked to be here with us on this important day but I always feel close to me.

To my partner, Gabriele, the person who understands me the most, whom I met in Belgium at the worst moment of my PhD, and with whom I hope to spend every day of my life together.

To all of you and to all the people I have met during this journey who have enriched me personally and professionally. Thank you from the bottom of my heart, *I dedicate this thesis to you.*

Abstract

This dissertation deals with the application of Kalman-based inverse methods to industrial use-cases for structural applications. Kalman filtering is a model-based technique which assumes physical knowledge of the system. In an industrial scenario, accurate modeling is difficult to achieve and the modeling uncertainties can impact the level of reliability of these kind of techniques. A key property of inverse methods is the observability of the identified quantity. In particular, when a large number of physical parameters or loads are estimated and monitored, the inverse identification becomes more challenging as it requires a large number of sensors.

The main goal of this thesis is to define a robust workflow for the application of Kalman filtering in industrial scenarios to solve joint input/parameter/state estimation by adopting the Augmented Kalman Filter (AKF) formulation.

As a first contribution, this dissertation proposes methods to increase the robustness of Kalman filtering by using a reduced set of sensors. Advanced methodologies are developed to study the Optimal Sensor Placement (OSP) to provide a more accurate and robust estimation of the augmented states. The techniques, named Advanced Optimal Sensor Placement (AOSP), are based on the minimization of the state error covariance and the maximization of the transfer function between the real and estimated state. The efficiency of the proposed approaches is demonstrated and validated on a rear twistbeam suspension tested with a 6 Degrees of Freedom shaker to simulate sinusoidal and random excitations. The results show good estimation accuracy of external loads and full-field response with improved accuracy with respect to state-of-the-art OSP methods.

As a second contribution, the PhD research enables the applicability of Kalman filtering to unexplored application domains. In particular, simplified modeling is proposed to approximate complex dynamics reducing the overall modeling effort. These simplifications can be compensated by properly tuning the Kalman filter which compensates for the lack of physics by means of a less accurate

estimation of the states with higher uncertainties. Moreover, novel methods are proposed to estimate a large number of parameters with a reduced set of sensors, reducing the observability requirement and therefore enabling the use of AKF for joint input/parameter/state estimation. Two use-cases are investigated to demonstrate the efficient Kalman filter estimation on unexplored application domains as distributed aerodynamic loads and damage monitoring in composite structures. In both situations, prior knowledge of the load or parameter distribution is embedded in the estimator. This knowledge normally comes from user experience, testing and simulations. The proposed approach reduces the required number of instrumented sensors and increases the computational efficiency of the filter.

Overall, this work therefore proposes a robust workflow that focuses on model calibration, which is an important step to efficiently apply Kalman-based methodologies to inverse identification. A key conclusion of the thesis shows that the AKF can compensate for a lack of physical knowledge embedded in the model via less accurate estimation of augmented states, which results in a high accuracy of full-field response estimation at the expense of unknown loads or parameters. Moreover, the AKF can leverage the proposed Advanced OSP strategies compared to other sensors-based or model-based methodologies.

Beknopte samenvatting

Dit proefschrift behandelt de toepassing van Kalman filter-gebaseerde inverse methodes op industriële gevallenstudies voor structurele toepassingen. Kalman-filtering is een modelgebaseerde techniek die uitgaat van de fysieke kennis van het systeem. Voor industriële scenario's is nauwkeurige modellering moeilijk te realiseren en kunnen modelleringsonzekerheden een belangrijke invloed hebben op het behaalde betrouwbaarheidsniveau van dit soort technieken. Een belangrijke eigenschap van inverse methodes is de waarneembaarheid (Engels: observability) van de geïdentificeerde grootheid. Met name wanneer een groot aantal fysieke parameters of krachten moet worden geschat en gemonitord, wordt de inverse identificatie hiervan een grote uitdaging gezien hiervoor een groot aantal sensoren en bijhorende metingen nodig is.

Het belangrijkste doel van dit proefschrift is het definiëren van een robuuste workflow voor industriële Kalman-filtering toepassingen, waarbij de gelijktijdige input/parameter/toestand-schattingen bekomen worden door gebruik te maken van de Augmented Kalman Filter (AKF)-formulering.

Als eerste bijdrage stelt dit proefschrift methodes voor om de robuustheid van Kalman-filtering te vergroten door middel van een kleiner aantal sensoren te gebruiken. Meer specifiek worden er geavanceerde methodologieën voorgesteld voor optimale sensor plaatsing (Engels: Optimal Sensor Placement) (OSP), om hiermee een nauwkeurigere en robuustere schatting van de uitgebreide toestanden te bekomen. Deze methodologieën zijn gebaseerd op enerzijds het minimaliseren van de toestandsschattingsfoutcovariantie en anderzijds het maximaliseren van de overdrachtsfunctie tussen de werkelijke en de geschatte toestanden. De efficiëntie van de voorgestelde aanpak wordt gedemonstreerd en gevalideerd aan de hand van een twistbeam-ophanging van een voertuig, die in het laboratorium getest is met een 6-vrijheidsgraden shaker om zowel sinusoïdale als willekeurige excitaties te simuleren. De resultaten tonen aan dat een goede schattingsnauwkeurigheid bekomen wordt van zowel de externe belastingen aangelegd door de shaker, alsook de volledige verdeelde respons.

Hierbij ligt de bekomen nauwkeurigheid hoger dan wat bekomen kan worden met andere bestaande state-of-the-art OSP-methodes.

Als tweede bijdrage maakt dit doctoraatsonderzoek het gebruiken van Kalman-filtering voor nieuwe toepassingsdomeinen mogelijk. Meer specifiek wordt een vereenvoudigde numerieke modelleringsaanpak voorgesteld om complexe dynamica te benaderen, waardoor de totale modelleringsinspanning wordt verminderd. Deze vereenvoudigingen kunnen worden gecompenseerd door de Kalman-filter goed af te stemmen, waarbij het gebrek aan gemodelleerde fysica gecompenseerd wordt door een minder nauwkeurige schatting van de toestanden met grotere onzekerheden. Ook worden nieuwe methodes voorgesteld om een groot aantal parameters te kunnen schatten met slechts een beperkt aantal sensoren, waardoor de waarneembaarheidsvereiste versoepeld wordt en tevens het gebruik van AKF mogelijk wordt. Twee gevallenstudies worden onderzocht om de efficiëntie van Kalman-filterschatting voor nieuwe toepassingsdomeinen zoals verdeelde aerodynamische belastingen en schademonitoring in composiet-constructies aan te tonen. In beide situaties is voorkennis van de belasting- of parameterverdeling in de schatter opgenomen. Deze kennis komt normaal gesproken voort uit gebruikerservaring, testen en simulaties. De voorgestelde aanpak verkleint het aantal benodigde sensoren en verhoogt de rekenefficiëntie van de filter.

Samengevat stelt dit werk een robuuste workflow voor die zich richt op modelkalibratie, wat een belangrijke stap is om Kalman-gebaseerde methodologieën efficiënt toe te kunnen passen voor inverse identificatie doeleinden. Een belangrijke conclusie van het proefschrift is dat de AKF het gebrek aan gemodelleerde fysica kan compenseren door middel van een minder nauwkeurige schatting van de uitgebreide toestanden. Dit resulteert in een hoge nauwkeurigheid van de geschatte volledige verdeelde respons, ten koste van de nauwkeurigheid van de geschatte onbekende belastingen of parameters. Bovendien kan de AKF de voorgestelde Advanced OSP-strategieën benutten en exploiteren, waar andere, op sensoren gebaseerde of modelgebaseerde methodologieën, dit niet kunnen.

List of Abbreviations

A-KF Adaptive Kalman Filter.

AEKF Augmented Extended Kalman Filter.

AI Artificial Intelligence.

AKF Augmented Kalman Filter.

ANN Artificial Neural Network.

AOSP Advanced Optimal Sensor Placement.

BDF Backward Differentiation Formulas.

BEMT Blade Element Momentum Theory.

CFD Computational Fluid Dynamics.

CNN Convolutional Neural Network.

CSD Computational Structural Dynamics.

DAE Differential Algebraic Equations.

DCB Double Cantilever Beam.

DIC Digital Image Correlation.

DKF Dual Kalman Filter.

DoF Degree of Freedom.

DT Digital Twin.

EKF Extended Kalman Filter.

FBGs Fiber Bragg Gratings.

FEM Finite Element Model.

FOM Full Order Model.

FRF Frequency Response Function.

GGL Gear, Gupta and Leimkuhler.

GKF Gillijns and De Moor Kalman Filter.

HUMS Health and Usage Monitoring System.

IEC Input Error Covariance.

iFEM Inverse Finite Element Modelling.

KF Kalman Filter.

LE Leading Edge.

LTI Liner Time Invariant.

.

MI Matrix Inversion.

ML Machine Learning.

MOR Model Order Reduction.

MS Mount Stiffness.

NDI Non Destructive Inspection.

ODE Ordinary Differential Equations.

OMA Operational Modal Analysis.

OSP Optimal Sensor Placement.

PBH Popov-Belevitch-Hautus.

PDF Probability Density Function.

pMOR parametric Model Order Reduction.

POD Proper Orthogonal Decomposition.

RMSE Root Mean Square Error.

ROM Reduced Order Model.

RTB Rotor Track and Balance.

.

SVD Singular Value Decomposition.

TE Trailing Edge.

TF Transfer Function.

TFI Transfer Function Identity Index.

TPA Transfer Path Analysis.

TRL Technology Readiness Level.

UKF Unscented Kalman Filter.

List of Symbols

$\dot{\mathbf{x}}$	Time derivative of $\mathbf{x}$
$\mathbf{\Phi}_l$	Local reduction basis
$\mathbf{\Psi}$	Reduction basis
$\mathbf{\Psi}_{nm}$	Normal mode basis
$\mathbf{\Psi}_{ram}$	Residual attachment modes basis
$\mathbf{A}$	System matrix
$\mathbf{A}^*$	Augmented system matrix
$\mathbf{A}_r$	Reduced system matrix
$\mathbf{B}$	Input matrix
$\mathbf{C}$	Output matrix
$\mathbf{D}$	Feedforward matrix
$\mathbf{F}^*$	Discrete-form of augmented system matrix
$\mathbf{H}^*$	Augmented output matrix
$\mathbf{K}$	Kalman gain
$\mathbf{P}$	State error covariance
$\mathbf{Q_u}$	Input covariance matrix
$\mathbf{Q}$	Process covariance matrix
$\mathbf{q}$	Generalized coordinates vector
$\mathbf{Q}^*$	Augmented process covariance matrix
$\mathbf{R}$	Measurement covariance matrix

$\mathbf{T}$	Transfer function
$\mathbf{u}$	Input vector
$\mathbf{v}$	Measurement noise
$\mathbf{w_u}$	Input noise
$\mathbf{w}$	Process noise
$\mathbf{w}^*$	Augmented process noise
$\mathbf{x}$	State vector
$\mathbf{x}^*$	Augmented state vector
$\mathbf{y}$	Measurement or output vector
$\mathbf{z}$	DoFs vector

Contents

Abstract v

Beknopte samenvatting vii

List of Abbreviations xi

List of Symbols xiv

Contents xv

List of Figures xvii

List of Tables xxv

Executive summary 1

1 Context and Motivation 2
- 1.1 The importance of inverse identification for structural monitoring 2
- 1.2 Problem statement 7
- 1.3 Objectives and Achievements 9
- 1.4 Outline of the dissertation 12

2 State of the Art and Methodologies 15
- 2.1 Inverse problems for structural applications 15
- 2.2 The model-based inverse problem 18
- 2.3 Overview of Kalman-filtering methods 20
  - Linear Time Invariant systems and Augmented formulation . . 21
  - Nonlinear dynamics: Extended Kalman Filter 24
  - Main principles of Kalman Filter 26
- 2.4 Application domains 32

2.5 Conclusions 34

3 Research Approach and PhD Achievements 36
3.1 Calibration of sensor location - Paper I 37
3.2 Advanced Optimal Sensor Placement - Paper II 38
3.3 Less-correlated numerical model compensated through AKF - Paper III 42
3.4 Estimation of distribution of loads and parameters - Paper IV . 45
3.5 Conclusions 47

4 Concluding remarks and future research opportunities 49

A Distributed aerodynamic load estimation on a fixed-root scaled helicopter blade 53

Publications 59

I — Kalman-based load identification and full-field estimation analysis on industrial test case 60

II — Advanced Optimal Sensor Placement for Kalman-based multiple-input estimation 86

III — State and Force Estimation on a Rotating Helicopter Blade through a Kalman-Based Approach 123

IV — Recursive parameter estimation for the on-line monitoring of delamination growth in composite structures 148

Bibliography 183

Curriculum Vitae 203

List of publications 205

List of Figures

1.1 Flight accidents from left to right: United Airlines flight 232 (1989), Aloha Flight 243 (1988), Eurocopter EC225 Super Puma helicopter (2016). 3
1.2 Example of forward and inverse problem on a cantilever beam. 5
1.3 Scheme of inverse methods: signal processing-based, model-based and data-based. The external load (blue arrow), corresponding to the sensor data (red markers), is estimated as output of each of the three different methods. 6
1.4 Goals and correspoding use-cases of the PhD. Twistbeam rear suspension (top), scaled helicopter blade (bottom left) and composite DCB (bottom right). 11

2.1 Forced 1 DoF mass-spring system. 20
2.2 Principle of Kalman Filter estimation at time step k. The states are predicted and corrected with the measurements. Both quantities have a Probability Density Function (PDF) with Gaussian distribution. The Kalman Filter combines these information to give an optimal estimate of the states. 23
2.3 Optimal Sensor Placement scheme grouped in two main steps: *Training* and *Screening*. 28
2.4 Observability decreasing obtained with PBH metric by using position-level measurements on a MKD system. 28
2.5 L-curve: log-log plot of the norm of a regularized solution versus the norm of the corresponding residual norm. 30
2.6 Example of inverse identification on a wing of an aircraft where local damages might occur and aerodynamic loads are distributed. 34

3.1 Strain rosette installed on the surface of a structure and its overlap on the FE model. Red marker and arrow are measured location and direction of the central strain gauge. Green marker and arrow are the optimized properties, identified in the uncertainty area (red box). 38
3.2 Static validation through optimization procedure: numerical and experimental strain comparison. FEM start: strain evaluated on the element identified by camera device. FEM opt: strain evaluated on the optimal element. 39
3.3 Scheme of transfer function $\mathbf{T}_{\hat{\mathbf{u}}\mathbf{u}}(s)$. 41
3.5 Estimation of 3 loads on a linear FE model [50]. Comparison between results reached with PBH and IEC metrics. 42
3.6 Estimation of aerodynamic loads with less-correlated model. . . 43
3.7 Distributed lift along the aerodynamic span in steady-state (left) and absolute error (right) on a scaled helicopter blade [53]. Reference data from simulation vs estimated. 44
3.8 Estimation of the velocities of 2 elements of the scaled helicopter blade [53]. Reference data from simulation vs estimated. 44
3.9 Schematic representation of progressive delamination in a DCB model. Each sample on the nonlinear $F - d$ curve corresponds to a configuration of process zone moving from the tip to the root of the beam. On the right, an example of distribution over 6 stiffness interface elements is shown. The first element is the master whose value is distributed over the other elements in the process zone. 46
3.10 Estimation of reaction force for the experimental DCB. 47
3.11 Estimated crack length for the experimental DCB. Euler-Bernoulli solution is considered to accurately represent the real behaviour of the specimen. 47

A.1 Scaled helicopter blade tested in wind tunnel in fixed root conditions. On the right, the corresponding FE model. 54
A.2 Wing profile with components (left) and strips with bushings at the root (right). 54
A.3 Instrumented sections along the blade span. 55
A.4 Aerodynamic lift distribution on symmetric airfoil in the chord-wise direction. Lift and chord are normalized. TE: trailing edge; LE: leading edge. 57
A.5 FE model with 5 loaded sections. Span-wise and chord-wise distributions are shown. Master load marked in red at the tip of the blade. 57

A.6 Estimation of total lift compared with reaction force measured through the load cell located at the beam root (left). Estimation of master load for each case. 58
A.7 Estimation of lift coefficient for different pitch angles and different wind velocity. 58
I.8 Optimal Sensor Placement strategy 68
I.9 Rear twistbeam suspension setup - operational configuration . 72
I.10 Optimization process for matching measured and simulated strain 73
I.11 Static validation through optimization procedure: numerical and experimental strain comparison. FEM start: strain evaluated on the element identified by ProCam. FEM opt: strain evaluated on the optimal element. 75
I.12 Location of selected sensors for load identification. Two different sets for Kalman-based and TPA techniques. 76
I.13 Run 1. Frequency content of estimated loads through TPA Matrix Inversion: comparison of the results for two different sets of indicators. 76
I.14 Run 1. Frequency content of estimated loads through AKF: comparison of the results for two different sets of sensors. KF 12/38opt: optimal sensors. KF 12/38 rand: random selection of sensors. 78
I.15 Run 1. Time-domain comparison between estimated loads through AKF and TPA Matrix Inversion for two different sets of sensors. 78
I.16 Run 2. Time-domain comparison between estimated loads through AKF and TPA Matrix Inversion for two different sets of sensors. Zoom on a shorter time interval. 79
I.17 Run 2. Frequency-domain comparison between estimated loads through AKF and TPA Matrix Inversion for two different sets of sensors. 79
I.18 Run 1. L-curve of the estimated input loads using the AKF (12/38opt sensors). Used values of $\mathbf{Q}_u$ are marked in red. 81
I.19 Strain comparison for unknown load (AKF) estimation: optimal vs random selection of sensors. 83
I.20 Strain comparison for known (KF) and unknown (AKF) load estimation. 84
I.21 Run 1 (left) and run 2 (right). Time histories of two strains: comparison between known (KF) and unknown (AKF) load estimation. 84
II.1 Optimal Sensor Placement strategy. 93
II.2 10 DoFs mass-spring system. 94

II.3 Observability index decrease (percentage value of O_m indicator) obtained by the removal of position sensors through the observability screening for a 10 DoFs mass-spring system is considered. 95
II.4 Standard OSP and AOSP block scheme. 96
II.5 Transfer function from estimated to real input loads. 101
II.6 Block scheme of the estimation process in Laplace domain: state-space model as input of the AKF. 102
II.7 Transfer function $\mathbf{T}_{\hat{\mathbf{u}}\mathbf{u}}$ obtained by using 10 displacement sensors. On the left, comparison of the results for the mass-normalized system and i) sensors expressed in meters, ii) sensors expressed in millimiters, iii) scaled sensors. On the rigth, sensors expressed in meters and system i) mass-normalized, ii) without normalization. 107
II.8 Transfer function $\mathbf{T}_{\hat{\mathbf{u}}\mathbf{u}}$ obtained by using 10 displacement sensors and 1 acceleration. Comparison of the results with sensors expressed in meters and system i) mass-normalized, ii) without normalization. 107
II.9 Steady-state error covariance $\mathbf{P}_{\hat{\mathbf{u}}\mathbf{u}}$ value obtained by using i) 10 displacement sensors and ii) 10 displacement and 1 acceleration sensors. 108
II.10 FEM of the rear twistbeam suspension. 109
II.11 Strain sensors position for the 3 criteria. The black marker indicates the *input point*. 110
II.12 Evolution of the selection indexes. 111
II.13 SNR of the set of sensors selected by the three metrics. 112
II.14 113
II.15 Inputs estimation performed using the sensors selected by IEC criterion. 114
II.16 Inputs estimation performed using the sensors selected by TFI criterion. 114
II.17 Normalized error on each estimated input through sensors selected by PBH, IEC and TFI criteria. 115
II.18 Identity index evaluated at $\bar{\phi} = 1$Hz for the 3 criteria: the numerical value reflects the accuracy of the estimations. 115
II.19 Sine sweep: inputs estimation performed using the sensors selected by PBH criterion. 116
II.20 Sine sweep: inputs estimation performed using the sensors selected by IEC criterion. 117
II.21 Sine sweep: inputs estimation performed using the sensors selected by TFI criterion. 117
II.22 Force 2 estimation performed using the sensors selected by TFI criterion in a frequency range [0.1-5]Hz and [0.1-30]Hz. 118

II.23 White noise signal: error in frequency domain between the reference and the estimated load. 118
II.24 White noise signal: inputs estimation performed using the sensors selected by PBH criterion. 119
II.25 White noise signal: inputs estimation performed using the sensors selected by IEC criterion. 119
II.26 White noise signal: inputs estimation performed using the sensors selected by TFI criterion. 120
II.27 Impulse loads: inputs estimation performed using the sensors selected by PBH criterion. 120
II.28 Impulse loads: inputs estimation performed using the sensors selected by IEC criterion. 121
II.29 Impulse loads: inputs estimation performed using the sensors selected by TFI criterion. 121
II.30 RMSE value of the estimated loads for different modelling errors 122
III.1 Two rigid bodies connected through elastic elements. a and b are the two faces of each body where the connections are. k_{12} is the total stiffness matrix given by the interaction of both elastic forces from faces B_{1b} and B_{2a}. 129
III.2 Velocity vector and angles definition for a blade station at distance r from the hub rotating frame. 131
III.3 Kalman filter scheme based on the prediction-correction principle. 135
III.4 Proposed workflow for distributed aerodynamic loads, based on Kalman filtering estimation. 137
III.5 Example of a blade discretized with 2 elements. The lift distribution per unit length is shown above. 137
III.6 A 4-element blade model with all aerodynamic forces (left) and a reduced set of significant forces (right). 139
III.7 Estimation of the states used as sensors. Reference noisy data. . 141
III.8 Estimation of the unmeasured velocity and position entities with reference to the sensor layout in Table III.2. Reference noisy data. 141
III.9 Force estimation on *elem3* and *elem4* with reference to the sensor layout in Table III.2. Reference noisy data. 142
III.10 Distributed lift and angle of attack along the aerodynamic span in steady-state, with 11 points of integration. Reference noisy data used in the estimation. 142
III.11 Absolute error of distributed lift and angle of attack—reference data in Figure III.10. 142
III.12 Graphic comparison between finite segment and finite volume modeling of a flexible element of free-length l. 143

III.13 Comparison of vertical displacement at *elem4* position *a*) without and *b*) with aerodynamics. The model is in rotation and under gravity. . . . 144
III.14 Estimation of the states used as sensors. Reference data from MBDyn. . . . 145
III.15 Estimation of the unmeasured velocity and position entities with reference to the sensor layout in Table III.2. Reference data from MBDyn. . . . 145
III.16 Distributed lift along the aerodynamic span in steady-state (left) and absolute error (right), with 11 points of integration. Reference data from MBDyn. . . . 146
III.17 Estimation of the velocities of *elem3* and *elem4* with reference to the sensor layout in Table III.3. Reference data from MBDyn. 146
IV.1 Flowchart of the paper structure. . . . 153
IV.2 Experimental DCB setup. . . . 155
IV.3 Schematic representation of the progressive delamination in a DCB model using a bi-linear cohesive law. . . . 155
IV.4 Shell elements with node-to-node springs. . . . 156
IV.5 Recursive parameter estimation without (top) and with (bottom) distribution. . . . 163
IV.6 Nonlinear (top) and linear (bottom) meshes with node-to-node spring interface. . . . 164
IV.7 Force versus displacement curve for the two values of G_{IC}. . . . 165
IV.8 Interface stiffness law in the process zone. K_n normalized spring stiffness. . . . 166
IV.9 Normalized stiffness distribution in the process zone of the nonlinear model with cohesive elements. . . . 166
IV.10 Crack propagation of model A and model B. Comparison between simulated curves and data retrieved from EB theory. . . . 167
IV.11 Singular Value Decomposition of parametric png basis. Red line: threshold value. . . . 168
IV.12 Estimated parameters (top left), samples of measurements (top right), estimated displacement field distribution at different time samples (bottom left) and corresponding estimation of boundary conditions (bottom right). . . . 175
IV.13 Normalized stiffness at each time step in the delaminated area. The span is from the initial delamination $a_0 = 38mm$ to a_f, i.e. delamination at the end of the simulation. The red box indicates a generic evaluation of process zone. . . . 175
IV.14 Shape reconstruction and crack length estimation on model A with different sensor networks. $n_{pz} = 7$ . . . 176

IV.15Absolute error of the simulated vs measured vertical displacements of model A, known loads. Sensor net 0,1,2,3 correspond to 14, 7, 3, 1 measurements on the top lamina employed in the estimator respectively. 176
IV.16Stiffness distribution: cohesive law (black, pz: 7-13) vs estimated linear (red, pz: 1-8) vs expected linear (green, pz: 6-13). 177
IV.17Joint input/parameter estimation results using model A. $n_{pz} = 7$ 177
IV.18Absolute error of the simulated vs measured vertical displacements of model A, unknown loads. Sensor net 0, 3 correspond to 14, 1 measurements on the top lamina employed in the estimator. 178
IV.19Joint input/parameter estimation results using model B. $n_{pz} = 4$ 178
IV.20Joint input/parameter estimation results on model A. $n_{pz} = 7$, 14 displacement sensors. Comparison between different imposed interface stiffness distributions. 179
IV.21Normalized nodal forces at the interface with respect to the value at the first undamaged element. *Linear* and *CZM* are retrieved from the forward simulation using the linear shell model with imposed stiffness distributions in the process zone. 179
IV.22Test setup for experimental modal analysis. 179
IV.23Crack propagation retrieved from experimental data. 180
IV.24Estimation of reaction force for the experimental DCB. 180
IV.25AEKF recursive estimation results on experimental DCB. 181

List of Tables

2.1 Comparison between most used inverse methods in literature. . 18

A.1 Properties of blade components. 55
A.2 Modal frequencies of blade clamped at the root. 56
I.3 Excitation of operational data 74
II.1 Sine loads parameters. 109
II.2 White noise signal parameters. 116
III.1 Blade and rotor features. 138
III.2 Sensor layout. 140
III.3 Sensors layout. 145
IV.1 Orthotropic material parameters. 164
IV.2 Cohesive parameters. 165
IV.3 Tip displacement. Effect of boundary conditions. 167
IV.4 Location of strain gauges on top lamina of the DCB. 172
IV.5 FE model validation - % errors with respect to experimental values 172

Executive summary

Chapter 1

Context and Motivation

1.1 The importance of inverse identification for structural monitoring

Travelling by plane or driving a car is nowadays safe thanks to frequent maintenance and inspections. However, the current level of reliability has been reached after several system improvements necessitated by past catastrophic events. Some examples of mechanical failures help to understand the progressive steps done by engineers during past decades:

- *Boeing-Vertol Model 234LR Chinook helicopter – November 6, 1986*: "The accident occurred because the spiral bevel ring gear in the forward transmission failed, causing desynchronisation of the helicopter's twin rotors. This allowed the rotors to collide which in turn led to the disintegration of the arcraft. The ring gear failure stemmed from corrosion fatigue which was initiated by the unpredicted wear and corrosion characteristics of the bolted joint attaching the gear to its shaft ... The manufacturer and airworthiness authorities failed to perceive the possibility that the change in the design of the bolted joint might lead to it performing in a radically different way to that previously experienced."[125]
- *United Airlines flight 232 - July 19, 1989*: "The fan disk failure was caused by a fatigue crack that initiated from a metallurgical defect located on the surface of the disk bore. The metallurgical defect formed during the initial manufacture of the titanium alloy material and was not detected by inspections performed during the manufacturing process. "[8]



Figure 1.1: Flight accidents from left to right: United Airlines flight 232 (1989), Aloha Flight 243 (1988), Eurocopter EC225 Super Puma helicopter (2016).

FAA introduced redundant safety systems and applied more strict engine inspections.

- *Aloha Flight 243 - April 28, 1988*: "The National Transportation Safety Board (NTSB) determined that the probable cause of the accident was the failure of the Aloha Airlines maintenance program to detect the presence of significant disbonding and fatigue damage of the fuselage skin lap splice. "[7] FAA began the National Aging Aircraft Research Program in 1991 to improve maintenance technology and ensure continued airworthiness of high-use and high-cycle aircraft [40].
- *Bond Offshore Helicopters Flight 85N – April 1, 2009*: "There was a catastrophic failure of the helicopter's Main Rotor Gearbox (MGB). ... The planet gear had fractured as a result of a fatigue crack, the precise origin of which could not be determined. However, analysis indicated that this is likely to have occurred in the loaded area of the planet gear bearing outer race. "[36] Maintenance procedures failed to prevent the failure.
- *CHC Helikopter Service Eurocopter EC225 Super Puma helicopter – April 29, 2016*: "The accident was a result of a fatigue fracture in a second stage planet gear in the epicyclic module of the main rotor gearbox. Cracks initiated from a micro-pit at the surface and developed subsurface to a catastrophic failure without being detected. There are no connections between the crew handling and the accident. The AIBN has also excluded material unconformity and mechanical failure, as well as maintenance actions by the helicopter operator. "[18] Airbus Helicopters could replicate after 1 year the cause of the accident in testing and considered the redesign of the gearbox. Later on, European Aviation Safety Agency and FAA decided to prohibit all flights with EC225LP and AS332L2 helicopters in Europe and USA.

The failure phenomena occurred during these events developed due to two main causes: i) the lack of knowledge about the operational stresses and loads led

to more relaxed design specifications and consequently, the design components could not support the real operating conditions; ii) the maintenance processes were not sufficient to detect e.g. material disbonding and defects, and prevent possible failures.

These events (and more) brought thus important improvements in the mechanical design of specific components and the introduction of more strict maintenance rules. This increased the level of reliability and ensured airworthiness of the aircraft but the structural parts are often oversized and a prolonged downtime is registered because of the periodic inspections.

Engineering technologies have been developed to prevent and detect damages sooner during design and operation, leading to less offline inspections requirements. Among different solutions, the field of inverse identification has been one of the most investigated in the last decades for civil, aerospace and automotive applications. Generally speaking, an inverse problem defined for a mechanical system is to calculate input loads or system parameters given a set of observations, i.e. measurements. Fig. 1.2 shows the difference between forward and inverse problems. Forward means that the solution is obtained by solving the governing system equations, given boundary conditions, loads and physical parameters (stiffness values illustrated in red in the top picture). The inverse problem, as stated, retrieves the inputs of the system from the solution, e.g. the displacement field. Some typical inverse identification applications are:

- **Design and testing phase**: In aerospace and automotive industries, most of the structural components are made of laminated Carbon Fiber Reinforced Plastic (CFRP), which are composed of several plies with different orientations. The choice regarding the shape of the part and the optimal stacking sequence is the result of several numerical and experimental studies. The part is tested under different loading conditions, including fracture phenomena. The failure in CFRP is normally analysed a posteriori using off-line monitoring techniques such as Non Destructive Inspection (NDI) [98], whose procedure is defined by international standard [2]. The critical load level at which some local failures, e.g. delamination, occur are often unknown and unobservable using standard machines and instrumentation. A monitoring technique based on inverse identification using sensor data can support these tasks by reducing the repetition of physical tests needed during design and reducing the need for off-line techniques for inspection after testing. The two accidents *Bond Offshore Helicopters Flight 85N* and *CHC Helikopter Service Eurocopter EC225 Super Puma* are two examples of lack of information regarding the physical behaviour of the damaged components during design under fatigue testing loads.

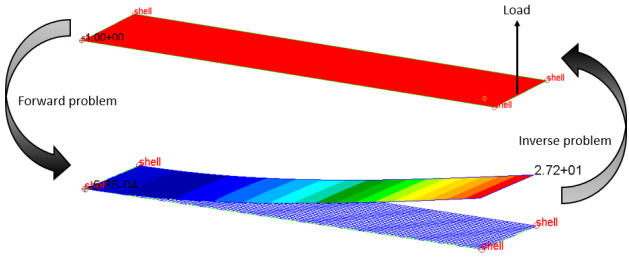

Figure 1.2: Example of forward and inverse problems on a cantilever beam.

- **Operation phase**: direct measurements of loads entering a structure are often difficult to obtain, since dedicated sensors can be intrusive, expensive and can rarely be equipped during the operational life of the system. The on-board integration of a health evaluation system performing inverse identification therefore emerges as a promising solution. This system can analyze the structural response and retrieve the applied loads, providing valuable insights into the stress and strain experienced by various components. This proactive approach helps mitigate the risk of catastrophic failure scenarios and enables the identification of potential damages at an earlier stage than conventional manual inspections. Most of the accidents listed above might have had a reduced risk level of catastrophic failure if an online monitoring system had been implemented on-board, leading to prompt safety measures. The ability to continuously assess the structural health in real-time enhances the overall safety and reliability of the system, contributing to a proactive and preventative maintenance strategy.

Three main categories of inverse identification for structural problems can be identified in literature:

- *Signal processing-based [48]:* these techniques extract structural properties or input loads from frequency content or time-histories of sensor signals. Specific numerical methodologies are involved, often called output-only methods. Some examples are Transfer Path Analysis (TPA) [170, 65] or Operational Modal Analysis (OMA) [38]. The research in this field is currently focused on i) Bayesian approaches able to include testing and operational uncertainties [17], ii) advanced sensor technologies, e.g. embedded sensors, metamaterials, wireless sensors [117, 169]. These solutions are among the most adopted in industry.
- *Model-based [63]:* these methods employ simulation data and compare

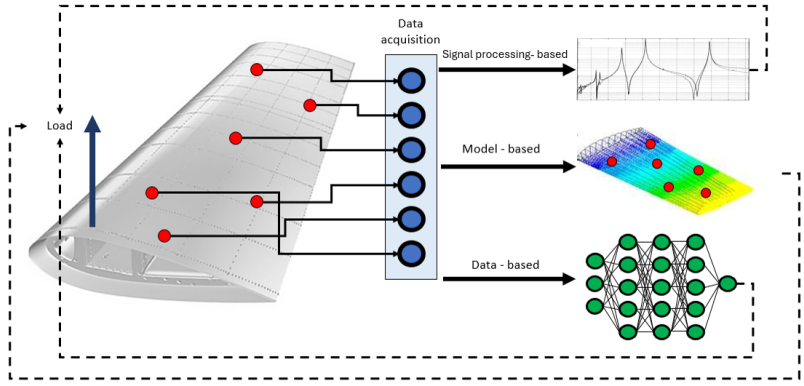

Figure 1.3: Scheme of inverse methods: signal processing-based, model-based and data-based. The external load (blue arrow), corresponding to the sensor data (red markers), is estimated as output of each of the three different methods.

the model with experimental signals in the frequency or time-domain or even transformed to modal parameters. The key point of these techniques is the prior knowledge of high-fidelity Finite Element Model (FEM) or complex analytical solutions. Predictive algorithms or estimators are often employed in combination with model-based approaches. These methods are currently investigated for real-time monitoring in the framework of Digital Twins (DT) for structural diagnosis.

- *Data-based [21]:* is based on pattern recognition principles. Supervised and unsupervised learning methods are adopted to replace model-based approaches, removing the need for a simulation model [21, 80]. These methods have caught the attention of many engineers and the industries are showing high interest in this area for real-time monitoring and damage detection in the DT framework. The need for large dataset and robust pre-trained algorithm is however still a bottleneck for many applications. Physics-Informed Neural Network (PINN) [99] solutions are also emerging in the field of inverse identification, merging data-driven and model-based approaches. The complexity of these solutions still needs to be carefully explored and they are therefore mostly employed by academic researchers.

Each category differs from the others regarding the numerical model employed to solve the inverse problem. Nevertheless, all approaches use sensor data as input and yield system parameters, e.g. external loads, as an output (Fig. 1.3).

The use of inverse methodologies in structural applications is firmly established and currently under development. With the swift digital transformation of structural assessment, the rise of various digital technologies is leading future trajectories of inverse problems. DT has attracted growing attention in engineering research and industry in the last decades. The main goal in the field of structures is to provide information about the current or future state of the structural behaviour by integrating real-time data. The development and employment of high-performance computing show a future increase of the applicability of DT for structural applications, addressing large-scale problems.

Examples of DT for structural assessment and engineering simulations implemented in commercial software are *Executable Digital Twin (xDT)* [167] from Siemens Digital Industries Software and *Ansys Twin Builder* [14]. Both employ physics-based or data-driven solutions.

The current trajectory in inverse identification for structural applications is marked by a pronounced focus on hybrid Artificial Neural Network (ANN) solutions, e.g. [105, 111, 59], which seamlessly combine model-based and data-driven principles. Despite this trend, the industry predominantly relies on signal processing-based and model-based methods, thanks to their proven robustness. An example of a model-based approach is the Kalman Filter (KF) [164], which has been proven to be a powerful solution for full-field response, load and parameter identification. This PhD research focuses on specific challenges identified in the application of Kalman filtering methods to structural problems.

1.2 Problem statement

Kalman-based methods have been widely explored in literature and applied to inverse problems across various scale levels, demonstrating high estimation accuracy. These methods have proven effective in both simulated and real test cases, showcasing distinct advantages over other established techniques. The estimator has become very attractive in the field of structural monitoring due to its real-time operation, leveraging current measurements to dynamically correct the states of the monitored system. Kalman filtering requires the usage of high-fidelity models. In the investigated framework, a Finite Element (FE) model is used to represent the structure as it allows to capture the fully distributed dynamics at high fidelity level. When dealing with this type of modelling, the employment of a Reduced Order Model (ROM) formulation, embedded in the KF, is required. This approach results in a smaller model size and faster computation while still preserving the dominant behavior of the model. Moreover, the Extended Kalman Filter (EKF) [164] further extends the applicability of the KF to deal with nonlinear and parametric systems. The incorporation of a proper parametric Model Order Reduction (pMOR)

technique enhances the versatility of the KF, expanding its range of effectiveness in scenarios where nonlinearity and parametric complexity pose challenges.

Although Kalman-based methods are nowadays well-known and robust techniques applied on several industrial fields, there are still opportunities to improve some key points. Two steps are needed for a successful estimation:

- **Model calibration** concerns Finite Element Model (FEM) updating/-validation in the frequency range of interest, positioning of sensors on the numerical model, modelling the dynamics of augmented states and to properly include these in the filter;
- **Filter calibration** concerns the tuning of process and measurement covariance matrices and the tuning of initial state covariance.

Filter calibration is out of scope of this PhD research. The following challenges are identified in the field of Kalman filtering:

- *Sensor calibration:* The positioning of sensors on the numerical model is required for the application of the KF. Even if the sensor location is known after being installed on the structure, the corresponding location on the numerical model could become a source of error because i) the mesh size of the FE model could not have a corresponding node or element to the location on the physical structure, ii) the sensor orientation is difficult to be known with high accuracy. These errors should be included in the measurement noise, but they are normally not evaluated because they are difficult to be modelled. A calibration of the sensor placement on the numerical model could help to improve the estimation;
- *Optimal Sensor Placement (OSP):* the optimal number, type and location of sensors is important first of all to guarantee the system observability and achieve a stable estimation. The effectiveness of the existing OSP method based on Popov-Belevitch-Hautus [75] (PBH) method for multiple loads estimation has been demonstrated and validated on numerical [175] and experimental cases [150]. However, this approach does not allow to assess the trade-off resulting from the noise corresponding to different sensor types and cannot take into account the impact of the sensor selection on the dynamic range of the obtained estimates. Moreover, in order to select an optimal set of observations, the OSP uses the condition number of the PBH matrix to quantify which set gives an observable system with an acceptable conditioning and a minimum number of sensors. This condition number is highly affected by the scaling of the measurements matrix and this can lead to poor reliability of the method. Indeed, the PBH method can state if a system is observable or not given a set of measurements,

but can not quantify how much a system is observable and thus if the set of measurements is optimal.

- *Need for high-fidelity models:* The use of high-fidelity models becomes relevant for the accurate analysis of complex systems, leading to time-consuming model updating/correlation and simulation analysis. Nevertheless, the process of inverse identification becomes more challenging in terms of modelling, involving specialized nonlinear filtering techniques.
- *Estimation of multiple loads and/or parameters:* Kalman-based techniques have been validated on real test cases for multiple load estimation [150, 39, 190] by employing the augmented formulation, i.e. Augmented Kalman Filter (AKF). One requirement of the AKF is that at least one position-level measurement for each augmented state is needed in order to guarantee the system observability. More requirements arise when loads and parameters are jointly estimated [39]. This poses a challenge when distribution of forces or physical parameters, e.g. mass or stiffness, are estimated simultaneously. An example is the estimation of aerodynamic forces on an airfoil: in a FE model formulation, a number of forces equal to the number of nodes of the airfoil should be estimated. This leads to an increase of the number of sensors needed.

1.3 Objectives and Achievements

The Kalman Filter and its class of estimators developed for nonlinear/parametric systems and for load estimation are recursive predictor-corrector algorithms. The estimators rely on statistical models to predict the system state and update these predictions based on incoming measurements. They incorporate information about the system dynamics and the measurement noise, using statistical distributions to iteratively refine its estimates. Altough KF estimators have been succesfully applied to a large field of application domains, there are still some key points to be addressed in order to improve the robustness of the method.

The primary objective of this PhD research is to develop innovative methods and workflows for Kalman-based joint input/parameter/state estimation to solve the inverse problem in different engineering domains and on different numerical models, addressing the challenges mentioned in Sec. 1.2 and overcoming common limitations identified in aerospace and automotive communities. Two innovation goals and corresponding objectives are identified:

1. **Increase the robustness of Kalman filtering methods**;

   (a) *Objective 1:* Provide a workflow for the applicability of multi-load estimation via AKF on an industrial use-case by i) using a reduced set of sensors and, ii) calibrating the sensor locations on the numerical model in order to reduce the sensor uncertainties.

   (b) *Objective 2:* Development of advanced Optimal Sensor Placement methodologies, which enable a more accurate and robust a-priori assessment of the impact of sensor selection on the AKF estimation.

2. **Extend and enable the usage of Kalman-based methods for unexplored application domains.**

   (a) *Objective 3:* Reduce modelling effort and computational costs needed in high-fidelity simulations involving complex dynamics or local effects.

   (b) *Objective 4:* Relax the observability requirements for the estimation of load or parameter distributions involving a high number of augmented states to be simultaneously estimated.

To achieve the research goals, three use-cases are presented, each one connected to one or more research objectives (Fig. 1.4):

- **Linear system, a twistbeam rear suspension:** this use-case demonstrates the applicability of the AKF to an industrial test-case for multiple load estimation. Its performance is compared with a signal processing-based technique, i.e. Transfer Path Analysis (TPA) [170, 65]. The existing OSP method based on PBH [175] is applied and the AKF reaches good accuracy on full-field strain data and experimental load reconstruction by using less sensors with respect to TPA. The contribution also proposes an optimization technique to minimize the errors on the match between real sensors and their virtual locations on the FE model. A following contribution provides two novel alternative metrics for OSP, based on: i) steady-state error covariance of the estimation, ii) estimator bandwidth, with respect to the available set of measurements. The three strategies are compared and discussed for multiple input/state estimation on the twistbeam rear suspension.

- **Nonlinear system, helicopter rotor blade:** this use-case demonstrates the application of Kalman filtering for aerodynamic load estimation on a rotating helicopter blade in steady aerodynamic conditions. A simplified multibody model is employed within the estimator and the Augmented Extended Kalman Filter (AEKF) is used. The proposed approach addresses the identification problem by modelling the aerodynamic loads as general external forces, reducing the modelling effort and the computational complexity. Accurate estimation of aerodynamic forces

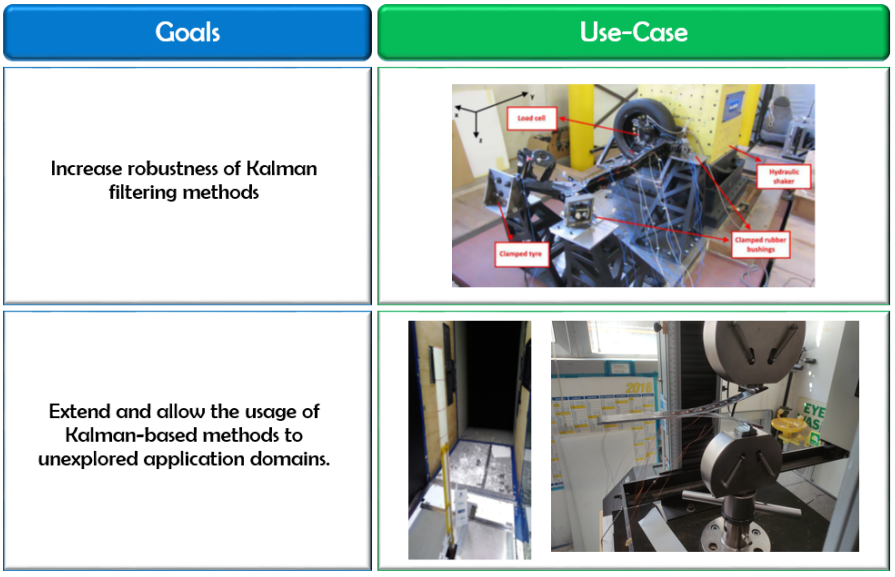

Figure 1.4: Goals and correspoding use-cases of the PhD. Twistbeam rear suspension (top), scaled helicopter blade (bottom left) and composite DCB (bottom right).

is achieved by evaluating the lift and drag formulas using the estimated states at every time step.

- **Parametric system, failure in composite structures:** this use-case applies the KF estimation to the field of composite structures. In particular, a Double Cantilever Beam (DCB) is proposed to study the monitoring of damage propagation in composite laminates by using the AEKF. The degradation of stiffness in the model is estimated jointly with the critical failure load. A simplified linear model is adopted and the optimal number of sensors is studied.

The following achievements can be summarized:

- Firstly, a clear workflow for *model calibration* within the KF framework is provided and demonstrated on an industrial use-case. The process involves three key steps to facilitate successful state and load estimation: i) Training scenario, ii) FEM validation, iii) Sensors calibration. By following these sequential steps, together with the usage of a suitable OSP strategy, the estimation process is optimized, meaning that the systematic approach helps mitigate potential sources of uncertainties arising from

both the numerical model and measurements, thereby enhancing the overall robustness and accuracy of the KF.

- The current PBH-based OSP is designed to meet the minimum requirement for system observability, a crucial aspect for ensuring stable estimation through KF. However, the existing approach relies on the PBH test and does not guarantee an optimal estimation given a subset of selected sensors. It can be demonstrated that the observability-based OSP strategy lacks robustness with respect to measurement scaling, compromising the reliability of the estimation process. To address these limitations, two innovative metrics have been introduced. They are based on steady-state error covariance and estimator bandwidth. The sensitivity to measurements scaling is mitigated with the proposed approaches. Moreover, both metrics have the advantage to include process and measurement noises, leading to an improved estimation of states and loads.
- The need for high-fidelity models when dealing with complex dynamics is alleviated by incorporating simplified models within the KF estimator. This is achieved by making specific assumptions tailored to the use-case. The AKF demonstrates its potential in compensating for modeling errors, allowing for the integration of a less accurate numerical model. This advantageous feature enables the adoption of mid-fidelity models, presenting a practical solution that not only simplifies the modeling process but also results in a more efficient and less time-consuming estimation.
- In the final stage, the challenge of estimating distributed loads and parameters has been tackled. The observability of the system in this specific context requires a substantial amount of sensor data, which is impractical for a real test case. A solution has been proposed by incorporating a priori knowledge of the spatial load/parameter distributions directly into the KF estimator. This integration is based on the principles of hyper-reduction techniques [26]. By leveraging this information, a reduced set of loads and parameters is estimated, translating in less sensors required to achieve the observability. The incorporation of a priori knowledge plays a key role in optimizing the estimation process for complex physical systems, enhancing the feasibility and efficiency of the observability requirement in real-world scenarios.

1.4 Outline of the dissertation

This section provides an overview of the structure of this dissertation. The thesis is divided in two main parts. **Part I** gives a summary of the scientific context

of the research with goals, objectives and achievements. **Part II** provides a collection of the four key publications.

Part I presents four main chapters. The current chapter introduces the context of this research, explaining the importance of inverse identification for structural applications, with particular focus on a model-based method such as the Kalman Filter estimator. This chapter also outlines the research goals and corresponding objectives, providing a brief summary of the achievements. Chapter 2 is intended to provide a general state-of-the-art overview of the field of inverse identification with a focus on the model-based inverse problem. A more detailed overview of the methodologies and assumptions adopted in this research is also provided in this chapter. Chapter 3 elaborates the research approach and the achievements of the thesis presented in the four publications. Chapter 4 summarizes main conclusions and formulates future research tracks.

Part II is a collection of the four key publications that have allowed to achieve the goals and objectives of the research. Each of the papers focuses on a different use-case of the three mentioned in Sec. 1.3 and aims to fulfill one or more objectives. Each contribution presents a proper state of the art, methodology description, numerical and/or experimental validation. All the papers are published in international journals and are listed in the following:

- **Paper I**: *Kalman-based load identification and full-field estimation analysis on industrial test case.* R. Cumbo, T. Tamarozzi, K. Janssens, W. Desmet. Mechanical Systems and Signal Processing 117 (2019), 771-785.

  The AKF is compared with a signal processing-based method to address the inverse identification problem for the estimation of multiple loads. Paper I describes the workflow for a correct application of KF to an industrial test case. The contribution shows all the steps to be performed off-line under *model calibration*, discussing FE model validation and improved estimation by adopting an OSP strategy. *Filter calibration* is also partially addressed.

- **Paper II**: *Advanced optimal sensor placement for Kalman-based multiple-input estimation.* R. Cumbo, L. Mazzanti, T. Tamarozzi, P. Jiranek, W. Desmet, F. Naets. Mechanical Systems and Signal Processing 160 (2021), 107830.

  Two novel metrics for OSP are proposed to provide a more robust approach, able to mitigate measurement scaling issues and incorporate uncertainties in the sensor selection. The methods are tested on the same FE model proposed and validated in Paper I. Results are compared with the PBH metric proposed in [175].

- **Paper III**: *State and Force Estimation on a Rotating Helicopter Blade through a Kalman-Based Approach.* R. Cumbo, T. Tamarozzi, P. Jiranek, W. Desmet, P. Masarati. Sensors, 2020(15), 4196.

  Paper III is a first contribution in an engineering field that has not been explored yet in the framework of KF estimation. It addresses the implementation of high-fidelity models for coupled structural-aerodynamic problems in the estimator. A multibody model is adopted with lower fidelity aerodynamic model that is compensated by the filter. A numerical validation is proposed.

- **Paper IV**: *Recursive parameter estimation for the on-line monitoring of delamination growth in composite structures.* R. Cumbo, D. De Gregoriis, F. Danzi, A. Kumar, F. Naets. Structural Health Monitoring, 2024(0), 1-20.

  Paper IV brings the KF to the field of composite materials. In particular, it addresses the problem of on-line identification of delamination growth on composite laminates. This contribution proposes a novel recursive estimation able to relax the observability requirement when high number of parameters are simoultaneously estimated. The a priori knowledge of interface stiffness distribution between two laminae is embedded in the filter to further reduce the number of parameters to be estimated, following the principles of hyper-reduction techniques. A numerical and experimental validation is proposed.

Chapter 2

State of the Art and Methodologies

2.1 Inverse problems for structural applications

Many inverse-identification techniques based on signal processing or on models have been proposed in literature. In the past, the field of signal processing has been widely applied to industrial applications because of its easy implementation. Vibration and time behaviour of any structure reveal dynamic properties of the system like structural parameters and input loads. The main known signal processing inverse methods, mostly adopted at industrial level, are Transfer Path Analysis (TPA) and Operational Modal Analysis (OMA). TPA was originally used to solve inverse identification during off-line testing and it involves measuring vibration data at different locations to analyzes how the energy is transmitted through different paths or components by solving a mathematical model. TPA is adopted to support and optimize engineering design to mitigate vibration and noise transmission paths. However, some disadvantages limit its usability as e.g., large number of sensors needed to improve the robustness. Operation Path Analysis (OPA) is a more efficient version of TPA but its causal assumption among outputs limits the applicability in most industrial application cases. OMA, on the other hand, allows to extract modal parameters, i.e. natural frequency, damping ratio, and mode shapes, of a structure during operation by analyzing vibration sensor data. Both TPA and OMA play crucial roles in noise and vibration engineering, aiding in design optimization and structural monitoring. Data-based methods can be considered a novel version of signal processing-based methodologies, even if the latter

require less computational effort and fewer sensor data. The introduction of data-based methods in structural technologies started with the advance of Artificial Neural Network (ANN) in the field of structural dynamics and mechanics: [90] applies ANNs to solve vibration-based inverse parametric identification problems, [112] proposes a review on ANNs for the inverse modelling of unknown constitutive laws, [182] proposes the usage of ANNs to predict inertial and stiffness parameters of a cantilever beam representative of an aircraft wing, while [47] explores the delamination prediction of fatigue loaded coupons by using Convolutional Neural Networks (CNNs). If a large dataset is available, these methodologies are nowadays the preferred option in the development of industrial products for structural applications. However, another disadvantage is in the limited number of information returned in output. Indeed, it is almost impracticable to simultaneously estimate a large number of loads, stiffness and damping parameters with a single ANN since issues occur during training when different orders of magnitude are involved. Even if this problem has been addressed for different application fields by scaling the outputs, the study of the optimal weights requires an increased level of effort. Moreover, estimation of full-field information is not possible if a model-based approach is not considered. Big steps have been taken in the field of PINN solutions [82] or hybrid FEM-ANN approaches for time series analysis [106, 105], but their applicability at industrial-level still requires improvements and robustness. The approach presented in [105] is a valid candidate to compete with model-based approaches as it can compensate modelling errors or missing physics with ANN black-box models. Further extension is still needed to employ this methodology for parameter and load estimation. Model-based approaches have the advantage to provide the full knowledge of the physical behavior of the system. In literature, two main methods are frequently applied even if for two different scopes: i) the Inverse Finite Element Modelling (iFEM) and ii) the Kalman Filter (KF) estimator. The iFEM was originally proposed by Tessler [180] and it is normally used to address the task of shape-sensing, i.e. reconstruction of the deformation field, based on local measured sensor data. The method is based on the minimization of a least-squares error function defined between the real measurement and the one computed by direct FEM and can be thus considered as a form of model updating. The inverse problem needs a detailed mesh and boundary conditions of the system and can be applied for full-field reconstruction and load identification, even if limited work is presented in literature for the latter case. As other inverse methods, the solution of iFEM can fall in local minima and regularization methods should be considered [189]. This inverse approach has been explored in literature for the static analysis of composite structures with different level of complexity. Some examples are compression buckling loads of a composite plate [136] and tension loads on a multistringer panel representative of helicopter fuselage part [137]. Full-field reconstruction through multimodal

information has also been investigated by combining strain measurements with Digital Image Correlation (DIC) displacement data [138, 100]. To the authors best knowledge, the iFEM is developed to solve only static problem and no dynamic cases have been presented in literature. Moreover, the iFEM is a deterministic approach that does not consider measurement noise and model errors that could arise from incorrect modelling of boundary conditions or other FE parameters. [60] proposed a study about the propagation of modelling uncertainties on the performances of the iFEM. Contrarily, the KF estimator approaches the inverse problem in a stochastic manner by considering both measurements and model uncertainties. KF has been widely applied to industrial applications for inverse identification of loads, parameters and full-field response [150, 39, 130, 19] on static and dynamic problems. The KF solves the inverse problem by minimizing the error on the estimated measurements and correcting the states of the system accordingly. The advantage of the KF over the iFEM is that less modelling effort is needed in terms of formulations accounted for in the method itself and it can be easily extended for nonlinear systems. Furthermore, limited work regarding the reconstruction of nonlinear phenomena through iFEM has been presented in literature. Different Kalman filtering schemes are instead available for nonlinear or parametric models. More details are discussed in Section 2.3, *Overview of Kalman-filtering methods*. KF, iFEM, ANN and hybrid ANN methods are compared in Table 2.1. As can be concluded:

- Model-based methods require high-fidelity models to reach high accuracy levels. KF can employ less-accurate models as it considers modelling and measurement uncertainties. Hybrid ANN methods employ FE models and compensate inaccuracies with black-box models.
- Training scenarios are always needed but the amount of data depends on the method employed. Model-based methods require much less data (needed for model validation) than ANN methods.
- All methods, with the excpetion of ANN, can perform full-field response, load and parameter identification and can be formulated for on-line monitoring. Purely ANN methods are limited to the set of sensor locations used for training.
- All methods can solve static and dynamic problems, including nonlinearities, with the exception of iFEM which is still of limited applicability.

The core of this PhD research is focused on Kalman filtering techniques and aims to address current limitations and challenges in industrial field.

	High-fidelity FEM	**Training scenario**	**Identification task**	**Nonlinear problems**	**Applications**
KF	Yes	Limited to model validation	Full-field response, loads, parameters	EKF	Static and Dynamic
iFEM	Yes	Limited to model validation	Full-field response, loads, parameters	Limited work presented	Static
ANN	No	Yes	Limited to output in the training scenario	Yes	Static and Dynamic
Hybrid ANN	No	Yes	Full-field response, loads, parameters	Yes	Static and Dynamic

Table 2.1: Comparison between most used inverse methods in literature.

2.2 The model-based inverse problem

With the advance of technology in the field of numerical modelling and simulation, model-based approaches have become very attractive and have shown to be powerful solutions in the field of inverse identification. The model-based inverse methods are used for three main tasks in structural mechanics and dynamics: i) design optimization, ii) model updating, iii) structural health monitoring. The inverse problem is by definition an optimization process, aiming to optimize a set of system parameters by minimizing the observation error. Design optimization of a structure normally requires several iterations by tuning model parameters and testing conditions. The optimal design is then chosen among these iterations as the one minimising the observation error. Similarly, the model updating is also an iterative problem falling under the umbrella of optimization problems.

A different application field of model-based inverse problems is structural health monitoring, where normally a set of parameters is selected based on experience and estimated under testing and operating conditions. Four stages of structural health monitoring can be identified: i) detection, ii) localization,

iii) quantification, iv) prognosis. The tasks from detection to quantification are addressed by combining the numerical model of the structure and a set of observations.

The employment of advanced simulation models i.e. FEM or Multibody Simulation (MBS) is thus relevant for model-based methods during the complete life of a mechanical component. The governing equation of a second order model in a FE formulation is the following:

$$\mathbf{M}\ddot{\mathbf{z}} + \mathbf{C}\dot{\mathbf{z}} + \mathbf{K}\mathbf{z} = \mathbf{B}\mathbf{u} \tag{2.1}$$

where $\mathbf{z}(t) \in \mathbb{R}^{n_d}$ is the vector of Degrees of Freedom (DoF), $\mathbf{M}$, $\mathbf{C}$ and $\mathbf{K}$ are respectively the mass, damping and stiffness matrices, $\mathbf{u}(t) \in \mathbb{R}^{n_u}$ is the vector of input loads and $\mathbf{B} \in \mathbb{R}^{n_d \times n_u}$ is the Boolean matrix distributin the input loads over the system DoFs.

An accurate simulation model requires detailed calibration of physical properties represented by $\mathbf{M}$, $\mathbf{C}$ and $\mathbf{K}$ and this is the biggest bottleneck of these techniques. Indeed, many challenges still exist in the field of model-based inverse identification:

- The accuracy of the numerical model gives a level of reliability of the inverse problem. If the model is not sufficiently accurate within the range of applicability of the mechanical system, the inverse solution will return wrong quantities. As an example, consider a simple 1 Degree of Freedom (DoF) mass-spring system with a static force applied to the mass. Given the measured displacement, if the assumed spring element stiffness is smaller than the correct value, the identified force will have a smaller amplitude to compensate (Fig. 2.1). During operating conditions, this could lead to underestimation of critical loads and consequent loss of reliability of the structural health monitoring system.
- Optimal sensor type and location selection is an active topic of research and currently there is no clear workflow for the definition of an optimal sensor network, with the exception of some specific methods, e.g. [175, 171, 142]. This is a common challenge of signal processing-based, model-based and data-based methods since in any case, the instrumented sensors need to guarantee the observability of the inverse problem.
- Model-based inverse problems have been validated on large structures at macro-scale level for the identification of global loads and global parameters. When composite materials are involved, local effects could arise like impact damages or delamination which require more complex modelling. Sensors are also difficult to be efficiently located in these situations. Some specific cases have been investigated in literature for

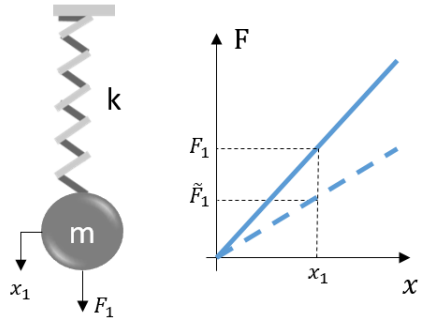

Figure 2.1: Forced 1 DoF mass-spring system. Correct (solid line) and estimated assuming too small stiffness value (dashed line).

in-house testing, but the technology is still far from being applied at industrial level, especially during operating life.

Nonetheless, numerical issues could also arise, as it is common for all categories of inverse problems:

- *Ill-posedeness:* the problem can be unstable, meaning that small changes in constraints can lead to large changes in the solution space. Given a set of physical constraints, the solution can be non-unique, thus the lack of constraints can lead to an unsolvable problem.
- *Ill-conditioned:* the problem can be sensitive to perturbations, meaning that small errors in the dataset can cause a large error in the computed solution.

Despite the advantages of model-based approaches over signal processing-based and data-driven methods, the above mentioned challenges still limit industries from employing such techniques at a large scale level, focusing more on the optimization of sensor technologies and advanced AI solutions. This PhD research aims to address these challenges at industrial scale level by employing Kalman-filtering methods.

2.3 Overview of Kalman-filtering methods

The KF was developed by Rudolf E. Kálmán in the 1960s [95] for linear (or linearized) systems with noisy or uncertain properties and it has been widely applied in several engineering fields. The filter is based on predictor-corrector algorithm [164]: it predicts the current state of the system by solving a forward

simulation. Then the state is updated using new physical measurements. The Kalman gain has an important role in the estimation since its value determines how reliable the predicted states or the actual measurements are and it is calculated using the state and covariance matrices. The higher the uncertainty of the prediction relative to the measurements, the smaller the Kalman gain, and vice versa.

The KF in its standard formulation is used for real-time full-field time-series reconstruction. When loads or parameters are unknown, the augmented formulation can be adopted. The key point of the Augmented Kalman Filter (AKF) [164] is the implementation of a force or parameter model in the filter. This task is particularly challenging since most of these quantities have a priory unknown distribution in time. However, a 0th order random walk model has been adopted for several applications resulting in explainable results [175, 115, 151, 129]. Other KF formulations exist in literature for the joint input/parameters/state estimation, e.g. the Dual Kalman Filter (DKF) [19], which is more computationally expensive since it approaches the estimation in two steps. When a nonlinear or parametric model is involved, the Extended Kalman Filter (EKF) [164] and the Sigma-Point Kalman Filters, e.g. Unscentent Kalman Filter (UKF) [164], are instead used.

An important requirement of the KF to obtain a stable estimation is that the sensors network guarantees system observability. Some general rules are:

- The number of DoFs of the model has to be equal or greater than the number of external loads and parameters to be estimated [130, 164];
- Given the 0th order random walk model of the unknown quantities, the number of position/strain measurements has to be equal or greater than the number of external loads and/or parameters to be estimated [130]. When the estimation of parameters is involved, the system observability leads to more constraints on the number and type of sensors [39].

Linear Time Invariant systems and Augmented formulation

Given a Linear Time Invariant (LTI) system, the following state-space formulation is considered:

$$\begin{cases} \dot{\mathbf{x}}(t) = \mathbf{A}\mathbf{x}(t) + \mathbf{B}\mathbf{u}(t) + \mathbf{w}(t) \\ \mathbf{y}(t) = \mathbf{C}\mathbf{x}(t) + \mathbf{D}\mathbf{u}(t) + \mathbf{v}(t) \end{cases} \tag{2.1}$$

where:

- $\mathbf{x}(t) \in \mathbb{R}^{n_s}$ and $\dot{\mathbf{x}}(t) \in \mathbb{R}^{n_s}$ are respectively the states vector and its time derivative;
- $\mathbf{u}(t) \in \mathbb{R}^{n_u}$ is the control input vector;
- $\mathbf{y}(t) \in \mathbb{R}^{n_m}$ is the vector of measurements;
- $\mathbf{A} \in \mathbb{R}^{n_s \times n_s}$ and $\mathbf{B} \in \mathbb{R}^{n_s \times n_u}$ are real matrices with embedded system properties. In particular, if a mechanical system is considered, the second-order equations of motion (Eq. 2.1) is formulated in a first-order scheme and the system matrix $\mathbf{A}$ will include mass $\mathbf{M}$, stiffness $\mathbf{K}$ and damping $\mathbf{C}$ matrices [149];
- $\mathbf{C} \in \mathbb{R}^{n_m \times n_s}$ and $\mathbf{D} \in \mathbb{R}^{n_m \times n_u}$ are real matrices with embedded measurements information;
- $\mathbf{w}(t)$ and $\mathbf{v}(t)$ are called respectively process and measurements noise with associated covariance matrices $\mathbf{Q}$ and $\mathbf{R}$.

The KF assumes that the noise in the system is white and follows a Gaussian distribution with zero-mean. In practice, the KF can still work reasonably well even if the noise deviates slightly from these assumptions.

When the loads $\mathbf{u}(t)$ are unknown, the augmented state vector and the process noise are defined:

$$\begin{cases} \mathbf{x}^* &= [\mathbf{x} \quad \mathbf{u}]^T \\ \mathbf{w}^* &= [\mathbf{w} \quad \mathbf{w_u}]^T \end{cases} \tag{2.2}$$

In order to define the augmented scheme of the KF, the dynamics of the input has also to be modeled. In this PhD research, a 0th-order random walk model is considered for the input as follows:

$$\dot{\mathbf{u}}(t) = \mathbf{0} + \mathbf{w_u}(t) \tag{2.3}$$

With $\mathbf{w_u}$ being a stochastic process associated with the covariance matrix $\mathbf{Q_u}$. The latter defines the variation of the input within a time-step Δt.

Given the state-space formulation in Eq. 2.1, the time-discrete Augmented Kalman Filter (AKF) formulation can be written as:

$$\begin{cases} \mathbf{x}_k^* = \mathbf{F}^* \mathbf{x}_{k-1}^* + \mathbf{w}_{k-1}^* \\ \mathbf{y}_k = \mathbf{H}^* \mathbf{x}_k^* + \mathbf{v}_k \end{cases} \tag{2.4}$$

where $\mathbf{F}^*$ is the discrete-time form of the augmented state matrix $\mathbf{A}^*$ derived from $\mathbf{A}$ and $\mathbf{B}$ [149], $\mathbf{H}^* = [\mathbf{C} \quad \mathbf{D}]$, and $\mathbf{Q}^*$ being a block diagonal matrix composed of $\mathbf{Q}$ and $\mathbf{Q_u}$. The matrices $\mathbf{F}^*$ and $\mathbf{Q}$ depend on the chosen discretization scheme [188].

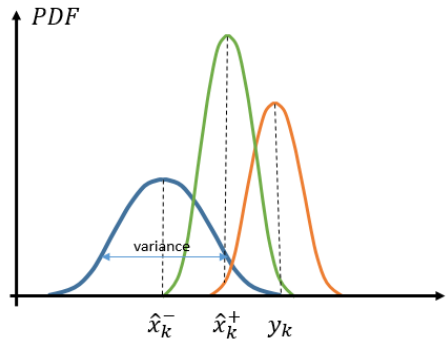

Figure 2.2: Principle of Kalman Filter estimation at time step k. The states are predicted and corrected with the measurements. Both quantities have a Probability Density Function (PDF) with Gaussian distribution. The Kalman Filter combines these information to give an optimal estimate of the states.

Considering the a-priori $\mathbf{x}_k^{*-}$, i.e. predicted states obtained by solving the numerical model, and a posteriori $\mathbf{x}_k^{*+}$, i.e. estimated states obtained by updating $\mathbf{x}_k^{*-}$ with measurements $\mathbf{y}_k$ (Fig. 2.2), the AKF predictor-corrector algorithm is as follows:

Time update

$$\hat{\mathbf{x}}_k^{*-} = \mathbf{F}^* \hat{\mathbf{x}}_{k-1}^{*+} \tag{2.5}$$

$$\mathbf{P}_k^{*-} = \mathbf{F}^* \mathbf{P}_{k-1}^{*+} \mathbf{F}^{*T} + \mathbf{Q}_{k-1}^* \tag{2.6}$$

Measurement update

$$\mathbf{K}_k = \mathbf{P}_k^- \mathbf{H}^{*T} \left(\mathbf{H}^* \mathbf{P}_k^- \mathbf{H}^{*T} + \mathbf{R}_k \right)^{-1} \tag{2.7}$$

$$\hat{\mathbf{x}}_k^{*+} = \hat{\mathbf{x}}_k^{*-} + \mathbf{K}_k \left(\mathbf{y}_k - \mathbf{H}^* \hat{\mathbf{x}}_k^{*-} \right) \tag{2.8}$$

$$\mathbf{P}_k^+ = \left(\mathbf{I} - \mathbf{K}_k \mathbf{H}^* \right) \mathbf{P}_k^- \tag{2.9}$$

The minimization of the trace of the error covariance matrix $\mathbf{P}_k$ is a fundamental aspect of the KF. The trace of the error covariance matrix is a measure of the overall uncertainty in the estimated state of the system and the KF aims to minimize this trace to achieve optimal state estimation. $\mathbf{P}_k$ is defined as:

$$\mathbf{P}_k = E \left[\left(\mathbf{x}_k^* - \hat{\mathbf{x}}_k^* \right) \left(\mathbf{x}_k^* - \hat{\mathbf{x}}_k^* \right)^T \right] \tag{2.10}$$

In order to have a stable estimator and thus to have $\mathbf{P}_k$ converging to a constant value, the augmented system in Eq. 2.4 has to be observable, i.e. the states of the dynamical system can be estimated from measurements. For a real structural dynamic system, the normal modes are all damped and this leads to a detectable system, i.e. its unmeasurable modes are stable. This is however not sufficient to ensure a a stable estimation with the AKF. Recalling the observability requirements in Sec. 2.3, the AKF is observable if the following conditions are satisfied [130]:

- the number of DoFs of the reduced model has to be equal or greater than the number of external loads to be estimated: $n_r \geq n_u$;
- the number of position-level measurements has to be equal or greater than the number of external loads to be estimated: $n_y \geq n_u$;
- in the case of full position measurements, the AKF leads to a fully observable system and to a stable estimator. Performing only acceleration measurements will typically not lead to a stable AKF for structural systems.

The AKF can be used also for parameter estimation. In that case, a parametric model is employed and the Extended Kalman Filter (EKF) scheme should be adopted [39].

Nonlinear dynamics: Extended Kalman Filter

The Extended Kalman Filter (EKF) is an extension of the traditional KF designed to handle non-linear systems by performing linearization at each time step. Considering a general nonlinear process and measurement models, i.e. $f(\mathbf{x}, \mathbf{u}, t)$ and $h(\mathbf{x}, \mathbf{u}, t)$, the Taylor series expansion truncated at the first order gives:

$$\dot{\mathbf{x}}(t) \approx f(\mathbf{x}_0, \mathbf{u}_0, t) + \frac{\delta f}{\delta \mathbf{x}}\Big|_0 (\mathbf{x} - \mathbf{x}_0) + \frac{\delta f}{\delta \mathbf{u}}\Big|_0 (\mathbf{u} - \mathbf{u}_0) \tag{2.11}$$

$$\mathbf{y}(t) \approx h(\mathbf{x}_0, \mathbf{u}_0, t) + \frac{\delta h}{\delta \mathbf{x}}\Big|_0 (\mathbf{x} - \mathbf{x}_0) + \frac{\delta h}{\delta \mathbf{u}}\Big|_0 (\mathbf{u} - \mathbf{u}_0) \tag{2.12}$$

where $\frac{\delta f}{\delta \mathbf{x}}$, $\frac{\delta f}{\delta \mathbf{u}}$, $\frac{\delta h}{\delta \mathbf{x}}$, $\frac{\delta h}{\delta \mathbf{u}}$ are the Jacobians of the system. $\mathbf{x}_0$ is the nominal state vector. The EKF scheme linearizes the system around the a posteriori estimated state, which becomes the nominal state.

The basic equations of time update and measurement update for the discrete-time EKF are modified as follows.

Time update

- The state prediction is obtained from the nonlinear system dynamics function f:

$$\hat{\mathbf{x}}_k^- = f(\hat{\mathbf{x}}_{k-1}, \mathbf{u}_{k-1}) + \mathbf{w}_{k-1} \tag{2.13}$$

- The Jacobian matrix $\mathbf{F}$ of the dynamics function f is computed as:

$$\mathbf{F} = \frac{\partial f}{\partial \mathbf{x}}\Big|_{\hat{\mathbf{x}}_{k-1}, \mathbf{u}_{k-1}} \tag{2.14}$$

- The predicted error covariance matrix $\mathbf{P}_k^-$ is updated using:

$$\mathbf{P}_k^- = \mathbf{F}\mathbf{P}_{k-1}\mathbf{F}^T + \mathbf{Q}_{k-1} \tag{2.15}$$

Measurement update

- The measurement prediction is obtained using the nonlinear measurement function h:

$$\hat{\mathbf{y}}_k = h(\hat{\mathbf{x}}_k^-) + \mathbf{v}_k \tag{2.16}$$

.

- The Jacobian matrix $\mathbf{H}$ of the measurement function h is computed as:

$$\mathbf{H} = \frac{\partial h}{\partial \mathbf{x}}\Big|_{\hat{\mathbf{x}}_k^-} \tag{2.17}$$

- The Kalman gain $\mathbf{K}_k$ is calculated as:

$$\mathbf{K}_k = \mathbf{P}_k^- \mathbf{H}^T \left(\mathbf{H}\mathbf{P}_k^- \mathbf{H}^T + \mathbf{R}_k\right)^{-1} \tag{2.18}$$

- The corrected state estimate and error covariance matrix are updated as:

$$\hat{\mathbf{x}}_k^+ = \hat{\mathbf{x}}_k^- + \mathbf{K}_k(\mathbf{y}_k - \hat{\mathbf{y}}_k) \tag{2.19}$$

$$\mathbf{P}_k^+ = (\mathbf{I} - \mathbf{K}_k\mathbf{H})\mathbf{P}_k^- \tag{2.20}$$

The Jacobian matrices are a key component of the linearization process. Their computation is influenced by the discretization scheme used in the process and measurement models. When linearizing these functions, the Jacobian matrix is employed to approximate the partial derivatives with respect to the state variables. Common time discretization schemes include Euler's method, the Runge-Kutta method, or more advanced implicit or explicit techniques methods. The choice of the discretization scheme can affect the accuracy of the linearization and, consequently, the performance of the EKF. In cases where the system dynamics are highly non-linear, the EKF might be less accurate, and alternative methods such as the Unscented Kalman Filter (UKF), or more in general a Sigma-Point Kalman Filter may be considered.

Main principles of Kalman Filter

Observability and Optimal Sensor Placement for multiple load estimation

The observability of a linear time-invariant system is generally addressed through the PBH (Popov-Belevitch-Hautus) test [75]. The observability matrix for a discrete-time system, denoted as:

$$PBH = \begin{bmatrix} \omega_d \mathbf{I_d} - \mathbf{A_d} \\ \mathbf{H} \end{bmatrix} \tag{2.21}$$

is formed by the system and measurement matrices $\mathbf{A_d}$ and $\mathbf{H}$. ω_d identifies the eigenvalues of $\mathbf{A_d}$. The PBH test states that a system is observable if and only if the rank of the observability matrix is equal or greater than the order of the system, meaning that the state can be accurately determined from the output measurements. When the loads are estimated and the 0th-order random walk model is considered, the PBH test should be evaluated at 0Hz, which is the corresponding frequency.

An Optimal Sensors Placement (OSP) method has been proposed in literature [175] for multi-load estimation and has been validated on a large-scale numerical model, based on the PBH test. The method is schematically shown in Fig. 2.3 and two main steps are defined as *Training* and *Screening*. The *Training* phase includes multiple steps: i) a large number of sensors e.g. position, strain, accelerometers are randomly selected over the numerical model; ii) the model is simulated under different training scenarios characterized by different amplitudes, frequencies and load directions and output are collected; iii) a first screening is performed based on sensors with higher sensitivity and distance metric; iv) the remaining sensors are merged to form the matrix $\mathbf{H}$ of Eq. 2.4 and all measurements are scaled to avoid that some sensors have higher influence with respect to others because of different order of magnitude. The *Training* aims thus to reach a reduced but still enough large amount of sensors to the last selecting step, i.e. *Screening*. The method proposed in [175] approches the screening through the PBH test to use the condition number of Eq. 2.21 to quantify which set gives an observable system with an acceptable conditioning and a minimum number of sensors. The following observability metric is implemented:

$$O = \frac{1}{n_u cond(PBH(0))} \tag{2.22}$$

In Eq. 2.22, n_u is the number of loads to be estimated. The PBH matrix is evaluated at $0Hz$ because it is the frequency corresponding to the 0th-order random walk model employed in the AKF in Eq. 2.3. The condition number is defined as the ratio between the largest and the smallest singular value of a matrix. If this number is high, the matrix is poorly conditioned and this typically lead to rank deficiency. It is worth noting that the OSP method has been developed for LTI systems but it can also be applied on linearized systems and thus employed in the EKF scheme.

The main limitation of the OSP is that the condition number is highly sensitive to $\mathbf{H}$ matrix scaling and this can lead to a loss of reliability of the method. As an example, consider a multiple DoFs mass-spring-damper system in Fig. 2.4 with load applied to the last mass on the right. Position measurements are considered for the evaluation of PBH test. A different decreasing of observability,

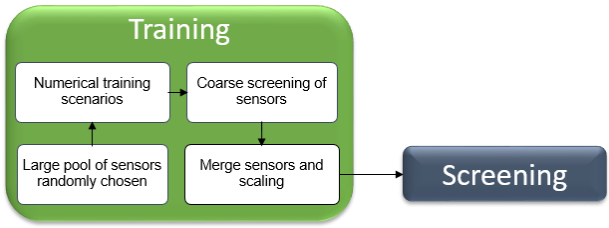

Figure 2.3: Optimal Sensor Placement scheme grouped in two main steps: *Training* and *Screening*.

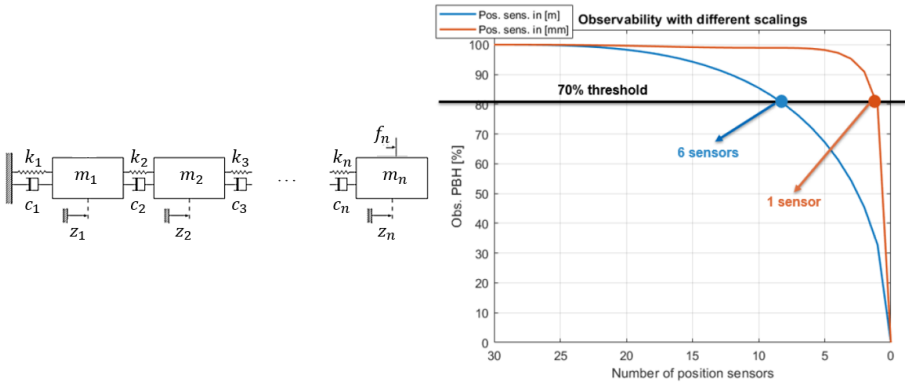

Figure 2.4: Observability decreasing obtained with PBH metric by using position-level measurements on a MKD system.

expressed by O, can be observed when the measurements are in millimiter $[mm]$ and meter $[m]$. Considering a threshold of 70% of decreasing, different numbers of sensors are selected for the optimal estimation of the applied load.

Role of covariance matrices

Two key factors of the KF estimation are the covariance matrices $\mathbf{Q}$ and $\mathbf{R}$, associated respectively to the model and the measurements uncertainties. The noise variables are assumed to be independent, zero-mean white noise processes and the covariance matrices are treated as time-invariant. $\mathbf{R}$ is always known a-priori from the level of noise of the installed sensor in a free-run acquisition. $\mathbf{Q}$, which is indicated as $\mathbf{Q}^*$ in the augmented formulation, is a block-diagonal

matrix:

$$\mathbf{Q}^* = \begin{bmatrix} \mathbf{Q}_m & \mathbf{0} \\ \mathbf{0} & \mathbf{Q}_u \end{bmatrix} \tag{2.23}$$

$\mathbf{Q}_m$ is the uncertainty associated to the FE model and indicates the discrepancies between the numerical and the real models. This level of uncertainty is often assumed to be zero or very low because FE model calibration or updating is performed before being implemented in the KF and is supposed to have reached the best level of accuracy in the predefined range. The higher source of uncertainty is instead in $\mathbf{Q}_u$ (or $\mathbf{Q}_p$ for parameter estimation), which is associated with unknown loads. Their values can be used to regularize the estimation and tackle, i.e. bias the KF to mainly correct these states, the ill-posedness of the problem. Several works in literature propose the use of the L-curve [83] in order to calibrate those values. The L-curve compare the smoothing norm, i.e. $\frac{\sum_{k=1}^{N} ||\hat{\mathbf{u}}_k||_2}{\sum_{k=1}^{N} ||\mathbf{u}_k||_2}$ and the error norm, i.e. $\sum_{k=1}^{N} ||\mathbf{y}_k - \mathbf{H}\hat{\mathbf{x}}_k^*||_2$. Normally, a low value of $\mathbf{Q}_u$ leads to high value of error norm and low value of smoothing norm. When $\mathbf{Q}_u$ increases, the error norm decreases and the problem reaches an optimal value. For higher values of $\mathbf{Q}_u$, the smoothing norm increases again. A typical trend of the L-curve is shown in Fig. 2.5 and the optimal value of $\mathbf{Q}_u$ is located on the corner of the curve. Another approach to select the value of $\mathbf{Q}_u$ is to use the following formula:

$$\mathbf{Q}_u = (\omega_u a_u \Delta t)^2 \tag{2.24}$$

with ω_u and a_u respectively as the expected values, i.e. indicative order of magnitude, of the frequency and amplitude of the load $\mathbf{u}$. Similar to the effect of a low-pass filter, this formulation allows to limit the variation of the estimated input during a time step Δt.

A more recent approach has been presented in literature, called Adaptive-noise Augmented Kalman Filter (A-AKF) [190]. The approach relies on the minimization of the error on the input load and estimated responses and aims to select the optimal covariance values addressing some disadvantages of the L-curve and Eq. 2.24:

- The L-curve does not always show the expected trend of Fig. 2.5 when joint input/state/parameter estimation is addressed;
- Eq. 2.24 requires user experience and does not always return the optimal covariance value.

The A-AKF operates by running a bank of AKF in parallel for a fixed time-window and for each combination of Q samples pre-defined within a given range.

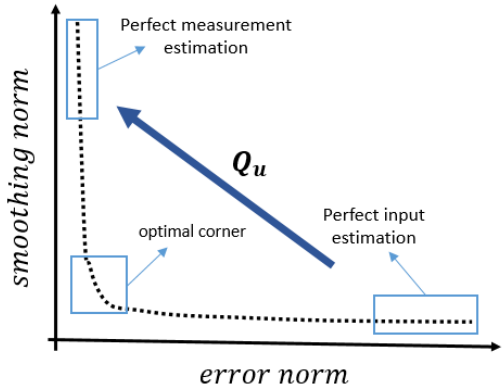

Figure 2.5: L-curve: log-log plot of the norm of a regularized solution versus the norm of the corresponding residual norm.

The method reaches good estimation accuracy but loses the near real-time properties of the AKF.

More in general, the effect of $\mathbf{R}$ and $\mathbf{Q}_m$ or $\mathbf{Q}_u$ can be understood comparing their values:

- if $\mathbf{Q}_{m,u} \gg \mathbf{R}$ the model or the input is less reliable and the estimated response field follows the measured data;
- if $\mathbf{Q}_{m,u} \ll \mathbf{R}$ the model or the input is highly reliable and the estimated response field follows the simulated data.
- if $\mathbf{Q}_m \ll \mathbf{Q}_u$ the highest source of uncertainties are in the input model.

All the applications fall normally in the first case, together with $\mathbf{Q}_m \ll \mathbf{Q}_u$, by assuming that the measured data are reliable and the FE model is highly-correlated with the real model. However, the value of $\mathbf{Q}_u$ should be carefully tuned because if too high, a very noisy input is estimated to match the noise present in the measurements. Under this situation, there is no more filtering, as explained in [150].

Reduced Order Modelling

Even if Reduced Order Modelling (ROM) techniques are not the core of this PhD research, they play a key role in the application of KF when large high-fidelity FE models are involved. Thus, a general overview is summarized here.

Model Order Reduction (MOR) is requested when the dimension of the numerical model is too big and the computational cost too high. The goal of MOR is to project the Full Order Model (FOM) onto reduction space by i) providing good approximation, ii) preserving the model properties, iii) provide computational efficiency. MOR can be used in many applications, both off-line and on-line. Some typical examples are the design optimization and DT, both model-based domains which require computational efficiency. The first concept of MOR has been introduced by Ritz and Galerkin discretization [37] in the definition of a FE model. Indeed, by discretizing a model means to reduce the number of DoFs from infinite (for a continuous model) to an acceptable number of DoFs (for a FE model). The application of a MOR technique on a discretized FE model means to further reduce the size of this model by further approximating the physical description of the model itself.

In case two or more normal modes are needed for a specific application of this model, two or more DoFs are needed in order to correctly describe the dynamics of the model. Projection-based MOR methods can be grouped in two main categories:

- *Linear systems:* MOR approximates the FOM in a compact way:

$$\dot{\mathbf{x}} = \mathbf{A}\mathbf{x}, \dot{\mathbf{x}}_r = \mathbf{A}_r\mathbf{x}_r, \mathbf{A}_r = \mathbf{\Phi}^T\mathbf{A}\Phi \tag{2.25}$$

  where $\mathbf{\Phi}$ is the reduction basis. Methods like modal reduction, balanced truncation and rational Krylov subspace can be applied [24].

- *Nonlinear or parametric model:* MOR can not approximate the FOM explicitly, resulting in a reduced model still embedding the full space:

$$\dot{\mathbf{x}} = f(\mathbf{x}), \dot{\mathbf{x}}_r = \mathbf{\Psi}^T f(\Psi\mathbf{x}) \tag{2.26}$$

  A well-known and accurate method is the Proper Orthogonal Decomposition (POD) [26], based on the Singular Value Decomposition (SVD) performed on a set of configurations of the nonlinear or parametric model. The POD forms the reduction basis by selecting the most meaningful modes, i.e. with higher energy content, among the SVs.

In this PhD contribution, the following reduction bases have been employed using projection-based MOR:

- *Residual attachment modes [46]*: have been used for the estimation of multiple loads through AKF on a LTI system. The reduction basis is expressed as follows:

$$\mathbf{\Psi} = [\mathbf{\Psi}_{ram} \quad \mathbf{\Psi}_{nm}] \tag{2.27}$$

where $\mathbf{\Psi}_{ram} \in \mathbb{R}^{n_{dof} \times n_{ram}}$ is the *residual attachment modes* matrix and $\mathbf{\Psi}_{nm} \in \mathbb{R}^{n_{dof} \times n_{nm}}$ is the matrix of *normal modes*. The first basis allows to have an exact representation of the static response of the structure for a given input location. For each external load, the relative residual attachment mode has hence to be included. The matrix $\mathbf{\Psi}_{nm}$ contains instead a limited number of eigenmodes in the frequency range of validation of the structure. The reduced FE model has a total of $n_r = n_{ram} + n_{nm}$ DoFs.

- *Proper Orthogonal Decomposition:* has been used for the estimation of parametric models through AEKF. The POD computes a global reduction basis by solving the Singular Value Decomposition (SVD) to select the modes with the highest contribution and to remove possible duplicated physical phenomena from different local bases. This approach is extremely powerful for nonlinear systems or parametric models and it can be applied in different ways:
  - *Time-domain POD:* is normally the case for a nonlinear system where time-histories are known and forms the matrix of snapshots $\mathbf{Y} = [\mathbf{y}_1, ...\mathbf{y}_{\mathbf{n_s}}]$, where $\mathbf{y}_j$ is the response of the system at $j-$th time sample;
  - *Parametric model:* each model sampled in the parameters space is known and a *local reduction basis* $\mathbf{\Phi}_l$ is computed through MOR techniques for linear systems. One of the most common approach is to concatenate local basis to form $\mathbf{Y} = [\mathbf{\Phi}_1, ...\mathbf{\Phi}_{\mathbf{n_s}}]$, with n the number of parameter samples.

  Given the matrix $\mathbf{Y}$, the SVD is computed:

$$\mathbf{Y} = \mathbf{U}\mathbf{S}\mathbf{V}^{\mathbf{T}} \tag{2.28}$$

  The global reduction basis is then defined by selecting the first r-left singular values, i.e. the r first column of $\mathbf{U}$. A typical approach is to truncate the singular values such that:

$$\frac{\sum_{i=1}^{r} \sigma_i^2}{\sum_{i=1}^{n_{sv}} \sigma_i^2} \geq 0.999 \tag{2.29}$$

2.4 Application domains

This section discusses the engineering areas in which Kalman-based methods have been employed to solve inverse identification problems. Unexplored areas with related state of the art are also briefly summarized. In literature, the following application domains are identified in the context of Kalman filtering estimation:

- **Civil Engineering:** [153] proposed the use of UKF to study shear frames in civil structures; [201] applied an adaptive EKF to estimate time-varying system parameters on a four-story building model subject to base excitation; [191] performed input identification via UKF on nonlinear hysteretic shear structures subjected to unknown base excitations; [200] proposed the Adaptive EKF (A-EKF) in the field of vibration control for seismic damages; [177] coupled dynamic substructuring and AKF on wind turbines; [179] studied the UKF for wind turbine nonlinearities as twist-bend coupling; [114] applied the joint input-state estimator of Gillijns and De Moor (GKF) [76] for external forces identification on a footbridge; [133] studied fatigue assessment on an offshore wind turbine; [178] compared DKF and GDF to predict the global response of a wind turbine lattice support and excitation loads assuming high modelling uncertainties.
- **Mechanical Engineering:** [150] proposed the AEKF to estimate the six wheel center loads and full-field response on a vehicle suspension test rig; [12] applied an Adaptive UKF (A-UKF) formulation to estimate the tyre–road friction, sideslip angles, tire slip angles and tire slip ratios in extreme driving conditions; [31] explored A-EKF and A-UKF for vehicle sideslip and positioning estimation, while [57] proposed the comparison for the estimation of sideslip and lateral tire force; many other works are presented in literature on the estimation of sideslip angle for stability control, e.g. [108, 15, 109, 94]; [193] estimated the friction coefficient between tires and road through UKF on a Volkswagen Golf GTE plug-in hybrid as test vehicle.
- **Aerospace Engineering:** [23] studied the identification problem of time-varying aerodynamic parameters in typical flight conditions trough the EKF; [110] proposed an adaptive EKF algorithm to estimate satellite attitude; [9] designed an invariant EKF to estimate turbulent wind on a fixed-wing Uncrewed Aerial Vehicle (UAV) in constant-altitude; A-EKF and A-UKF have been explored in several works for aircraft flight parameters estimation, e.g [43, 10, 121, 102, 70, 126]; [116] applied Kalman-based methods to estimate engine parameters under flight operating conditions.
- **Robotics and Control systems:** several Kalman-based methods have been explored in these areas for e.g. model-based control and trajectory planning in robotic systems [42]. However, this field does not fit the focus of this PhD thesis, which is instead focused on mechanics.

Despite composite materials being employed in aerospace, mechanical and civil engineering, this field is still not explored in literature in the context of model-

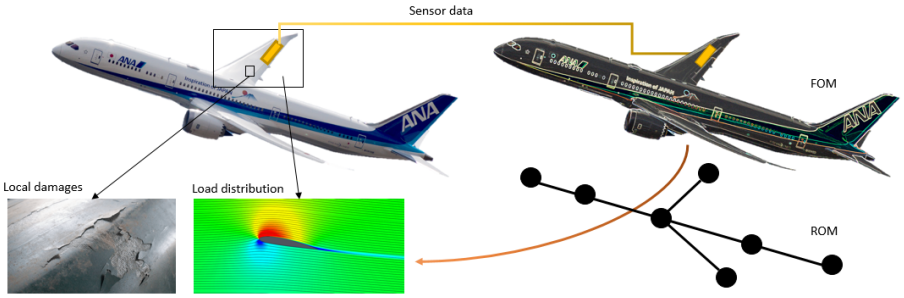

Figure 2.6: Example of inverse identification on a wing of an aircraft where local damages might occur and aerodynamic loads are distributed.

based inverse identification. The research direction in this field is focused on damage detection through AI methods. However, the need of a large dataset limits their implementation during operation because of the intrinsic uncertain nature of composite materials and failure phenomena (Fig. 2.6) that compromise the robustness of the method itself. Failures are often unpredictable during operation and critical loads are studied only in off-line testing. Model-based inverse methods and in particular Kalman filtering algorithms can be of interest in this research area by detecting and monitoring failures from a reduced set of sensors. KF and other Bayesian techniques are also particularly suitable to consider sources of uncertainties in composites applications.

Another gap in the state-of-the-art concerns the estimation of aerodynamic loads distribution (Fig. 2.6), which is present in most of the mentioned engineering fields. Estimating a distribution of loads (or parameters) leads inevitably to an increase of the number of states and consequent observability issues.

This PhD research pays attention to these two unexplored fields, providing solutions to overcome potential issues that can limit the applicability of Kalman-based methods (Fig. 2.6).

2.5 Conclusions

In this chapter, the state-of-the-art of inverse identification methods used in structural applications is reviewed, with particular attention to model-based approaches. The focus of the PhD research is on Kalman filtering techniques. Formulations for linear and nonlinear systems and augmented scheme are briefly explained. A detailed overview of the main principles of the KF is also provided.

Different Kalman filtering approaches are proposed in literature, addressing model nonlinearities, undertainties modelling, input and parameters identification, computational efficiency, observability and stability of the filter. To summarize, the main algorithms are:

- **Kalman Filter (KF):** the standard formulation for state estimation of linear systems.
- **Extended Kalman Filter (EKF):** extension of the KF to address non-linear or parametric systems by performing model linearization. It can be employed for an acceptable level of nonlinearities.
- **Unscented Kalman Filter (UKF):** as for the EKF, it addresses nonlinearities, but solves the system without linearization. It is particularly suitable for complex systems with high nonlinearities, when linearization is not applicable.
- **Augmented Kalman Filter (AKF):** is designed for external load estimation of linear systems. AEKF and AUKF can be employed for nonlinear systems.
- **Gillijns and De Moor Kalman Filter (GKF):** as for the AKF, it is designed for external load estimation of linear systems. The GKF is a recursive estimation process, modelling the input dynamics with another estimator.
- **Dual Kalman Filter (DKF):** has been proposed to overcome numerical issues of the GKF.
- **Adaptive Kalman Filter (A-KF):** is used in time-varying situations. It dynamically adjustes the filter parameters, such as the process and measurement noise covariances, following the evolving characteristics of the system. A-EKF and A-UKF can be employed for nonlinear systems.

All these Kalman filtering schemes have been applied to many engineering fields and allow to reach high estimation accuracy.

In this PhD research, the KF, AKF and AEKF are adopted to analyze the three use-cases discussed in Sec. 1.3. The 0th-order random walk model is adopted for loads and parameters in the augmented formulations. The errors made in the model linearization step of the AEKF are assumed to be negligible for the investigated applications.

Chapter 3

Research Approach and PhD Achievements

This PhD research focuses on advancing the state of the art of the application of Kalman filtering methods to industrial test cases by proposing novel approaches to overcome current limitations.

The employment of Kalman filtering in the industrial field has become more frequent given its advantages over other model-based and signal processing-based methods. In particular, the properties of the KF result to be particularly suitable for their employment in a DT framework and application in the field of structural monitoring. Indeed, the KF allows real-time filtering and performs full-field response estimation or shape sensing of the structure. Moreover, the KF has been validated for the estimation of multiple loads and parameters reaching good levels of accuracy and this opens the opportunity to operate in the field of structural durability and prognosis.

Despite the proven performances and advantages of the KF, some challenges still limit its application or require large modelling and calibration effort. This work is a contribution towards the solution of the identified challenges:

- Positioning of sensors on the numerical model to reduce uncertainties associated to measurements;
- More robust optimal sensor placement able to quantify the level of observability provided by the reduced set of sensors;
- Enabling the use of less-correlated models in order to reduce overall modelling effort;

- Estimation of distributed loads and parameters using a reduced set of sensors.

These are the current gaps found in the application of KF within an industrial context. The following achievements have been reached within this PhD research, fulfilling the objectives of the thesis and addressing all the identified challenges.

3.1 Calibration of sensor location - Paper I

The first challenge in the application of Kalman-based strategies is the overlap between measured and simulated data. Taking the example of a strain measurement, it is particularly challenging to match the exact location and direction of a strain gauge with a location on a FE model. Similarly, an accelerometer sensor installed on curved surfaces makes it difficult to exactly know the measured direction. However, for strain measurements, this issue is much more critical with respect to other sensors because high strain gradients could be present on the structure. A common issue in the matching procedure is the not perfect geometry representation of the real model, combined with the inaccuracies of the instrument used to measure the location of the real sensors as e.g. a camera device.

An optimization process is thus proposed in [52] in order to calibrate the sensor locations on the FE model and thus reduce the errors associated with the measurements. The following steps, generalized for all types of sensors, are defined:

- Starting from the measured locations (red marker in Fig. 3.1), an area of uncertainty (red box in Fig. 3.1) is defined around each sensor. This area can be correlated with the precision of the measuring instrument and the geometrical accuracy of the FE model;
- A simulation training scenario is defined, e.g a set of static loads. Output values for each node/element in the considered area of uncertainty are collected for each forward simulation;
- The node/element within the predefined area (green marker in Fig. 3.1) which returns the minimum error with respect to reference data is selected.

The optimization involves not only the correction of the measured location but also the direction of measurements (red/green arrows in Fig. 3.1), which is usually difficult to be acquired with high precision.

This calibration approach should be run off-line before the estimation process and it is part of the FE model calibration, together with the model updating step which is performed using some dynamic and static tests. This optimization

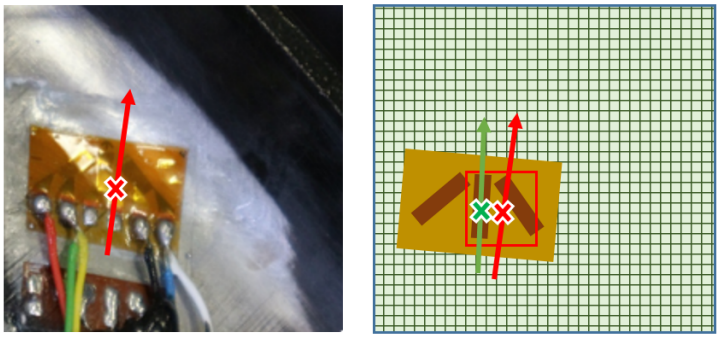

Figure 3.1: Rosetta installed on the surface of a structure and its overlap on the FE model. Red marker and arrow are measured location and direction of the central strain gauge. Green marker and arrow are the optimized properties, identified in the uncertainty area (red box).

step is important in order to minimize the error propagation within the filtering approach since all the modelling errors are compensated by the augmented states, e.g. loads.

Fig. 3.2 shows the measured strain value of each sensor on a twistbeam rear suspension (**Paper I** [52]) for two static load cases, 30N and 80N, compared with the one evaluated on the FE model on sensors locations measured with a camera device, and the one evaluated on the optimized location, showing improved accuracy.

The proposed approach for sensor calibration reaches a Technology Readiness Level (TRL) 4 [131] as it can be still improved with a more robust optimization approach. However, the whole workflow proposed in **Paper I** for multi-load estimation has been adopted at industrial level and can be classified as TRL 7/8.

3.2 Advanced Optimal Sensor Placement - Paper II

The existing OSP strategy based on the PBH method has been developed and validated for multi-load estimation via AKF. The PBH method is a metric evaluating the observability of the system given a set of output measurements. This strategy is unable to identify the optimal set of sensors providing the higher level of observability because of its sensitivity to system scaling. Two alternative metrics have been thus developed:

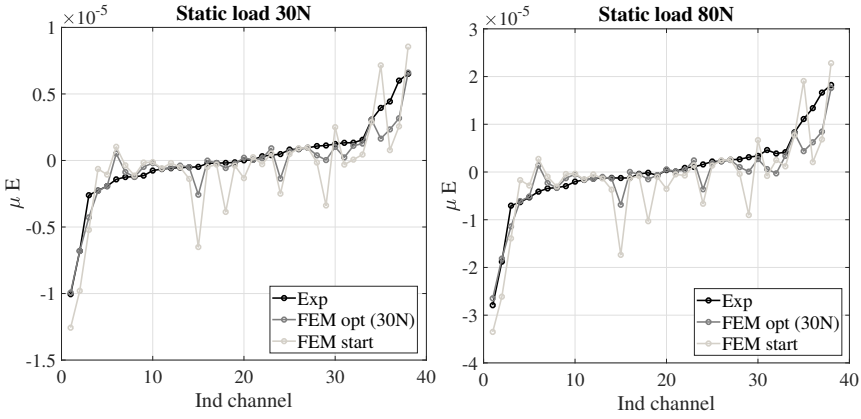

Figure 3.2: Static validation through optimization procedure: numerical and experimental strain comparison. FEM start: strain evaluated on the element identified by camera device. FEM opt: strain evaluated on the optimal element.

- Input Error Covariance (IEC) based on steady-state estimator covariance convergence;
- Transfer Function Identity Index (TFI) based on closed-loop estimator bandwidth.

Both metrics aim to replace the observability screening proposed in the original OSP method (Fig. 2.3).

- **Input Error Covariance (IEC)** This metric considers the continous-time formulation of the Kalman Filter, named Kalman-Bucy filter [96]. The selection of the optimal set of sensors is obtained by minimizing the time evolution of the trace of the input estimation error covariance matrix, leading to the steady-state value, i.e. $\dot{\mathbf{P}} = 0$, which is computed by solving the continuous algebraic Riccati equation:

$$\mathbf{A}^*\mathbf{P} + \mathbf{P}\mathbf{A}^{*^T} + \mathbf{Q}^* - (\mathbf{P}\mathbf{H}^T\mathbf{R}^{-1})\mathbf{R}(\mathbf{P}\mathbf{H}^T\mathbf{R}^{-1})^T = 0 \tag{3.1}$$

  Eq. 3.1 allows the definition of the optimal Kalman gain for a given measurement matrix $\mathbf{H}$ and leads thus to the best estimation. After the training scenario of the standard OSP method, a greedy selection is performed to find the set of measurements which gives the higher contribution to the steady-state input error covariance. The metric aims to minimize at every time step the trace of the submatrix of the error covariance matrix corresponding to the estimated loads:

$$IEC = trace(\mathbf{P}_{uu}) \tag{3.2}$$

where $\mathbf{P}_{uu} = E(\hat{\mathbf{u}} - \mathbf{u})(\hat{\mathbf{u}} - \mathbf{u})^T$.

This metric considers the process and measurement noises, parameters in Eq. 3.1. The contribution [50] explains also how to address the IEC metric when multiple loads and torques are estimated.

- **Transfer Function Identity index (TFI)** This metric is based on the estimator transfer function $\mathbf{T}_{\hat{\mathbf{u}}\mathbf{u}}$ between the estimated and the real input $\hat{\mathbf{u}}$ and $\mathbf{u}$, evaluated in the dynamic range of interest. The selection of optimal set of sensors resides in the one whose corresponding transfer function is the most relevant for the estimation. Ideally, in a perfect estimation scenario, $\mathbf{T}_{\hat{\mathbf{u}}\mathbf{u}}$ should return a unit value in all the dynamic range (Fig. 3.4). $\mathbf{T}_{\hat{\mathbf{u}}\mathbf{u}}$ can be evaluated as the product of the input-output transfer function $\mathbf{T}_{\mathbf{uy}}$ computed from state-space model and the output-estimated input transfer function $\mathbf{T}_{\mathbf{y}\hat{\mathbf{u}}}$ computed through AKF (Fig. 3.3):

$$\mathbf{T}_{\hat{\mathbf{u}}\mathbf{u}} = \mathbf{H}_{\hat{\mathbf{u}}}((\mathbf{I}s - \mathbf{A}^* + \mathbf{G}\mathbf{H})^{-1}\mathbf{G})(\mathbf{C}(\mathbf{I}s - \mathbf{A})^{-1}\mathbf{B} + \mathbf{D}) \tag{3.3}$$

where $\mathbf{G}$ is the steady-state Kalman gain and $\mathbf{H}_{\hat{\mathbf{u}}}$ is a Boolean selection matrix, i.e. $\mathbf{H}_{\hat{\mathbf{u}}} = [\mathbf{0}, \mathbf{0}, \mathbf{I}]$ such that $\hat{\mathbf{u}} = \mathbf{H}_{\hat{\mathbf{u}}}[\hat{\mathbf{q}}, \hat{\dot{\mathbf{q}}}, \hat{\mathbf{u}}]$. As for the IEC metric, a greedy selection strategy is in place for the selection of sensors after the training scenario. The identity index $I_I(s)$ is proposed to quantify the system observability, defined as:

$$I_I(s) = \frac{\sum_{j=1}^{n_u} |1 - |T_{\hat{u}u}^{jj}(s)||}{n_u} + \frac{\sum_{j=1}^{n_u} \sum_{i=1, i\neq j}^{n_l} |T_{\hat{u}u}^{ji}(s)|}{n_u(n_u - 1)} \tag{3.4}$$

This index assumes value 0 when the condition $\mathbf{T}_{\hat{\mathbf{u}}\mathbf{u}}(s) = \mathbf{I}$ is met. As for the IEC metric, the contribution [50] explains how to address the TFI metric when multiple loads and torques are estimated.

The two approaches showed that both metrics are measurements unit-independent, which is an advantage with respect to the existing OSP. Moreover, both TFI and IEC estimation showed a noise reduction because of the covariance matrices $\mathbf{Q}^*$ and $\mathbf{R}$ are considered in the metrics definition. An example of multi-load estimation on a linear model is extracted from **Paper II** [50] and shown in Fig. 3.5: PBH and IEC metrics results are compared, each one obtained with a different selection of optimal set of sensors. Contrarily to PBH, IEC reaches high accuracy with noise filtering on the estimated loads. TFI performances are not shown because similar results are obtained. From a computational point of view, IEC metric is more advantageous since TFI requires the computation at every frequency line within the dynamic range.

The technology proposed in **Paper II** can be classified with TRL 8. In particular, the IEC metric is currently implemented in the *Simcenter 3D Smart Virtual Sensing* [168] software.

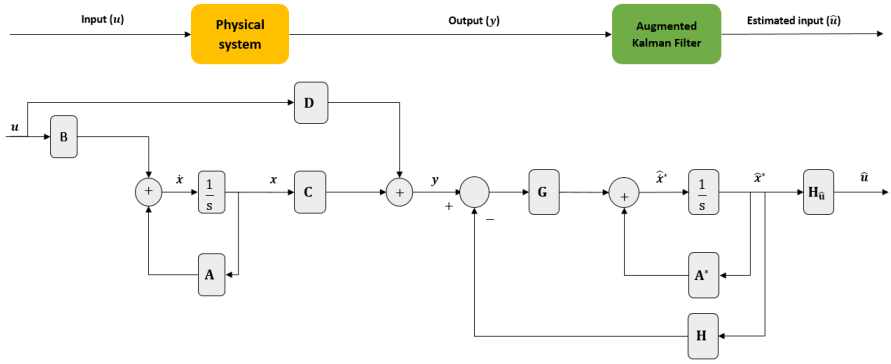

Figure 3.3: Scheme of transfer function $\mathbf{T}_{\hat{\mathbf{u}}\mathbf{u}}(s)$.

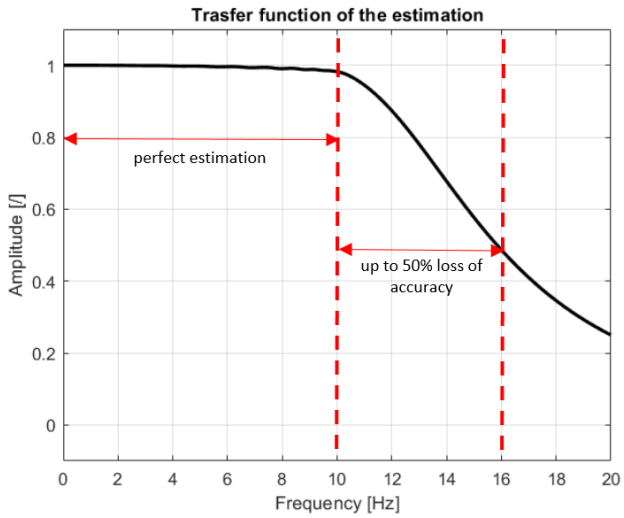

Figure 3.4: Example of transfer function $\mathbf{T}_{\hat{\mathbf{u}}\mathbf{u}}$ evaluated in a frequency range $[0-20]$Hz for a given set of sensors. A perfect estimation is observed in the range $[0-10]$Hz, followed by a gradual loss of accuracy.

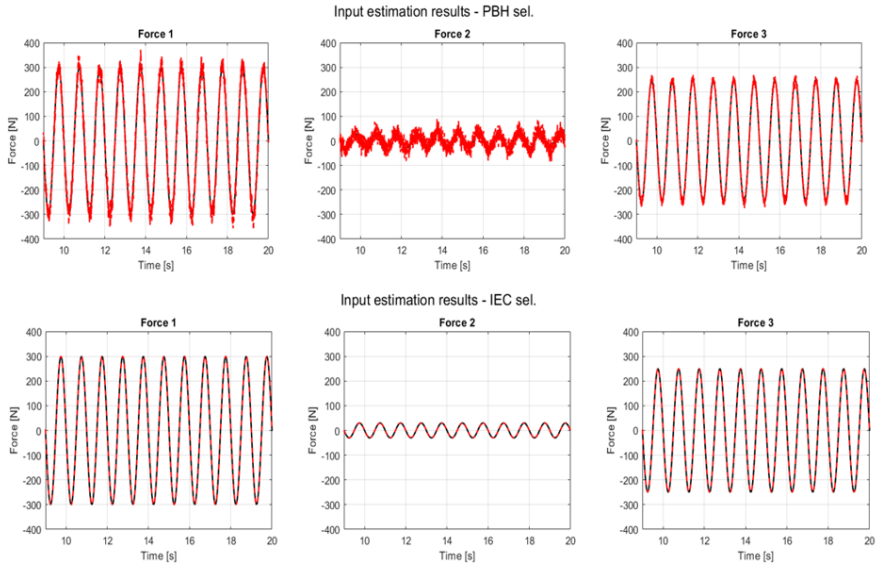

Figure 3.5: Estimation of 3 loads on a linear FE model [50]. Comparison between results reached with PBH and IEC metrics.

3.3 Less-correlated numerical model compensated through AKF - Paper III

The level of accuracy of the AKF highly depends upon the level of reliability of the numerical model. When complex systems are involved, high-fidelity models are required and the correlation analysis becomes time-consuming. An example is the aerodynamic field generated during helicopter flight, which requires complex multi-body models coupled with specialized CFD tools. This kind of model can lead to some difficulties in embedding all the physical information in the AKF scheme. Moreover, distributed aerodynamic loads should be estimated.

However, when modelling errors are present, the estimator compensates them via the estimation of the states with higher associated uncertainties. This has been shown in [52] on a twistbeam rear suspension case. In the AKF scheme, all the applications presented in literature have applied a high level of uncertainty to the augmented states as loads or parameters. Indeed, [52] showed that the full-field response estimation can reach good levels of accuracy when loads are estimated because the modelling errors have been compensated with a lower accurate estimation of the loads. This principle has been adopted in [53] to

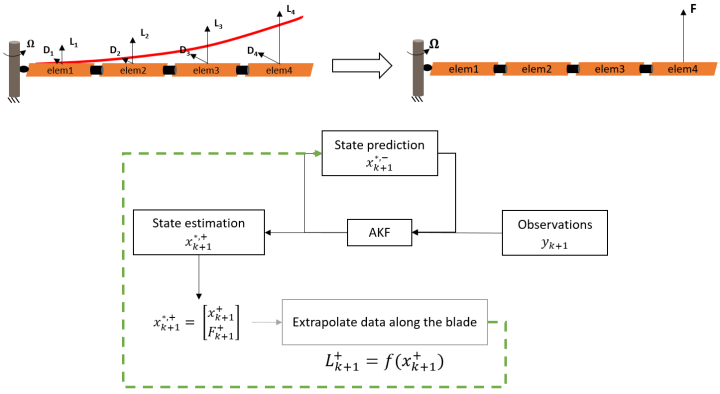

Figure 3.6: Estimation of aerodynamic loads with less-correlated model.

simplify the estimation of aerodynamic loads on a steady-state flight condition of a 2-blade helicopter rotor. Generally speaking, the aerodynamic forces can be expressed as a function of the system states:

$$\mathbf{L} = f(\mathbf{x}) \tag{3.1}$$

Which requires more effort in embedding the numerical (parametric) model in the filter. Leveraging from the results obtained in [52], a standard AKF scheme has been used in [53] by using the classical 0th-order random walk formulation to model the aerodynamic loads, then an additional step has been added to estimate correctly the aerodynamic forces. The workflow is described below and schematically shown in Fig. 3.6:

- *Prediction-Correction:* forward simulation of the coupled structural-aerodynamic model. The dynamics of the aerodynamic loads is described by a random walk model. An equivalent load is selected and considered in the estimation to reduce the number of physical sensors needed to guarantee the observability. The predicted states are corrected with the optimal set of sensors providing an optimal state estimation. F in Fig. 3.6 is treated as quantity to compensate for modelling errors.
- *Evaluation of distributed loads:* the accurate estimation of states reached with the AKF scheme at every time step is used to compute the exact formulae of aerodynamic loads and applied at the next time step to the structural system, ad in Eq. 3.1.

In the proposed workflow, the estimated augmented states (normally loads) have the only role to compensate modelling errors arising from the simplification

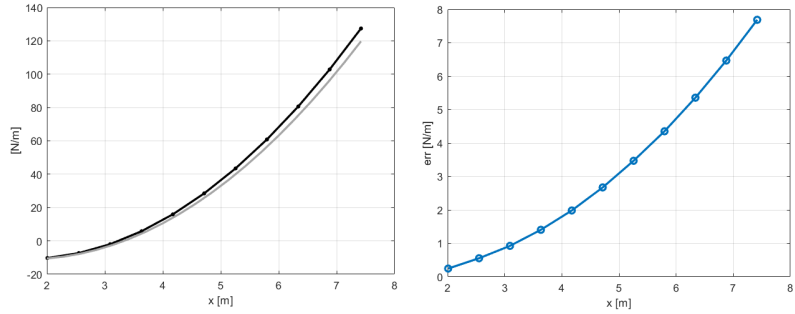

Figure 3.7: Distributed lift along the aerodynamic span in steady-state (left) and absolute error (right) on a scaled helicopter blade [53]. Reference data from simulation vs estimated.

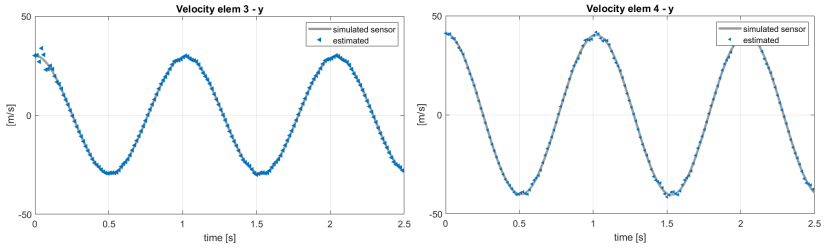

Figure 3.8: Estimation of the velocities of 2 elements of the scaled helicopter blade [53]. Reference data from simulation vs estimated.

made on the number and position of concentrated loads estimated in the filtering process. The methodology has the advantage to reduce modelling effort and to estimate distributed loads with a reduced set of sensors by adding a step after the standard prediction-correction scheme. Fig. 3.7 and Fig. 3.8 (**Paper III** [53]) show respectively the estimation of the aerodynamic load and the system states, i.e. velocity of each blade element, obtained through the application of the workflow in Fig. 3.6. The modelling errors are compensated in the estimation of the aerodynamic load, showing a lower accuracy (Fig. 3.7).

The approach proposed in **Paper III** is considered a first step towards the applicability of Kalman filtering methods for complex systems requiring high-fidelity models. However, regarding the coupled structural-aerodynamic problem, the methodology is classified as TRL 2, as further investigation studies should be performed for its implementation on a real flight case scenario.

3.4 Estimation of distribution of loads and parameters - Paper IV

When a distribution of loads or physical parameters has to be estimated, the AKF requires a high number of sensors in order to guarantee system observability. This can be the case of aerodynamic loads acting on the whole surface of the structure, or general pressure loads or even a distribution of physical parameters like interface degradation in composite laminates.

In [49], this problem is addressed on a real test case of a DCB specimen which is normally used to determine the mode I fracture toughness of composite laminates. This use-case has been particularly interesting from estimation point of view, since it allowed the development of a novel recursive estimation approach. The interface degradation in a FE scheme can be modelled as the decreasing of the stiffness value in the connection between two surfaces. Composite laminates exhibit a process zone during delamination, representing an area at the interface where the perfect glue is lost and a distribution of stiffness is observed. This process zone moves in time towards the root of the specimen as shown in Fig. 3.9 . Two challenges are identified in this problem:

- Estimation of the distribution of parameters in the process zone;
- Estimation of the distribution of parameters in the full interface.

If all the nodal interface stiffness parameters are simultaneously estimated, an excessive number of sensors should be employed. To overcome this issue, the information regarding the shape of the distribution has been embedded in the estimator as follows:

$$\mathbf{p} = \mathbf{B}\mathbf{p_m} \tag{3.1}$$

where $\mathbf{p_m}$ is the master parameter, $\mathbf{B}$ is a shape matrix distributing $\mathbf{p_m}$ over all the parameters in the process zone included in the vector $\mathbf{p}$, as shown in Fig. 3.9. This approach can be applied when the shape of the distribution is known a-priori and thus a reduced set of parameters can be estimated. The same reduction approach has been applied in [174] for the estimation of loads. Appendix A shows additional work that has been carried out during the PhD but has not been published. It shows the estimation of distributed aerodynamic forces acting on a real composite blade tested in fixed-root conditions in a wind tunnel.

The particular properties of the analysed problem on a DCB specimen has led to the development of a recursive estimation approach that helps to further reduce the number of physical parameters to be estimated and consequently a reduction of the computational costs. The model parametrization is dynamically updated

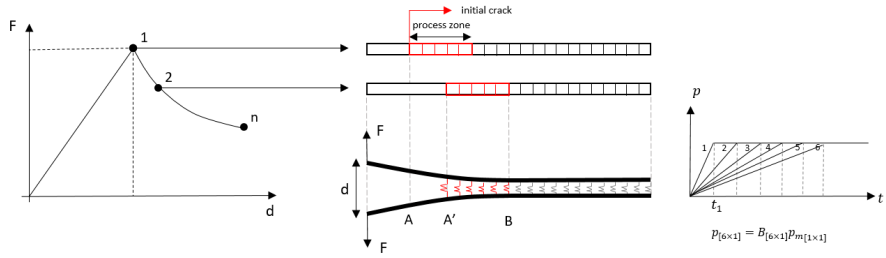

Figure 3.9: Schematic representation of progressive delamination in a DCB model. Each sample on the nonlinear $F-d$ curve corresponds to a configuration of process zone moving from the tip to the root of the beam. On the right, an example of distribution over 6 stiffness interface elements is shown. The first element is the master whose value is distributed over the other elements in the process zone.

in the presented scheme: when the master parameter of the first developed process zone goes to a zero stiffness value, the next parameter becomes the master of the new process zone. Specifically, as shown in Fig. 3.9, the master parameter corresponds to the stiffness value of the interface element located at the crack tip (point A or A'). Without loss of generality, the parametric augmented state-space formulation in Eq. 2.4, at time sample 2 in Fig. 3.9, can be stated as:

$$\begin{cases} \mathbf{x}_2^* = \mathbf{F}^*(\mathbf{p}_{m,1} = \mathbf{p}_{ref}, \mathbf{p}_{m,2}, \mathbf{B}_2)\mathbf{x}_1^* + \mathbf{w}_1^* \\ \mathbf{y}_2 = \mathbf{H}^*\mathbf{x}_1^* + \mathbf{v}_1 \end{cases} \tag{3.2}$$

where $\mathbf{p}_{m,2}$ and $\mathbf{B}_2$ are the master parameter A' and the corresponding shape matrix respectively, while $\mathbf{x}_2^* = [\mathbf{x}_2, \mathbf{p}_{m,2}]^T$. Eq. 3.2 is valid until $\hat{\mathbf{p}}_{m,2}$: $k_{m,2} = 0$, where $\hat{\mathbf{p}}_{m,2}$ is the estimated parameter and $k_{m,2}$ is the stiffness value associated to the master element. The notation in [49] states that $\mathbf{p}_{ref} - \mathbf{p}_m = k_m$, where $\mathbf{p}_{ref}$ is the initial interface stiffness value in the model.

Paper IV addresses the estimation of distributed loads and parameters and brings two novelties in the filtering problem: i) shape distribution embedded in the estimator, ii) recursive estimation. Key results are presented in Fig. 3.10 and Fig. 3.11 [49], showing respectively the estimation of the critical load and the crack propagation of a real DCB specimen, obtained by applying the recursive estimation approach with a reduced set of sensors. The methodology can be classified with TRL 3/4 and has the potentiality to advance to TRL 5. However, it is important to underline that the proposed approach is limited to situations where the behavior of parameters or loads is sufficientely known

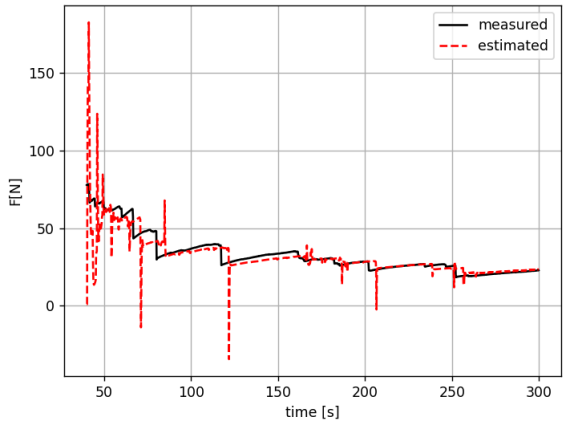

Figure 3.10: Estimation of reaction force for the experimental DCB.

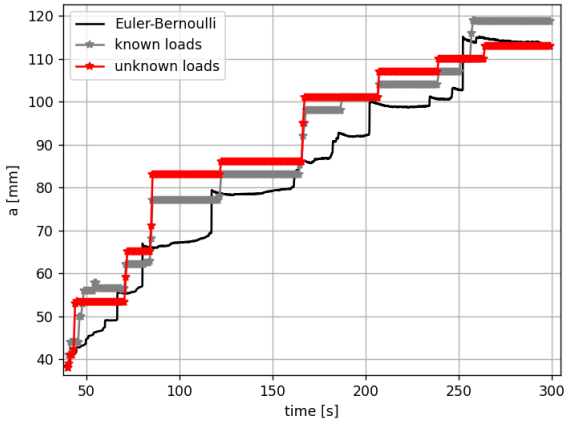

Figure 3.11: Estimated crack length for the experimental DCB. Euler-Bernoulli solution is considered to accurately represent the real behaviour of the specimen.

with a certain level of uncertainties. Once the distribution is constrained to pre-defined shapes, other events can not be predicted.

3.5 Conclusions

To summarize, all the key papers contribute to shaping the workflow for an optimal *model calibration* and Optimal Sensor Placement strategy, enhancing estimation through the Augmented Kalman Filter. This calibration step is

performed off-line together with the *filter calibration*, which remains an integral part of the overall process, even if not explored in this research. The sequential steps of the workflow are outlined below:

1. Training scenario: in-house testing of the structure to collect training data as reference for the next steps. Different amplitudes, frequencies and loads directions are applied, covering the range of interest. Sensor data is collected at this stage. The sensors should not be necessarily the same as the set selected by OSP strategy, which is analyzed in a later stage;
2. FE model updating and validation in the frequency range of interest. Normally modal analysis and static load cases are analyzed. The accuracy of modal validation in the operational frequency range is crucial to prevent modeling errors from compromising the estimation. The condition $\mathbf{Q_m} << \mathbf{Q_u}$ may no longer be valid in situations where modal validation accuracy is compromised.
3. Study of distribution (if any) of loads and parameters through simulated and tested data. This step is performed depending on the use-case. If simulated time-histories of loads/parameters distributions are available from high-fidelity simulation, the information can be used to analyze shapes and master loads/parameters;
4. OSP to select minimum number of sensors, types and locations with respect to a loading scenario. Once the model is validated, it can be used for OSP analysis. If it is run before model validation, results might not be reliable;
5. Calibration of sensor locations on the FE model considering the training scenario at point 1. This step is the last one before running the KF in operating conditions. A minimization of this source of error allows to adopt these two assumptions:
    - $\mathbf{R}$ calculated from sensor noise;
    - $\mathbf{R} << \mathbf{Q_u}$: the measurements are more reliable than the input model in the AKF.

Chapter 4

Concluding remarks and future research opportunities

This PhD thesis addresses the main challenges identified in the state-of-the-art of Kalman filtering techniques for industrial-level structural applications. This topic has been widely investigated in literature and this research should be considered as improvement and optimization of existing methodologies. The objectives and goals have been successfully achieved and addressed in the four key publications. Important conclusions are summarized as follows:

- The AKF has been tested on three industrial use-cases, showing that an accurate load estimation is obtained for most of the analyzed cases. The filtering approach shows also several advantages over signal processing-based techniques, reaching more accurate estimation with a smaller amount of sensor data.
- The AKF requires however user-effort in model and filter calibration, two steps to be run offline. The calibration accuracy highly influences the estimation performances.
- The KF performs better when the loads are unknown, thus in its augmented formulation. The improvement of the results is shown for the full-field estimation cases. Modelling errors are compensated by a less accurate estimation of the loads. This property of the AKF is valid for linear, nonlinear and parametric models where simoultaneous state/input/parameter estimation is performed.
- The AKF can leverage OSP strategies by selecting an optimal type and minimum number of sensors.

Despite the positive conclusions and successful application of Kalman-filtering techniques on different use-cases, touching different engineering areas, their employment on more complex systems still requires further studies in order to bring these techniques at higher level. Indeed, the TRL reached in **Paper III** and **Paper IV** is limited to the research level and further effort should be put to advance the methodologies to development levels. The biggest issue, common to the most of model-based methods, is on modelling and often the user is in the situation to take a decision on the trade-off between accuracy of the model and accuracy of the estimator. Higher accuracy of the model means higher complexity and thus higher required computational efforts. The accuracy of the estimator is driven also by filtering parameters. However, the correlation of the model with respect to the real behavior has a greater influence on the estimation and any assumption and simplification is propagated through the filter. The future research opportunities are identified and summarized in the following:

- **Model uncertainties:** the process noise involves the uncertainties associated to the states of the system, including the augmented states as e.g. loads, parameters. The level of noise assumed on the FE model is a quantification of the mismatch with respect to the real system dynamic. A FE model updating is normally performed off-line, during the calibration phase. However, it is highly improbably to have a perfect knowledge of the system behaviour a-priori and some nonlinearities or other unexpected dynamics could arise during operation. Robust methods in the field of uncertainty quantification should be analysed in order to improve the accuracy of the estimation on complex cases. These uncertainties affect also the performances of the off-line selection of optimal sensors. Two new metrics have been proposed in this PhD research for the sensors selection for the estimation of multiple loads. Even if it has been demonstrated that both IEC and TFI metrics outperform PBH strategy, only a simulated test case is proposed to validate the methodologies. The metrics consider the level of process and measurement noises but the effect of an under-estimation of these uncertainties on the selection of sensors has not been studied on a real scenario. Moreover, during operation, the direction and location of loads cannot be easily identified. A sensitivity analysis with respect to these load parameters should be also properly addressed. A future direction of research could be to compensate missing physics with black-box models. Recent research has been presented in literature on a hybrid filtering approach called Neural Extended Kalman Filter (NEKF) [111] and it is a potential improvement of the standard EKF, allowing to compensate inaccuracies in the model. More research should be performed, exploring e.g. an augmented formulation, observability issues and the required amount of training data.

- **Estimation of complex nonlinear dynamics:** The most popular nonlinear filtering technique is the Extended Kalman Filter (EKF), which employs an instantaneous linearization of the considered nonlinear system. The EKF parameters can be hard to tune when dealing with significant nonlinearities and it might exhibit divergence for extremely nonlinear cases. The problems associated with the EKF have been greatly attributed to the approximation introduced by the linearization of the system dynamics. An example of dynamics with extremely nonlinear effects is a rotordynamic model and it could lead to a non-convergent solution. Further development of the virtual sensing strategy might be needed by adopting a more appropriate type of filtering technique, such as the Unscented Kalman Filter (UKF), even if this results in additional computational cost. If the system is considerably large and nonlinear, observability issues might become relevant requiring the use of more sensors. System observability is an important requirement for an efficient application of the Kalman Filter algorithms. Available criteria for observability of non-linear systems often require the analytical form of the equations or the numerical computation of higher order derivatives. In order to simplify the computation, a linearization of the system is often adopted. The model linearization poses a particular challenge in the quality of the system identification through the use of a Kalman filtering technique.
- **Application domain:** The employment of Kalman-based techniques has not been explored much for some engineering fields. An example is the composite materials domain. Composites exhibit inherent brittleness properties and a propensity to develop delaminations. Moreover, the failure modes of composite structures are much more complex in nature than metallic ones as local damages at intra- or inter-lamina level can occur and propagate causing catastrophic failures. Preventing these effects is not trivial and a robust solution for operational life is still missing in literature. The work presented in this PhD thesis for the monitoring of delamination growth on a small specimen is a first step towards the application of Kalman-based methods in the field of composite materials. However, the challenges on a medium and large-scale test case are not addressed. As shown in the presented contribution, collocated measurements with respect to current damage position highly improve the system observability. On a real test case, the location where the damage occurs is normally unknown. A possible approach is to identify an area with high probability of failure and to select the optimal set of sensors in that localized area of the structure. However, the accurate identification and monitoring of delamination growth might be expensive to model. From operational point of view, this level of accuracy might be not needed and thus less-correlated models could be enough for the identification of critical damages.

While the assumptions adopted in Kalman filtering techniques are valid for most applications, some key limitations still exist in this regard. Even if these are not considered the most urgent research topics, they are summarized for completeness as follows:

- **Gaussian White Noise Assumption and Unimodal distributions:** Kalman filters assume that the process and measurement noise follow Gaussian distributions. This assumption is not always applicable and, in such situations, the performance of the filter can degrade significantely. Kalman filters also assume unimodal distributions, which means that the uncertainties have a probability distribution characterized by a single peak. However, in real-world scenarios involving nonlinearities or discontinuities, this assumption may not hold and the system exhibit multimodal distributions. In these situations, more advanced techniques may be required, such as particle filters or other Bayesian filters.
- **Initialization Sensitivity:** The accuracy of the initial state estimate determines the time needed by the filter to converge. If the user assumes a value far from the true state, the filter will take more time to predict the correct state. Moreover, for parameter estimation cases, the incorrect initial parameter values might influence the initial mathematical stiffness and/or stability of the problem.
- **Noisy Measurements:** In the presence of outliers or highly noisy measurements, the Kalman filter may give more weight to these measurements, leading to suboptimal results. Robust versions of Kalman filters or outlier rejection techniques may be needed in such cases.
- **Memory Requirements:** The Kalman filter requires storing and updating covariance matrices, which can become challenging for high order models if limited memory resources are available or real-time constraints are present, relevant for edge hardware deployment.

Despite these limitations, Kalman filters remain a powerful tool, and many variations and extensions have been developed to address specific challenges in different application domains. Choosing the right filtering technique often depends on the specific characteristics of the system and the nature of the data. As a conclusion, there is no best inverse identification technique, neither best Kalman filtering approach for all the application domains. But there is an optimal Kalman filtering scheme for a given problem. Even if all the presented limitations would be addressed, it is important to keep in mind that the employment of a Kalman based methodology will always need the two steps of *model calibration* and *filter calibration*. Future research should aim to improve and optimize the existing methodologies in order to allow for the smoothest application.

Appendix A

Distributed aerodynamic load estimation on a fixed-root scaled helicopter blade

This appendix shows a real test case for the estimation of distributed loads by embedding representative shapes into the AKF scheme in order to reduce the number of estimated states and the number of physical sensors needed to guarantee observability. To this end, a composite scaled blade is tested in the wind tunnel ($1m$ by $1.5m$) at the lab of university *Politecnico di Milano*. The experimental setup is shown in Fig. A.1 [174]: the root of the blade is fixed at a 6-axis load cell on the wind tunnel floor with a mechanism adjusting the pitch angle. The load cell acquires the total aerodynamic pressure in the 6 directions. The blade is composed by three main components:

- **Core:** Rohacell 51 WF;
- **Strips:** unidirectional glass fiber. 2 plies turning around the bushing to create a single 4-ply laminate (Fig. A.2);
- **Skin:** woven glass fiber. 2 plies with sequence $[+45^o, -45^o]$.

The wing section is shown in Fig. A.2 and available materials properties are listed in Table A.1.

The blade is instrumented with embedded Fiber Bragg Gratings (FBGs) sensors to measure bending and torsion strains at five sections, identified along the blade span at a distance from the root about $46mm$, $90mm$, $135mm$, $270mm$, $540mm$ (Fig. A.3). Static load tests and modal analysis have been first performed to

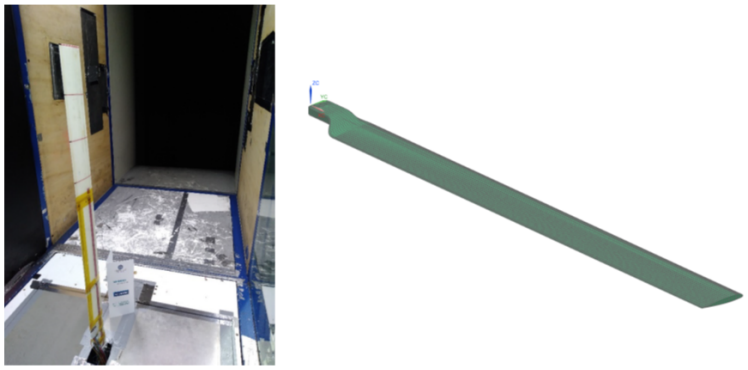

Figure A.1: Scaled helicopter blade tested in wind tunnel in fixed root conditions. On the right, the corresponding FE model.

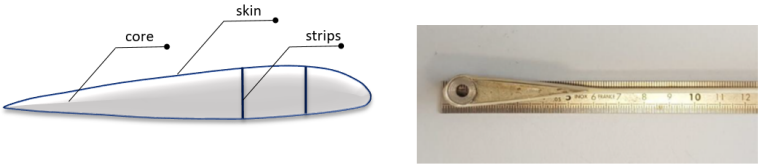

Figure A.2: Wing profile with components (left) and strips with bushings at the root (right).

validate the FE model. Table A.2 compares experimental modal frequencies with the ones obtained from the validated model. The normal modes correspond to clamped root condition. The first in-plane bending mode shows high percentage behavior mismatch due to difficulties in exciting the structure laterally. However, this dynamic does not influence the blade in wind tunnel testing. Then, all the other *model calibration* steps explained in Sec. 3.5 are applied. No OSP strategy has been adopted in this case for the simplicity of the test case. Properties shown in Table A.1 are the numerical values obtained after FE model validation. The calibration of FBGs sensors location has been reported in [174]. The FE model of the blade is shown in Fig. A.1 with a total of 25563 nodes. The blade has a span of $900mm$, a $75cm$ chord, linear built-in twist of -8° root to tip, and the airfoil is a NACA23012 (non-symmetric).

Different wind speed and angles of attack have been set for a total of 33 quasi-steady flight conditions. The wind profile has been acquired from $0m/s$ to the steady value, ranging between $5m/s$ and $15m/s$, and down again to $0m/s$.

	Density [$\mathbf{g/cm^3}$]	**Young Modulus** $\mathbf{E_{xx}}$[GPa]	**Young Modulus** $\mathbf{E_{yy}}$[GPa]	**Shear Modulus** $\mathbf{G_{xy}}$[GPa]	**Poisson** ν_{xy}	**Ply thickness** [mm]
Core	0.052	0.075	0.075	0.024	-	-
Strips	1.8-1.9	45.7	13.5	5.41	0.27	0.21
Skin	3.0	23.0	23.0	2.0	0.05	0.12

Table A.1: Properties of blade components.

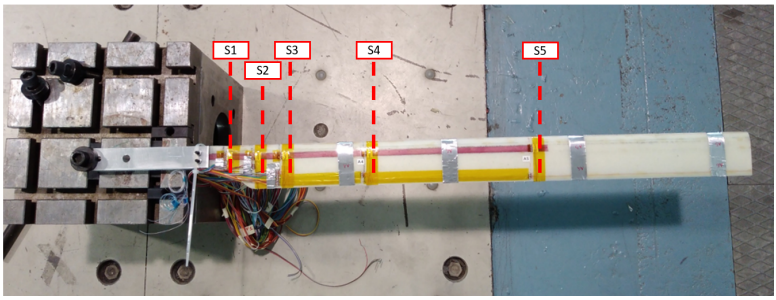

Figure A.3: Instrumented sections along the blade span.

The pitch angle α ranges from -8° to 10°. The test case aims to estimate the aerodynamic loads distribution. Normally, estimating the pressure field might not be needed in a mechanics problem and the total equivalent loads might be sufficient. However, an accurate estimation of distribution reduces the modelling errors in the AKF estimation process. For a linear model, the state-space formulation of a general dynamic system can be expressed as:

$$\dot{\mathbf{x}} = \mathbf{A}\mathbf{x} + \mathbf{B}\mathbf{u} \tag{A.1}$$

Where $\mathbf{x}$ and $\dot{\mathbf{x}}$ are respectively the system states vector and its time derivatives, $\mathbf{u}$ is the input vector, $\mathbf{A}$ is the system matrix and $\mathbf{B}$ is a Boolean input shape matrix that distributes the inputs over the states of the system. Similarly to [49] where the distribution of parameters is addressed, the distribution of loads can be approximated as a linear combination of pre-defined shapes. The last term of Eq. A.1 becomes:

$$\mathbf{B}\mathbf{u} = \mathbf{B}\mathbf{B}_\mathbf{u}\mathbf{u}_\mathbf{m} \tag{A.2}$$

where $\mathbf{u_m}$, $\mathbf{B_u}$ are respectively the master load and the shape matrix which distributes $\mathbf{u_m}$ over the other loads in $\mathbf{u}$. $\mathbf{u_m}$ can be evaluated through hyper-reduction approaches as e.g. Discrete Empirical Interpolation Method (DEIM)

Modes	Freq. exp. [Hz]	Freq. FEM [Hz]	Error %
I bending	4.04	4.25	5
I in-plane bending	18.09	16.07	11
II bending	27.57	26.71	3
III bending	75.98	72.84	4
I torsional	102.68	109.71	7

Table A.2: Modal frequencies of blade clamped at the root.

[41], for nonlinear cases. In this example, a single shape can be identified in the span-wise (linear constant distribution) and chord-wise directions. The latter can be found by assuming a polynomial function which satisfies the following constraints:

$$\begin{cases} \sum_i^{n_u} L_i = L_{1/4} \\ L_{TE} = 0 \\ \sum_i^{n_u} L_i(r_i - r_{1/4}) + \sum_i^{n_u} M_{1/4} = 0 \end{cases} \tag{A.3}$$

Eq. A.3 are translated in:

- The sum of chordwise lift contributions L_i, is equal to the total lift $L_{1/4}$. Moments are referred to the quarter chord, where the lift is prescribed to assume its maximum value;
- Zero lift at the Trailing Edge (TE) and zero pitch moment at the quarter chord (symmetric airfoil under static pitch).

These assumptions are valid for symmetric airfoils. However, for non-symmetric airfoils, the error is expected to be negligible. No analytical formula is readily available, but semi-empirical data can be used. The set of constraints in Eq. A.3 identifies the shape distribution shown in Fig. A.4 which is used in this example. To summarize, a single load is estimated, acting at the quarter chord at the tip of the blade. The estimation is then distributed over the full aerodynamic surface through the weight coefficients in the matrix $\mathbf{B_u}$.

Each section defined on the FE model has a regular mesh with approximately 20 nodes, thus 20 lift forces are applied in the model. Aerodynamic drag and torque are not considered because their values are negligible for the tested conditions. In order to reduce the computational cost needed to predict the system states with high number of loads, only a reduced number of equally spaced sections are selected along the blade span. Given the high-refined mesh, this assumption is sufficiently accurate if enough sections are considered. 5, 10 and 40 sections are tested (Fig. A.5), for a total number of loaded nodes equal to 95, 190 and 760 respectively. For all the cases however, only one master load

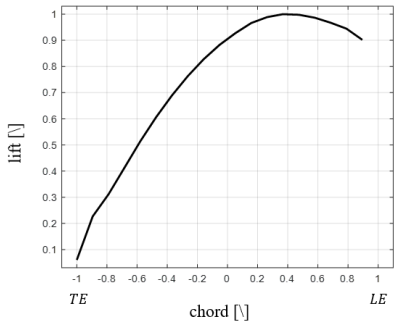

Figure A.4: Aerodynamic lift distribution on symmetric airfoil in the chord-wise direction. Lift and chord are normalized. TE: trailing edge; LE: leading edge.

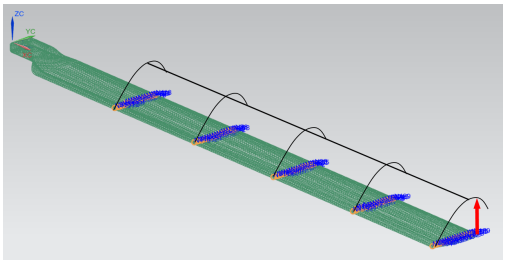

Figure A.5: FE model with 5 loaded sections. Span-wise and chord-wise distributions are shown. Master load marked in red at the tip of the blade.

is estimated and then redistributed through $\mathbf{B_u}$ matrix. The results in terms of total estimated aerodynamic forces and master load are shown in Fig. A.6, for wind speed $5m/s$ and pitch angle $\alpha = 4deg$. The estimation is performed by using only 1 sensor located at the root of the blade (S2 in Fig. A.3), measuring strain bending. The case with 5 sections shows a lower Root-Mean-Square Error (RMSE) value and thus a lower performance with respect to the cases with 10 and 40 sections. The explanation of the level of accuracy reached in the estimation for the three configurations of sections is in the approximation considered by estimating only a subset of sections. In the real test case, all the sections are loaded. For this reason, if only few sections are considered, a higher load is estimated to reach the same equilibrium. Good results can be achieved for the case with 10 sections. This estimation setting is used to evaluate all the other tested flight conditions in the following. The measured vs estimated curves of aerodynamic lift coefficient C_l are shown in Fig. A.7.

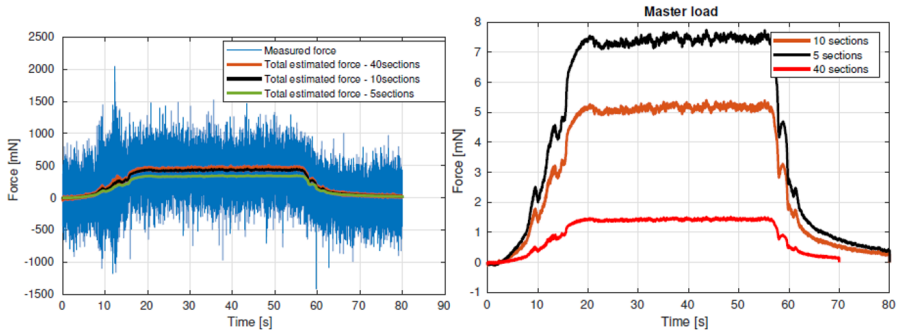

Figure A.6: Estimation of total lift compared with reaction force measured through the load cell located at the beam root (left). Estimation of master load for each case.

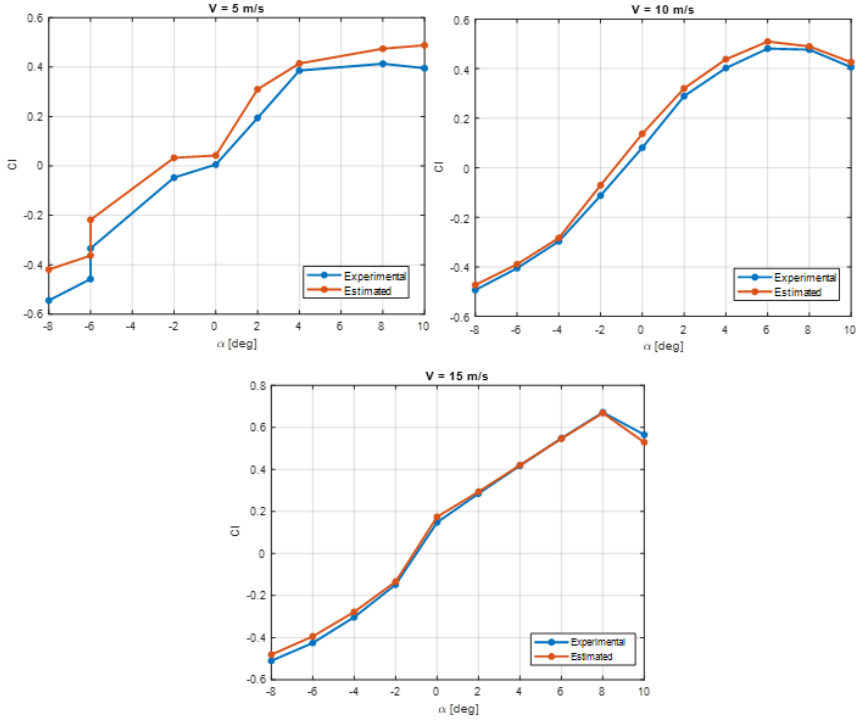

Figure A.7: Estimation of lift coefficient for different pitch angles and different wind velocity.

Publications

Publication I

Kalman-based load identification and full-field estimation analysis on industrial test case

Published in Mechanical Systems and Signal Processing 117 (2019) 771-785
DOI: 10.1016/j.ymssp.2018.08.045

Kalman-based load identification and full-field estimation analysis on industrial test case

Roberta Cumbo[1], Tommaso Tamarozzi[1,2], Karl Janssens[1], Wim Desmet[2]

[1] *Siemens Industry Software NV, Interleuvenlaan 68, B-3001 Leuven, Belgium*
[2] *KU Leuven, Department of Mechanical Engineering, Celestijnenlaan 300 B, B-3001 Heverlee, Belgium*

Abstract

The potential of the Augmented Kalman Filter algorithm is tested in this paper for joint state-input estimation in structural dynamics field. In view of inverse load identification, the filter is compared with the Transfer Path Analysis Matrix Inversion technique, commonly used for industrial applications. An existing Optimal Sensor Placement strategy for Kalman Filter is adopted and validated on real experimental data. The advantages of the proposed methods, through strain measurements information, are identified in the effort needed for data-acquisition and data-processing. The effectiveness of the filter and the quality of the results are demonstrated in this paper for an industrial test-case, such as a rear twistbeam suspension.

Keywords: State-input estimation, Augmented Kalman Filter, Inverse load identification, Strain-based TPA Matrix Inversion, Full-field response estimation

Introduction

Inverse load identification and full-field measurement technologies are very active fields of research in structural dynamics. Inverse load identification is generally linked to the solution of ill-conditioned systems of equations and it is notorious to be hard to solve in the case in which multiple loads are unknown on stiff structures [170, 6, 175]. The role of inverse load identification technologies is nonetheless of paramount importance. In fact engineers and analysts with different backgrounds often need an accurate knowledge of loads entering a structure or an electromechanical system. These input loads are often difficult to measure directly since dedicated sensors can be intrusive, expensive and can rarely be equipped during the operational life of the system. For these reasons, estimation of external loads represents a crucial task in many automotive, aerospace and manufacturing applications. If the loads are known, the design process of a component can be improved and the reliability and lifetime of a product can be increased. Within the last decades, several test-based and simulation-based technologies have been researched and developed aiming to deal with these issues. Inverse load identification were initially solved through off-line test-based strategies. One of such strategies relates to the field of Transfer Path Analysis (TPA), where the Matrix Inversion (MI) and Mount Stiffness (MS) [170, 65, 122, 64] approaches are among the most commonly used methods, in particular for mechanical applications. The purely experimental nature of TPA and the low computational cost represent great advantages over other available inverse identification methods. The MS approach can be used when the external loads is acting on the structure through flexible mounts and if mount stiffness data is available. When this is not the case, the MI approach can be adopted. However, several numerical disadvantages might limit its usability. Over-determination of the matrix generally improves the robustness of the inversion and a large set of sensors is hence selected. This in turns leads to large measurement efforts and costs. Well-chosen measurement points around the loaded area of the structure are selected as sensors' locations [187], but an objective optimal criteria is not yet defined. A more time efficient-approach named Operational Path Analysis (OPA) is presented in [91], but its causal assumption among outputs limits the applicability in most industrial application cases. When going towards simulation-based methods, a common approach in the field of structural mechanics is the off-line estimations through Finite Element (FE) models. An example is reported by Adams [6] making use of a time domain approach in a deterministic setting. When the structural complexity of the system increases, the complexity of the proposed inverse method becomes a great disadvantage. More recently, thanks to the advancement of computational performances of numerical strategies used to solve complex models, estimators such as Kalman-based filters [95, 164, 148, 118] have been used to approach the

problem of inverse load identification in an on-line fashion. The potential of on-line Kalman-based techniques was first tested on full-field response estimation (e.g. purely state estimation). A numerical and experimental application is reported in [140], performing the simultaneous usage of multiple types of measurements (e.g. accelerations and strains). If no direct measurements of the input are available but the input location is known, the estimation problem can be solved by using a joint state-input estimation algorithm. This Kalman-based approach gives the possibility to estimate full fields such as strains, displacements and accelerations concurrently with the unknown input. Gillijns and De Moor [77, 77] studied the problem for linear discrete-time systems. A recursive filter was proposed, with the structure of a Kalman filter, except that the true value of the input is replaced by an optimal estimate. The numerical performances of this algorithm are investigated and applied to structural systems by Lourens et al. [114]. The feasibility of the method for industrial applications was demonstrated on a complex case for distributed load identification. Under certain conditions, inaccuracies of the response estimation occur and the effect of modelling errors is not compensated. A drift effect on the estimation of input and displacements is observed by Azam et al. [19, 20]. That is linked to the integral nature of those quantities in the presence of acceleration information. A dual formulation of the simultaneous input and state estimation is hence proposed in [19] to prevent the mentioned numerical problems. The so-called Dual Kalman Filter (DKF) approaches the estimation of the input and states in two different stages. The effectiveness of this filter was tested on large industrial test cases [19, 146]. Another way to perform joint state-input estimation is identified by the so-called Augmented Kalman Filter (AKF) [164]. Within this framework, the system state vector is augmented by including the unknown input variables. That defines a reduction of the computational cost needed for the execution of the DKF. One of the key points of both methods resides in the fact that a force model has to be introduced in the filter. This task is particularly challenging since mostly input loads have an erratic and a priory unknown distribution in time. The AKF was recently applied to structural dynamics in [130, 115, 151]. A detailed explanation regarding the applicability of this filter to dynamic mechanical systems is described in [149]. Lourens et al. [115] perform force identification through acceleration measurements. The results show that when measurements can only be performed at locations relatively far from the force identification, the AKF fails to predict the applied force. Naets et al. [130] propose an analytical analysis of the stability of the Kalman-based force estimation techniques and show that only using acceleration measurements inherently leads to unreliable results. That was also demonstrated with real data in [19, 20]. Tamarozzi et al. [175] propose an Optimal Sensor Placement (OSP) strategy aimed to optimally define type (position/strain/acceleration) and location of sensors to be used in the joint state-input identification problem.

The performance of the method is numerically tested. Significant reduction of sensors installation costs can be obtained.

Within the present work, the potential of the AKF through the OSP strategy was investigated on an industrial test case. In order to illustrate the effectiveness of the filter, the results about load identification are compared against the TPA MI technique and a direct force measurement through a 6 degrees of freedom force cell. Measurement acquisition and data processing will be analyzed and compared in details, including remarks on noisy experimental data and model accuracy. Furthermore, the applicability of the Kalman-based strategy for full strain field estimation is also analyzed. The paper presents the following structure. First, an overview of Kalman Filter applied to mechanical systems is reported together with the modelling techniques used within this work i.e. state-space formulation for structural dynamics problems and linear Model Order Reduction (MOR). Furthermore, the main principles of the OSP strategy are explained. First, a brief theoretical background about TPA Matrix Inversion is reported. The experimental setup of a rear twistbeam suspension is showed and the comparison between AKF and TPA is proposed for force identification. The potential of OSP for AKF applications is demonstrated on the acquired experimental data. In the second part, the state estimation through Kalman Filter is performed in two conditions of known and unknown external loads. Finally, concluding remarks and future developments are discussed..

Theoretical Background

Augmented Kalman Filter for joint state-input estimation

This section addresses the Kalman-based strategy applied on a dynamic mechanical system. The governing equation of a second order model in a Finite Element [202] formulation is the following:

$$\mathbf{M_z}\ddot{\mathbf{z}}(t) + \mathbf{C_z}\dot{\mathbf{z}}(t) + \mathbf{K_z}\mathbf{z}(t) = \mathbf{B_z}\mathbf{u}(t) \tag{I.4}$$

where $\mathbf{z}(t) \in \Re^{n_{dof}}$ is the Degrees of Freedom (DoF) vector (n_{dof} number of DoFs of the model), $\mathbf{M_z}$, $\mathbf{C_z}$, $\mathbf{K_z}$ denote the mass, damping and stiffness matrices respectively; $\mathbf{u}(t) \in \Re^{n_i}$ (n_i number of loads) is the input vector and $\mathbf{B_z} \in \Re^{n_{dof} \times n_i}$ is the Boolean input shape matrix that distributes the inputs over the DoFs of the system.
In order to reduce the size of the FE model and thus the computational costs needed for computing the Kalman Filter equations, a Model Order Reduction (MOR) technique is used. As shown in [175, 130, 149], the following reduction basis is used:

$$\mathbf{\Psi} = [\mathbf{\Psi}_{ram} \quad \mathbf{\Psi}_{nm}] \tag{I.5}$$

where $\mathbf{\Psi}_{ram} \in \Re^{n_{dof} \times n_{ram}}$ is the *residual attachment modes* [46] matrix and $\mathbf{\Psi}_{nm} \in \Re^{n_{dof} \times n_{nm}}$ is the matrix of *normal modes*. The first basis allows to have an exact representation of the static response of the structure for a given input location. For each external load, the relative residual attachment mode has hence to be included. The matrix $\mathbf{\Psi}_{nm}$ contains instead a limited number of eigenmodes in the frequency range of validation of the structure. Usually, only the eigenmodes that are validated by experimental correlation are considered, in order to have a reduced model that remains fully representative of the real structure in the frequency range of interest. The reduced FE model has a total of $n_{red} = n_{ram} + n_{nm}$ DoFs. From the model order reduction, the DoFs vector can be approximated as:

$$\mathbf{z} \simeq \mathbf{\Psi q} \tag{I.6}$$

where $\mathbf{q} \in \Re^{n_{red}}$ contains the generalized coordinates of the system. By projecting Eq. I.4 onto the reduction basis, the equation of motion of the reduced system will be:

$$\mathbf{M_r}\ddot{\mathbf{q}}(t) + \mathbf{C_r}\dot{\mathbf{q}}(t) + \mathbf{K_r}\mathbf{q}(t) = \mathbf{B_r}\mathbf{u}(t) \tag{I.7}$$

with $\mathbf{M_r} = \mathbf{\Psi^T M_z \Psi}$, $\mathbf{C_r} = \mathbf{\Psi^T C_z \Psi}$, $\mathbf{K_r} = \mathbf{\Psi^T K_z \Psi}$ and $\mathbf{B_r} = \mathbf{\Psi^T B_z}$ respectively mass, damping, stiffnes and input shape matrix of the reduced system.
In order to define the Kalman-based strategy, the second-order equation of motion has to be formulated as a first-order equation (i.e. state-space representation). Starting from Eq. I.7, coupled with the response equation, the state-space form is written as:

$$\begin{cases} \dot{\mathbf{x}}(t) = \mathbf{A}\mathbf{x}(t) + \mathbf{B}\mathbf{u}(t) \\ \mathbf{y}(t) = \mathbf{C}\mathbf{x}(t) + \mathbf{D}\mathbf{u}(t) \end{cases} \tag{I.8}$$

where $\mathbf{x} = [\mathbf{q} \quad \dot{\mathbf{q}}]^T$ defines the state vector. $\mathbf{A}$, $\mathbf{B}$, $\mathbf{C}$, and $\mathbf{D}$ are real matrices. The firsts two are functions of mass, stiffness and damping matrices of the reduced system [149], while $\mathbf{C}$ and $\mathbf{D}$ depend on the output response type $\mathbf{y}$. The latter defines the measurement vector containing the observed quantities. Detailed explanation on how to build $\mathbf{C}$ and $\mathbf{D}$ in relation with acceleration, strain or position measurements is reported in [149]. If both measurements and input are known, a linear Kalman Filter can be applied to the system of Eq. I.8 and a simple state estimation (leading to a full-field response) can be performed. Since the joint state-input estimation is of interest in this paper, the augmented state vector has to be defined as follows:

$$\mathbf{x}^* = [\mathbf{x} \quad \mathbf{u}]^T \tag{I.9}$$

In order to define the augmented filter, the dynamics of the input has also to be modeled. In this work, a zeroth-order random walk model is introduced for the input [175, 115, 151, 129]:

$$\dot{\mathbf{u}}(t) = \mathbf{0} + \mathbf{w_u}(t) \tag{I.10}$$

with $\mathbf{w_u}$ stochastic process associated to the covariance matrix $\mathbf{Q_u}$. This parameter defines the variation of the input within a time-step Δt. The following formulation is used in this paper to evaluate the values of the matrix $\mathbf{Q_u}$:

$$\mathbf{Q_u} = (\Delta t \cdot \bar{\omega}_u \cdot \bar{a}_u)^2 \tag{I.11}$$

with $\bar{\omega}_u$ and $\bar{a}_u$ respectively as the expected value (i.e. indicative order of magnitude) of the frequency and amplitude of the input $u(t)$. Similar to the effect of a low-pass filter, this formulation allows to limit the variation of the estimated input in a time-step Δt. Further explanation can be done by considering for example a sinusoidal input. From Eq. I.10, the first derivative will be hence function of the frequency and the amplitude of the input shape. The time-discrete formulation of Eq. I.8 is:

$$\begin{cases} \mathbf{x}_k = \mathbf{F}\mathbf{x}_{k-1} + \mathbf{G}\mathbf{u}_{k-1} + \mathbf{w}_{k-1} \\ \mathbf{y}_k = \mathbf{C}\mathbf{x}_k + \mathbf{D}\mathbf{u}_k + \mathbf{v}_k \end{cases} \tag{I.12}$$

where $\mathbf{F}$, $\mathbf{G}$ are the discrete-time forms of the matrices $\mathbf{A}$, $\mathbf{B}$ respectively. Vectors $\mathbf{w}$ and $\mathbf{v}$ are mutually uncorrelated Gaussian variables (process and measurement noise), not usually included in the equations of motion. They are now introduced to take into account model and measurement uncertainties, with associated covariance matrices $\mathbf{Q} = E\{\mathbf{w}_k\mathbf{w}_l^T\} \geq 0$ and $\mathbf{R} = E\{\mathbf{v}_k\mathbf{v}_l^T\} \geq 0$ respectively. If all the inputs are unknown, Eq. I.12 can be written in the augmented filter formulation:

$$\begin{cases} \mathbf{x}_k^* = \mathbf{F}^*\mathbf{x}_{k-1}^* + \mathbf{w}_{k-1}^* \\ \mathbf{y}_k = \mathbf{H}^*\mathbf{x}_k^* + \mathbf{v}_k \end{cases} \tag{I.13}$$

with $\mathbf{H}^* = [\mathbf{C} \quad \mathbf{D}]$. The symbol * is assigned to indicate all the augmented quantities. $\mathbf{Q}^*$ is now defined as a block diagonal matrix composed by $\mathbf{Q}$ and $\mathbf{Q_u}$, that are the covariance matrices referred to the model and input uncertainties respectively. The Eq. I.13 is referred to the case of all unknown external loads. Simultaneous estimation of states and inputs of the system is hence possible. The formulation of $\mathbf{F}^*$ and $\mathbf{Q}^*$ depends on the chosen discretization scheme (see [188] for more details). In this work, an exponential time integration is used,

thus leading to [149]:

$$\mathbf{F}^* = \begin{bmatrix} e^{\mathbf{A}\Delta t} & \mathbf{A}^{-1}\left(e^{\mathbf{A}\Delta t} - \mathbf{I}\right)\mathbf{B} \\ \mathbf{0} & \mathbf{I} \end{bmatrix} \tag{I.14}$$

$$\mathbf{Q}^* = \int_0^{\Delta t} e^{\mathbf{A}t}\mathbf{Q}e^{\mathbf{A}^T t}d\tau \tag{I.15}$$

The discrete-time version of the Augmented Kalman Filter [164] can be formulated as following, by considering the time and measurement update. The a priori $\hat{\mathbf{x}}_k^{*-}$ (without taking into account the new measurement at time k) and a posteriori $\hat{\mathbf{x}}_k^{*+}$ augmented states are easily obtained:

Time update

$$\hat{\mathbf{x}}_k^{*-} = \mathbf{F}^*\hat{\mathbf{x}}_{k-1}^{*+} \tag{I.16}$$

$$\mathbf{P}_k^- = \mathbf{F}^*\mathbf{P}_{k-1}^+\mathbf{F}^{*T} + \mathbf{Q}_{k-1}^* \tag{I.17}$$

Measurement update

$$\mathbf{K}_k = \mathbf{P}_k^-\mathbf{H}^{*T}\left(\mathbf{H}^*\mathbf{P}_k^-\mathbf{H}^{*T} + \mathbf{R}_k\right)^{-1} \tag{I.18}$$

$$\hat{\mathbf{x}}_k^{*+} = \hat{\mathbf{x}}_k^{*-} + \mathbf{K}_k\left(\mathbf{y}_k - \mathbf{H}^*\hat{\mathbf{x}}_k^{*-}\right) \tag{I.19}$$

$$\mathbf{P}_k^+ = \left(\mathbf{I} - \mathbf{K}_k\mathbf{H}^*\right)\mathbf{P}_k^- \tag{I.20}$$

The latter set of equations represents the unbiased linear state estimator, designed to be optimal in the sense that it minimizes the trace of the error covariance $\mathbf{P}_k$, which is defined as:

$$\mathbf{P}_k = E\left[\left(\mathbf{x}_k^* - \hat{\mathbf{x}}_k^*\right)\left(\mathbf{x}_k^* - \hat{\mathbf{x}}_k^*\right)^T\right] \tag{I.21}$$

In order to have a stable estimator (i.e. $\mathbf{P}_k$ converges to a constant value for $k \to \infty$), the augmented system in Eq. I.13 has to be observable. The requirements for guaranteeing the observability of a structural system can be summarized as following ([118, 130]):

- the number of DoFs of the reduced model has to be equal or greater than the number of external loads to be estimated: $n_{red} \geq n_i$;
- the number of position/strain measurements has to be greater than the number of external loads to be estimated: $n_y \geq n_i$;
- in the case of full position measurement the AKF leads to a fully observable system and to a stable estimator. Performing only acceleration

measurements will typically not lead to a stable AKF for structural systems.

Since the observability of the system is a key point for having good estimation through Kalman-based approach, a new strategy focused on the system observability was developed in [175] selecting the optimal number, type and location of sensors for the loads identification. In the following section, the Optimal Sensor Placement (OSP) criterion will be briefly described.

OSP: theory and experimental validation

Full scale experimental validation for inverse load identification need information coming from sensors that are often located in the interested input area or, more in general, in the areas that are more sensitive to the external excitation. This selection criterion is adopted for the TPA identification analysis and it will be discussed later. The safety of the sensors is lower if they are installed in the loaded area. How to locate sensors is an open question also for numerical reasons, since inverse load identification methods result often in ill-conditioned and ill-posed problems. At last, also the type of measurement is an important choice for the Kalman Filter: requirements related to observability have to be taken into account (as described in Sec. *Augmented Kalman Filter for joint state-input estimation*). In [175], an Optimal Sensor Placement (OSP) strategy is developed to deal with these issues for Kalman-based load identification, by allowing a smart selection of optimal type, number and sensors location. Five steps are identified and schematically shown in Fig. I.8:

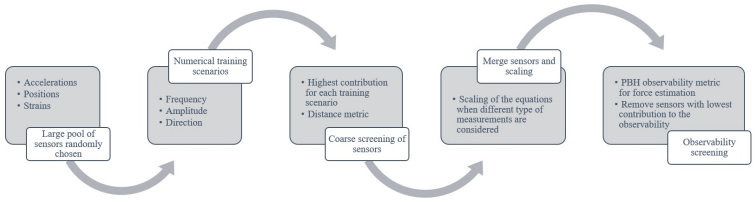

Figure I.8: Optimal Sensor Placement strategy

- **Pool of sensors:** First, a large number of random nodes and elements for position/strain/acceleration responses are selected over all the FE model. Choosing sensors located on all available nodes and elements is the optimal way to chose the optimal set of sensors, but a restricted number has to be selected for reducing the computational cost.
- **Training scenarios:** The FE model is simulated under static and dynamic loads with different direction, amplitude and frequencies. The excitation is applied to the known input location of the external loads to identify.

- **Coarse screening:** From the first step, a data set of position/strain/acceleration responses is collected. This step removes all the sensors with the lowest contribution for each training scenario i.e. low Signal/Noise ratio. A second screening removes the selected sensors of the same type too close to each other.
- **Merge sensors and scaling:** All the measurements identify the C matrix of the state-space system in Eq. I.8. The rows of the matrix is scaled so that the following step (based on PBH criterion) doesn't take into account different type of sensors.
- **Observability screening:** a loop is performed by selecting the sensors with the main contribution to force identification i.e. the highest effect on the system observability. The observability is quantified as following [129]:

$$O_m = \frac{1}{n_i \cdot cond(\mathbf{PBH}(0))} \tag{I.22}$$

where n_i is the number of loads to estimate and **PBH** is the observability matrix, defined as:

$$\mathbf{PBH} = \begin{bmatrix} \omega_d \mathbf{I} - \mathbf{A_d} \\ \mathbf{C_s} \end{bmatrix} \tag{I.23}$$

This matrix comes from the so-called *PBH observability test* [75], which shows that the system is observable only if the **PBH** matrix has full rank for each eigenvalue of the system. In Eq. I.23, $\mathbf{A_d}$ and ω_d identify the discretized matrix $\mathbf{A}$ of the system and the eigenvalues of $\mathbf{A_d}$ respectively. As mentioned before, an exponential time integration is used in this work. $\mathbf{A_d}$ is hence given by:

$$\mathbf{A_d} = e^{\mathbf{A}\Delta t} \tag{I.24}$$

The **PBH** matrix, related to the reduced and augmented model and evaluated for each ω_d of the discretized system, has size $(n_y + 2n_{red} + n_i) \times (2n_{red} + n_i)$. In Eq. I.22, the condition number of the **PBH** matrix is evaluated for the eigenvalues related to the residual attachment modes. That means the **PBH** matrix is evaluated at 0Hz which is the frequency related to the random walk model.

Some numerical results in [175] show the performance of this strategy. A key contribution of this paper resides in evaluating its effectiveness on experimental data. In the presented load identification analysis, the OSP criterion is used in the pre-processing phase to select sensors for the measurement campaign. A further development of the OPS could be considered taking under consideration

additional conditions required for an efficient estimation of the Kalman Filter [118]. In particular, the condition of instantaneous system inversion could find a suitable position for improving the optimal selection of the type of sensors. This conditions guarantee the inversion of the system without any time delay on the estimated quantities and it is directly translated into the needed number of acceleration measurements (at least equal to the number of input to be estimated). A detailed explanation and investigation is reported by Maes et al. [119], whom propose a formulation of the invertibility condition in terms of the modal characteristics of the structure. The merging of this metrics into the *coarse screening* step could be considered in the future as improvement of the OSP strategy.

TPA Matrix Inversion

To show the quality of the results obtained through AKF, the load identification is compared with the Transfer Path Analysis technique. That is an experimental method which aims to identify the vibro-acoustic transfer path in a structural system. This methodology is applied in many manufacturing industries and can be used for all types of structures such as cars, boats, wind turbines or even full aircrafts. Wide applications are currently studied in the automotive field. Performing TPA on a car engine, for example, helps reducing interior noise, driving wheel and seats vibration that means an improvement of comfort. The main strong advantage of TPA is that it allows engineers to perform simulation using only test data.

A TPA experimental model of a structure has to be identified by the so-called active and passive parts. The active part is the source; the passive part contains the receiver points where the output responses are measured. In an automotive example, the engine identifies the source and the chassis is the receiver. The loads acting on the receiver are defined at the interface between the active and the passive part and the relationship between a load and a receiver is defined by the Frequency Response Functions (FRFs). In the framework of inverse load identification, TPA proposes two approaches: Mount Stiffness (MS) and Matrix Inversion (MI) methods. The use of MS occurs when the active and the passive structures are connected through flexible mounts. For transfer path which comprises of rigid connections or where the mount stiffness is very large with respect to the body impedance, the MS method cannot be used for load identification. In that case, the MI technique can be adopted. The formulation requires the inversion of the FRFs matrix which has to be measured off-line, when the source is disconnected from the receiver. The so-called indicator responses are also measured on the receiver in operational conditions. Usually, they are located close to the source connection. The relationship in frequency domain between the FRF matrix (for multiple inputs) and the indicator data is

the following:

$$\mathbf{y}(\omega) = \mathbf{H}(\omega)\mathbf{f}(\omega) \tag{I.25}$$

where $\mathbf{y}$ and $\mathbf{f}$ are the vector of the measured quantities (as accelerations or strains) and the vector of the loads acting on the receiver respectively, both functions of the spectral lines ω. By inverting the FRF matrix $\mathbf{H}$ and by multiplying this with the operational data $\mathbf{y}$, the load identification can be performed:

$$\mathbf{f}(\omega) = \mathbf{H}(\omega)^{-1}\mathbf{y}(\omega) \tag{I.26}$$

Even if the analyst could be interested in estimating only one force direction or more in general a subset of all 6 loads, the knowledge of the full FRFs matrix is still needed. Indeed Eq. I.26 can be rewritten in a general form as:

$$\mathbf{f}_u(\omega) = \mathbf{H}_u(\omega)^{-1}\left(\mathbf{y}(\omega) - \mathbf{H}_k(\omega)\mathbf{f}_k(\omega)\right) \tag{I.27}$$

where the indices k and u are referred to known and unknown loads respectively. The matrix inversion often leads to some numerical issues [170, 122, 185, 33]. The number of measured data must exceed the number of loads to be estimated in order to overcome this issue and a large number of sensors are needed. This hence leads to the calculation of the pseudo-inverse matrix in Eq. I.26 and Eq. I.27. Inaccuracies in the measured FRFs data (as impact direction) can results in large errors on the estimated loads [155].

Inverse load identification on a rear twistbeam suspension

This work aims to validate the applicability of the Kalman-based strategy for industrial applications. The proposed Kalman Filter allows a coupled identification of the external loads acting on a system together with the estimation of full-field responses. In this section, the load identification is first analyzed and in this framework, the effectiveness of the filter is compared with TPA MI. The object of the analysis is a rear twistbeam suspension, which is shown in Fig. I.9: the test-rig was realized by clamping both bushings and one tyre. The right side tyre is in free condition and the load identification will be performed on its central point i.e. known input point. This tyre is excited by a 6 DoFs hydraulic shaker available at the University of Leuven (KUL) laboratory. The shaker is a unique piece of equipment that allows to retain full control on the desired excitation spectrum up to high frequency (around 200Hz) and in 6 directions independently. The shown setup is indicated in the following as

operational configuration. A force cell is also used in order to collect experimental load data for validating the estimated results. Accelerometers and strain gages are installed on the structure to cover the output response requirements for both MI and Kalman Filter estimations. Two different criteria for the selection of sensors location are thus adopted and two sets of measurements data are collected for applying both techniques. The advantages of the filtering method are defined starting from the effort needed for the instrumentation and for the measurement campaign, followed by the data-processing. In the proposed analysis, only strain measurements are taken into account.

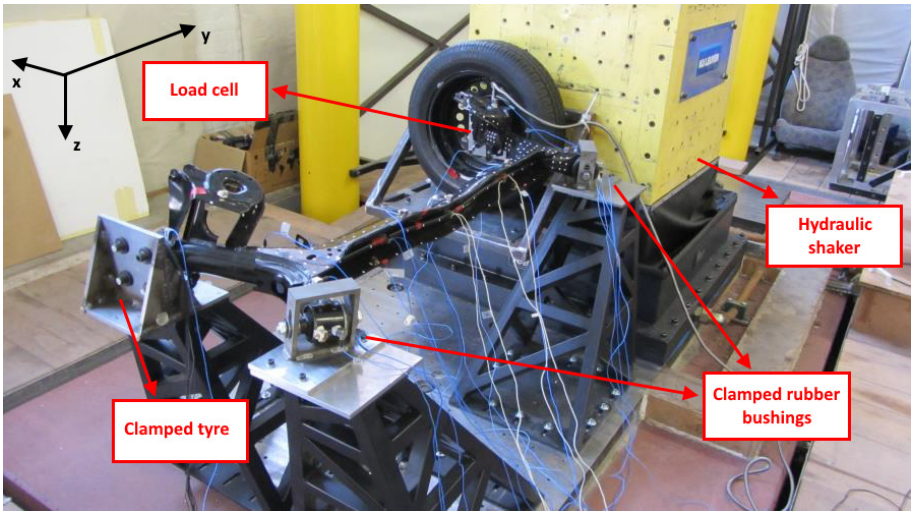

Figure I.9: Rear twistbeam suspension setup - operational configuration

The application of Kalman Filter on a structural system needs the knowledge of the operational response data. The latter is used on the FE model aimed to perform purely state estimation (e.g. strain/stress field) or coupled state/input estimation. A Model Order Reduction is firstly performed as described in Sec. I. The residual attachment modes are computed by simulating the FE model under a set of 6 static loads (one force and one torque for each direction) that are applied on the known input point. The normal modes matrix contains instead the eigenvectors that show good correlation with the experimental modes. In this application, four normal modes are considered. The size of the reduction basis of Eq. I.5 is thus $[n_{dof} \times 10]$. In this paper, the linear FE model (shell mesh with 50533 CQUAD elements) detailed described in [45] is used. In addition to the model validation performed in [45], the bushings are modeled as grounded springs in each direction.

The challenge in the Kalman-based strategy is the matching between measured and simulated data. Taking the example of a strain measurements, it is particularly challanging to match the exact location and direction of a strain gage and locate it on a finite element model. This issue has particular relevance for strain measurements that are located in areas with high stress gradient and further investigation is here reported. After the instrumentation phase, the location and measurement direction of each sensor were acquired through the use of an optical device AICON ProCam camera [172]. This system comprises an active mobile probe with a high resolution camera. Thanks to this data acquisition, a sensors map of the experimental setup is available. Overlap the obtained map on the FE model is not a straightforward task. A common issue is the not exact geometry representation of the model, combined to the inaccuracies of the camera device. This in turns might lead to a not negligible level of uncertainty in the finite elements selection. An optimization process for the elements selection is developed and proposed in this contribution to overcome this issue. Looking at the Fig. I.10, the following steps are performed:

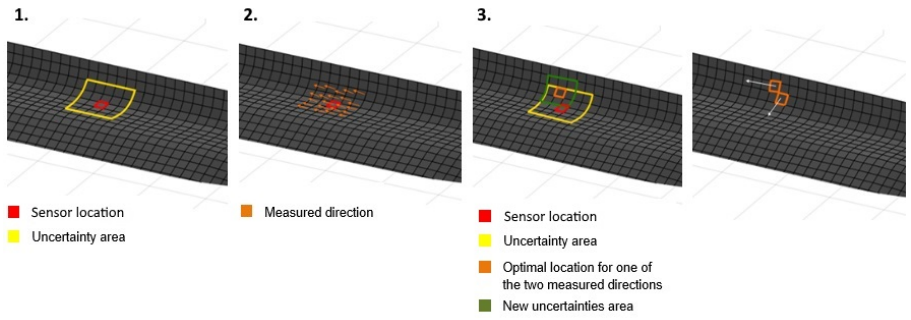

Figure I.10: Optimization process for matching measured and simulated strain

1. Starting from the location (red) identified by ProCam camera, it is possible to define for each sensor an area of uncertainties (yellow) considering the precision of the measuring instrument and the geometrical accuracy of the FE model.
2. Evaluate strain quantity along the measured direction on each element which is included in the considered grid. Find the element that minimize the error between numerical and experimental data for a set of training scenarios.
3. If rosettes are considered, another step is needed: a new uncertainty area (green) is defined around the optimal location (orange) found by the previous step (performed for one of the two measured directions). This

area is smaller since it takes into account only the size of the rosetta. The steps 1-2 are then performed on the green area for the remaining direction.

The application of the proposed method starts from the knowledge of a strain dataset corresponding to a training load case. Before performing the load identification, this preliminary step is hence introduced for a static load case. The latter is applied on the free tyre (input point) in operational conditions of the twistbeam: two sets of data are collected for 30 and 80 N applied in z direction (from frame of reference shown in Fig. I.9). In Fig. I.11, the measured strain value of each sensor (ind channel in the picture) for the load cases 30N and 80 N is compared with the one evaluated on the finite element identified by ProCam (FEM start) and the one evaluated on the element in the uncertainty area that better matches the experimental data (FEM opt). No optimization procedure for strain matching is performed for the load case 80N, indeed the optimal elements are the ones selected for 30N to verify if the selection is still optimal for other dataset. The results show that only few elements are not optimal for 80N (ind. channels 23 and 32 in the picture). Note that this static validation was performed only for one direction and low amplitude load cases, such that the static behavior of the structure can still be considered as linear. The efficiency of this selection is later evaluated in operational conditions where the structure is subject to 6 loads (3 forces and 3 torques) with higher amplitudes. In the following Kalman-based analysis, the optimal elements selected for 30N dataset are considered for matching the measured signals on the FE model. Performing the proposed optimization process allows to obtain more accurate results but longer experimental and numerical procedures linked to the proposed Kalman-based approach.

Experimental results

In this section the effectiveness of Kalman-based strategy against TPA Matrix Inversion dealing with load identification is illustrated by means of the measurement campaign performed on the rear twistbeam suspension. Joint state-input estimation is computed through AKF. Two excitation scenarios, reported in Tab. I.3, are performed thanks to the hydraulic shaker collecting operational data measurements. In the table, the amplitude is expressed in terms of shaker displacement.

Run	**Type**	**Freq. [Hz]**	**Amplitude [mm]**
1	sine	1	5
2	pseudo-random	5-50	30

Table I.3: Excitation of operational data

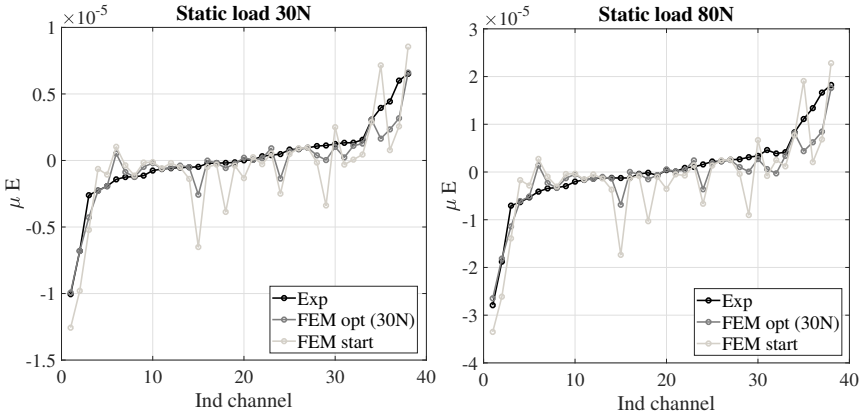

Figure I.11: Static validation through optimization procedure: numerical and experimental strain comparison. FEM start: strain evaluated on the element identified by ProCam. FEM opt: strain evaluated on the optimal element.

Here, the results related to load estimation of run 1 and run 2 are shown. These two cases are used to better understand limitations and advantages of both load identification techniques. First, some analysis are conducted to answer to the following questions:

- how many sensors are needed for obtaining good load estimation?
- which is the best sensor location for load estimation?

A sensitivity analysis is performed on the dataset of run 1 and separately shown for TPA and AKF. Two sets of loads are acting on the tyre, identifiable in 3 forces and 3 torques in each direction.

Looking at Fig. I.12, the twistbeam was instrumented for TPA application purpose by locating 10 and 8 strain gages close to the load and clamp area respectively. The sensors are located both close to and far from the load area. This choice aims to verify which area is more sensitive in a clamped configuration of the system subject to a given external excitation, depending on the type of response (strain or accelerations). In Fig. I.13, the frequency content of forces and torques prediction is compared with the reference ones, which are referred to the data measured through the 6 DoFs load cell. In the legend, "TPA - local" indicates the results obtained by using the information coming from the 8 sensors located in the load area. "TPA - all" is referred instead to all the available sensors. In this latter case, a better estimation for a set of the 6 loads is obtained for two reasons: the number of local subset of sensors is not enough for inverse identification of 6 loads and moreover, the information coming from

the clamped area is of more relevance in the operational configuration. The latter might not be true if accelerations data are considered. Indeed, in that case the loaded area would be more sensitive to the external excitation and no additional information coming from the accelerations on the clamped area could be helpful for load identification.

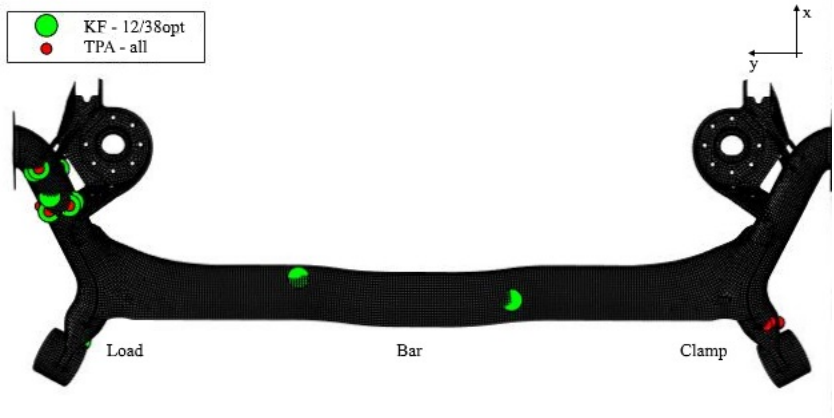

Figure I.12: Location of selected sensors for load identification. Two different sets for Kalman-based and TPA techniques.

The OSP strategy was instead adopted for AKF load identification, extending the numerical work proposed in [175]. Performing some simulations on the

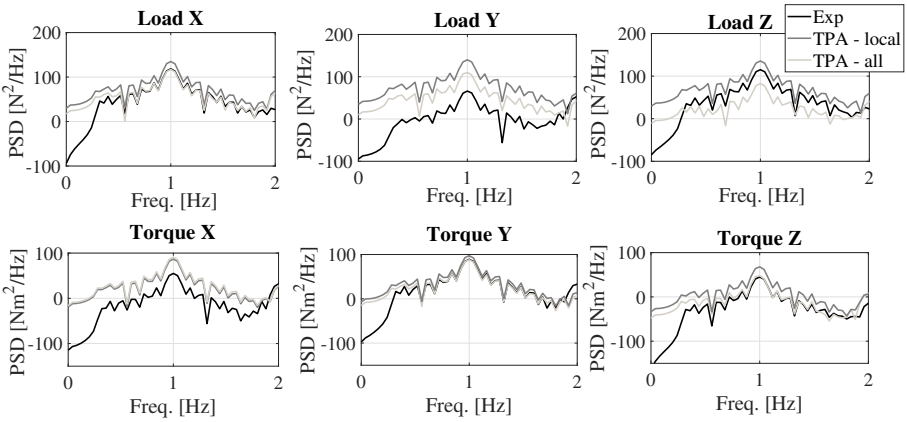

Figure I.13: Run 1. Frequency content of estimated loads through TPA Matrix Inversion: comparison of the results for two different sets of indicators.

FE model (steps described in Sec. *OSP: theory and experimental validation*), a set of 38 strain gages are selected over the structure. First, the needed minimum number of sensors (between the optimal ones) are identified for the identification of the loads. The results of this sensitivity analysis (based on the observability measure) showed that 12 optimal strains are needed in order to obtain an acceptable load identification. Starting from this set of sensors, the frequency content of the 6 estimated loads is compared against the results obtained by selecting 12 random sensors over the structure. The load comparison in frequency domain is proposed in Fig. I.14. The distribution of sensors for both cases is the following:

- **12/38opt:** 10 and 2 sensors located in the load and central bar area respectively
- **12/38rand:** 9 and 3 sensors located in the central bar and clamp area respectively

Even if all the 38 sensors are optimal with respect to observability (since they were selected in the pre-processing OSP simulation analysis), the 12 that are chosen as optimal between all the available sensors show better evaluation. The effectiveness of the OSP strategy is considerable especially on the forces estimation. The subset of 12 optimal sensors was selected evaluating the observability contribution as indicated in Eq. I.22. Note that, from the second observability requirement, reported in Sec. I, 6 strain measurements should be enough for the estimation of 6 loads. That is true for overcoming numerical issues, but since we are dealing with experimental data and FE model inaccuracies occur, an higher number of sensors is needed to obtain good estimation of the external loads.

The results shown in Figg. I.13 and I.14, are summarized together in time-domain in Fig. I.15, where the TPA method uses 18 strains and the AKF approach uses the 12 optimal sensors. In order to have a complete overview of the estimated loads, a further case is analyzed which is referred to the pseudo-random excitation (run 2). A zoom of the results in time-domain is shown in Fig. I.16 The frequency content is also reported in Fig. I.17 to give a better representation of the results.

Fig. I.15 shows that good simultaneous prediction of 6 loads can be reached through the optimal sensor selection for AKF application. Similar results are obtained with TPA, even if the estimation of 6 loads led to loss of accuracy mostly on "Load Z" which is referred to the more flexible direction of the structure. A first explanation lies in the quality of the measured FRFs used for Matrix Inversion. Before applying the method, a correction of each strain FRFs at low frequencies needs to be performed, since issues related to noise, bridge settings and temperature drift occur on the static value. If the problem concerns

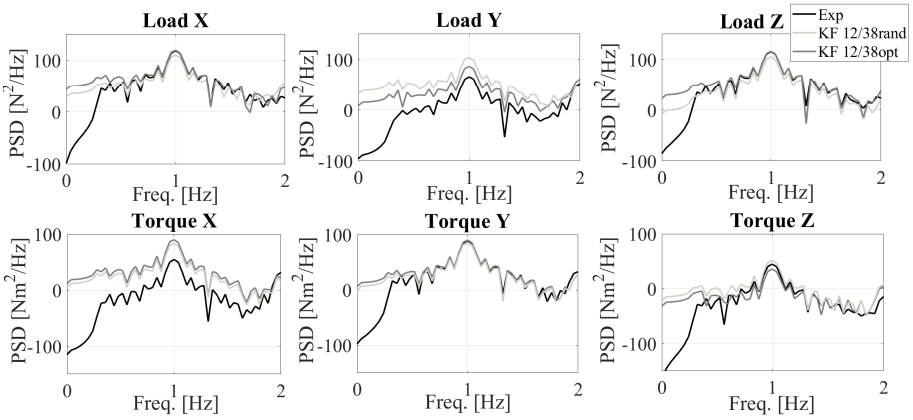

Figure I.14: Run 1. Frequency content of estimated loads through AKF: comparison of the results for two different sets of sensors. KF 12/38opt: optimal sensors. KF 12/38 rand: random selection of sensors.

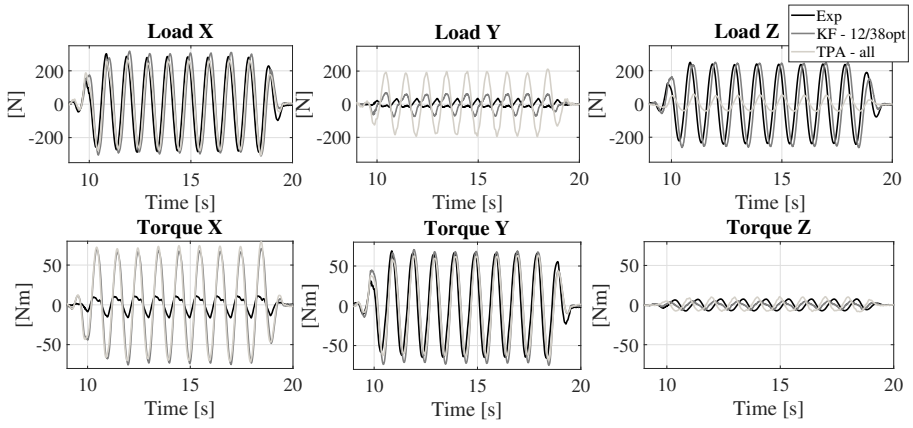

Figure I.15: Run 1. Time-domain comparison between estimated loads through AKF and TPA Matrix Inversion for two different sets of sensors.

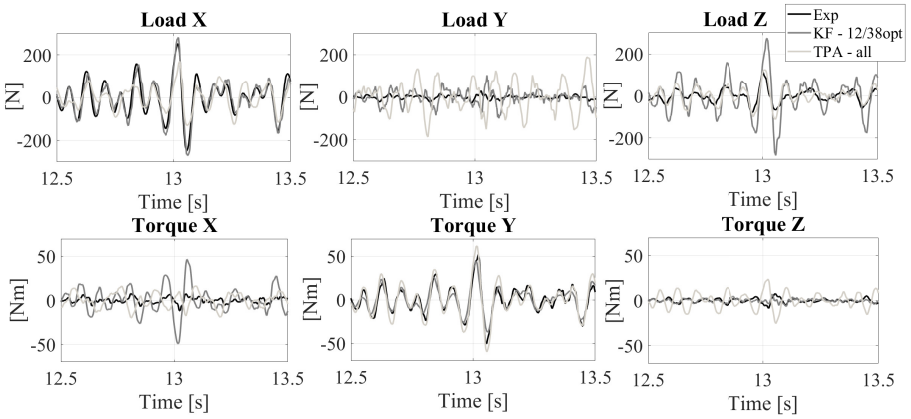

Figure I.16: Run 2. Time-domain comparison between estimated loads through AKF and TPA Matrix Inversion for two different sets of sensors. Zoom on a shorter time interval.

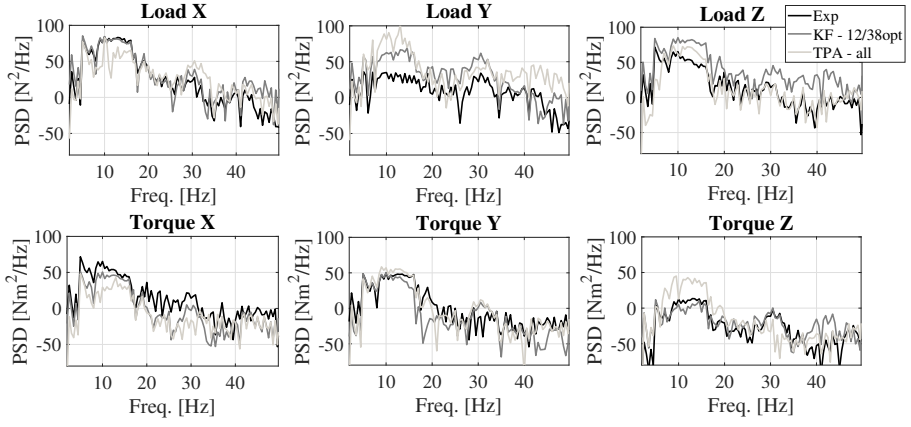

Figure I.17: Run 2. Frequency-domain comparison between estimated loads through AKF and TPA Matrix Inversion for two different sets of sensors.

a wide number of FRFs involved in the computation of the matrix inversion, a loss of accuracy can occur on the estimation. On the other hand, issues about quality of the measured FRFs occur also in high frequency range, where giving good excitation to the structure is always a challenging task. This observation is reflected in the results shown in Fig. I.17, that are referred to pseudo-random excitation (run 2). Loss of accuracy occurs in the frequency range of interest for TPA estimation, with the exception of "Load X" and "Torque Y". The direction of the stinger of the shaker used for FRFs acquisition is also a source of influence for the estimation.
Regarding the performance of AKF, the results show the same trend of estimation from run 1 to run 2, even if worse prediction is given for "Load Z" in Fig. I.17. Looking at the complete frequency range, some loss in accuracy is present also for AKF at higher frequencies. The explanation resides in the dynamic validation of the model, thus the load prediction is also affected by model errors. An observation is needed with regard to "Load Y", that results in a wrong estimation from both techniques. The reason resides in the stiffness of the structure along Y direction which is definitely the stiffer one i.e. axial direction. The wrong order of magnitude estimated from TPA is given by the ill-conditioning problem caused by the different stiffness distribution of the structure along the different directions of estimation. Indeed, applying a static load to the input location of the FE model along Y direction results in a much lower deformation as compared to the same static load applied along Z or X directions. Defining the static stiffness K for each direction as the ratio between the amplitude of the load and the displacement evaluated at the same input point, it results in large ratios K_y/K_z and K_y/K_x. That is directly translated into an ill-conditioned inverse problem. An improvement is obtained from AKF: it has to be noticed that in the model-based inverse problems, the only link between the estimated forces and the responses is the model itself. Contrarily, the link for TPA is given by measured FRFs which results in the issues mentioned above. The results obtained through AKF can be hence considered acceptable. However, the effort needed to deal with a well validated FE model is very similar to the one needed for the acquisition and the post-processing of FRFs data. Some parameters of the filter had to be set for the shown analysis. The initial state of the system was assumed to be known and equal to zero. Thus, the initial covariance matrix $\mathbf{P}_0$ is set to be zero. The block-diagonal covariance matrix $\mathbf{Q}^*$ was chosen by considering that the higher source of uncertainty in the model is given by the unknown input, such that $\mathbf{Q}_u >> \mathbf{Q}$. The matrix $\mathbf{Q}$ is thus set to zero, as the off-diagonal terms of $\mathbf{Q}_u$. The diagonal terms of $\mathbf{Q}_u$ are instead evaluated from Eq. I.11 and each value can be used to regularize the estimation problem. Several works in literature [118, 20, 115] propose the use of the L-curve [83] in order to calibrate those values. Fig. I.18 shows the effect of $\mathbf{Q}_u$ on the loads and measurements estimation of run 1. In the picture, the

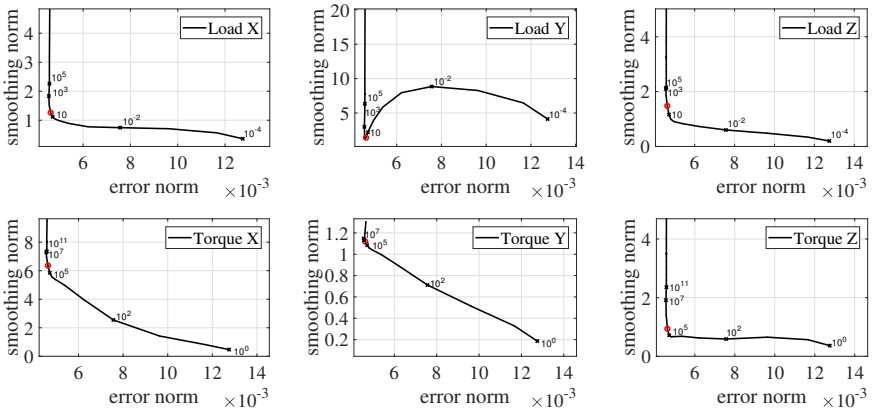

Figure I.18: Run 1. L-curve of the estimated input loads using the AKF (12/38opt sensors). Used values of $\mathbf{Q}_u$ are marked in red.

smoothing norm is defined as $\frac{\sum_{k=1}^{N} ||u(k)||_2}{\sum_{k=1}^{N} ||u_{ref}(k)||_2}$, with $u(k)$, $u_{ref}(k)$ respectively as estimated and measured input at time step k and with N as total number of time steps. The *error norm* is instead linked to the response quantities $\mathbf{y}$ and it is defined as $\sum_{k=1}^{N} ||\mathbf{y} - \mathbf{H}^*\mathbf{x}^*||_2$. It is observed that the error norm decreases with an increasing values of the covariance matrix $\mathbf{Q}_u$, reaching a stable situation with a constant value of the error norm and an increasing value of the smoothing norm. The marked points in Fig. I.18 indicate the values of $\mathbf{Q}_u$ used in the presented analysis (Fig. I.15) and selected from Eq. I.11. Their locations show that the method explained trough Eq. I.11 leads to values that are almost optimal (i.e. minimum smoothing error and error norm) in the L-curve. Regarding the measurement noise, the diagonal matrix $\mathbf{R}$ assumes instead the values of the covariance associated to each measurement. A noise acquisition data was performed during the test campaign for this purpose. An analysis of sensitivity of the accuracy of the input estimation with respect to the level of measurement noise is conducted on simulated data and shown in [175].

State estimation: Kalman Filter vs Augmented Kalman Filter

This section concerns the full-field response estimation through Kalman-based strategy under two different hypothesis. When the external input excitation is

known, a linear Kalman Filter can be applied for state estimation. On the other hand, if these quantities are not measurable, a joint state-input estimation is needed. In the previous section, results about AKF were reported by showing only the estimated loads. Here, the estimated states (strain quantities) of run 1 and 2 dataset are compared against the ones obtained by Kalman Filter. Two observations about the selected optimal sensors used as input for state estimation are underlined:

1. The set of sensors used for AKF are optimal in view of load identification, thus no improvement effect on the state estimation is given thanks to the selected optimal set. Indeed, the observability check for coupled state-input estimation (Eq. I.22) is restricted to the eigenvalues related to the residual attachment modes.

2. As mentioned in the previous point, since the OSP strategy aims at load identification, no optimal sensors selection is used for purely state estimation performed through Kalman Filter. In this case, the random selection is hence adopted in the following analysis.

Before the comparison between state estimation obtained from KF and AKF, the validation of what is mentioned in the first point is proposed in Fig. I.19: the absolute value of the amplitude and the RMS value of each estimated strain signal is compared respectively for run 1 and run 2. The comparison shows that full-field estimation has almost the same trend if optimal or random selection of sensors is used for AKF. The slight differences shown in the pictures are given by the accuracy of the used sensors matched on the FE model. The red points on each curve are marked to indicate that the measured information coming from that channels are used as input for the filter. Note that, for improved reliability, the channels are ordered from minimum to maximum experimental values, thus the "Ind Channel" scale is different from the one indicated for the static analysis of Fig. I.11.

In Fig. I.20, the full-field strain estimation is shown for both analysis (run 1 and 2): the strain trend obtained under unknown loads (AKF) condition follows the experimental trend within an acceptable error (indicated by "abs err" and "RMSE" in the picture). That is consistent with part of the analysis performed by Lourens et al. [113], showing that when the load location is known, the coupled state-input algorithm results in high accurate estimation. When the loads are known (KF), the system is instead simulated under the measured loads and some selected strains (given as input data to the filter) are matched on the simulated response output. If the model contains some uncertainties, the system is "forced" to match strain quantities that result to be wrong with respect to the simulated data. This gives an explanation of some high discrepancies on the estimated strain trend through KF. When all known loads are considered,

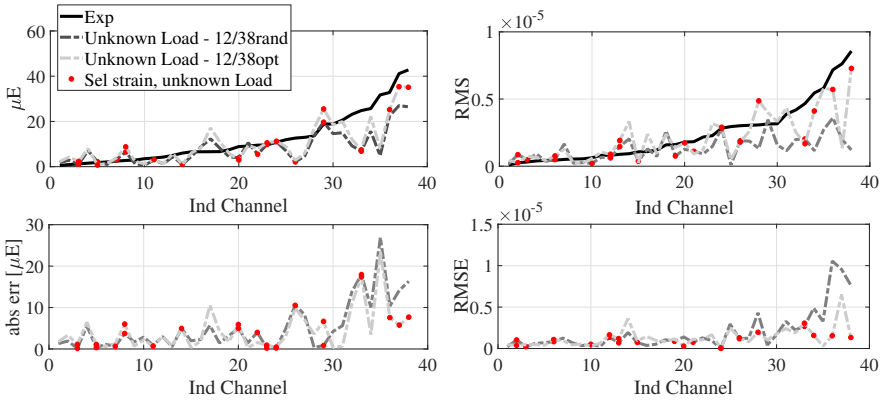

(a) Run 1 (b) Run 2

Figure I.19: Strain comparison for unknown load (AKF) estimation: optimal vs random selection of sensors.

the covariance matrix $\mathbf{Q}$ (related only to model uncertainties) cannot be set equal to zero. More in general, the effect of $\mathbf{Q}$ can be understood comparing its value with the one assumed by $\mathbf{R}$, which represents the response uncertainties:

- if $\mathbf{Q} >> \mathbf{R}$ the model is less reliable and the estimated response field follows the measured data
- if $\mathbf{Q} << \mathbf{R}$ the model is highly reliable and the estimated response field follows the simulated data

The results of KF in Fig. I.20 are obtained assuming $\mathbf{Q}$ with an order of magnitude higher than the one assumed by $\mathbf{R}$. That is a reasonable assumption since the used strain quantities are measured and the source of uncertainties is related to the signal noise. Uncertainties about the reduced FE model are hence of more relevance. Despite we assumed that $\mathbf{Q} >> \mathbf{R}$, the KF fails in the prediction of some strains resulting in higher errors. In Fig. I.21, the quality of the estimation proposed in Fig. I.20 is better quantified by showing the time-histories of strains Ind Channel n. 29 and 38 related to both run 1 and 2 (blue marked points in Fig. I.20).

In conclusion, the full-field estimation does not depend on the set of chosen sensors (if appreciable match on the FE model is considered) but on which information are given as input to the filter.

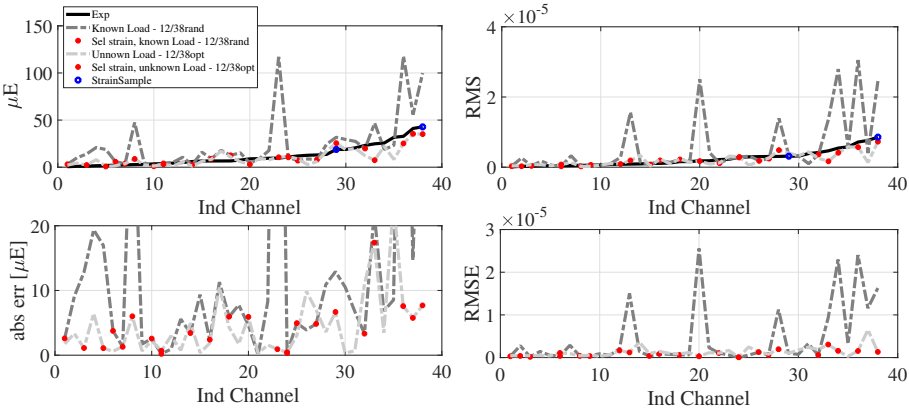

(a) Run 1 (b) Run 2

Figure I.20: Strain comparison for known (KF) and unknown (AKF) load estimation.

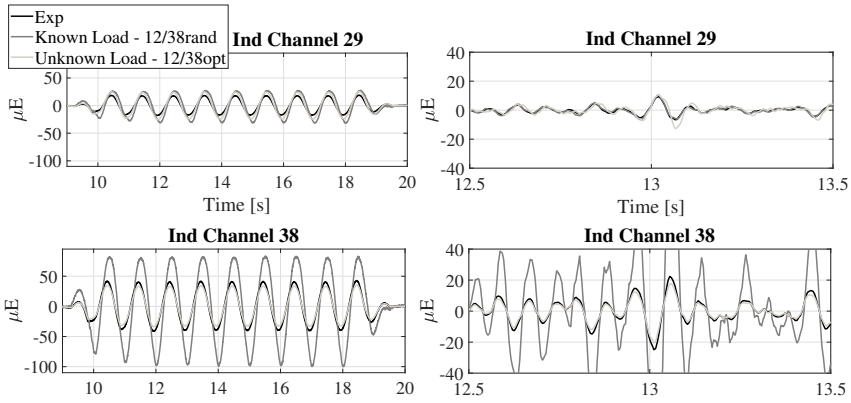

Figure I.21: Run 1 (left) and run 2 (right). Time histories of two strains: comparison between known (KF) and unknown (AKF) load estimation.

Conclusions

The potential of a Kalman-based strategy for load identification is presented in details and compared with the off-line technique TPA Matrix Inversion, currently used in multiple industrial application purposes. An Optimal Sensor Placement approach for Augmented Kalman Filter is adopted in this work to validate and demonstrate the quality of the method on real test-case data. A rear twistbeam suspension setup is investigated by simulating and experimentally exciting the structure under different excitation scenarios. The results showed that an accurate load estimation can be obtained through Augmented Kalman Filter for most of the analyzed input. Even if the stiffer direction of the structure fails in the load prediction, an improvement of the estimation is obtained through the Augmented Kalman Filter against the Matrix Inversion technique. Furthermore, less sensors are needed for the Augmented Kalman Filter. The preliminary analysis shown for AKF led to the conclusions that both proposed techniques need high effort in FRFs acquisition and FE model updating for TPA and Kalman Filter respectively. The quality of strain field (state) estimation over the structure is also tested through Kalman strategy. The analysis showed that the filter get accurate results when the external loads are unmeasured, that represents a common test scenario where no installation of dedicated devices as load cell is possible. Future investigation aims to evaluate the improvement of the results combining strains and accelerations data. External excitation scenarios with different frequencies and amplitudes will be also explored in order to evaluate the consistency of the results. Regarding the full-field estimation, the OSP strategy will be extended in future work for purely state estimation when the external loads are measured.

Acknowledgements

The authors acknowledge the VLAIO (Flemish Innovation & Entrepreneurship) through the Innovation mandate IWT project VIRTUAL MATES (nr. 140778).

Publication II

Advanced Optimal Sensor Placement for Kalman-based multiple-input estimation

Published in Mechanical Systems and Signal Processing 160 (2021) 107830
DOI: 10.1016/j.ymssp.2021.107830

Advanced Optimal Sensor Placement for Kalman-based multiple-input estimation

Roberta Cumbo[1,2], Lorenzo Mazzanti[1,2,3], Tommaso Tamarozzi[1,2], Pavel Jiranek[1], Wim Desmet[2,4], Frank Naets[2,4]

[1] *Siemens Industry Software NV, Interleuvenlaan 68, B-3001 Leuven, Belgium*
[2] *KU Leuven, Department of Mechanical Engineering, Celestijnenlaan 300 B, B-3001 Heverlee, Belgium*
[3] *University of Ferrara, Engineering Department, Via Ariosto 35, 44121 Ferrara, Italy*
[4] *DMMS core lab, Flanders Make, Belgium*

Abstract

The direct measurement of the external loads acting on a mechanical component represents often a challenge in many engineering applications. In this context, the attention of many researchers is focused on the field of inverse load identification. Several techniques are proposed in literature to address this problem by means of experimental methodologies, often coupled with simulation solutions. In this paper, a Kalman-based methodology is considered, which solves the problem of inverse load identification in a predictive manner. The common issue of most of the techniques is the selection of an optimal set of sensors which gives the best load estimation. In the Kalman-filtering framework, an Optimal Sensor Placement (OSP) strategy has been proposed by the authors and it aims to find the best set of sensors in terms of system observability, which is the minimum requirement of a stable estimation. However, this does not guarantee the most accurate load estimation. In this contribution, two alternative metrics are proposed, based on: i) steady-state error covariance of the estimation, ii) estimator bandwidth, with respect to the available set of measurements. Both criteria will be included in the existing OSP to improve the sensors selection. A comparison of the three strategies for multiple input/state estimation is discussed on an industrial-scale Finite Element Model, in order to show the improvement in the accuracy of the estimated quantities.

Keywords: Augmented Kalman Filter, Inverse load identification, Optimal Sensor Placement, Steady-state error covariance, Estimator bandwidth, Observability

Introduction

The problem of inverse load identification is an active research topic in the field of structural mechanics since several years [165, 84, 97, 134, 56]. In mechanical, aerospace or civil applications, indirect load identification is of great importance in many in-service situations when the installation of transducers in the load path is intrusive or too expensive, and the load measurement cannot be obtained directly. In such cases, one interesting possibility is to identify the loads from a set of easy-to-measure responses combined with a numerical model. This is exactly the opposite framework of a forward problem, which evaluates the outputs from given inputs.

The solution of the inverse load identification problem can be achieved in time or frequency domain [56], using test-based [187] or simulation-based [76, 135, 28, 184] techniques. In this paper, the attention is focused on time-domain identification within the framework of estimators. Currently, the most widespread and used estimation algorithms are based on the Kalman Filtering (KF) [95, 96], which can act as an optimal estimator [164]: for linear systems under the assumption of unbiased random uncertainty, the state-estimates converge to an expected value which minimizes the state covariances. The application of the KF requires the combination of both simulated and measured data. Among the broad range of Kalman filtering techniques [19, 146, 140, 115], the Augmented Kalman Filter (AKF) [96] has recently been demonstrated to be particularly effective in the framework of load identification [52, 51, 150, 130, 151, 149, 115] on complex industrial cases. On a mechanical component, the AKF aims to identify the behavior of the system in terms of external loads (forces and torques) and full-field responses (e.g. strain, acceleration, displacement), starting from a (limited) set of response measurements (output) along the structure. Lourens et al. [115] present an application of AKF in structural dynamics, underlining the importance of using collocated or non-collocated measurements in the estimation process. Naets et al. [130] investigate the accuracy of the estimation paying attention to the stability of the filter. The presented studies proved that the type of measurements (e.g. acceleration, strain) influences the accuracy and stability of the estimation. In order to obtain a stable estimation, a number of position-level (i.e. positions, strains) outputs equal or greater to the number of forces to be identified is required. Acceleration measurements alone will lead to instability resulting from the unobservability of the system. Recent contributions [176, 113] showed also the applicability of the AKF for the identification of generalized and equivalent forces.

The selection of the optimal type and location of sensors is a common issue in experimental design and inverse identification problems. Recently, Mohamed et al. [101] proposed an optimal sensor placement method for damage identification.

The problem is formulated to minimize the a-posteriori KF estimation error in the discrete-time formulation and it selects the optimal sensors using a recursive gradient-based screening starting from the full model. Maes et al. [119] define an optimal sensors layout for load identification by satisfying the conditions of stability and direct invertibility, which lead respectively to a minimum set of position-level and acceleration-level sensors equal to the number of forces to be estimated. The proposed approach is based on the modal characteristics of the system and it has been demonstrated in [120]. Tamarozzi et al. [175] proposed a different approach defined as Optimal Sensor Placement (OSP) strategy aimed to select the optimal type (position/acceleration/strain), number and location of the sensors needed to identify a certain set of external loads. This OSP strategy is based on three main steps [175]:

- Generation of a pool of potential sensors: random selection of limited set of sensors over the structure.
- Coarse screening: remove sensors with lower sensitivity to the input(s) to be identified.
- Observability screening: selection of sensors with highest contribution to condition number of a system observability metric.

The steps are explained in more details in [175, 52]. As remarked in the last point, the focus of this method is dedicated merely to the condition number of a system observability metric. Observability is a minimum requirement to obtain a stable estimation through Kalman filtering techniques [164]. The effectiveness of this strategy for AKF estimation has been demonstrated on numerical [175] and experimental cases [150, 52]. However, this approach does not allow to assess the trade-off resulting from the noise on different sensor types, and cannot take into account the impact of the sensor selection on the dynamic range of the obtained estimates.

In this work a novel Advanced Optimal Sensor Placement (AOSP) is developed and presented, which enables a more accurate a-priori assessment of the impact of sensor selection. Two key metrics are proposed for the sensor selection:

- evaluation of the steady-state estimation error covariance matrix;
- evaluation of the sensor bandwidth through the transfer function between real and estimated inputs.

Within the present work, the improvement of the estimation process through the AKF is investigated in terms of used sensors. The proposed framework is numerically validated both in single and multiple input estimation cases, to illustrate the effectiveness of the filter in combination with the presented

AOSP strategy. Furthermore, potential limitations of the AOSP are analyzed in details.

In Sec. *Problem Statement*, the augmented formulation of a second order structural dynamic system and the reference observability based optimal sensor placement for load identification are briefly presented. Following, the Advanced Optimal Sensor Placement is introduced and described in the two proposed formulations in Sec. *Advanced Optimal Sensor Placement Strategy.* Finally, Sec. *Numerical validation* presents a numerical validation of the proposed AOSP scheme on the input estimation of a rear twistbeam suspension, and demonstrates the superior estimation performance for sensor selected using the newly proposed AOSP scheme.

Problem Statement

Optimal Sensor Placement is here referred to as a selection strategy which aims to find the optimal type and location of sensors used for input-estimation through Augmented Kalman filtering techniques. In order to understand the main principle of the OSP and introduce the AOSP, the augmented state-space formulation of a dynamic system is first summarized in Sec. *Augmented Kalman Filter for joint state-input estimation on a dynamic system.* In Sec. *Optimal Sensor Placement strategy*, the refernce OSP is described with main focus on the observability screening, and advantages and limitations are highlighted.

Augmented Kalman Filter for joint state-input estimation on a dynamic system

The equations of motion for a mechanical dynamic system in the continuous time-invariant first-order state-space formulation [25] are:

$$\begin{cases} \dot{\mathbf{x}}(t) = \mathbf{A}\mathbf{x}(t) + \mathbf{B}\mathbf{u}(t) \\ \mathbf{y}(t) = \mathbf{H}\mathbf{x}(t) + \mathbf{D}\mathbf{u}(t) \end{cases}, \qquad \mathbf{x} = [\mathbf{q} \quad \dot{\mathbf{q}}]^T, \tag{II.1}$$

where $\mathbf{x} \in \mathbb{R}^{2n_d}$, where n_d is the number of degrees-of-freedom (DoF), defines the state vector, $\mathbf{q} \in \mathbb{R}^{n_d}$ represents the generalized coordinates of the system and $\mathbf{u} \in \mathbb{R}^{n_i}$ (n_i = number of external loads) is the input vector. $\mathbf{A} \in \mathbb{R}^{2n_d \times 2n_d}$ and $\mathbf{B} \in \mathbb{R}^{2n_d \times n_i}$ are represented as the following real matrices:

$$\mathbf{A} = \begin{bmatrix} \mathbf{0} & \mathbf{I} \\ -\mathbf{M}^{-1}\mathbf{K} & -\mathbf{M}^{-1}\mathbf{C} \end{bmatrix}, \qquad \mathbf{B} = \begin{bmatrix} \mathbf{0} \\ \mathbf{M}^{-1}\mathbf{S_f} \end{bmatrix}, \tag{II.2}$$

with $\mathbf{M} \in \mathbb{R}^{n_d \times n_d}$, $\mathbf{K} \in \mathbb{R}^{n_d \times n_d}$ and $\mathbf{C} \in \mathbb{R}^{n_d \times n_d}$ as mass, stiffness and damping matrix respectively, and $\mathbf{S_f} \in \mathbb{R}^{n_d \times n_i}$ is a selection matrix of position(s) and

DoF(s) related to the external load(s). The second equation of Eq. (II.1) defines the system measurements, where $\mathbf{y} \in \mathbb{R}^{n_o}$ (n_o = number of output) is the output vector, while $\mathbf{H} \in \mathbb{R}^{n_o \times n_d}$ and $\mathbf{D} \in \mathbb{R}^{n_o \times n_i}$ depend on the output response type, e.g. acceleration, position, strain [149].

In order to derive the AKF equations, the augmented state-space model is defined for the linear time-invariant system in Eq. (II.1), such that the unknown inputs $\mathbf{u}$ can also be considered as states. The unknown input dynamics are modelled as a random walk model due to a general lack of additional prior information on the input behavior. For the discretization of this input model we employ a zero-order hold scheme, such that the resulting augmented state model equations become:

$$\begin{cases} \dot{\mathbf{x}}^* = \mathbf{A}^* \mathbf{x}^* \\ \mathbf{y} = \mathbf{H}^* \mathbf{x}^* \end{cases}, \qquad \mathbf{x}^* = [\mathbf{x} \quad \mathbf{u}]^T, \qquad \mathbf{A}^* = \begin{bmatrix} \mathbf{A} & \mathbf{B} \\ \mathbf{0} & \mathbf{0} \end{bmatrix}, \qquad \mathbf{H}^* = \begin{bmatrix} \mathbf{H} & \mathbf{D} \end{bmatrix}, \tag{II.3}$$

where $\mathbf{x}^* \in \mathbb{R}^{(n_d+n_i)}$ and $\mathbf{A}^* \in \mathbb{R}^{n_a \times n_a}$ ($n_a = 2n_d + n_i$) are respectively the augmented state and system matrix. For a mechanical dynamic system:

- if both measurements and external inputs are known, the standard formulation of the Kalman Filter [95, 96] can be applied to Eq. (II.1) in order to estimate the state vector.
- if the measurements are known and no information about the external input is available, the augmented formulation of the Kalman Filter [115] can be applied to Eq. (II.3)

From the latter statement, we can already underline that one can rely on the AKF to solve the inverse load identification only if the input location/direction is known.

The discrete-time formulation of the augmented state-space model of Eq. (II.3) is:

$$\begin{cases} \mathbf{x}_k^* = \mathbf{A}_d^* \mathbf{x}_{k-1}^* \\ \mathbf{y}_k = \mathbf{H}^* \mathbf{x}_k^* \end{cases}, \tag{II.4}$$

where $\mathbf{A}_d^* \in \mathbb{R}^{n_a \times n_a}$ is the time-discrete form of the augmented matrix $\mathbf{A}^*$ and its formulation depends on the chosen discretization scheme [188]. In the remainder of the presented theoretical analyses, we will use the continuous-time description from Eq. (II.3), but for the actual Kalman filter evaluation the discrete time model Eq. (II.4) is employed.

The observability of an inverse problem is a requirement for a stable estimation through the AKF and can be summarized as following ([118, 130]):

- the number of DoFs of the structural model has to be equal or greater than the number of external loads to be estimated: $n_d \geq n_i$;
- the number of position/strain measurements has to be greater than the number of external loads to be estimated: $n_y \geq n_i$.

Optimal Sensor Placement strategy

An OSP strategy aims to select the optimal location, number and type of sensors needed to solve the inverse load identification through the AKF. In the frame of augmented Kalman filtering an OSP was initially developed for linear systems [175, 154] and further extended for non-linear systems in [150], and this approach will serve as the reference OSP in this work. Moreover, in this contribution only linear systems are investigated. In order to perform the reference and proposed OSP, we start from two important assumptions:

- A-priori knowledge of location and direction of the loads to be identified is available;
- The minimum number of position-level sensors is equal or greater than the number of loads to be identified, which is necessary guarantee stability [130].

A scheme of the reference OSP is shown in Fig. II.1 and a detailed description can be found in [175, 52]. The steps grouped in the blue block are referred in this contribution to as *Training*. Once a reduced set of sensors is selected from the *coarse screening* in terms of type and location, the matrix $\mathbf{H}$ of the measurements can be defined. Each row of this matrix is scaled to have a maximum unity value. In this way, the following step (based on the Popov - Belevitch - Hautus PBH [75] criterion) will not privilege one sensor type with respect to another because of the different unit and/or different order of magnitude. The *Training* in Fig. II.1 aims to bring a reduced but still sufficiently large amount of sensors to the last selecting step, i.e. *observability screening*. The latter is the key step of the reference OSP strategy and it is chosen to satisfy the stability of the AKF, which is guaranteed by the observability of the system, as stated in Sec. *Augmented Kalman Filter for joint state-input estimation on a dynamic system*. The observability screening will be explained in details in the next subsection and investigated in terms of robustness of the strategy in Sec. *Advanced Optimal Sensor Placement Strategy*.

Observability screening

The key idea of the reference OSP proposed in [175] is to define a combination of sensors evaluating its performance in terms of a scalar that quantifies how "observable" the system is. The observability metric used for this scope is the

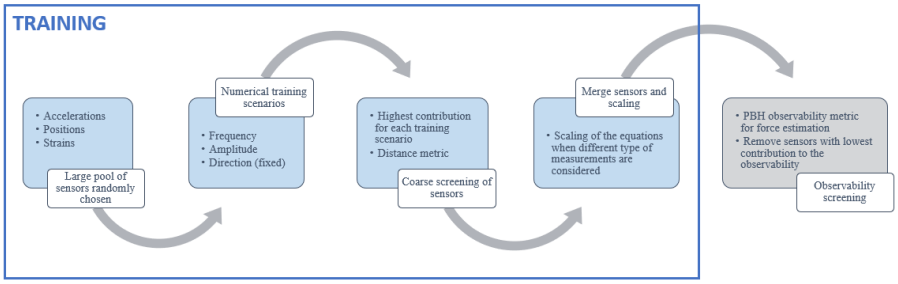

Figure II.1: Optimal Sensor Placement strategy.

PBH criterion, which can be applied directly to the continuous time model or to the discrete time model as well. The two models will differ on the definition of the eigenvalues, which for one case are expected to be on the right half-plane for stable systems and in the other case in the unit circle. The stability of the system will not change from the continuous to the discrete time model if an appropriate discretization scheme is used. For the system of Eq. (II.3), the PBH observability matrix $\mathbf{O}_{PBH}$ is defined as:

$$\mathbf{O}_{PBH}(s) = \begin{bmatrix} s\mathbf{I} - \mathbf{A}^* \\ \mathbf{H}^* \end{bmatrix}, \tag{II.5}$$

In Eq. (II.5), the matrix $\mathbf{A}^*$ can be replaced with $\mathbf{A}^*_{\mathbf{d}}$ if the system of Eq. (II.4) is considered. A system is observable if the observability matrix O_{PBH} is of full column rank for all s in the complex plane. More in particular this implies that the system observability needs to be verified at each eigenfrequency of the augmented system, which includes natural frequencies of the structure as well as the eigenvalues associated to the input dynamics. A random walk model is introduced for the unknown load, since no information about the input entering the system is available:

$$\dot{\mathbf{u}}(t) = \mathbf{0} + \mathbf{w}_{\mathbf{u}}(t). \tag{II.6}$$

In Eq. (II.6), $\mathbf{w}_{\mathbf{u}}$ is a stochastic process with a covariance matrix $\mathbf{Q}_{\mathbf{u}} \in \mathbb{R}^{n_i \times n_i}$. The validation on the usage of a zeroth-order random walk model for inverse load identification and a detailed explanation on how to set the value of $\mathbf{Q}_{\mathbf{u}}$ matrix can be found in [52, 150, 130]. The eigenvalue associated to the input model in Eq. (II.6), which could lead to stability issues, is at 0Hz.

The observability metric proposed in the last step of the reference OSP strategy does not directly use the PBH rank, as this is a numerically ambiguous metric, but the matrix condition number, which quantifies how close the matrix is to

rank deficiency. The observability metric is proposed as following:

$$O_m = \frac{1}{n_i \cdot cond(\mathbf{O}_{PBH}(0))} \tag{II.7}$$

where n_i is the number of loads to estimate. There are two reasons why the PBH matrix is evaluated only at 0Hz:

- The reference OSP mainly aims to identify the input loads and the corresponding problematic dynamics is at this frequency;
- For a real structural dynamic system, the normal modes are all damped and this leads to a detectable system, i.e. its unobservable modes are detectable [164], which is sufficient if the user is interested in input identification [118].

If the matrix **H** includes different type of sensors, the evaluation of Eq. (II.7) can lead to the criterion privileging one type with respect to another (e.g. accelerometers instead of strains) because of different units and order of magnitude for the different quantities. In [52, 175], the scaling of each row of **H** is proposed in order to obtain a unit-less matrix and meaningfully compare the rows of **H** associated to each sensor. The optimal set of sensors is then chosen as greedy optimization algorithm [132, 156]: starting from the reduced number of sensors selected after the Training, one sensor per iteration is removed from the pool if its removal implies the lowest decrease in O_m. The final selection is identified when the decrease of O_m reaches a certain threshold fixed by the user.

An example of observability screening

A simple example is proposed on a serial 10 DoFs mass-spring system, shown in Fig. II.2.

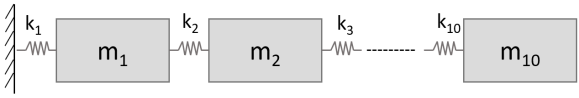

Figure II.2: 10 DoFs mass-spring system.

Fig. II.3 shows the decrease in O_m, evaluated as in Eq. (II.7), for a decreasing number of sensors.

Starting from a set of measurements including position sensors on all the available DoFs, the observaility screening of Sec. *Observability screening* is applied and sequentially removes one sensor per iteration. In Fig. II.3a, the

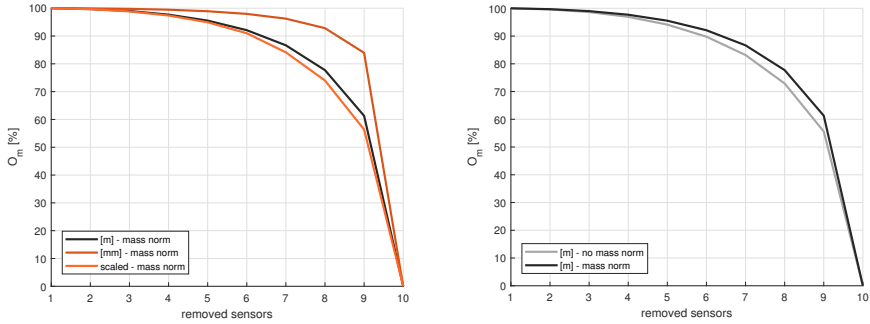

(a) (b)

Figure II.3: Observability index decrease (percentage value of O_m indicator) obtained by the removal of position sensors through the observability screening for a 10 DoFs mass-spring system is considered.

decreasing trend is different if the measurements are expressed in [m], [mm] or scaled quantities (as applied in [52, 175]). This implies that, if the user defines a threshold of observability decreasing to select the minimum set of sensors, the final selection will be different depending on which unit the measurements are expressed, which is clearly not a desired behavior. Indeed, if for example a threshold of 80% is chosen, the observability metric select a different number of sensors if the model is expressed in [m] or in [mm]. In the first case, three sensors are selected while in the second case, only one sensor is chosen. The case shown in Fig. II.3a is related to a mass-normalized numerical model. If another model normalization is adopted, another trend is obtained and shown in Fig. II.3b. In conclusion the index expressed in Eq.II.7 defines *'how much'* a system is observable depending upon the scaling of measurements and physical system, and then naturally calls into question how this scaling should be practically done. The main reason resides in the fact that the concept of observability is generally meant to be a binary trait of a system. Thus it is in principle possible to state if a system is observable or not, but quantifying a 'degree' of observability is a much more complex issue. Moreover, this reference OSP does not account for the different noise characteristics for different sensors, or model uncertainties, which often drives sensor selection in practice.

The following subsection presents several approaches which can be adopted to improve the optimal sensor placement such that a more robust framework is obtained and to circumvent the issues described here.

Advanced Optimal Sensor Placement Strategy

In this work we propose a novel Advanced Optimal Sensor Placement strategy (AOSP) which revolves around two key properties which are important for any, real or virtual sensor selection:

- *Expected noise levels*: evaluating a sensor set performance by solving the Riccati equation [195] for the steady-state error covariance **P** and choosing the sensors which minimize the estimation error. As stated by Kalman and Bucy in [96] and detailed described in [164], the Kalman Filter estimation is optimal in the sense that minimizes the filtering error, i.e error covariance. The minimization of the nonlinear Riccati equation allows the definition of the optimal Kalman gain and leads thus to the best estimation. Nevertheless, other parameters, e.g. set of measurements, can affect the minimization of the error covariance, as will be explained in Sec. *Steady-state error covariance*,
- *Expected dynamic range*: evaluating a sensor set performance by defining the frequency-domain transfer function between the true inputs entering the state-space system and the estimated ones. The selection resides in the sensors whose corresponding transfer function is the most relevant for the estimation.

The above metrics are proposed to replace the *observability screening* in Sec. *Observability screening* defining two versions of the Advanced Optimal Sensor Placement (AOSP), based respectively on the Input Error Covariance (IEC) or Transfer Function (TF). As shown in Fig. II.4, the novelty of the two approaches is after the *Training*, including the measurements scaling. It will be verified that the proposed approaches are not affected by scaling issues as was the case for the reference OSP. In the following sections, these two metrics will be explained in details and then included in the AOSP.

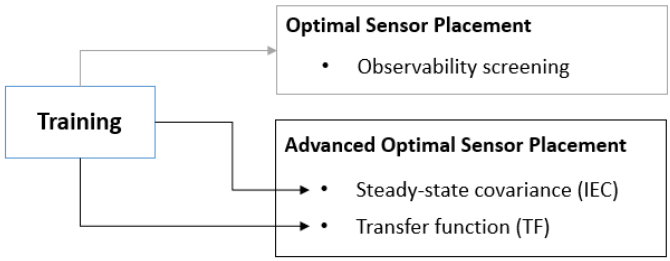

Figure II.4: Standard OSP and AOSP block scheme.

Steady-state error covariance

Recalling Eq. (II.3), the linear stochastic formulation of the continuous-time augmented state-space model is:

$$\begin{cases} \dot{\mathbf{x}}^* = \mathbf{A}^*\mathbf{x}^* + \mathbf{w}^* \\ \mathbf{y} = \mathbf{H}^*\mathbf{x}^* + \mathbf{v} \end{cases}, \tag{II.8}$$

Vectors $\mathbf{w}^*$ and $\mathbf{v}$ are mutually uncorrelated Gaussian variables (augmented process and measurement noise), with associated covariance matrices $\mathbf{Q}^* = E\{\mathbf{w}_l^*\mathbf{w}_l^{*T}\} \geq 0$ and $\mathbf{R} = E\{\mathbf{v}_l\mathbf{v}_l^T\} \geq 0$ respectively. $\mathbf{Q}^*$ is defined as a block diagonal matrix composed by $\mathbf{Q}$ and $\mathbf{Q_u}$, that are the covariance matrices referred to the model and input uncertainties respectively. Given these quantities, the filter supports the state estimation even when the precise nature of the model system is unknown [192]. An important remark is about the formulation of $\mathbf{Q}^*$: for all the studies presented in this paper, it is assumed that $\mathbf{Q} << \mathbf{Q}_u$, as in [52, 150, 130], implying that the structural model is relatively accurate with respect to the in zero-order hold input model. The main source of uncertainty therefore is $\mathbf{Q}_u$, and $\mathbf{Q}^*$ can be approximated as:

$$\mathbf{Q}^* = \begin{bmatrix} \mathbf{0} & \mathbf{0} \\ \mathbf{0} & \mathbf{Q}_u \end{bmatrix}, \tag{II.9}$$

$\mathbf{R}$ and $\mathbf{Q}^*$ are important parameters that characterize the AKF.

The continuous-time equivalent of the Kalman filter is also known as the Kalman-Bucy filter [96]:

$$\hat{\dot{\mathbf{x}}}^*(t) = \mathbf{A}^*\hat{\mathbf{x}}^*(t) + \mathbf{K}_{kal}(t)(\mathbf{y}(t) - \mathbf{H}^*\hat{\mathbf{x}}^*(t)) \tag{II.10}$$

$$\dot{\mathbf{P}}(t) = \mathbf{A}^*\mathbf{P}(t) + \mathbf{P}(t)\mathbf{A}^{*\mathbf{T}} + \mathbf{Q}^* - \mathbf{K}_{kal}(t)\mathbf{R}\mathbf{K}_{kal}(t)^T$$

$$\mathbf{K}_{kal}(t) = \mathbf{P}(t)\mathbf{H}^T\mathbf{R}^{-1},$$

where $\mathbf{K}_{kal}$ represents the Kalman gain. Even though this continuous time method is not appropriate for a practical computer implementation, it is very convenient for the theoretical analysis of the estimator properties, as presented in this work. In this work, the continuous-time formulation is considered to evaluate the steady-state error covariance problem, but the discrete-time formulation could also be used. In the discrete time case, a correct selection of the discretization scheme is required to avoid inaccuracies in the covariance estimation [157], so by considering only the continuous time model in this work, we circumvent this potential issue. The second equation of Eq. (II.10) describes the state covariance evolution and the steady-state value, i.e. $\dot{\mathbf{P}}(t) = 0$, for a

time-invariant system, leads to:

$$\mathbf{0} = \mathbf{A}^*\mathbf{P}(t) + \mathbf{P}(t)\mathbf{A}^{*\mathbf{T}} + \mathbf{Q}^* - (\mathbf{P(t)}\mathbf{H}^{*\mathbf{T}}\mathbf{R}^{-\mathbf{1}})\mathbf{R}(\mathbf{P(t)}\mathbf{H}^{*\mathbf{T}}\mathbf{R}^{-\mathbf{1}})^T, \tag{II.11}$$

which is known as the Continuous Algebraic Riccati Equation (CARE) [195, 152] and its solution allows to evaluate the converged steady state error covariance for the estimators. Several approaches exist in literature to solve the CARE [27, 197], and these methods are generally available in technical computing packages [123, 159]. Eq. (II.11) allows for an optimal state estimation by means of the trace minimization of the error covariance matrix $\mathbf{P}$. The minimization defines the optimal Kalman gain $\mathbf{K}_{kal}$ [164]. With reference to the augmented state $\mathbf{x}^*$ in Eq. (II.3), the covariance matrix $\mathbf{P}$ is defined as:

$$\mathbf{P} = \begin{bmatrix} \mathbf{P_{xx}} & \mathbf{P_{xu}} \\ \mathbf{P_{ux}} & \mathbf{P_{uu}} \end{bmatrix}, \tag{II.12}$$

where $\mathbf{P_{uu}} = E(\hat{\mathbf{u}} - \mathbf{u})(\hat{\mathbf{u}} - \mathbf{u})^T$ expresses the expected covariance of the unknown input error. In the case of structural dynamics, when different types of input loads are considered, e.g. forces $\mathbf{f}$ and torques $\mathbf{m}$, the augmented state $\mathbf{x}^*$ can be expressed as:

$$\mathbf{x}^* = [\mathbf{x} \quad \mathbf{u}]^T = [\mathbf{x} \quad \mathbf{f} \quad \mathbf{m}]^T, \tag{II.13}$$

and consequently:

$$\mathbf{P_{uu}} = \begin{bmatrix} \mathbf{P_{ff}} & \mathbf{P_{fm}} \\ \mathbf{P_{mf}} & \mathbf{P_{mm}} \end{bmatrix}. \tag{II.14}$$

The diagonal terms of this matrix are the variances of the estimation error for each input of the systems. These are a key point in the sensor selection proposed for the IEC criterion discussed in Sec. *Input Error Covariance (IEC) metric*. In the framework of an AKF, this choice resides in the direct connection between the noise obtained by a virtual sensor, i.e. estimated output, and the estimated augmented state covariance. The latter quantity also gives information about the system observability: if a system is unobservable, the solution of Eq. (II.11) diverges to infinity; if the system is observable, the solution of Eq. (II.11) converges to a finite value.

From Eq. (II.11), one can already observe that this metric takes into account the noise level of each measurement as well as the input uncertainty, expressed respectively by $\mathbf{R}$ and $\mathbf{Q}^*$, as in Eq. (II.9).

The question that could arise from a metric based on the error covariance is if it also effectively circumvents the unit scaling issue for the measurements, as was encountered in the reference OSP shown i Sec. *An example of observability*

screening. To assess this, we consider a rescaled measurement matrix $\mathbf{H}_\alpha$ defined as $\mathbf{H}$ multiplied by a scaling factor α:

$$\mathbf{H^*}_\alpha = \alpha \mathbf{H^*}, \quad \alpha > 0 \quad . \tag{II.15}$$

The corresponding sensor covariance becomes:

$$\mathbf{R}_\alpha = \alpha^2 \mathbf{R} \quad . \tag{II.16}$$

We can now substitute this rescaled sensor model in Eq. (II.11):

$$\begin{aligned}
\mathbf{0} &= \mathbf{A^*P} + \mathbf{PA^{*T}} + \mathbf{Q^*} - (\mathbf{PH^{*T}_\alpha R^{-1}_\alpha})\mathbf{R}_\alpha(\mathbf{PH^{*T}_\alpha R^{-1}_\alpha})^T \\
&= \mathbf{A^*P} + \mathbf{PA^{*T}} + \mathbf{Q^*} - (\mathbf{P}\alpha\mathbf{H^{*T}}\frac{\mathbf{1}}{\alpha^\mathbf{2}}\mathbf{R^{-1}})\alpha^\mathbf{2}\mathbf{R}(\mathbf{P}\alpha\mathbf{H^{*T}}\frac{\mathbf{1}}{\alpha^\mathbf{2}}\mathbf{R^{-1}})^T \\
&= \mathbf{A^*P} + \mathbf{PA^{*T}} + \mathbf{Q^*} - (\mathbf{PH^{*T}R^{-1}})\mathbf{R}(\mathbf{PH^{*T}R^{-1}})^T
\end{aligned} \tag{II.17}$$

We could trivially generalize this proof to the case where α is a diagonal matrix, such that it is clear that different scalings could be applied to the different sensors. As in Eq.(II.17), all contributions from α cancel out, the steady-state value of $\mathbf{P}$ is not influenced by the measurement scaling, and therefore provides a more robust selection metric than the observability based criterion. In the following subsection, the steady-state estimator covariance is proposed as a sensor selection metric, i.e. Input Error Covariance (IEC), to replace the observability screening step proposed in the reference OSP.

Input Error Covariance (IEC) metric

In order to replace the observability screening of the reference OSP strategy, a performance indicator such as the one proposed in Eq. (II.7) has to be defined. The reduced set of sensors entered in the IEC step are the ones available after the Training, explained in Sec. *Optimal Sensor Placement strategy*. A greedy strategy is still adopted to sequentially select the sensors through the IEC. The general idea of the proposed scheme is to find a predefined number of sensors which lead to the minimal uncertainty on the estimated inputs $\mathbf{P_{uu}}$. This should ideally enforce the optimal estimation of the Kalman Filter in its augmented formulation. Indeed, it is known that even if the Kalman gain is defined as optimal, a set of measurements which leads to a non-convergence of the solution exists. The minimization of the input error covariance can thus help in a more stable and accurate estimation since the input is jointly estimated with the system states and a non-convergent input estimation will lead to a non-convergence of the entire solution. In this sense, the input error covariance can be seen also as regularization parameter of the AKF: even if it can not be

tuned a-priori or during the estimation process, its value during the estimation plays an important role in the convergence of the filter. The following steps are proposed to use the IEC metric for optimal sensor selection starting from a set of n_s^0 possible sensors:

1. Evaluation of Eq. (II.11) by using all the n_s^0 sensors selected in the *Training* $\mathbf{H}^{n_s^0} \in \mathbb{R}^{n_s^0 \times (n_d+n_i)}$. The resulting matrix defines the reference estimation error covariance $\mathbf{P_{uu}^0}$.
2. Greedy selection: at each iteration k, a set of sensors with corresponding measurement matrix $\mathbf{H}^{n_s^0-k} \in \mathbb{R}^{(n_s^0-k)\times(n_d+n_i)}$ will lead to a steady-state covariance $\mathbf{P_{uu}^k}$. The removal of a single sensor from iteration k to $k+1$ is performed by evaluating the $\mathbf{P_{uu}^k}$ for the removal of each sensor $g \in \mathbf{H}^{n_s^0-k}$, resulting in $\mathbf{P_{uu}^{k,g}}$. The sensor $\bar{g}$ whose removal leads to the lowest increase of the trace of $\mathbf{P_{uu}^{k,g}}$ matrix will will be excluded from the sensor set $\mathbf{H}^{n_s^0-\bar{k}} \in \mathbb{R}^{(n_s^0-\bar{k})\times(n_d+n_i)}$ at the next iteration $\bar{k} = k+1$. The excluded sensor had the smallest contribution to the error covariance. This removal selection is outlined in Algorithm 1. The iterations continue until the selection reaches a desired number of $\bar{n}_s$ sensors predefined by the user.

The choice to predefine the number of sensors (rather than the required accuracy) is inspired by engineering practice where often the number of deployable sensors is limited by the number of channels available on the signal acquisition system.

Algorithm 1 IEC sensors selection

1: Execute the iterative process to find the $\bar{n}_s$ optimal sensors: $\mathbf{k = 0 : (n_s^0 - \bar{n}_s)}$

2: given the measurement matrix $\mathbf{H}^{n_s^0-k}$ evaluate CARE of Eq. (II.11)

3: $\mathbf{P}_{uu}^k = care(H^{n_s^0-k})$

4: Iterate on the subset of sensors $n_s^0 - k - 1$: $\mathbf{g = 1 : (n_s^0 - k - 1)}$

5: remove sensor g from $\mathbf{H}^{n_s^0-k}$ to obtain $H^{n_s^0-k-1}$, with $g \notin (n_s^0 - k - 1)$

6: $\mathbf{P}_{uu}^{k,g} = care(H^{n_s^0-k-1})$

7: Evaluate the sensor $\bar{g}$ which gives the lowest contribution to the covariance matrix:

8: $\bar{g} := min(trace(\mathbf{P}_{uu}^k) - trace(\mathbf{P}_{uu}^{k,g}))$

9: remove sensor $\bar{g}$ from $\mathbf{H}^{n_s^0-k}$ to obtain $\mathbf{H}^{n_s^0-\bar{k}}$, with $\bar{k} = k+1$

Remark: when n_l input loads are considered, e.g. forces and torques, the diagonal terms of the covariance matrix $\mathbf{P_{uu}}$ will have different physical meaning

and units. In order to ensure a consistent quantity in the evaluation of the trace matrix, each diagonal term j at each iteration k is normalized with respect to the corresponding value in the initial covariance matrix $\mathbf{P_{uu}^0}$ as following:

$$\bar{\mathbf{P}}_{\mathbf{uu,j}}^{\mathbf{k,g}} = \frac{\mathbf{P}_{\mathbf{uu,j}}^{\mathbf{k,g}}}{\mathbf{P}_{\mathbf{uu,j}}^{\mathbf{0}}}, \quad j = 1, ..., n_l \tag{II.18}$$

The non-dimensional terms are then mediated in order to obtain the following metric in order to replace the trace of the covariance:

$$\bar{P}^{k,g} = \frac{\sum_{j=1}^{n_l} \bar{\mathbf{P}}_{\mathbf{uu,j}}^{\mathbf{k,g}}}{n_l} \tag{II.19}$$

Input estimation bandwidth: Transfer Function (TF) between real and estimated input

This section aims to determine the transfer function between the load inputs applied to the dynamic system (quantity to be estimated) and the estimated inputs through the AKF in order to assess the expected dynamic performance of the input estimator. The estimator is analyzed here in the Laplace domain, defining $s = i\omega = 2\pi i\phi$ (ϕ frequency content expressed in Hz). As shown in Fig. II.5 the full transfer function (TF) $\mathbf{T_{\hat{u}u}}$ of the estimated and real input loads consists of two main contributions:

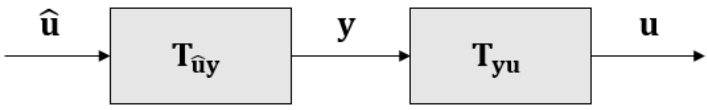

Figure II.5: Transfer function from estimated to real input loads.

- $\mathbf{T}_{yu}$ real output - real input transfer function from the physical plant;
- $\mathbf{T}_{\hat{u}y}$ estimated input - real output transfer function from the AKF estimation.

It is important to remark for the following steps that the steady-state Kalman Filter [164] is considered for this analysis. This allows to work with time-invariant TFs. From past experience it has also been shown that the estimator covariance rapidly converges, such that the assumption of a steady-state filter behavior is valid [130, 52]. In Fig. II.6, the transfer function from Fig. II.5 is shown in more detail.

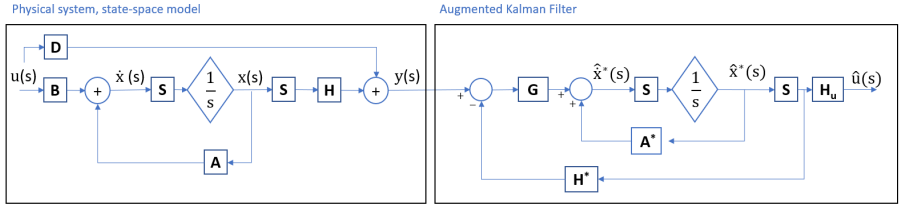

Figure II.6: Block scheme of the estimation process in Laplace domain: state-space model as input of the AKF.

The TF of the physical plant can be described as:

$$\mathbf{T_{yu}}(s) = \mathbf{HS}(s)(\mathbf{S}(s)s - \mathbf{AS}(s))^{-1}\mathbf{B} + \mathbf{D}, \tag{II.20}$$

such that

$$\mathbf{y}(s) = \mathbf{T_{yu}}(s)\mathbf{u}(s). \tag{II.21}$$

In this Eq. II.20, the matrix $\mathbf{S}(s)$ is introduced and it describes the conversion of a general second order dynamic system into a first order state-space formulation in the Laplace domain. This additional transformation is necessary to account for the dynamic dependence between the displacement and velocity states which are now combined in a single state vector, as described in more detail in *Appendix A*. The matrix $\mathbf{S}(s)$ is expressed as:

$$\mathbf{S}(s) = \begin{bmatrix} \mathbf{I} & \mathbf{0} \\ \mathbf{0} & \mathbf{I}s \end{bmatrix}. \tag{II.22}$$

Ideally the plant transfer function would be obtained from the physical system directly. However, in practice this is not explicitly possible to determine $\mathbf{T}_{yu}$ directly. As a surrogate for the real TF, we propose to employ the same system model as employed for the Kalman filter to evaluate the TF. Even though this generally leads to an overly optimistic view on the final KF performance, it is typically the only information which is available and will allow to assess the best-case scenario for the estimator.

Next we can define the transfer function for the AKF:

$$\mathbf{T_{\hat{u}y}}(s) = \mathbf{H_u S}^*(s)(\mathbf{S}^*(s)s - \mathbf{A}^*\mathbf{S}^*(s) + \mathbf{GH}^*\mathbf{S}^*(s))^{-1}\mathbf{G}, \tag{II.23}$$

such that

$$\hat{\mathbf{u}}(s) = \mathbf{T_{\hat{u}y}}(s)\mathbf{y}(s), \tag{II.24}$$

and the second order transformation matrix $\mathbf{S}^*(s)$ is (see App. II):

$$\mathbf{S}^*(s) = \begin{bmatrix} \mathbf{I} & \mathbf{0} & \mathbf{0} \\ \mathbf{0} & \mathbf{I}s & \mathbf{0} \\ \mathbf{0} & \mathbf{0} & \mathbf{I} \end{bmatrix}. \tag{II.25}$$

$\mathbf{G}$ is the steady-state Kalman gain matrix, which can be derived from the steady-state error covariance $\mathbf{P}^\infty$ obtained from Eq. (II.11), such that:

$$\mathbf{G} = \mathbf{P}^\infty \left(\mathbf{H}^*\right)^T \mathbf{R}^{-1} \quad . \tag{II.26}$$

Moreover, $\mathbf{H_u}$ in Eq. (II.23) is a boolean matrix whose purpose is the selection of the TF related to the input state included in the augmented variable $\hat{\mathbf{x}}^*$. Recalling the augmented state in Eq. (II.3):

$$\hat{\mathbf{u}} = \mathbf{H_u}\hat{\mathbf{x}}^* = \begin{bmatrix} \mathbf{0} & \mathbf{0} & \mathbf{I} \end{bmatrix} \begin{bmatrix} \hat{\mathbf{q}} \\ \hat{\dot{\mathbf{q}}} \\ \hat{\mathbf{u}} \end{bmatrix}, \tag{II.27}$$

and combining the two TFs from Eq. (II.20) and Eq. (II.23), the relation between the estimated input load $\hat{\mathbf{u}}$ and the real input load $\mathbf{u}$ can be approximated (assuming the known system model):

$$\mathbf{T}_{\hat{\mathbf{u}}\mathbf{u}}(s) = \mathbf{T}_{\hat{\mathbf{u}}\mathbf{y}}(s)\mathbf{T}_{\mathbf{y}\mathbf{u}}(s), \qquad \hat{\mathbf{u}}(s) = \mathbf{T}_{\hat{\mathbf{u}}\mathbf{u}}(s)\mathbf{u}(s) \tag{II.28}$$

For a perfect estimator the TF should have a completely flat spectrum with gain 1, and without cross-coupling between the different inputs. However, in practice dynamic model limitations, sensor restrictions and limited tuning capabilities of the AKF scheme will inhibit this perfect behavior. In order to show that the presented TF analysis is not influenced by output scaling, the same approach proposed in Sec. *Steady-state error covariance* is adopted. Considering a scaling factor α, the following scaled matrices can be defined:

$$\mathbf{H}_\alpha = \alpha\mathbf{H}, \tag{II.29}$$

$$\mathbf{D}_\alpha = \alpha\mathbf{D}, \tag{II.30}$$

$$\mathbf{G}_\alpha = \mathbf{P}_\alpha^\infty \mathbf{H}_\alpha^T \mathbf{R}_\alpha^{-1}. \tag{II.31}$$

From Eq. (II.17) it is known that the steady-state covariance is not influenced by the scaling such that $\mathbf{P}_\alpha^\infty = \mathbf{P}^\infty$, and hence:

$$\mathbf{P}_\alpha^\infty \mathbf{H}_\alpha^T \mathbf{R}_\alpha^{-1} = \frac{1}{\alpha}\mathbf{P}\mathbf{H}^T\mathbf{R}^{-1} = \frac{1}{\alpha}\mathbf{G}. \tag{II.32}$$

By substituting the latter matrices in Eq. (II.28), it is easy to verify that the TF is not influenced by measurements scaling. Finally it is important to highlight that both $\mathbf{H}$ and $\mathbf{H}^*$ are assumed constant and frequency independent in the current analysis. This implies that the presented scheme does not account for the band-pass characteristics or internal dynamics some sensors may have. For the current work we assume that those dynamic properties are typically unknown to the developer of the estimator. However if this information is indeed available in model form, it would be possible to include this as well in the presented framework to allow for a more accurate sensor selection.

In the following subsection a metric, i.e. the Transfer Function Identity index (TFI), based on the analyzed TF is proposed to replace the observability screening of the OSP in oder to find the optimal set of sensors which gives the best input estimation in the desired frequency range. The method will be generalized for multiple-input estimation.

Transfer Function Identity index (TFI) metric

The target in the sensor selection is a unity value of $\mathbf{T}_{\hat{\mathbf{u}}\mathbf{u}}(s)$ in the frequency range of interest, which will lead to an identity matrix for multiple-input estimation: $\mathbf{T}_{\hat{\mathbf{u}}\mathbf{u}}(s) = \mathbf{I}$.

From Eq. (II.28) a general transfer matrix for an equal number of applied and estimated inputs can be defined as:

$$\mathbf{T}_{\hat{u}u}(s) = \begin{bmatrix} T^{11}(s) & T^{12}(s) & \dots & T^{1n_l}(s) \\ T^{21}(s) & \ddots & \vdots & \\ \vdots & & \ddots & \vdots \\ T^{n_l 1}(s) & \dots & \dots & T^{n_l n_l}(s) \end{bmatrix}, \tag{II.33}$$

with n_l = number of total loads to be estimated. We define the so-called identity index $I_I(s)$ to assess the similarity of the TF $\mathbf{T}_{\hat{u}u}$ to a unity matrix at a given pulsation s:

$$I_I(s) = \frac{\sum_{j=1}^{n_l} |1 - |T_{\hat{u}u}^{jj}(s)||}{n_l} + \frac{\sum_{j=1}^{n_l} \sum_{i=1, i\neq j}^{n_l} |T_{\hat{u}u}^{ji}(s)|}{n_l(n_l - 1)} \tag{II.34}$$

The identity index $I_I(s)$ assumes a value equal to 0 when the condition $\mathbf{T}_{\hat{\mathbf{u}}\mathbf{u}}(s) = \mathbf{I}$ is met. The first term of Eq. (II.34) expresses the average difference of the diagonal terms with respect to the target value of one. The final term introduces a penalization for the requirement on zero valued off-diagonal terms, by accounting for the average absolute value of the off-diagonal terms.

The following steps can then be defined for an optimal sensor selection:

- Definition of the frequency range of interest $\bar{\phi} = [\phi_1, \phi_2]$;
- Greedy selection strategy: at each iteration k, a set $\mathbf{H}^{n_s^0-k} \in \mathbb{R}^{(n_s^0-k)\times(n_d+n_i)}$ of sensors will give a transfer function $\mathbf{T}^k_{\hat{u}u}(\phi)$ and a corresponding identity index $I^k_I(\phi)$. The frequency spectrum of $I^k_I(\phi)$ is then averaged along ϕ in order to obtain an unique index $\bar{I_I}^k$. The recursive removal of one sensor from iteration k to $k+1$ is performed by evaluating the identity index for each removal of sensor $g \in \mathbf{H}^{n_s^0-k}$, resulting in $\bar{I_I}^{k,g}$. The sensor $\bar{g}$ whose removal gives the lowest variation of the mean index $\bar{I_I}^{k,g}$ will not be included in the set $\mathbf{H}^{n_s^0-\bar{k}} \in \mathbb{R}^{(n_s^0-\bar{k})\times(n_d+n_i)}$ at the next iteration $\bar{k} = k+1$, because it means that sensor gives the lowest contribution to identity index. This removal selection is indicated in Algorithm 2. The iterations will continue until the selection of a desired number of $\bar{n}_s$ sensors fixed by the user.

Remark: When multiple inputs of different type, e.g. forces $\mathbf{F}$ and torques $\mathbf{M}$, are considered in the estimation, the elements of the TF matrix in Eq. (II.28) are not dimensionally-consistent:

$$\hat{\mathbf{u}}(s) = \begin{bmatrix} \hat{\mathbf{F}}(s) \\ \hat{\mathbf{M}}(s) \end{bmatrix} = \begin{bmatrix} \mathbf{T}_{\hat{\mathbf{F}}\mathbf{F}}(s) & \mathbf{T}_{\hat{\mathbf{F}}\mathbf{M}}(s) \\ \mathbf{T}_{\hat{\mathbf{M}}\mathbf{F}}(s) & \mathbf{T}_{\hat{\mathbf{M}}\mathbf{M}}(s) \end{bmatrix} \begin{bmatrix} \mathbf{F}(s) \\ \mathbf{M}(s) \end{bmatrix} \tag{II.35}$$

Recalling the identity index in Eq. (II.34), it is possible to observe that the inconsistency is in the summation of the cross-terms of $\mathbf{T}_{\hat{\mathbf{u}}\mathbf{u}}(s)$. It is also true that this unit inconsistency is not meaningful for the sensors selection, since an accurate estimation should theoretically provide off-diagonal terms with negligible values. If it does not happen, the estimation accuracy is compromised, since $\mathbf{T}_{\hat{u}u} \neq \mathbf{I}$ and thus $\hat{u}_{jj} \neq u_{jj}$.

Numerical validation

In order to evaluate the effectiveness of the two metrics based on IEC and TFI in the context of input estimation, a two numerical experiments are performed and compared with the results obtained from the reference OSP. First the academic 10 mass-spring-damper system from Sec. *An example of observability screening* is reconsidered in Sec. *Academic 10-mass-spring-damper system*, and next a full scale complexity structural system, modelled through a finite-element approach, is considered in Sec. *Numerical validation on a Finite Element Model (FEM).*

Academic 10-mass-spring-damper system

The aim of this numerical example is to show the robustness of the two proposed metrics with respect to the changing of system and measurements units. In Sec.

Algorithm 2 TFI sensors selection

1: Define the frequency range of interest $\bar{\phi} = [\phi_1, \phi_2]$.

2: Execute the iterative process to find the $\bar{n}_s$ optimal sensors: $\mathbf{k = 0 : (n_s^0 - \bar{n}_s)}$

3: Given the measurement matrix $\mathbf{H}^{n_s^0-k}$, evaluate $\mathbf{T}_{\hat{u}u}^k$ of Eq. (II.28) and the identity index:

4: $I_I^k(\phi) = \frac{\sum_{j=1}^{n_l} |1-|T_{\hat{u}u}^{k,jj}(s)||}{n_l} + \frac{\sum_{j=1}^{n_l}\sum_{i=1,i\neq j}^{n_l} |T_{\hat{u}u}^{k,ji}(s)|}{n_l(n_l-1)}$

5: $\bar{I_I}^k = mean(I_I^k(\phi)) \mid_\phi$

6: Iterate on the subset of sensors $n_s^0 - k - 1$: $\mathbf{g = 1 : (n_s^0 - k - 1)}$

7: remove sensor g from $\mathbf{H}^{n_s^0-k}$ to obtain $\mathbf{H}^{n_s^0-k-1}$, with $g \notin (n_s^0 - k - 1)$;

8: evaluate $\mathbf{T}_{\hat{u}u}^k, g$ of Eq. (II.28) and the identity index $I_I^{k,g}(\phi)$;

9: $\bar{I_I}^{k,g} = mean(I_I^{k,g}(\phi)) \mid_\phi$

10: Evaluate the sensor $\bar{g}$ which gives the lowest contribution to the mean identity index:

11: $\bar{g} := min(\bar{I_I}^k - \bar{I_I}^{k,g})$

12: remove sensor $\bar{g}$ from $\mathbf{H}^{n_s^0-k}$ to obtain $\mathbf{H}^{n_s^0-\bar{k}}$, with $\bar{k} = k + 1$

An example of observability screening, a 10DoFs mass-spring-damper system has been considered in order to show the sensitivity of the PBH metric with respect to scaling issues, leading to non-consistent results. Recalling the system in Fig. II.2 and considering one unknown external force acting on mass m_{10}, 10 displacement sensors are first included in the evaluation of the steady-state covariance $\mathbf{P}$ and the transfer function $\mathbf{T_{\hat{u}u}}$. The results with respect to different scale factors are shown in Fig. II.7 in terms of transfer function, verifying what is stated and proof numerically in Sec. *Input estimation bandwidth: Transfer Function (TF) between real and estimated input.* The values at each frequency is constant when different scaling factors are applied. The same conclusion can be easily found for the steady-state covariance value.

In Fig. II.7, a unit value of the transfer function can be observed only at 0Hz. By selecting an acceleration sensor on mass m_{10}, the unit value covers higher frequencies as shown in Fig II.8, which means that an improvement of the estimated input can be obtained by using a different set of sensors. A smaller value of covariance $\mathbf{P_{uu}}$ obtained with this set of sensors is shown in Fig. II.9 and compared with the higher value from the set of sensors with only displacement measurements. Fig II.8 also shows the robustness of the metric

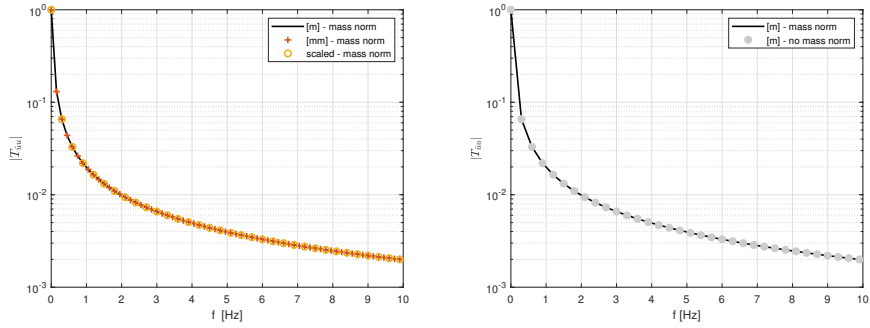

(a) (b)

Figure II.7: Transfer function $\mathbf{T}_{\hat{\mathbf{u}}\mathbf{u}}$ obtained by using 10 displacement sensors. On the left, comparison of the results for the mass-normalized system and i) sensors expressed in meters, ii) sensors expressed in millimiters, iii) scaled sensors. On the rigth, sensors expressed in meters and system i) mass-normalized, ii) without normalization.

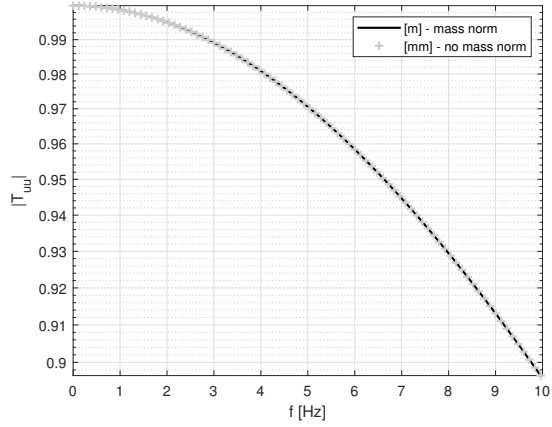

Figure II.8: Transfer function $\mathbf{T}_{\hat{\mathbf{u}}\mathbf{u}}$ obtained by using 10 displacement sensors and 1 acceleration. Comparison of the results with sensors expressed in meters and system i) mass-normalized, ii) without normalization.

with respect to scaling factors even with the usage of mixed type of sensors. The same comparison can be performed on the covariance value, which results to be insensitive to the scaling as well.

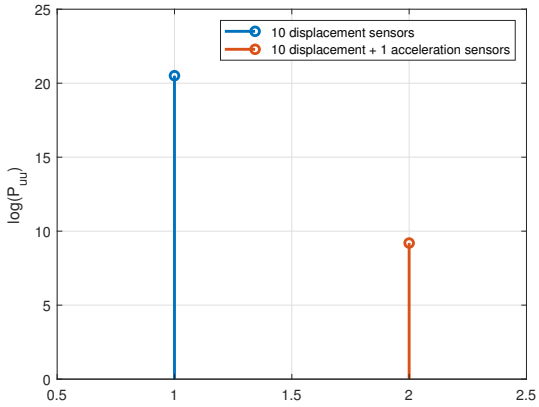

Figure II.9: Steady-state error covariance $\mathbf{P}_{\hat{\mathbf{u}}\mathbf{u}}$ value obtained by using i) 10 displacement sensors and ii) 10 displacement and 1 acceleration sensors.

In this example, we assume to know $\mathbf{Q}$ and $\mathbf{R}$, but a numerical experimental validation could explain the influence of both matrices. However, the investigation of this effect is out of the scope of this contribution.

In the next section, a more complex system is considered for the validation of the optimal sensor selection.

Numerical validation on a Finite Element Model (FEM)

A linear FEM of a rear twistbeam suspension [45, 52] shown in Fig. II.10 is used for this purpose. It is defined by shell mesh with 50533 4-node quadrilateral elements. The loads are applied at the central point of the right side wheel, indicated as *input point*. The other tyre and the bushings are clamped. The target is the estimation of 6 loads, i.e. 3 forces and 3 torques, applied at the *input point* along x, y and z directions (reference in Fig. II.10). As stated in Sec. *Introduction*, a minimum number of 6 position-level sensors, e.g. positions or strains, are needed to obtain a stable estimation. The target of this example is to find a set of 6 optimal strain measurements.

Four set of loads are investigated: i) sinusoidal loads with zero-phase (amplitude and frequency are listed in Table II.1), ii) sweep sine loads with frequency varying from 1Hz to 20Hz in 5 seconds, iii) white noise signals, iv) impulse loads. These loads are firstly applied to execute a forward simulation and collect output responses. Gaussian noise is then added on these data and the input estimation is performed considering the loads as unknowns. Loads at low

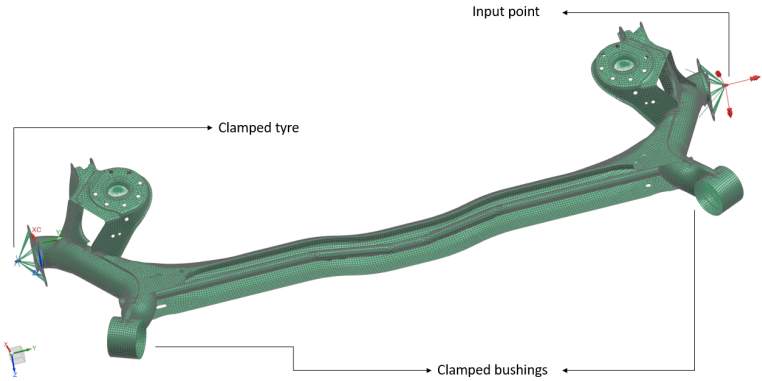

Figure II.10: FEM of the rear twistbeam suspension.

frequency are presented, but same considerations about results can be made at other frequencies since a linear model is considered. The $\mathbf{Q}_u$ value was selected using the same approach adopted in [52]. The formula is the following:

$$\mathbf{Q}_u = (\Delta t \cdot \bar{\omega}_u \cdot \bar{a}_u)^2 \quad , \tag{II.36}$$

with $\bar{\omega}_u$ and $\bar{a}_u$ as indicative expected value of the frequency and the amplitude of the input shape, chosen by the user.

Load	**Amplitude**	**A**	**Frequency**	ϕ
F_1	300	[N]	1	[Hz]
F_2	30	[N]	1	[Hz]
F_3	250	[N]	1	[Hz]
T_1	10000	[N mm]	1	[Hz]
T_2	65000	[N mm]	1	[Hz]
T_3	7000	[N mm]	1	[Hz]

Table II.1: Sine loads parameters.

As described in Sec. *Optimal Sensor Placement strategy*, before the final selection based upon PBH, IEC and TFI metrics, the *Training* procedure is performed. A starting pool of 2000 strain sensors is randomly placed on the component and the selection is then reduced to 87 post-*Training* sensors. The selected frequency range for the TFI criteria is $[\phi_1 = 0.1, \phi_2 = 5]$ Hz, with frequency step $\Delta\phi = 0.1$ Hz. In Sec. *Input estimation*, the results on the input estimation

are shown for the two load cases and in Sec. II the effect of modelling errors is assessed.

Input estimation

The location of the sensors selected by PBH, IEC and TFI is shown in Fig. II.11. It's possible to observe that both IEC and TFI select sensors in similar positions. It should also be noted that, since each of the starting virtual sensors represents a biaxial strain gauge, it may happen that a criteria selects one or both measurement directions for a given sensor. In Fig. II.11, the PBH criterion shows 6 selected monoaxial strain sensors, while both IEC and TFI select 5 monoaxial and 1 biaxial strain sensors.

The selection indexes for the 3 criteria are shown in Figure II.12. It's possible to observe that their behavior is coherent with the effect of the removal of a sensor. O_m decreases, while $\bar{P}$ and I_I increase. The red markers in Fig. II.12 indicate the value of the indexes at the last selection loop.

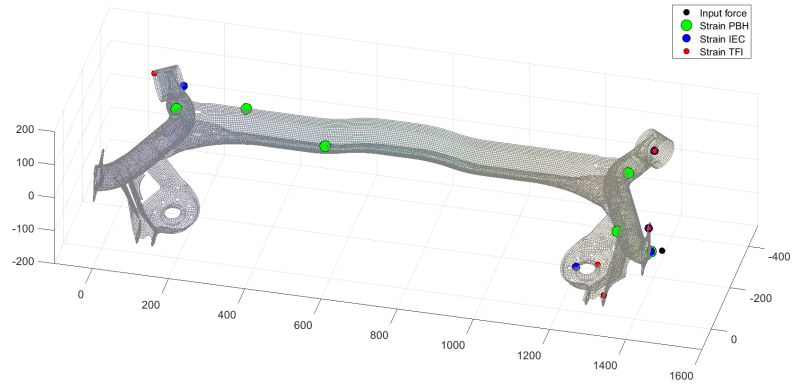

Figure II.11: Strain sensors position for the 3 criteria. The black marker indicates the *input point*.

Sinusoidal loads

The results of the input estimation obtained using the sensors selected by the PBH criterion are shown in Fig.II.14a for sine signals: the shape of the sinusoidal inputs is accurately estimated, but zooming in it's possible to observe that there's considerable noise on the estimation (Fig. II.14b). The inaccuracy of the estimated signal is produced by the selection of noisy sensors. An example of sensor chosen by the PBH criterion is shown in Figure II.14c: the amount

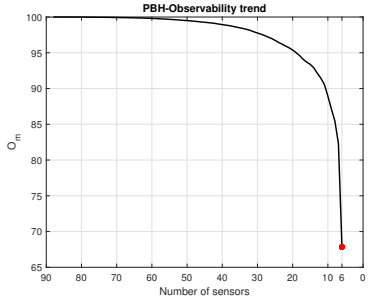

(a) O_m value in the PBH selection.

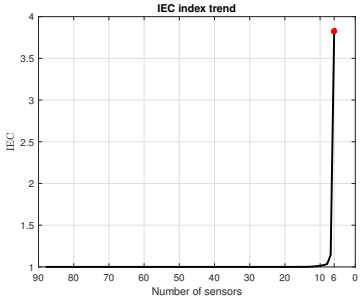

(b) $\bar{\mathbf{P}}$ value in the IEC selection.

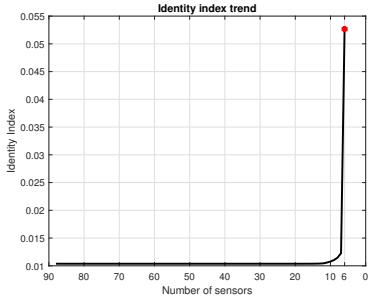

(c) I_I value in the TFI selection.

Figure II.12: Evolution of the selection indexes.

of noise on the strain signals compromises the accuracy of the estimation. In Fig. II.13, the signal-to-noise ratio (SNR) of the set of sensors selected by the three metrics is compared (expressed in decibel dB). The SNR is evaluated as $\frac{P_s}{P_n}$, where P_s and P_n are the signal and noise power.

This problem does not occur in the case of both IEC and TFI selection: the corresponding estimation results are shown in Fig. II.15 and Fig. II.16. The inputs are estimated with good accuracy and this is due to the fact that the sensors selected by both criteria have higher signal-to-noise ratio. Since both IEC and TFI consider matrix $\mathbf{R}$ and $\mathbf{Q}_u$, they are able to select the sensors that assure the most accurate output, thus leading to a lower amount of noise on the input estimation. The normalized input estimation errors are shown in Fig. II.17. Each error is normalized using the difference between the real input's maximum and minimum value.

Evaluating $I_I(\phi)$ for the selected sensors combinations at $\bar{\phi} = 1$Hz (Fig. II.18), it's possible to observe that the numerical value for the index corresponds to the accuracy of the estimations: $I_I(\bar{\phi})$ is close to 0.02 for IEC and TFI, while

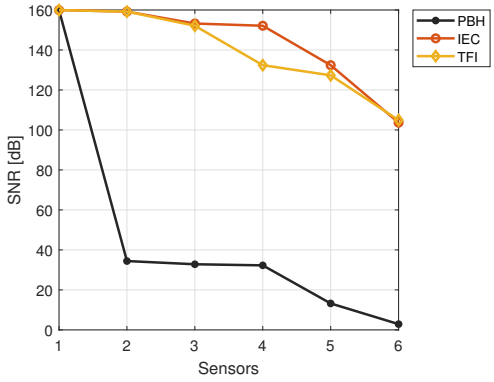

Figure II.13: SNR of the set of sensors selected by the three metrics.

PBH results in $I_I(\bar{\phi}) > 0.1$. Testing the system under different conditions, it emerged that an optimal threshold value for the index is $I_I(\bar{\phi}) < 0.05$: if the selection results in an index less then this value, the inaccuracy on the estimation increases. Given these values, the performance of the set of sensors selected by IEC and TFI is due to the fact that their corresponding transfer function matrix is closer to an identity matrix if compared with the one obtained through the PBH.

Sine sweep loads

The three metrics are compared for a sine sweep signal varying from 1Hz to 20Hz in 5 seconds. The results of the sine sweep loads are shown in Fig. II.19, II.20, II.21 and the obtained behavior is in accordance to the results obtained for the single sine load. One remark needs to be underlined for TFI estimation: the sensors have been selected in the frequency range [0.1, 5] Hz, which does not include all the frequencies excited by the input signal. More accurate results can be obtained by increasing this range. As example, Fig. II.22 shows the comparison on the input load Force 2 between the estimated load for a training frequency range [0.1, 5] Hz and the one obtained by selecting the sensors in a training frequency range up to 30Hz.

White noise signals

The improvement on the input estimation can be observed on the white noise case in Fig. II.23. The variance and mean value of the input signals are listed in Table. II.2. Fig. II.23 shows the results in frequency domain f in terms of error ϵ evaluated as follows:

$$\epsilon = |log(\mathbf{u}(f)) - log(\hat{\mathbf{u}}(f))| \tag{II.37}$$

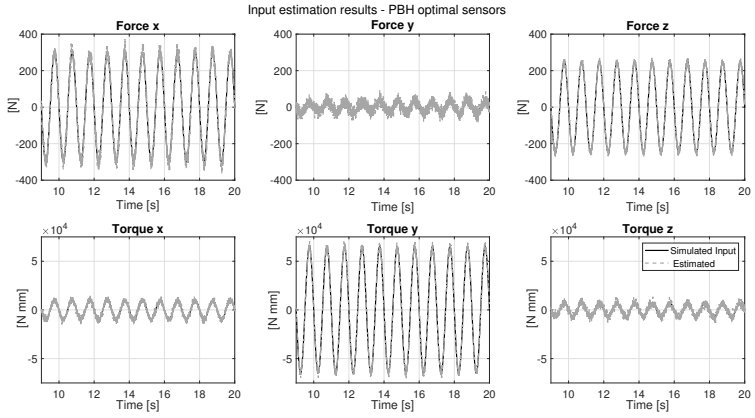

(a) Inputs estimation performed using the sensors selected by PBH criterion.

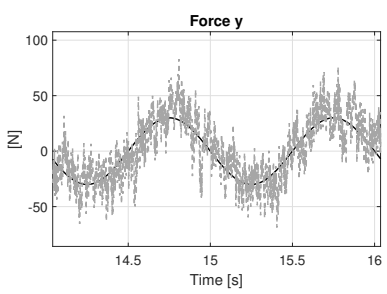

(b) Zoom of $\hat{F}_y$ shown in Fig. II.14a.

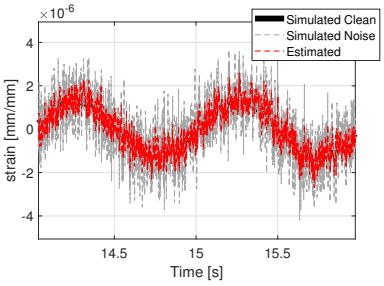

(c) One of the sensors selected by PBH criterion.

Figure II.14

For illustrative purpose, Fig. II.24, II.25, II.26 show that the overall estimation of the six loads in time domain significantly improve.

Impulse loads

For completeness of the results, the impulse loads case is considered for the estimation and the results are shown in Fig. II.27, II.28, II.29. The conclusions on the improvement of the estimation are in line with the previous examples and thus remain unchanged.

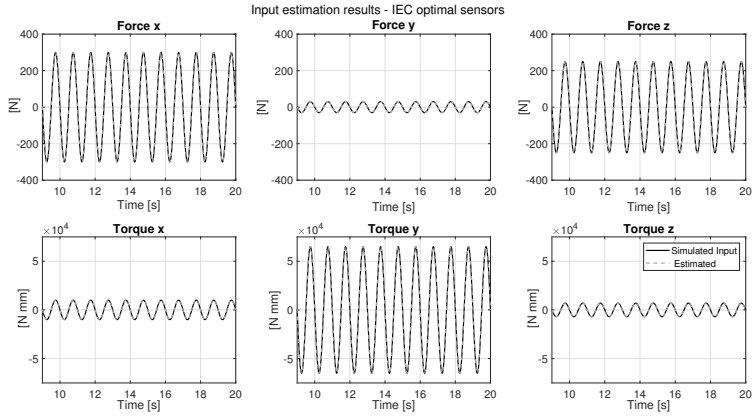

Figure II.15: Inputs estimation performed using the sensors selected by IEC criterion.

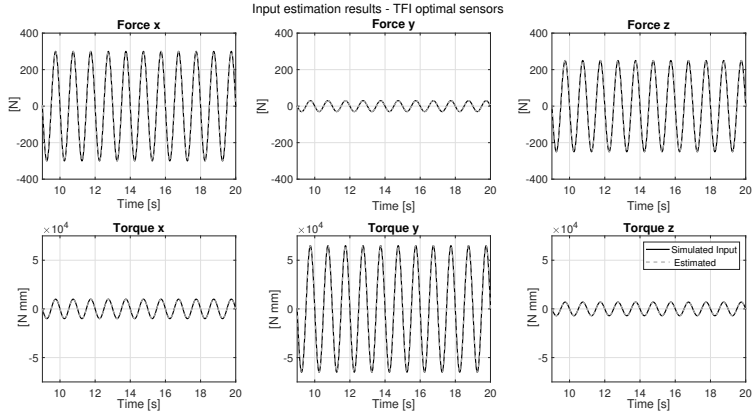

Figure II.16: Inputs estimation performed using the sensors selected by TFI criterion.

Modelling errors

In this section, the effect of having modelling errors is investigated on the input estimation. The model used in the filter is still the same as in Sec. *Input estimation*, thus the optimal sensor selection is not changed. The measurements used in the filter as reference data are instead generated by simulating the same model with a percentage error on the Young Modulus (E) of the material.

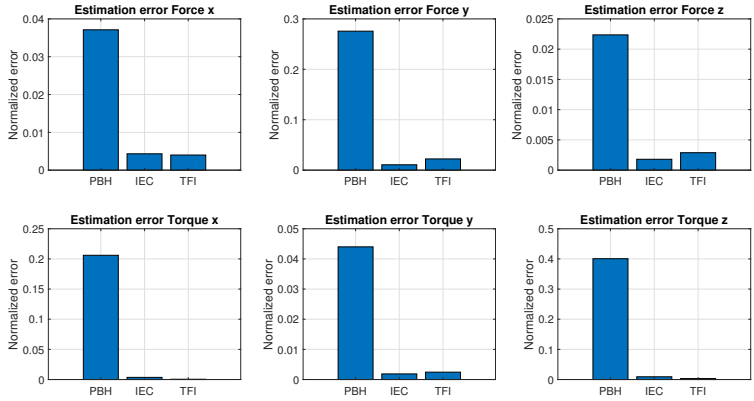

Figure II.17: Normalized error on each estimated input through sensors selected by PBH, IEC and TFI criteria.

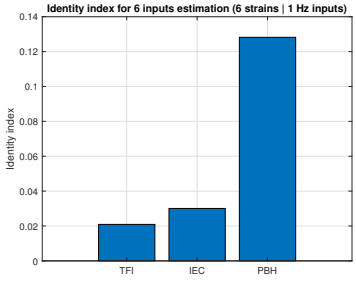

Figure II.18: Identity index evaluated at $\bar{\phi} = 1$Hz for the 3 criteria: the numerical value reflects the accuracy of the estimations.

Fig. II.30 shows the evolution of the Root-Mean-Square-Error (RMSE) on forces and torques estimation obtained by increasing the percentage error of E on the set of measurements. It is possible to observe that if the modelling errors increase, the accuracy on the estimation decreases for all the metrics. This is because, as the modelling errors increase, the assumption of the input model as only source of uncertainties fails. However, the performance of the three criteria is not the same: IEC and TFI shows to be more robust to modelling errors for most of the loads.

Load	Variance		Mean	
F_1	$9.15E04$	$[\mathrm{N}^2]$	-1.10	[N]
F_2	$9.09E02$	$[\mathrm{N}^2]$	0.28	[N]
F_3	$6.19E04$	$[\mathrm{N}^2]$	0.62	[N]
T_1	$9.96E07$	$[\mathrm{N}^2\ \mathrm{mm}^2]$	-135.26	[N mm]
T_2	$4.26E09$	$[\mathrm{N}^2\ \mathrm{mm}^2]$	$1.54E03$	[N mm]
T_3	$4.92E07$	$[\mathrm{N}^2\ \mathrm{mm}^2]$	0.52	[N mm]

Table II.2: White noise signal parameters.

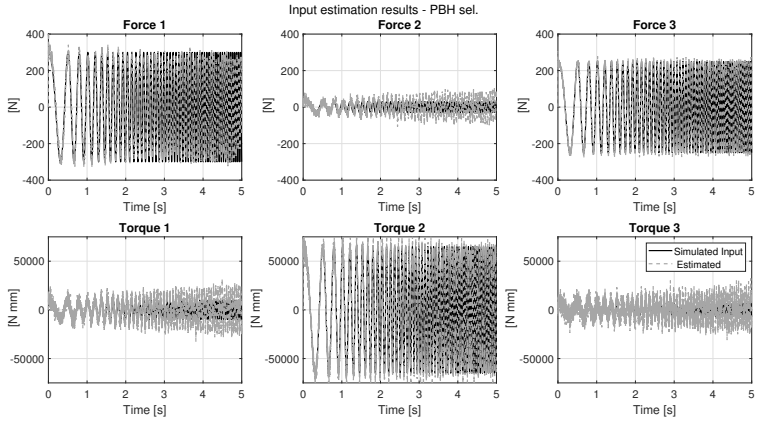

Figure II.19: Sine sweep: inputs estimation performed using the sensors selected by PBH criterion.

Conclusions

This paper presents a novel approach for the optimal selection of sensors used for load identification of mechanical dynamic systems. An improvement on the existing Optimal Sensor Placement in the framework of AKF is proposed, replacing the observability screening criterion with more reliable approaches. Two Advanced Optimal Sensor Placement strategies are proposed: one based on the estimation error covariance (IEC) and the other based on the frequency domain transfer function (TFI) between the real and the estimated input. The main issue in the usage of the observability screening is in the type of sensors considered and also in the used units. The latter concerns both the units of the model itself and also the measurement equations. It is demonstrated through an example that, if position measurements expressed in [m] or [mm] are

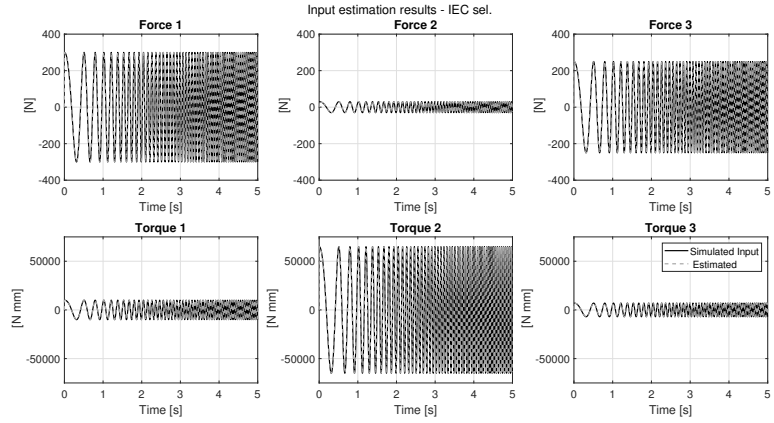

Figure II.20: Sine sweep: inputs estimation performed using the sensors selected by IEC criterion.

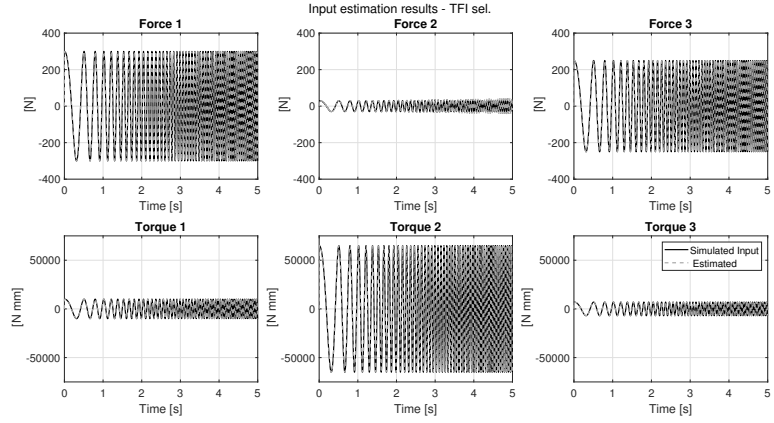

Figure II.21: Sine sweep: inputs estimation performed using the sensors selected by TFI criterion.

included in the selection, two different results are obtained in terms of optimal locations. Both IEC and TFI metrics are not affected by scaling problems. The effectiveness of the proposed approaches is shown through a numerical example on an industrial FE model. Multiple load estimation (3 forces and 3 torques) is performed using three different sets of sensors obtained from the two novel metrics and the existing observability screening. The results show

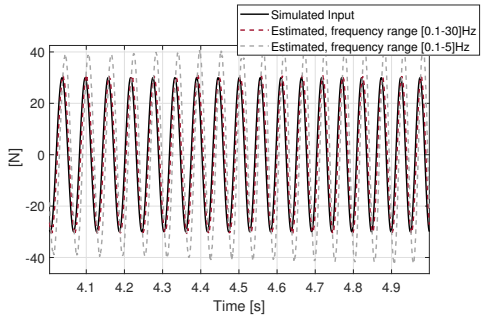

Figure II.22: Force 2 estimation performed using the sensors selected by TFI criterion in a frequency range [0.1-5]Hz and [0.1-30]Hz.

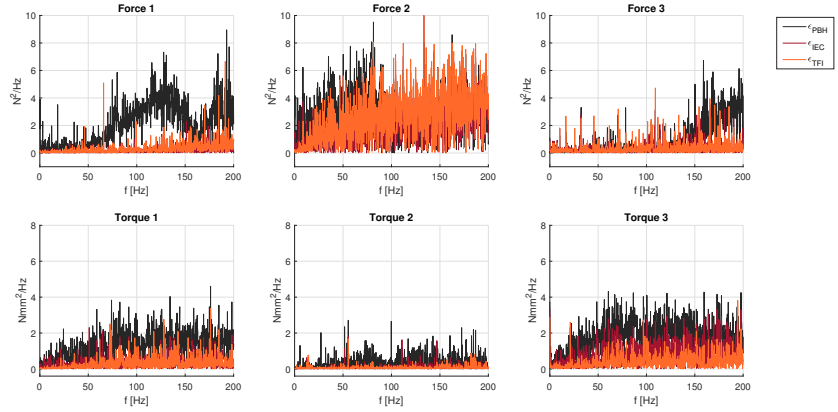

Figure II.23: White noise signal: error in frequency domain between the reference and the estimated load.

that the estimation given by the OSP strategy is highly noisy. This can be explained underlying another issue related to this sensor selection. Indeed, it does not take into account for process and measurement covariances. The proposed approaches include intrinsically this information and it results in more accurate load estimation. Future investigation aims to test IEC and TFI metrics for multiple loads estimation on a real test case. Different load scenarios will be considered, e.g. out- and in-phase or random excitation, to evaluate the robustness of the methods.

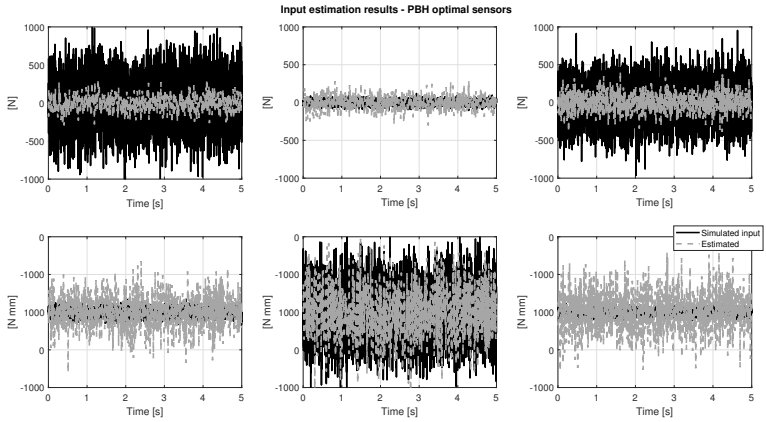

Figure II.24: White noise signal: inputs estimation performed using the sensors selected by PBH criterion.

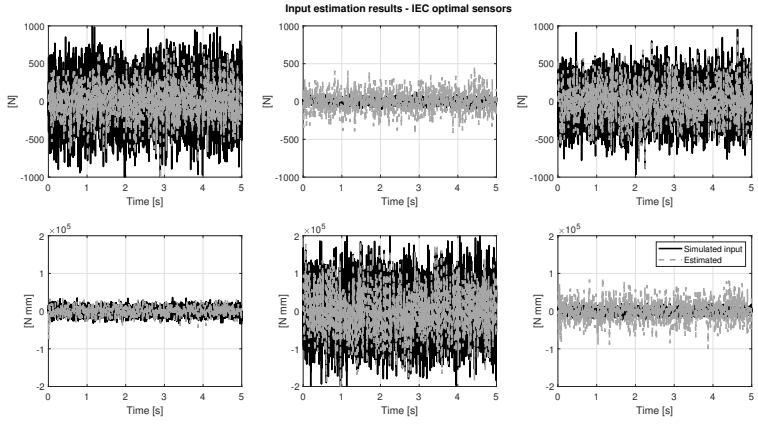

Figure II.25: White noise signal: inputs estimation performed using the sensors selected by IEC criterion.

Acknowledgement The authors gratefully acknowledge the support and contribution of VLAIO Flemish Innovation & Entrepreneurship through the Baekeland Mandate project SINCRO n. HBC.2018.2086, Flanders Make through ICON project VSFlex n. HBC.2019.0082, and the European Commission with Marie Sklodowska Curie program through the ETN ECO DRIVE project n. GA 858018.

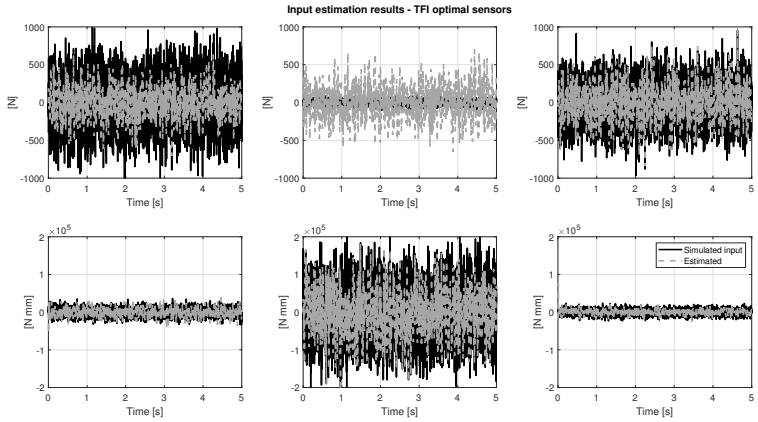

Figure II.26: White noise signal: inputs estimation performed using the sensors selected by TFI criterion.

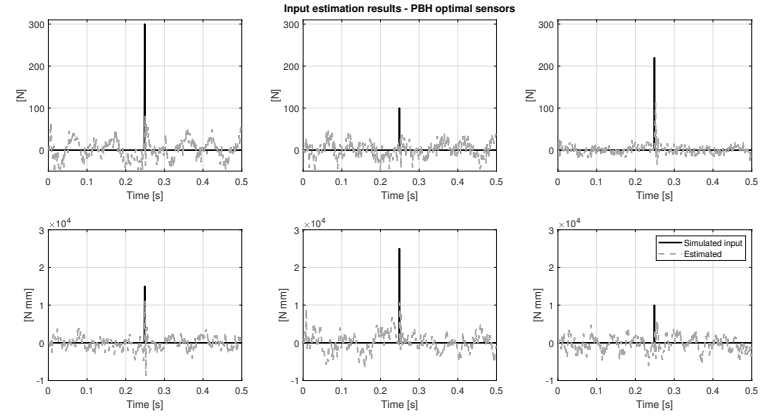

Figure II.27: Impulse loads: inputs estimation performed using the sensors selected by PBH criterion.

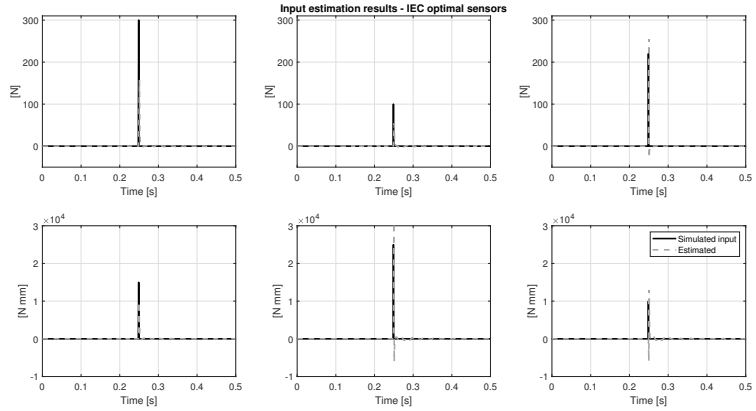

Figure II.28: Impulse loads: inputs estimation performed using the sensors selected by IEC criterion.

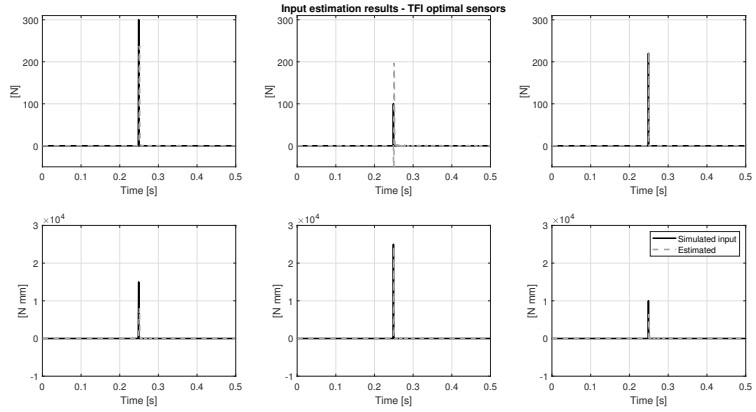

Figure II.29: Impulse loads: inputs estimation performed using the sensors selected by TFI criterion.

Appendix A: Laplace transform for second order system expressed as first order system

Starting from the equation of motion of a second order mechanical dynamic system:

$$\mathbf{M}\ddot{\mathbf{x}}(t) + \mathbf{C}\dot{\mathbf{x}}(t) + \mathbf{K}\mathbf{x}(t) = \mathbf{u}(t) \tag{II.38}$$

the first order model is:

$$\begin{bmatrix} \dot{\mathbf{x}}(t) \\ \ddot{\mathbf{x}}(t) \end{bmatrix} = \begin{bmatrix} \mathbf{0} & \mathbf{I} \\ -\mathbf{K}/\mathbf{M} & -\mathbf{C}/\mathbf{M} \end{bmatrix} \begin{bmatrix} \mathbf{x}(t) \\ \dot{\mathbf{x}}(t) \end{bmatrix} + \begin{bmatrix} \mathbf{0} \\ \mathbf{I} \end{bmatrix} \mathbf{u}(t) \tag{II.39}$$

Eq. (II.38) and (II.39) are both expressed in time-domain. The corresponding first order model in Laplace Domain is:

$$\begin{bmatrix} s\mathbf{x}(s) \\ s^2\mathbf{x}(s) \end{bmatrix} = \begin{bmatrix} \mathbf{0} & \mathbf{I} \\ -\mathbf{K}/\mathbf{M} & -\mathbf{C}/\mathbf{M} \end{bmatrix} \begin{bmatrix} \mathbf{x}(s) \\ s\mathbf{x}(s) \end{bmatrix} + \begin{bmatrix} \mathbf{0} \\ \mathbf{I} \end{bmatrix} \mathbf{u}(s) \tag{II.40}$$

from which one can derive the matrix $S(s)$:

$$\begin{bmatrix} \mathbf{I} & \mathbf{0} \\ \mathbf{0} & s\mathbf{I} \end{bmatrix} \begin{bmatrix} s\mathbf{x}(s) \\ s\mathbf{x}(s) \end{bmatrix} = \begin{bmatrix} \mathbf{0} & \mathbf{I} \\ -\mathbf{K}/\mathbf{M} & -\mathbf{C}/\mathbf{M} \end{bmatrix} \begin{bmatrix} \mathbf{I} & \mathbf{0} \\ \mathbf{0} & s\mathbf{I} \end{bmatrix} \begin{bmatrix} \mathbf{x}(s) \\ \mathbf{x}(s) \end{bmatrix} + \begin{bmatrix} \mathbf{0} \\ \mathbf{I} \end{bmatrix} \mathbf{u}(s) \tag{II.41}$$

Repeating the same steps for the augmented formulation, it is easy to derive also the augmented matrix $S^*(s)$.

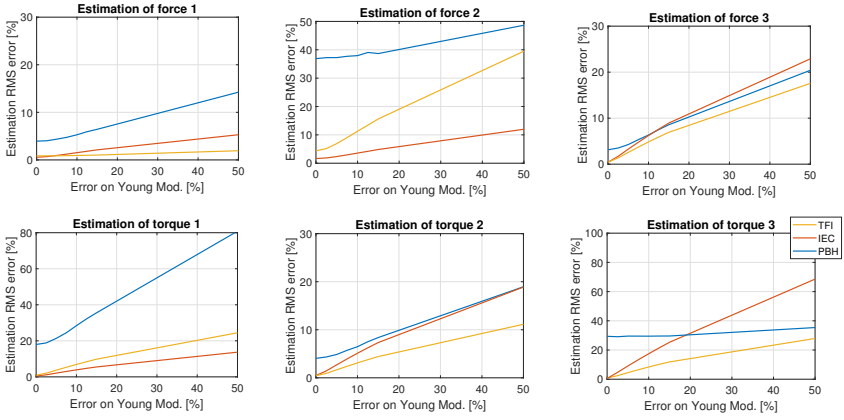

Figure II.30: RMSE value of the estimated loads for different modelling errors

Publication III

State and Force Estimation on a Rotating Helicopter Blade through a Kalman-Based Approach

Published in Sensors 15 (2020) 4196
DOI: 10.3390/s20154196

State and Force Estimation on a Rotating Helicopter Blade through a Kalman-Based Approach

Roberta Cumbo[1,2], Tommaso Tamarozzi[1,2], Pavel Jiranek[1], Wim Desmet[2,3], Pierangelo Masarati[4]

[1] *Siemens Industry Software NV, Interleuvenlaan 68, B-3001 Leuven, Belgium*
[2] *KU Leuven, Department of Mechanical Engineering, Celestijnenlaan 300 B, B-3001 Heverlee, Belgium*
[3] *DMMS-D Core lab, Flanders Make, 3001 Leuven, Belgium*
[4] *Dipartimento di Scienze e Tecnologie Aerospaziali, Politecnico di Milano, Via la Masa 34, 20156 Milano, Italy*

Abstract

The interaction between the rotating blades and the external fluid in non-axial flow conditions is the main source of vibratory loads on the main rotor of helicopters. The knowledge or prediction of the produced aerodynamic loads and of the dynamic behavior of the components could represent an advantage in preventing failures of the entire rotorcraft. Some techniques have been explored in the literature, but in this field of application, high accuracy can be reached if a large amount of sensor data and/or a high-fidelity numerical model is available. This paper applies the Kalman filtering technique to rotor load estimation. The nature of the filter allows the usage of a minimum set of sensors. The compensation of a low-fidelity model is also possible by accounting for sensors and model uncertainties. The efficiency of the filter for state and load estimation on a rotating blade is tested in this contribution, considering two different sources of uncertainties on a coupled multibody-aerodynamic model. Numerical results show an accurate state reconstruction with respect to the selected sensor layout. The aerodynamic loads are accurately evaluated in post-processing.

Keywords: State and load estimation, Inverse identification, Kalman filter, Multibody modeling

Introduction

The main rotor is the most significant component of any helicopter because it generates the needed lift supporting the weight of the entire rotorcraft and provides the control moments required for the execution of different maneuvers. The flexible rotating blades are constantly interacting with the aerodynamic flow and are thus the main source of vibratory loads. These excitations are transmitted to the rotor hub; consequently, their knowledge becomes of significant importance to preventing failures and other undesirable mechanical effects on the entire rotorcraft. Besides, the variability of the aerodynamic loads produced by the structure and flow interaction is of high complexity and cannot be easily predicted or generalized for the same rotorcraft in different flight conditions. Therefore, the problem of structural monitoring in helicopters covers many aspects of rotorcraft design and operations. Several methodologies have been proposed in the literature. This problem can be approached in two related fields of research: structural component monitoring and prediction of structural behavior or aerodynamic loads.

A review of existing helicopter rotor health monitoring systems and techniques is presented in [144]. The health and usage monitoring system (HUMS) and the rotor track and balance (RTB) system have been considered valuable instruments to increase failure detection information and flight safety. Nevertheless, they do not provide detailed information about the structural status of the rotor components. Ganguli et al. [66] studied the damage detection problem at the blade level, in terms of localized changes of structural, inertia and aerodynamic properties. In a subsequent study, Ganguli et al. [69] extended the previous work by presenting one of the first contributions on the usage of artificial neural network (ANN) algorithms applied to damage modeling. Despite the disadvantage of a large amount of data needed for training, ANNs appears in several works [81, 67, 68] in the field of loads and damage monitoring in the helicopter area. In the last few decades, these techniques have become widely used for force reconstruction [158, 72] and aerodynamic flow interaction [32, 22] problems. One of the main advantages of ANN is that no physical model is required behind the application of the methodology. When model-based techniques are employed, the accurate analysis of rotor blade loads needs a coupled computational fluid dynamics (CFD) and computational structural dynamics (CSD) simulation, as accurately reported in [5].

In recent years, focus is being placed on the combination of test and model solutions [78, 34, 29, 160]. Among these techniques, the so-called blade shape sensing [29] has been demonstrated to be an efficient modal-based approach to reconstruct the shape of the blade, combining a limited set of measurements with assumed modal shapes. The optimal number and positions of sensors

still constitute an open field of research, together with the application of the technique to more complex systems, such as a full helicopter rotor. The assembled structure is difficult or time-consuming to obtain in terms of structural modeling and aerodynamic load computation with respect to the level of accuracy. The intention of this contribution is to propose an approach able to perform appreciable prediction of structural/aerodynamic information saving time in the modeling phase. The proposed approach makes use of the estimators, and in particular, of the Kalman filter [164, 95], which aims at solving a state space model taking into account the model and observation (e.g., measurements in a real test case) uncertainties. Besides the standard formulation, a robust Kalman filter has been also presented in the literature [196, 127, 198] to address the problem of state estimation by being robust against the model's uncertainty. Indeed, when some unknown modeling errors exist, the estimation of the standard Kalman filter might be not enough accurate. The robust Kalman filter is instead designed to consider all possible uncertainties [196] by modeling an energy bounded noise, against the stochastic white noise in the standard formulation [127]. The solution of two algebraic Riccati equations [196] is needed in the robust Kalman filter and this might be a disadvantage. The modeling of the uncertain system is also constrained to a norm-bound value, which has conceptually the same role of the model covariance matrix as the standard Kalman filter [164]. Some works (e.g. [11, 88]) already report the usage of the Kalman filter for damage detection in rotorcraft applications. Different formulations of the standard Kalman filter (KF) are widely used in the literature, such as the extended Kalman filter (EKF) and the unscented Kalman filter (UKF) [164]. The EKF is one of the possible non-linear versions of the Kalman filter. The main principle is the linearization of the non-linear system around the current estimated state using a first-order truncation of the Taylor series expansion of the model equations. Some references on the application of the EKF can be found in [58, 150, 186]. The UKF is instead a recursive estimator that addresses some of the approximation issues of the EKF. The UKF does not explicitly approximate the nonlinear process and observation models; it uses instead the true nonlinear models and approximates the distribution of the state random variable. However, in many application cases, the EKF becomes more efficient from a computational point of view. An accurate comparison between EKF and UKF can be found in [186]. When a joint states/inputs estimation is performed, both EKF and UKF can be employed in a variant way. In this context, two different approaches are presented in the literature: the dual Kalman filter (DKF) [19] and the augmented Kalman filter (AKF) [164]. The DKF operates in two estimation stages, while the AKF estimates the states and the inputs simultaneously by introducing an augmented state vector and this defines a reduction of the computational cost. The AKF has been applied in many fields and was recently demonstrated to give accurate

results for automotive applications [52, 150]. The results showed that, when the adopted structural model was not accurate enough, the AKF still provided a good estimation of the states at the expense of the loads' accuracy. Given the dependence of the aerodynamic loads on the states of the rotor blades [92], the proposed approach performs a multiple-load and state estimation, with the aim of reaching high accuracy for the states of the blades and re-using this information to compute the aerodynamic loads in post-processing.

As already stated, the Kalman filtering technology has been widely applied in a lot of research, but the intent of the authors is to demonstrate its potential in the rotorcraft field for load prediction, thereby exploring the advantages in the model complexity and needed sensor data. A multibody model [162] of the blades has been developed, following the finite segment formulation [44] approach. The model can be considered as simplified because the blade flexibility is not modeled with high accuracy like in a finite element modeling approach. This is, anyway, an acceptable simplification for quasi-steady flight conditions and also if the user is interested mainly in aerodynamic loads instead of blade deformations. Increasing the complexity of the model is out of the scope of this work, but it is the intent of the authors to investigate the proposed methodology on highly accurate rotor models in the future. Given the non-linear nature of a general multibody model, the EKF formulation has been adopted in its augmented formulation. A steady flight condition is investigated in this contribution. The 2-blade rotor model is first validated by comparing its results with those obtained using MBDyn—free, general-purpose multibody software [55]—and then used to predict aerodynamic load distribution and the displacement/velocity field along the blade span. This paper is structured as follows. First, the theoretical background is provided, giving a generic overview on all the touched-upon topics with the formulations used: rotor multibody modeling, aerodynamic modeling and augmented Kalman filter. In the second part, the developed workflow needed for states and loads' prediction is presented, followed by a numerical validation of the developed model and numerical results of the estimation problem. Concluding remarks are then discussed.

Methodologies: Theoretical Background

In the present contribution, the structural model of the rotating blades is developed using a multibody simulation approach [162] based on the finite segment theory presented in [44]. A quasi-steady formulation is adopted for the aerodynamic loads and a uniform inflow model is used, based on the blade element momentum theory (BEMT) [79]. The prediction of aerodynamic loads and states of the developed multibody model is proposed using a Kalman-based approach.

Multibody Structural Model

In structural modeling, a multibody dynamics simulation is a convenient approach when the system is complex and phenomena caused by nonlinearities cannot be neglected. A rotating blade is subject to high stresses and deformations and is connected to the hub through some mechanisms, e.g., pitch, flap and lag hinges, which need to be modeled in order to reproduce the correct behavior of the fully assembled structure. There are two main classes of formulations for multibody analysis: ordinary differential equations (ODE) and differential-algebraic equations (DAE). A detailed explanation of the differences between the two formulations is provided in [85, 163]. In this contribution, an index-2 DAE approach is chosen, which formulates the equations of motion of a constrained system as:

$$\begin{cases} \dot{\mathbf{q}}(t) - \mathbf{v}(t) = \mathbf{0} \\ \mathbf{M}(\mathbf{q}(t))\dot{\mathbf{v}}(t) + \mathbf{f}(\mathbf{q}(t), \mathbf{v}(t), t) - \mathbf{B}(\mathbf{q}(t))^T \boldsymbol{\lambda_s}(t) = \mathbf{0} \\ \mathbf{B}(\mathbf{q}(t))\mathbf{v}(t) = \mathbf{0} \end{cases} \tag{III.1}$$

where t is the time variable; $\mathbf{q} \in \mathbf{R}^n$ and $\mathbf{v} \in \mathbf{R}^n$ are the n-coordinates and n-velocity vectors of the system; $\mathbf{M} \in \mathbf{R}^{n \times n}$ is the mass matrix; $\mathbf{f} \in \mathbf{R}^n$ is a general non-linear term including all the other forces, e.g., elastic, external and quadratic contributions; $\mathbf{B} \in \mathbf{R}^{n \times m}$ is the Jacobian matrix of the constraints, given by differentiating the constraint condition with respect to $\mathbf{q}$; $\boldsymbol{\lambda_s} \in \mathbf{R}^m$ is the vector of m Lagrange multipliers; and $\dot{\mathbf{q}}$ and $\dot{\mathbf{v}}$ are the time derivatives of $\mathbf{q}$ and $\mathbf{v}$. The set of equations in (III.1) includes only the velocity constraint. A way to enforce the index-2 formulation is to use a variant form given by Gear, Gupta and Leimkuhler (GGL) [71]:

$$\begin{cases} \dot{\mathbf{q}}(t) - \mathbf{v}(t) + \mathbf{B}(\mathbf{q}(t))^T \boldsymbol{\mu_s}(t) = \mathbf{0} \\ \mathbf{M}(\mathbf{q}(t))\dot{\mathbf{v}}(t) + \mathbf{f}(\mathbf{q}(t), \mathbf{v}(t)) - \mathbf{B}(\mathbf{q}(t))^T \boldsymbol{\lambda_s}(t) = \mathbf{0} \\ \mathbf{B}(\mathbf{q}(t))\mathbf{v}(t) = \mathbf{0} \\ \mathbf{g}(\mathbf{q}(t)) = \mathbf{0} \end{cases} \tag{III.2}$$

In Equation (III.2), additional multipliers $\boldsymbol{\mu_s}$ at velocity level and a set of algebraic equations $\mathbf{g}(\mathbf{q}(t)) \in \mathbf{R}^m$, i.e., position constraints, are included. The GGL formulation is the one adopted in the multibody solver used in this work. For sake of simplicity, the time dependence of all variables will be omitted in the next sections.

Finite Segment Beam Formulation

Each multibody model of the blades is composed by N_e rigid bodies, connected by $N_e - 1$ flexible elements. In the finite segment approach [44], these are spring

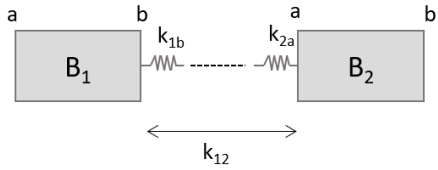

Figure III.1: Two rigid bodies connected through elastic elements. a and b are the two faces of each body where the connections are. k_{12} is the total stiffness matrix given by the interaction of both elastic forces from faces B_{1b} and B_{2a}.

elements, as shown in Figure III.1. Given two bodies B_1 and B_2, the equivalent stiffness k_{12} is:

$$k_{12} = \frac{k_{1b}k_{2a}}{k_{1b} + k_{2a}} \tag{III.3}$$

A rigid body in space has six degrees of freedom (DOFs), i.e., three positions and three rotations; thus, the stiffness parameter in Equation (III.3) results in a 6 by 6 matrix $\mathbf{k}_{12}$. For a certain body j, the elemental stiffness matrix at the generic face f can be derived from a finite element beam theory [147] formulation:

$$\mathbf{k}_{jf} = \begin{bmatrix} \frac{EA}{l} & 0 & 0 & 0 & 0 & 0 \\ 0 & \frac{12EI_z}{l^3(1+\Phi_y)} & 0 & 0 & 0 & \frac{-6EI_y}{l^2(1+\Phi_z)} \\ 0 & 0 & \frac{12EI_y}{l^3(1+\Phi_z)} & 0 & \frac{6EI_z}{l^2(1+\Phi_y)} & 0 \\ 0 & 0 & 0 & \frac{GJ}{l} & 0 & 0 \\ 0 & 0 & \frac{6EI_z}{l^2(1+\Phi_y)} & 0 & \frac{(4+\Phi_z)EI_y}{l(1+\Phi_z)} & 0 \\ 0 & \frac{-6EI_z}{l^2(1+\Phi_z)} & 0 & 0 & 0 & \frac{(4+\Phi_y)EI_z}{l(1+\Phi_y)} \end{bmatrix} \tag{III.4}$$

where l is the free-length of the beam; EA, EI_y, EI_z and GJ are the cross-sectional properties of the beam; and Φ_y and Φ_z are two coefficients to account for shear deformation effects.

Aerodynamic Model

The interaction between a rotating blade and the external fluid defines a complex aerodynamic field and a 3D analysis should be used to enable an accurate performance estimation of the rotor. However, this contribution aims to outline a general workflow for loads and states prediction on a rotating blade in a realistic aerodynamic scenario. The employment of highly accurate aerodynamic modeling, such as CFD analysis, is thus out of the scope of this work. In this paper, MBDyn is first used as the reference code for validation

purpose and then to generate reference data for Kalman filtering estimation. A 2D aerodynamic model is employed, computing the inflow velocity based on the BEM theory. An advantage that will be underlined in Section *Workflow for Estimation of States and Loads on a Rotor Blade* is the dependence of the aerodynamic loads on the states of the blade structural model. All the analyses presented in the paper refer to a quasi-steady aerodynamic model.

Aerodynamic Loads

Figure III.2 shows a sketch of an airfoil in the rotating reference frame which is adopted in the presented rotor model. It is identified by $\{X, Y, Z\}$ with corresponding unit vectors $\{\hat{i}_1, \hat{i}_2, \hat{i}_3\}$. In the helicopter modeling, the rotating frame follows the motion of the hub, which rotates with rotational speed Ω. The elemental lift dL and drag dD, evaluated at the stage $\mathbf{r}$, can be written as:

$$dL = \frac{1}{2}\rho \dot{\mathbf{q}}_{\mathbf{r}}^T \dot{\mathbf{q}}_{\mathbf{r}} C_L c dr \tag{III.5}$$

$$dD = \frac{1}{2}\rho \dot{\mathbf{q}}_{\mathbf{r}}^T \dot{\mathbf{q}}_{\mathbf{r}} C_D c dr$$

dL and dD are respectively orthogonal and parallel to the air velocity $\mathbf{u}$. From Equation (III.5):

- ρ is the air density.
- $\dot{\mathbf{q}}_{\mathbf{r}}$ is the velocity vector evaluated at the stage $\mathbf{r}$. Considering the blade modeled as a rigid body, $\dot{\mathbf{q}}_{\mathbf{r}}$ is expressed as:

  $$\dot{\mathbf{q}}_{\mathbf{r}} = \Omega \hat{i}_3 \times \mathbf{r} + \dot{\beta}|\mathbf{r}|\hat{i}_3 + (u_1 \hat{i}_1 + u_2 \hat{i}_2 + u_3 \hat{i}_3) \tag{III.6}$$

  where $\dot{\beta}$ is the flapping velocity, which is defined as the time-derivative of the angle β shown in Figure III.2. $u_{1,2,3}$ are the components of the air velocity. In hovering flight, the air velocity is reduced to only the vertical contribution along $\hat{i}_3$, naming the inflow velocity u_i. If the point resides on an axis parallel to $\hat{i}_1$, then:

  $$\dot{\mathbf{q}}_{\mathbf{r}} = \Omega|\mathbf{r}|\hat{i}_2 + \dot{\beta}|\mathbf{r}|\hat{i}_3 + (u_1 \hat{i}_1 + u_2 \hat{i}_2 + u_3 \hat{i}_3) \tag{III.7}$$

- C_L and C_D are the aerodynamic coefficients; in general, they are tabular values for a given airfoil. Important for the evaluation of the total thrust produced by the rotating blades is the expression of the lift coefficient C_L. This contribution focuses on small angles of attack α and low values of the Mach number, such that a linear relation $C_L = a\alpha$ is guaranteed, with a representing the lift slope of the section, and $\alpha = \theta - \Phi$ (Figure III.2). θ and Φ are respectively the pitch and inflow angles of the section. More

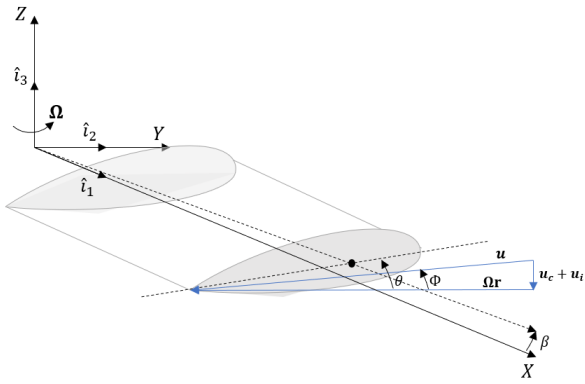

Figure III.2: Velocity vector and angles definition for a blade station at distance r from the hub rotating frame.

details about the derivation of Φ are given in Section *Uniform Inflow Model*.

- c indicates the chord of the blade at stage r.

In this work, the assumption of constant slope a and angle Φ for all the points of a given section is made. The elemental lift in Equation (III.5) can be rewritten as:

$$dL = \frac{1}{2}\rho \dot{\mathbf{q}}_{\mathbf{r}}^T \dot{\mathbf{q}}_{\mathbf{r}} a(\theta - \Phi) c dr \tag{III.8}$$

By integrating the elemental lift along the radius R, the total thrust produced by a rotor with b blades at time t is:

$$T = \frac{1}{2}\rho a b \Omega^2 \int_0^R c(\theta - \Phi) r^2 dr \tag{III.9}$$

Further details can be found in reference [35].

Uniform Inflow Model

In the previous section, the inflow velocity u_i was introduced. It indicates the contribution of the volume of air that is moved by the rotor on the blade velocity. An inflow model based on the BEM theory is used with the assumption of uniform distribution, which is an acceptable approximation for hovering or in general in quasi-steady flight conditions. The inflow velocity can thus be

written as:

$$u_i = \sqrt{\frac{T}{2\rho A}} \tag{III.10}$$

with $A = \pi R^2$ being rotor disk area. In the following, we will refer to the induced velocity as its dimensionless value $\lambda_i = \frac{u_i}{\Omega R}$. The sectional inflow angle becomes:

$$\Phi = \frac{u_i}{\Omega r} = \frac{\lambda_i}{x} \tag{III.11}$$

with $x = r/R$, i.e., the dimensionless spanwise position of the blade section. From Equation (III.10), it is clear that the value of the induced velocity is constantly updated depending on the value of the thrust produced at time t. Such dependence drops for a steady condition, but it is still important, for this work, to take into account time-dependent conditions, e.g., the transient regime from initial conditions to steady-state. Dynamic inflow models (e.g., Pitt–Peters, Peters–He [145]) are available, but they are not necessary in our estimation, as they mainly address very low frequency transients usually associated with flight dynamics, rather than vibrations. Since the thrust T depends on the inflow angle (Equation (III.9)), an implicit problem needs to be solved iteratively. Two numerical approaches are presented in the literature [107], based on fixed-point or Newton–Raphson iteration. The latter is used in this contribution for the aerodynamic solver. It is reported in the following because of its importance in understanding the full aerodynamic model and the Kalman estimation principle. Introducing μ as the dimensionless air velocity parallel to the rotor disk, i.e., $\mu = \frac{|\boldsymbol{u}|cos\alpha}{\Omega r}$ in the plane of rotation, the following implicit function is defined:

$$f(\lambda) = \lambda - \frac{C_T(\lambda)}{2\sqrt{\mu^2 + \lambda^2}} = 0 \tag{III.12}$$

with $\lambda = \mu \tan(\alpha) - \lambda_i$. C_T is the blade-loading coefficient or dimensionless thrust, defined as: $C_T = \frac{T}{\rho A(\Omega R)^2}$. Equation (III.12) is solved with the Newton–Raphson iteration scheme, and for small values of μ, the usage of the hover value as a first guess of λ, i.e., $\lambda_0 = \sqrt{\frac{C_T}{2}}$, generally allows it to converge with a limited number of iterations.

Kalman Filter for Implicit Scheme

This section aims to give an overview of the main principle of the Kalman filter (KF) and to understand how and in which formulation it can be applied to a DAE system—for instance, Equation (III.2). The filter operates on a state-space

form in two phases, i.e., prediction and correction. The model predicts the state in the next time instant and the same prediction is then corrected using the observations given as input to the algorithm at each time step. These two steps for a linear time invariant (LTI) system are translated in the state-space system:

$$\begin{cases} \dot{\mathbf{x}} = \mathbf{A}\mathbf{x} + \mathbf{B}\mathbf{p} \\ \mathbf{y} = \mathbf{C}\mathbf{x} + \mathbf{D}\mathbf{p} \end{cases} \tag{III.13}$$

where $\mathbf{x}$, $\mathbf{p}$ and $\mathbf{y}$ are respectively the state, input and observation vectors. $\mathbf{A}$ and $\mathbf{B}$ are matrices depending on the dynamics of the system; $\mathbf{C}$ and $\mathbf{D}$ depend on the nature of the observations. If the problem presents non-linearities, the system (III.13) becomes a set of non-linear implicit functions:

$$\begin{cases} \mathbf{h}(\mathbf{x}, \dot{\mathbf{x}}, \mathbf{p}) = \mathbf{0} \\ \mathbf{y} = \mathbf{k}(\mathbf{x}, \mathbf{p}) \end{cases} \tag{III.14}$$

This set of equations can be easily identified in the GGL form in Equation (III.2) of a multibody system, defining the following state vector and its time derivative:

$$\mathbf{x} = [\mathbf{q}, \mathbf{v}, \boldsymbol{\lambda}_s, \boldsymbol{\mu}_s]^T \tag{III.15}$$

$$\dot{\mathbf{x}} = [\dot{\mathbf{q}}, \dot{\mathbf{v}}, \dot{\boldsymbol{\lambda}}_{\boldsymbol{s}}, \dot{\boldsymbol{\mu}}_{\boldsymbol{s}}]^T \tag{III.16}$$

A mismatch between Equation (III.14) and Equation (III.2) can be observed because no information about the input vector $\mathbf{p}$ is included in the GGL set of equations. The dynamics of $\mathbf{p}$ should be added. Given the unknown nature of this entity in the estimation context, a good assumption is that of zeroth-order dynamics, i.e., zero time-derivative of $\mathbf{p}$, which leads to $\dot{\mathbf{p}} = \mathbf{0}$. This model has been widely adopted and validated in the literature [52, 150, 115, 129], and a clearer explanation will be provided in the following. In this contribution, the estimation process is performed in discrete-time domain, and thus the discretization of the continuous-time GGL formulation expressed in Equation (III.2) is needed. The multibody solver used in the present work executes this step by applying the implicit backward differentiation formulas (BDF) integration method [16]:

$$\dot{\mathbf{z}}_{k+1} = \sum_{j=0}^{s} \alpha_j \mathbf{z}_{k+j} \tag{III.17}$$

with s and α respectively as order and coefficients of the adopted BDF scheme, and z as a general variable with time derivative $\dot{z}$. Given the nature of the Kalman filter which estimates the states at time step $k+1$ from the estimated

quantity at the previous time step k, a first order integrator has been adopted. From Equation III.17, the first order integration of $\dot{\mathbf{x}}$ takes the form:

$$\dot{\mathbf{x}}_{k+1} = \alpha(\mathbf{x}_{k+1} - \mathbf{x}_k) \tag{III.18}$$

The discrete-time scheme of Equation (III.2) becomes:

$$\begin{cases} \dot{\mathbf{q}}_{k+1} - \mathbf{v}_{k+1} + \mathbf{B}(\mathbf{q}_{k+1})^T \boldsymbol{\mu}_{s,k+1} = \mathbf{0} \\ \mathbf{M}(\mathbf{q}_{k+1})\dot{\mathbf{v}}_{k+1} + \mathbf{f}(\mathbf{q}_{k+1}, \mathbf{v}_{k+1}) - \mathbf{B}(\mathbf{q}_{k+1})^T \boldsymbol{\lambda}_{s,k+1} = \mathbf{0} \\ \dot{\mathbf{p}}_{k+1} = \mathbf{0} \\ \mathbf{B}(\mathbf{q}_{k+1})\mathbf{v}_{k+1} = \mathbf{0} \\ \mathbf{g}(\mathbf{q}_{k+1}) = \mathbf{0} \end{cases} \tag{III.19}$$

in which the first-order time derivatives are evaluated at the time-step $k+1$ by applying Equation III.18. The zeroth-order input dynamic is also included in the third row of Equation III.18, where $\dot{\mathbf{p}} \in \mathbf{R}^p$ and p is the number of inputs. The final goal of this work is to estimate or predict jointly the state vectors $\mathbf{x}$ and $\dot{\mathbf{x}}$, and the external loads identified in $\mathbf{p}$, which will not be considered anymore as an input to the system, but another set of quantities to be estimated. This is the field of application of the augmented Kalman filter (AKF), which defines an augmented state vector $\mathbf{x_a}$ and its time-derivative:

$$\mathbf{x_a} = [\mathbf{q}, \mathbf{v}, \mathbf{p}, \boldsymbol{\lambda_s}, \boldsymbol{\mu_s}]^T \tag{III.20}$$

$$\dot{\mathbf{x}}_\mathbf{a} = [\dot{\mathbf{q}}, \dot{\mathbf{v}}, \dot{\mathbf{p}}, \dot{\boldsymbol{\lambda}}_\boldsymbol{s}, \dot{\boldsymbol{\mu}}_\boldsymbol{s}]^T \tag{III.21}$$

The filter estimates both variables; thus, a new vector is introduced: $\bar{\mathbf{x}}_\mathbf{a} = [\mathbf{x_a}^T, \dot{\mathbf{x}}_\mathbf{a}^T]^T$. An important feature of the AKF is that it considers the inaccuracies of model and observations, which are respectively identified in zero-mean Gaussian noise $\mathbf{w}_{\bar{x}_a}$ and $\mathbf{w}_y$. A covariance matrix associated with each noise vector is defined as $\mathbf{Q} = E\left[\mathbf{w}_{\bar{x}_a}\mathbf{w}_{\bar{x}_a}^T\right]$, $\mathbf{R} = E\left[\mathbf{w}_y\mathbf{w}_y^T\right]$.

At this stage, all the ingredients needed to apply the AKF to the DAE system have been described. The estimation process can be divided into the two following steps, shown in Figure III.3:

1. *Prediction*—integration of the equation of motion (III.19) by using the first-order BDF integrator scheme in Equation III.17.
2. *Correction*—updating of the solution of the previous step with the available observations $\mathbf{y}$:

$$\bar{\mathbf{x}}_\mathbf{a}{}^+_{k+1} = \bar{\mathbf{x}}_\mathbf{a}{}^-_{k+1} + \mathbf{K}_{k+1}(\mathbf{y}_{k+1} - \mathbf{k}(\bar{\mathbf{x}}_\mathbf{a}{}^-_{k+1})) \tag{III.22}$$

where $\mathbf{K}$ is the Kalman gain, obtained in the definition of the filter by minimizing the estimation covariance. Further details on the derivation

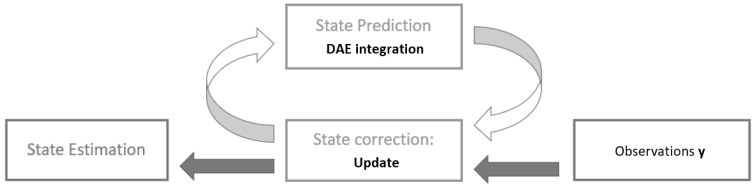

Figure III.3: Kalman filter scheme based on the prediction-correction principle.

of **K** and on the update of the covariance matrices during the estimation can be found in [164].

Workflow for Estimation of States and Loads on a Rotor Blade

In the previous section, all the methodologies needed to approach the estimation problem for a coupled multibody-aerodynamic rotating system have been presented. As stated in the introduction, and indicated in Equation (III.5), the aerodynamic loads are functions of the states of the system, and in particular of the velocity and orientation vector of the airfoil section where the aerodynamic contribution is evaluated. The estimation problem could thus be approached in two ways:

1. Writing the vector $\mathbf{p}$ in Equation (III.19) as a function of $\mathbf{q}$ and $\dot{\mathbf{q}}$, i.e., the orientation and velocity of a given point;
2. Modeling the aerodynamic forces as external loads without explicit dependence on the states.

Both options are feasible, depending on which problem we want to solve. In the first case, a simple KF can be applied, and only the state vector $\mathbf{x}$ is estimated. This option is feasible but can hardly reach high accuracy, particularly when a low-fidelity model is used. The second option is the case of the AKF; it is the most suitable option in the present cases, since it can compensate for modeling errors at the expense of the quality of the estimated loads. The question that arises is: how does this approach take into account the underlying aerodynamic model? In this case the aerodynamic model, coupled with the structural one, is needed only as a *reference case*. That means it allows the user to generate the data used as the input of the filter, i.e., the *observations*. Most importantly, the knowledge of the aerodynamic model, referring to the observations, is needed to post-process the estimation data and extract the correct aerodynamic loads.

The proposed approach is schematically shown in Figure III.4. It will be explained in the following through an example. Consider a blade discretized with two rigid bodies (Figure III.5) and *i)* modeled as indicated in the formulation of Section *Finite Segment Beam Formulation*, or *ii)* with aerodynamic loads acting at the application point of each body (usually at the quarter chord of the section). It is worth noticing that the distributed aerodynamic loads are evaluated on a more refined fictitious aerodynamic line (Figure III.5) or surface, and the equivalent aerodynamic loads L, D and M (namely lift, drag, and the pitch moment) are applied on the rigid bodies. If a flexible finite element blade is considered, a more complex approach is needed to reduce the aerodynamic forces distribution on the structural model; this represents a possible future development of the present work. The preparation of the estimation process can be summarized as:

- *Collection of measurements that make the system observable.* This is an important requirement for Kalman-based techniques. For load estimation, it more strictly translates into a number of position-level observations equal to or greater than the number of loads to be estimated [118, 129].
- *Definition of the set of loads.* This decision should be made in conjunction with the previous step. For multiple distributed loads, the definition of a subset of loads $\mathbf{p}$ could be useful to reduce the number of observations needed. For the case in Figure III.5, the full input vector is $\mathbf{p} = [L_1, D_1, M_1, L_2, D_2, M_2]$; a good choice could be the selection of loads close to the tip $\mathbf{p}_s = [L_2, D_2, M_2]$, because their contributions to the dynamics of the blade are higher.

The AKF will estimate the data $\mathbf{q}_1^+$, $\mathbf{v}_1^+$, $\mathbf{q}_2^+$, $\mathbf{v}_2^+$, together with the chosen subset of equivalent loads comprising the compensation of modeling errors $\mathbf{p}_s^+ = [L_2^+, D_2^+, M_2^+]$. The results of similar studies in other fields of application can be summarized as:

$$\mathbf{q}^+ = \mathbf{q} + \epsilon_q \tag{III.23}$$

$$\mathbf{v}^+ = \mathbf{v} + \epsilon_v \tag{III.24}$$

$$\mathbf{p}^+ = \mathbf{p} + \epsilon_p \tag{III.25}$$

with ϵ_q and ϵ_v at small and acceptable values, while ϵ_p assumes higher values as much as the modeling errors do. At this stage, the states at position and velocity level are accurate enough and can be re-used to evaluate the distributed lift contribution of Equation (III.5). Two steps are thus proposed:

- *Extrapolation of $\dot{\mathbf{q}}$ along the blade span.* The components of the velocity vector along the blade can be approximated as a linear function of the

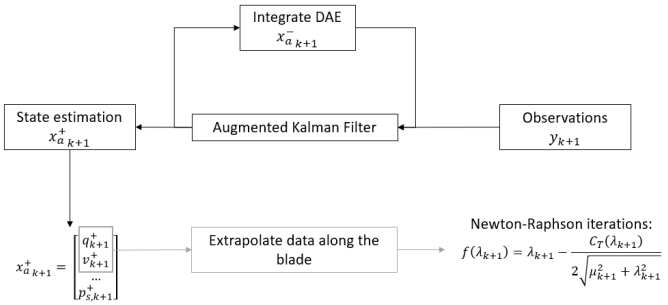

Figure III.4: Proposed workflow for distributed aerodynamic loads, based on Kalman filtering estimation.

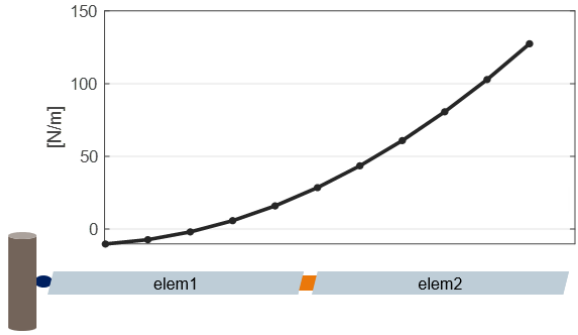

Figure III.5: Example of a blade discretized with 2 elements. The lift distribution per unit length is shown above.

position r:

$$\dot{q}(r)i_2 = \Omega r \tag{III.26}$$

$$\dot{q}(r)i_3 = \dot{\beta} r \tag{III.27}$$

- *Evaluation of the lift distribution along the blade span.* Recalling Equation (III.5), and given a certain flight condition with known pitch angle θ, the only unknown in the elemental lift will be the inflow angle ϕ:

  $$dL = dL(\lambda_i) \tag{III.28}$$

  The iterative process in Section III can thus be applied to find the exact value of λ_i at each time-step.

Table III.1: Blade and rotor features.

Blade Structural Properties			**Blade Elastic Properties**		
Total mass	82.76	kg	EA_{elem}	5.69E8	N
Chord	0.537	m	$EI_{yy,elem}$	4.00E5	Nm^2
Total Length	6.988	m	$EI_{zz,elem}$	4.00E5	Nm^2
Radius	7.420	m	GJ_{elem}	8.40E5	Nm^2/rad
Root hinges - distance from Hub			**Root hinges - elastic properties**		
Flap offset	0.289	m	Flap damping characteristic	7.50E3	Nms/rad
Lag offset	0.269	m	Lag damping characteristic	7.00E3	Nms/rad
Pitch offset	0.432	m			

Numerical Validation on a 2-Blade Rotor Model

This section presents a numerical example of the methodology presented in Section *Workflow for Estimation of States and Loads on a Rotor Blade* on a 2-blade rotor model. Python [1] multibody code with embedded aerodynamic force evaluation was used. Each blade was modeled as composed by four rigid bodies, connected through elastic elements with properties listed in Table III.1 and uniform chord. No twist angle was considered. Two different experiments were done:

- Noisy reference observation data generated in Python code by simulating the coupled structural-aerodynamic model. Estimation of a subset of lumped loads on the same structural model without aerodynamic and subsequent distributed load evaluations.
- Reference observation data generated in MBDyn on a similar, but independently-formulated structural-aerodynamic model. Estimation of a subset of lumped loads on the structural Python model and subsequent evaluation of distributed loads.

One flight condition is shown in this contribution for the two cases: rotational speed $\Omega = 60$ rpm and pitch angle $\theta = 3$ deg. The airfoil used in the aerodynamic solver was a symmetric NACA0012 profile. To reduce the complexity of the entire problem, in this initial work the hub was fixed to the ground. Gravity was also applied.

Kalman-Based Estimation

The estimation process first requires the collection of a set of observations/measurements to be used as reference data. In a real test case, this means that a

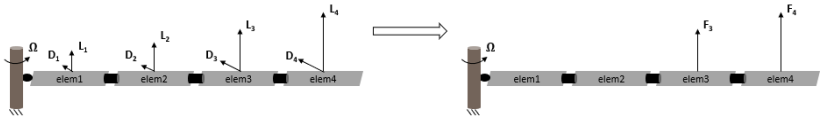

Figure III.6: A 4-element blade model with all aerodynamic forces (left) and a reduced set of significant forces (right).

sensor layout needs to be designed satisfying the observability conditions, which allows for a robust estimation. As stated in Section *Workflow for Estimation of States and Loads on a Rotor Blade*, the first step is thus the definition of which states in terms of modes, loads or parameters the user wants to estimate. The scope of the AKF is the estimation of the external loads $\mathbf{p}$, together with the states of the system. The normal modes of a structural dynamic model are all damped, resulting in an asymptotically stable system, a sufficient condition when the target is the estimation of the input loads. For further details on observability and stability requirements of the Kalman filter, refer to [118].

Considering a single blade as represented in Figure III.6, a total of eight equivalent loads L and D are defined in the model. If the NACA airfoil is not symmetric, the pitch moment for each element has to be added. As explained in Section *Kalman Filter for Implicit Scheme*, a number of position-level sensors equal to or greater than the number of loads to be estimated is needed. For two blades modeled as in Figure III.6, this means the usage of at least eight position sensors. If a more refined blade with a higher number of elements is modeled, the number of required sensors becomes unreasonable from a practical point of view, i.e., installation. As proposed in Section *Workflow for Estimation of States and Loads on a Rotor Blade*, a further simplification is adopted in this study by estimating a reduced set of loads acting on the most sensitive sections of the blade. Assuming that:

- The aerodynamic loads give higher contribution in the proximity of the blade tip;
- The in-plane loads are much smaller than the out-of-plane ones, namely, $L \gg D$,

then the selection falls on two generic forces acting on $elem3$ and $elem4$, as shown in Figure III.6. The subset of loads indicated as $\mathbf{p}_s$ will be: $\mathbf{p}_s = [F_3, F_4]^T$.

Reference Noisy Data

Starting from the above-mentioned assumptions, the sensors' layout in Table III.2 is defined. x, y and z are the directions in the fixed reference

Table III.2: Sensor layout.

Position sensors		**Velocity sensors**	
elem3	z	elem3	z
elem4	z	elem4	z

frame. The selection was performed considering the forces modeled on *elem3* and *elem4* and thus the sensors were located on the same elements because they were considered to be more sensitive. Moreover, two velocity sensors were also included in order to capture the flapping motion. For a more complex system, an observability study is needed and it will be the focus of further development of this work. Starting from this layout, a coupled multibody-aerodynamic simulation was performed and position/velocity sensor data were stored by applying additive white Gaussian noise, which defines the covariance matrix $\mathbf{R}$. The missing information was on the model covariance $\mathbf{Q}$. In previous work [52, 150], a higher source of uncertainties was considered on the load states, such that $\mathbf{Q}_p \gg \mathbf{Q}_x$. This was a valuable assumption, since we can assume that the model used was accurate enough, but no information on the external loads is available. The zeroth-order input model in the discrete time formulation will be read as:

$$\mathbf{p}_{k+1} = \mathbf{p}_k + \mathbf{w}_p \tag{III.29}$$

with $\mathbf{w}_p$ Gaussian noise associated with vector $\mathbf{p}$, an important tuning parameter of the filter [52, 150].

The results of the estimation can be observed in Figures III.7 and III.8 showing respectively the estimation of the states used as sensors and some of the unmeasured states along the blade. A good identification of the out-of-plane quantities is obtained, because the used sensors guarantee the observability of the flapping mode. Some delay in the time-histories of the in-plane estimation was instead observed, because of two assumptions made at the beginning:

- The sensor layout does not include in-plane quantities, e.g. position sensors in $y-$direction.
- Only out-of-plane loads are considered in the estimation, even if the reference sensors come from a coupled multibody-aerodynamic simulation which includes lift and drag forces. The choice to not estimate the drag forces was because the resulting magnitude would be comparatively small with respect to the computed lift.

These modeling errors were, however, compensated by the filter on the estimated loads shown in Figure III.9. The real aerodynamic loads L_3 and L_4 evaluated in

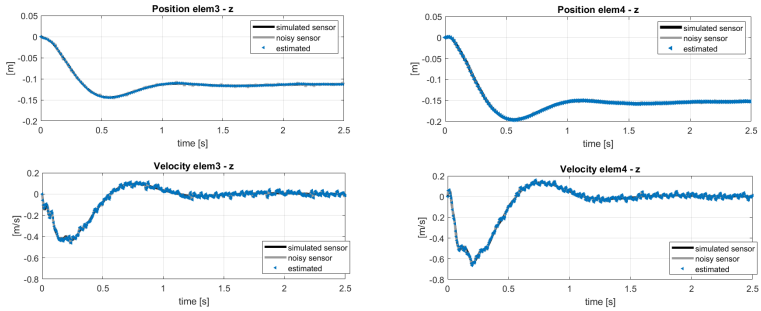

Figure III.7: Estimation of the states used as sensors. Reference noisy data.

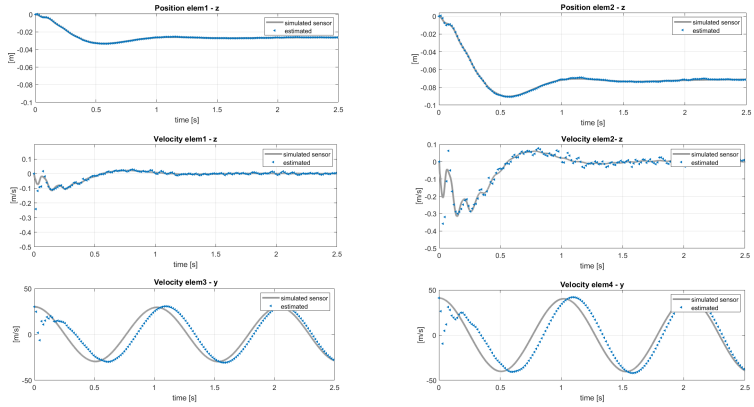

Figure III.8: Estimation of the unmeasured velocity and position entities with reference to the sensor layout in Table III.2. Reference noisy data.

the simulation were compared with the estimated quantities F_3 and F_4, which showed mean values that did not match the reference ones. The good results to be considered are the ones on the states in Figure III.8. At this point, the approach proposed in Section *Workflow for Estimation of States and Loads on a Rotor Blade* and shown in Figure III.4 could be executed. Performing an interpolation of the states $\dot{q}_y$ and $\dot{q}_z$ in order to extrapolate data on 11 points along the blade and applying the iterative Newton–Raphson method for inflow evaluation, the distributed lift field can be reconstructed. The results in terms of lift and angle of attack reached at the steady-state condition are shown in Figure III.10. The absolute error, defined as the absolute value of the difference between simulated and estimated data, i.e., $err = |y_s - y_e|$, is shown in Figure III.11.

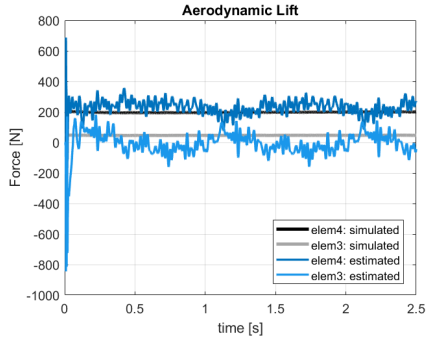

Figure III.9: Force estimation on *elem3* and *elem4* with reference to the sensor layout in Table III.2. Reference noisy data.

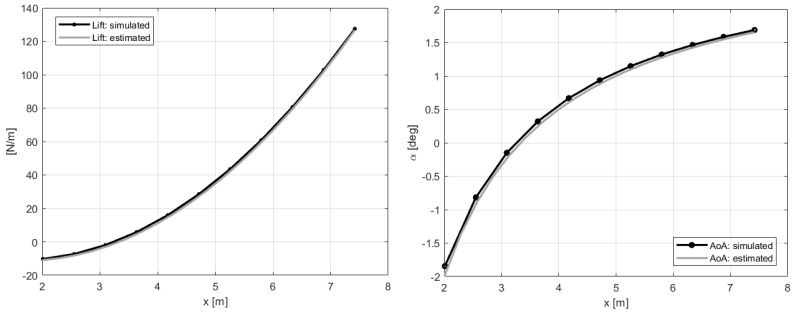

Figure III.10: Distributed lift and angle of attack along the aerodynamic span in steady-state, with 11 points of integration. Reference noisy data used in the estimation.

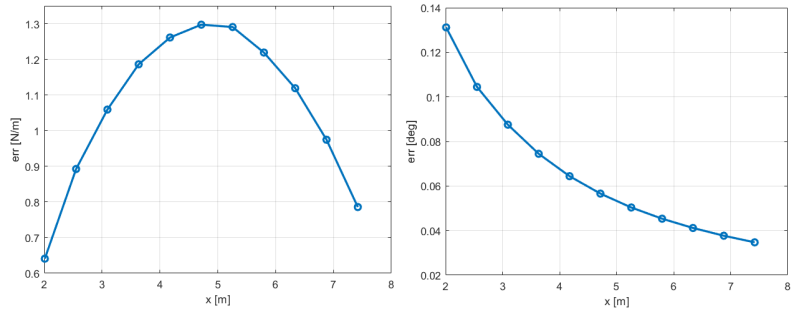

Figure III.11: Absolute error of distributed lift and angle of attack—reference data in Figure III.10.

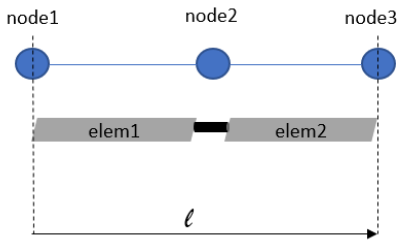

Figure III.12: Graphic comparison between finite segment and finite volume modeling of a flexible element of free-length l.

Reference Data from Mbdyn

In this section, the same analyses presented in Section *Reference Noisy Data* are performed. The difference is in the reference data used, which, in this case, were generated from MBDyn. The scope of this analysis is to further demonstrate the usability of the KF for a rotating blade, using data from an independent model as a different source of uncertainty. In the previous section, the uncertainty was introduced by adding noise on the reference data. In this case, the uncertainty is instead in the reference model itself, which presents a different formulation/modeling with respect to the one adopted in the Python solver. This framework is similar to a real test-case, where the numerical model usually cannot be perfectly correlated with the real one.

The discrepancies encountered in the blade multibody modeling are in the finite segment formulation, which, for the MBDyn software, is replaced by the finite volume formulation [73]: the flexible beam element connects three nodes, i.e., bodies, and the internal forces are evaluated in well-chosen points between the two endpoints. Details can be found in the referenced paper. The different modeling also translates in a mismatch of mass distribution along the blade. A sketch of the two approaches for one flexible element of free-length l is shown in Figure III.12. The relationship between rigid bodies and flexible elements is:

- Finite segment: $n_{bodies} = 2(n_{flex} - 1)$;
- Finite volume: $n_{bodies} = 2n_{flex} + 1$.

In the finite segment approach, two bodies are present in the length l; for the finite volume approach, three bodies are instead modeled. The total mass is the same for both formulations but a different distribution is observed. The reference blade in MBDyn has been modeled with the same properties listed in Table III.1, seven rigid bodies and three flexible elements. This discretization was arbitrarily chosen, preserving the same number of flexible element used

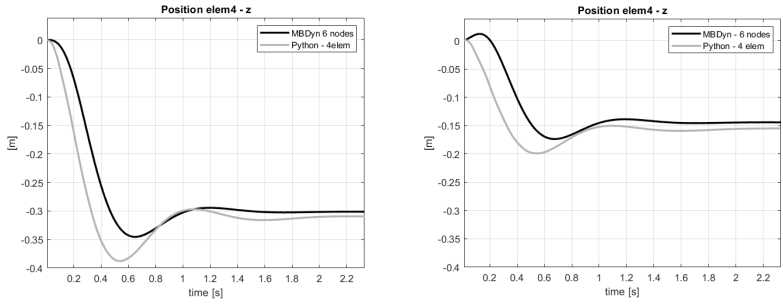

(a) (b)

Figure III.13: Comparison of vertical displacement at *elem4* position *a*) without and *b*) with aerodynamics. The model is in rotation and under gravity.

in the Python model. A comparison between the two models can be found in Figure III.13a, which shows the vertical displacement evaluated at the same position of *elem*4 for both models, under gravity (applied gradually) and in rotating conditions. In Figure III.13b, the same comparison is shown but also aerodynamic loads were used. The errors for the steady value are around 3% and 7%, and the transient regime shows a slightly different dynamic behavior. Here, the scope of the application of the AKF is to compensate these modeling errors identified in a different response of the blade elements. The results of the same analysis performed in the previous section, with the sensor layout in Table III.2, are shown in terms of estimated sensors and states in Figure III.14 and Figure III.15. In this case, the filter cannot compensate for both modeling and force errors and this is observed on the velocities in the y direction in Figure III.15: these quantities should be the same in the two models, because the in-plane velocity is almost equal to Ωr for each position r along the blade span. By applying the post-processing iterative method for inflow evaluation, the distributed aerodynamic lift was obtained and shown in Figure III.16 with the corresponding absolute error. The mismatch between the reference lift and the estimated one increases going from the root to the tip, because of its sensitivity to the in-plane velocity. In order to increase the accuracy of the estimation, a different sensor layout can be employed, including in-plane information of the blade, as listed in Table III.3. With this set of sensors, the in-plane velocity can be correctly estimated and the results on *elem*3 and *elem*4 are shown in Figure III.17.

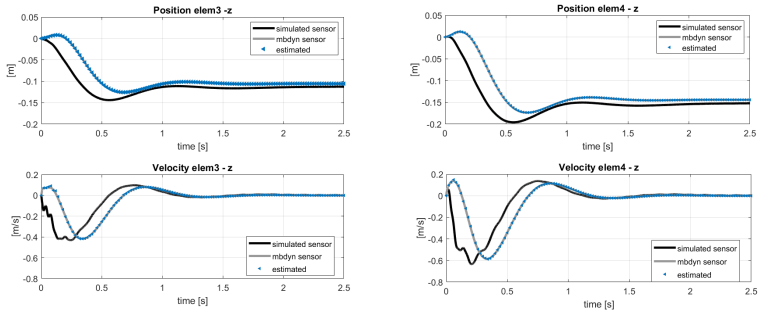

Figure III.14: Estimation of the states used as sensors. Reference data from MBDyn.

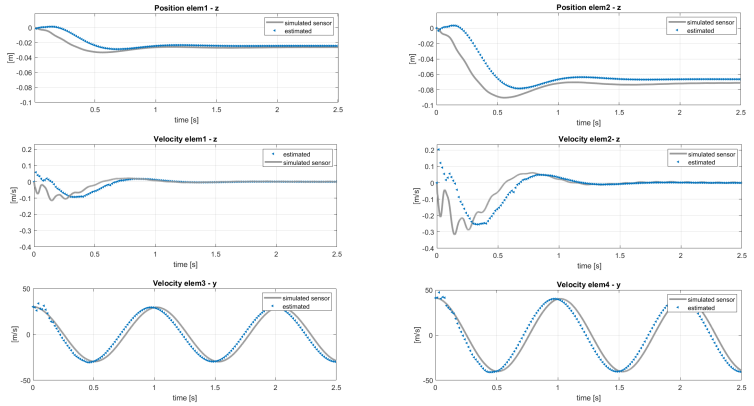

Figure III.15: Estimation of the unmeasured velocity and position entities with reference to the sensor layout in Table III.2. Reference data from MBDyn.

Table III.3: Sensors layout.

Position sensors		**Velocity sensors**	
elem3	z	elem3	z
elem4	z	elem4	z
elem4	y		

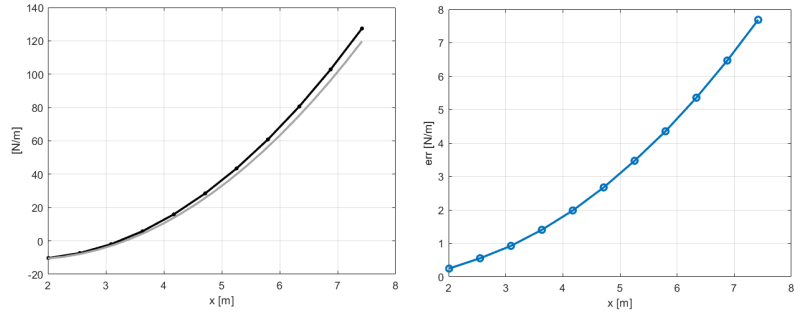

Figure III.16: Distributed lift along the aerodynamic span in steady-state (left) and absolute error (right), with 11 points of integration. Reference data from MBDyn.

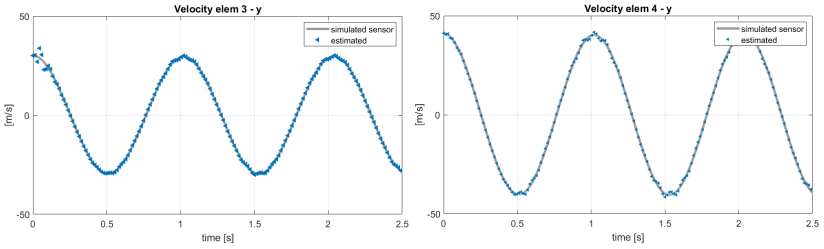

Figure III.17: Estimation of the velocities of *elem3* and *elem4* with reference to the sensor layout in Table III.3. Reference data from MBDyn.

Conclusions

In this paper, the problem of identifying states and aerodynamic loads on a rotating helicopter blade is addressed. A well-known and validated Kalman-based approach is proposed, as it has never been used before for this purpose in the rotorcraft field. A multibody articulated rotor with two blades is developed based on the finite segment theory, and a steady aerodynamic condition is considered with a uniform inflow model from the blade element momentum theory. One of the advantages of the Kalman filtering technique is in the usage of a reduced set of sensors which guarantee the observability of the system, or more specifically, of the estimated quantities. Although a thorough observability study has not been carried out because of the simplified model, the efficiency of the Kalman filter estimation has been proven by using simulated noisy sensors and reference data generated in MBDyn, independent multibody simulation software. Both cases have confirmed the conclusions made in previous work:

when some modeling errors are present, e.g., structural properties or load location, all the uncertainties are compensated in the load estimation while still providing an accurate state reproduction. This is a great advantage of the Kalman filter in the augmented formulation over other techniques cited in the literature, reducing the need for highly accurate models, which are highly time-consuming to use, especially in the rotorcraft field. In the specific case of quasi-steady aerodynamic loads, the formulation of lift and drag is easily expressed in terms of the system states. Given a set of available sensor data, the proposed approach addressed the identification problem by modeling the aerodynamic loads as general external forces, while aiming to reach high accuracy only on states at position and velocity-level. This is already an advantage, because no aerodynamic evaluation is needed during the estimation. From the knowledge of the estimated states at each time step, an extrapolation of the velocity field data is proposed and the distributed lift will preserve only the dependence from the inflow velocity. At this stage, an implicit function can be iteratively solved. Velocity and position sensors are not feasible in a real test case, but the intent of the authors was to investigate the usage of other sensors, e.g., strain, and validate the presented work on experimental data. This research aims also to extend the proposed approach on a more complex system, by employing a flexible finite element blade model. In that case, the selection of the reduced set of loads will become a challenge in the estimation process.

Author Contributions: Investigation, data curation and writing, R.C.; conceptualization and methodology, R.C, T.T. and P.J.; supervision, T.T., W.D. and P.M. All authors have read and agreed to the published version of the manuscript.

Funding: This research was funded by VLAIO (Flemish Innovation and Entrepreneurship) through its Baekeland Mandate project SINCRO (a general strategy for load and parameter identification for helicopter main rotor system), number HBC.2018.2086.

Conflicts of Interest: The authors declare no conflict of interest.

Publication IV

Recursive parameter estimation for the on-line monitoring of delamination growth in composite structures

Published in Structural Health Monitoring 0(0) (2024) 1-20
DOI: 10.1177/14759217241299057

Recursive parameter estimation for the on-line monitoring of delamination growth in composite structures

Roberta Cumbo[1,2], Daniel De Gregoriis[3], Federico Danzi[1], Abhishek Kumar[1], Frank Naets[2,4]

[1] *Leonardo S.p.A., Lab of Materials Technologies, Via Tiburtina km 12.400, Rome, 00156 RM, Italy*
[2] *KU Leuven, Department of Mechanical Engineering, Celestijnenlaan 300 B, B-3001 Heverlee, Belgium*
[3] *Siemens Industry Software NV, Interleuvenlaan 68, B-3001 Leuven, Belgium*
[4] *E2E Core lab, Flanders Make, 3001 Leuven, Belgium*

Abstract

One of the main failure phenomena on composite materials is the delamination, which consists in the progressive separation of plies. The augmented scheme of the Extended Kalman Filter is tested in this contribution for the delamination growth monitoring. In particular, a novel recursive estimation for parameter identification is proposed within the joint input-parameter scheme and it allows a reduction of the number of physical sensor data needed. The proposed methodology enables full-field response reconstruction, interface stiffness degradation monitoring and critical load identification. The methodology is validated on simulated and experimental data of a carbon fiber Double Cantilever Beam.

Keywords: Delamination growth, Composite materials, Damage monitoring, Kalman Filter, Input-Parameter estimation

Introduction

Nowadays, laminated composites are widely used in primary and secondary structural components in aerospace industries. The failure and instability of composite materials are difficult to predict and occur due to several phenomena, including delamination, which can drastically lead to a reduction of the mechanical performances of the component. Delamination is a local phenomenon and its monitoring during operation is extremely challenging. Despite the extensive work presented in literature on Optimal Sensor Placement (OSP) [139, 171, 62] for Structural Health Monitoring (SHM), a robust approach to select an optimal map of sensors for delamination growth monitoring during operation is not yet available due to the complexity of the phenomenon. Indeed, the exact location of damage is often unpredictable and the resulting high concentration of stresses and non-linear effects make the design of a monitoring system much more complicated. Different kinds of SHM techniques applied to composite structures have been explored in the recent literature and can be identified and classified into two main groups: model-based and sensor-based. Model-based methods undertake simulation data and compare the model with experimental signals in frequency or time-domain or even as modal parameters [203, 128]. The main disadvantage of these methods is the requirement for prior knowledge from high-fidelity nonlinear Finite Element Model (FEM) simulations or complex analytical solutions. In this case, model validation is expensive in terms of computation and experiments since local damage information can be mainly identified at high frequencies and this requires high model accuracy. The usage of models in these cases is thus challenging. To overcome this limitation, sensor-based methods can be considered to detect damage by comparing response signals with baseline measurements [103]. Most of the recent studies presented in literature on SHM for composite materials focus on sensor technologies for online structural monitoring, e.g. piezoelectric materials and sensors [183, 93, 4] and Fiber Bragg Gratings (FBGs) [173, 141, 104], in contrast to standard Non Destructive Test (NDT) [74] approaches which are usually employed by industries as offline damage monitoring. With the advance of Machine Learning (ML) in the field of structural mechanics and composite materials, several data-driven and physics-informed architectures have also been proposed [47, 181, 87, 86] to solve the inverse identification problem from time-series data and frequency shifts in sensor signals. By summarizing the state-of-the-art regarding SHM for delamination growth monitoring, the following main limitations in the implementation of such techniques at industrial-scale level can be identified:

- Limited works are presented in literature regarding the study of optimal sensors placement for the identification and monitoring of local effects;

- Artificial Intelligence (AI)-based methodologies outperform other techniques because of their ease of implementation as these require only sensor data. However, the need for training data is the most obvious limitation, especially in the field of composite structures where uncertainties play an important role;
- Model-based approaches are of limited usage due to the required level of accuracy in FE modelling;
- Limited focus on the identification of critical loads causing failure in composite laminates.

This contribution proposes an estimation approach that relies on a trade-off between the amount of sensor data and level of accuracy of the FE model to perform inverse system identification for delamination growth monitoring. A well-known approach is the Kalman Filter (KF) which has been widely used for structural mechanical applications for the online identification of full-field response, external loads and physical parameters [52, 150, 39, 129]. Moreover, Optimal Sensor Placement (OSP) techniques for KFs have been developed to ensure an optimal estimation by employing a reduced set of sensors [50]. When going towards FE modelling, a common approach is to reduce the computational cost by using Model Order Reduction (MOR) techniques. However, it is important to underline that the implementation of MOR in KF requires some form of training data, depending on the nature of the system:

- *Linear systems*: FE model calibration/validation in the frequency domain of interest which allows a direct eigenvalue analysis to compute the reduction basis;
- *Parametric or nonlinear systems*: FE model calibration/ validation within the full range of parameters/nonlinearities. Parametric Model Order Reduction (pMOR) can be employed requiring a training scenario. [89, 13, 199]

The Proper Orthogonal Decomposition (POD) method is one of the most used and efficient approaches to calculate a reduction basis for nonlinear systems [26]. The main advantage of POD is that it employs on linear matrix operations, projecting the nonlinear system onto a subspace that allows to preserve the nonlinear dynamics. Moreover, POD is computationally efficient when compared to other pMOR techniques [26]. The main principle of the POD is in the selection of the meaningful shapes or modes of the solution corresponding to the full range of the parameter space. This contribution employs the POD method for the computation of the global reduction basis, starting from the concatenation of local bases. Each of the latter corresponds to the eigenvalue solution of the linearized model being evaluated for the sampled parameter values. The

delamination can be associated to a local degradation of stiffness parameters of the model. The delamination curve is thus sampled and the corresponding linear models constitute the training scenario of the pMOR. This approach has the advantage that it avoids simulation of a nonlinear FE model which is computationally expensive and requires a complex formulation. Therefore, in this work a less time-consuming workflow for the on-line monitoring of delamination growth in composite materials is proposed by embedding pMOR into the KF, as demonstrated in literature [39] for an isotropic structure. Moreover, a novel recursive parameter estimation is proposed which allows to further reduce: i) the computational cost associated to an increase of the number of estimated parameters and, ii) the number of sensors required to guarantee system observability. Some of the limitations mentioned above are thus addressed. A unidirectional carbon fiber Double Cantilever Beam (DCB) specimen is tested under static loading to validate the methodology using both simulated and experimental data. The target estimation quantities are the delamination growth, i.e. decreasing of the interface stiffness, as well as the critical loads.

The motivations behind this work and research contributions are summarized as follows:

- To the authors' best knowledge, the employment of Kalman-based techniques for the online monitoring of delamination growth in composite materials is not yet addressed in literature. Preventing failure in composite structures is not trivial and a robust solution for operational life is still missing from literature. The work presented in this paper for the monitoring of delamination growth in a small specimen is a first step towards the application of Kalman-based methods in the field of composite materials.
- The applicability of a Kalman-based solution allows for the online detection and monitoring of delamination during flight conditions, which therefore allows to reduce maintenance costs and downtime due to manual inspections.
- The Kalman filter estimation problem becomes intractable when the number of unknowns is too high, as it consequently requires a high number of sensors and therefore the computational cost increases substantially. This article presents a novel recursive parameter estimation approach that embeds parametric model order reduction, which allows the applicability of Kalman-based techniques for the estimation of high dimensional parameter spaces. Even though the approach is demonstrated for the estimation of delamination growth monitoring, it can be applied and generalized to other fields as well, including the extension to multiple load estimation.

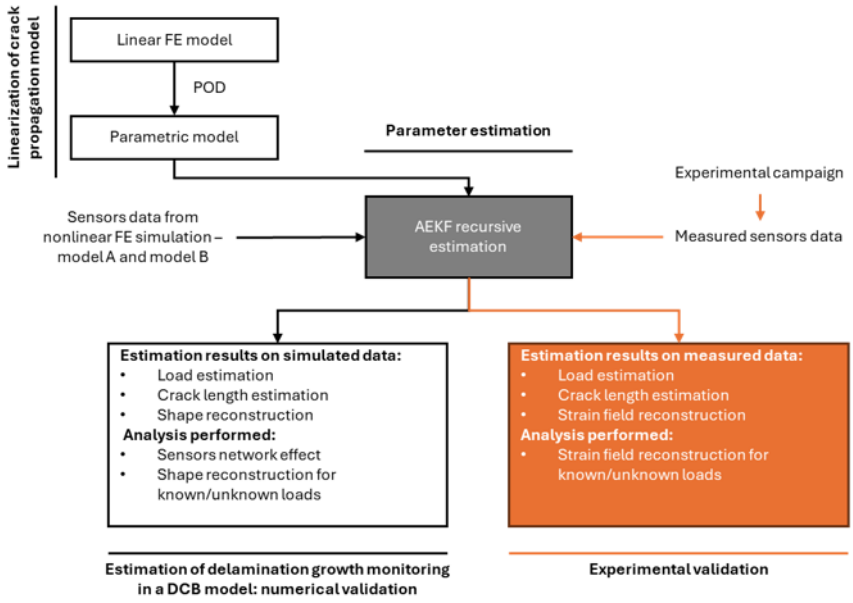

Figure IV.1: Flowchart of the paper structure.

The remainder of this paper is structured as follows and illustrated in the flowchart in Fig.IV.1: *Section 2* describes the linearized parametric FE model and the pMOR methodology, *Section 3* presents the Augmented Extended Kalman Filter (AEKF) recursive parameter estimation, *Section 4* validates the estimation workflow with simulated data and studies the optimal number of sensors, *Section 5* includes the experimental validation using a real DCB specimen instrumented with strain-gauges sensors and finally, *Section 6* discusses concluding remarks and future developments of the presented methodology for industrial level applications.

Linearization of the crack propagation model

The mode-I interlaminar fracture toughness of a Carbon Fiber Reinforced Plastic (CFRP) composite laminate is generally determined by testing a DCB specimen, in compliance with the EN 6033 [161] standard. The test is performed as shown in Fig. IV.2: the two arms, i.e. cantilever beams, are pulled apart by applying a tip displacement in opposite direction and in quasi-static conditions. The initial crack present in the specimen will propagate along the specimen span until the sample breaks or the maximum displacement is reached. Fig. IV.3 shows a

schematical overview of the progressive propagation of the delamination in a DCB sample using a bi-linear interface cohesive law [143]:

$$\begin{cases} \tau = K_c\delta, & D = 0 \\ \tau = (1-D)K_c\delta, & D = \frac{\delta_f(\delta-\delta_c)}{\delta(\delta_f-\delta_c)} \\ \tau = 0, & D = 1 \end{cases} \tag{IV.1}$$

where τ and δ are the normal stress and displacement, respectively, K_c is the interface stiffness, δ_c and δ_f are respectively the critical and the final interface displacements and D is the damage variable. Once the critical stress in the first (virtual) interface element is reached - *point 1 shown in Fig. IV.3* - the crack starts to propagate and all the elements in the process zone move to the softening region. Each elemental stress in the process zone lies on the $\tau - \delta$ curve, which is representative of the cohesive law of the normal opening mode I. The following significant points can be identified: i) general element A ahead of the crack tip shows a zero stiffness associated to the separation of the two arms in that point ($D = 1$); ii) element A' is the current crack tip approaching the zero stiffness ($D = 1$); iii) segment $A' - B$ is the fracture process zone where the linear-elastic behavior is exceeded and a gradual decreasing of the elemental stiffness is observed from point B to point A', iv) the segment O-B where the elements exhibit a linear elastic behaviour ($D = 0$). Considering this representation of the crack and its relative fracture process zone, it turns out that each generic point of the $F - d$ curve of the DCB coupons can be represented by an equivalent linear elastic model as presented by Dimitri et al. [54]. The FE model consists of two linear beams connected with interface elements as node-to-node springs. The springs from the specimen root to point B are characterized by very high stiffness values, relative to the overall model, i.e. $1.0e^6 \frac{N}{mm}$, to represent the perfect bonding amount between the two coupon arms.

Parametric model

Given a linear elastic FE [202] model with n_d number of Degrees of Freedom (DoFs), the equations of motion describing the system dynamics excited by the input load vector $\mathbf{u}(t) \in R^{n_u}$, can be formulated as:

$$\mathbf{M}\ddot{\mathbf{z}}(t) + \mathbf{C}\dot{\mathbf{z}}(t) + \mathbf{K}\mathbf{z}(t) = \mathbf{B}\mathbf{u}(t) \tag{IV.2}$$

where $\mathbf{M} \in \mathbb{R}^{n_d \times n_d}$, $\mathbf{C} \in \mathbb{R}^{n_d \times n_d}$, $\mathbf{K} \in \mathbb{R}^{n_d \times n_d}$ are respectively the mass, damping and stiffness matrices of the system, $\mathbf{B} \in \mathbb{R}^{n_d \times n_u}$ is the Boolean input shape matrix that distributes the inputs, i.e. loads, over the DoFs of the system, $\mathbf{z}(t) \in \mathbb{R}^{n_d}$ is the vector of DoFs while $\ddot{\mathbf{z}}(t) \in \mathbb{R}^{n_d}$ and $\dot{\mathbf{z}}(t) \in \mathbb{R}^{n_d}$ are the second and first time-derivative of $\mathbf{z}(t)$. By considering two linear 2D shell elements

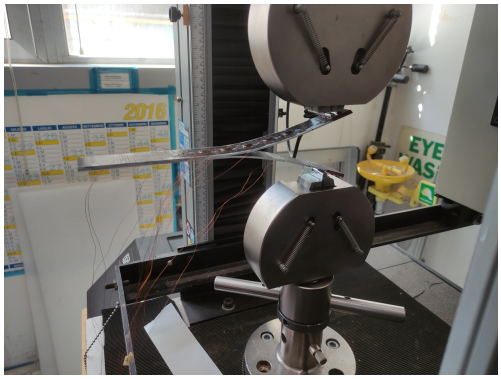

Figure IV.2: Experimental DCB setup.

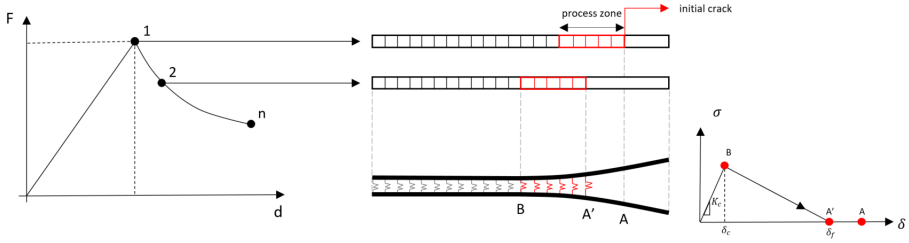

Figure IV.3: Schematic representation of the progressive delamination in a DCB model using a bi-linear cohesive law.

connected with node-to-node springs (Fig. IV.4), the FE stiffness matrix $\mathbf{K}$ can be parameterized with respect to the nodal spring stiffness parameter k_s as follows:

$$\mathbf{K} = \mathbf{K}(k_s) = \begin{bmatrix} \mathbf{K}_{el}^{d=x,y,r_x,r_y} & \mathbf{K}_{el,C} \\ \mathbf{K}_{el,C} & \mathbf{K}_{el}^{d=z} + k_s \bar{\mathbf{K}} \end{bmatrix} \tag{IV.3}$$

where $\mathbf{K}_{el}^{d=x,y,r_x,r_y}$ is the elastic stiffness matrix of the FE model without the translational DoF z corresponding to the vertical displacement of the nodes where the springs are applied. Five DoFs for each node are considered for the shell elements [202] employed in the FE models used in this work. The nodal elastic contribution corresponding to DoF z is denoted as $\mathbf{K}_{el}^{d=z}$ and $\bar{\mathbf{K}}$ can be organized as follows:

$$\bar{\mathbf{K}} = \begin{bmatrix} \mathbf{I}^{4\times4} & -\mathbf{I}^{4\times4} \\ -\mathbf{I}^{4\times4} & \mathbf{I}^{4\times4} \end{bmatrix} \tag{IV.4}$$

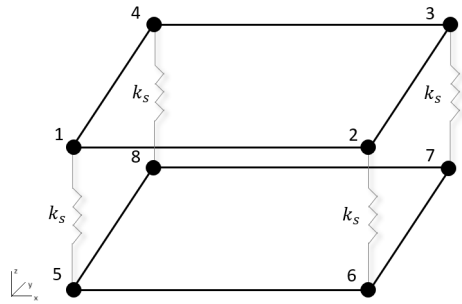

Figure IV.4: Shell elements with node-to-node springs.

Here, $\mathbf{K}_{el,C}$ is the coupled stiffness matrix between DoFs and $\mathbf{I}^{4\times4}$ is the 4×4 identity matrix. When dealing with large FE models, a Reduced Order Model (ROM) is defined by projecting the Full Order Model (FOM) on a subspace, with $\mathbf{q} \in \mathbb{R}^{n_r}$ the vector of reduced DoFs, such that $n_r << n_d$. The $\mathbf{z}$ vector can be approximated as follows:

$$\mathbf{z} \simeq \mathbf{\Phi_g q} \tag{IV.5}$$

where $\mathbf{\Phi_g} \in \mathbb{R}^{n_d \times n_r}$ is a global reduction basis that spans the parameter space of interest [26]. By projecting Eq. IV.2 onto the subspace spanned by $\mathbf{\Phi_g}$, the following equations of motion for the reduced model are obtained:

$$\mathbf{M_r}\ddot{\mathbf{q}}(t) + \mathbf{C_r}\dot{\mathbf{q}}(t) + \mathbf{K_r}\mathbf{q}(t) = \mathbf{B_r}\mathbf{u}(t), \tag{IV.6}$$

$$\mathbf{M_r} = \mathbf{\Phi_g}^T\mathbf{M}\mathbf{\Phi_g}, \mathbf{M_r} \in \mathbb{R}^{n_r \times n_r}$$

$$\mathbf{K_r} = \mathbf{\Phi_g}^T\mathbf{K}\mathbf{\Phi_g}, \mathbf{K_r} \in \mathbb{R}^{n_r \times n_r}$$

$$\mathbf{C_r} = \mathbf{\Phi_g}^T\mathbf{C}\mathbf{\Phi_g}, \mathbf{C_r} \in \mathbb{R}^{n_r \times n_r}$$

$$\mathbf{B_r} = \mathbf{\Phi_g}^T\mathbf{B}, \mathbf{B_r} \in \mathbb{R}^{n_r \times n_u}$$

where $\mathbf{M_r} \in \mathbb{R}^{n_r \times n_r}$, $\mathbf{C_r} \in \mathbb{R}^{n_r \times n_r}$, $\mathbf{K_r} \in \mathbb{R}^{n_r \times n_r}$, $\mathbf{B_r} \in \mathbb{R}^{n_r \times n_u}$ are the reduced mass, damping, stiffness and input matrices respectively.

Reduction basis

This contribution employs the POD method to compute the reduction basis of the parametric Reduced Order Model (pROM). The main principle of the POD

is to find a global reduction basis $\mathbf{\Phi_g}$, spanning the full parameter subspace of interest, by selecting the meaningful shapes or modes of the solution provided by local reduction bases $\mathbf{\Phi_l}$. In the specific case of DCB model (Fig. IV.3), local bases are computed by solving the linear eigenvalue problem of the corresponding sub-system $l = 1, ..., n$ laying on the $F - d$ curve. The number of samples is equal to the number of discretized elements in the interface. Each sample differs from the next one by removing progressively one spring element, such that:

$$n_s^l = n_s^{l+1} + n_n \tag{IV.7}$$

where n_s^l is the number of springs in the l-th model and n_n is the number of nodes along the width of the model.

The most common ways to compute $\mathbf{\Phi_g}$ are by interpolating or concatenating local POD bases $\mathbf{\Phi_l}$ obtained for each sample [26]. When the number of samples is limited, the concatenation approach is preferred. Given a set of n concatenated local subspace bases, the Singular Value Decomposition (SVD) is computed in order to remove possible linear dependencies among all the subspaces, as follows:

$$\mathbf{U\Sigma W} = [\mathbf{\Phi_1}\ \mathbf{\Phi_2}\ \mathbf{\Phi_3}\ \dots\ \mathbf{\Phi_n}] \tag{IV.8}$$

where $\mathbf{U}$ and $\mathbf{W}$ are the left and right singular vectors, while $\mathbf{\Sigma}$ is a diagonal matrix of singular values. The global reduction basis $\mathbf{\Phi_g}$ of the parametric system is identified by selecting the first r-left singular vectors, such that the following minimization problem is reached:

$$\min \|\mathbf{z} - \mathbf{\Phi_g q}\|_2 \tag{IV.9}$$

The number of selected values depends on the threshold criterion. A typical approach is to truncate the singular values such that [26]:

$$\frac{\sum_{i=1}^{r} \sigma_i^2}{\sum_{i=1}^{n_{sv}} \sigma_i^2} \geq 0.999 \tag{IV.10}$$

where n_{sv} is the number of total singular values σ_i.

Parameter estimation

The estimation of stiffness degradation in fracture process zone of the DCB model is here addressed by using the Augmented Extended Kalman Filter (AEKF) [150, 39, 164]. This choice is justified by the following rationale:

- The Augmented Kalman FIlter (AKF) concurrently estimates the system states, external loads and parameters. As part of its formulation, physical

coupling is preserved and leveraged to obtain optimal estimates of the system states, external loads and parameters. In general, this approach is also more computationally efficient and robust than e.g. the Dual Kalman Filter (DKF) [19].

- The extended formulation, i.e. Extended Kalman Filter (EKF), is an extension of KF for nonlinear or parametric systems by performing model linearization. Other formulations, e.g. Unscented Kalman Filter (UKF) [2], can be adopted when model linearization is not applicable. These approaches however do come at an increased computational cost, as they require the evaluation of so-called sample points per iteration step, whereas the EKF only requires a single evaluation per iteration step. Furthermore, constraint handling is typically more challenging, as the sampling approach has to be modified accordingly. Enforcing constraints within the EKF does not require these extensive modifications.

The AEKF scheme uses the dynamic system equations, i.e. equations of motion, in a state-space formulation as follows:

$$\begin{cases} \dot{\mathbf{x}}^*(t) = \mathbf{A}^*(\mathbf{x}^*)\mathbf{x}^*(t) + \mathbf{B}^*_{kn}\mathbf{u}_{kn}(t) \\ \mathbf{y}(t) = \mathbf{H}\mathbf{x}^*(t) \end{cases} \tag{IV.11}$$

where $\mathbf{x}^*(t)$ is the augmented state vector, i.e. $\mathbf{x}^*(t) = [\mathbf{q}^T \dot{\mathbf{q}}^T \mathbf{u}^T_{ukn} \mathbf{p}^T]^T \in \mathbb{R}^{2n_r + n_{u_{ukn}} + n_p}$ with $n_{u_{ukn}}$ and n_p respectively the number of unknown loads and physical parameters to be estimated. The lattest is defined by the number of submodels included in the pROM. The vector of known input loads is denoted as $\mathbf{u}_{kn}$. The second equation in Eq. IV.11 describes the measurement evolution in time $\mathbf{y}(t)$. The dynamic model of $\mathbf{u}_{ukn}$ and $\mathbf{p}$ has to be defined. Both quantities are described in this contribution as zero-th order random walk models [39, 129, 115]:

$$\dot{\mathbf{u}}_{ukn}(t) = \mathbf{0} + \mathbf{w}_u(t) \tag{IV.12}$$

$$\dot{\mathbf{p}} = \mathbf{0} + \mathbf{w}_p(t)$$

where $\mathbf{w}_u$ and $\mathbf{w}_p$ are white Gaussian noise terms.
In Eq. IV.11, the state matrix $\mathbf{A}^*$ is function of the augmented state $\mathbf{x}^*$ by defining a parametric dependency of the system. The parametric form of the $\mathbf{A}^*$ with respect to parameter vector $\mathbf{p} = [k_s^{l=1\dots n}]$ is defined as follows:

$$\mathbf{A}^*(\mathbf{x}^*) = \begin{bmatrix} \mathbf{0} & \mathbf{I} & \mathbf{0} & \mathbf{0} \\ -\mathbf{M_r}^{-1}\mathbf{K_r}(\mathbf{p}) & -\mathbf{M_r}^{-1}\mathbf{C_r}(\mathbf{p}) & -\mathbf{M_r}^{-1}\mathbf{B_{r,ukn}} & \mathbf{0} \\ \mathbf{0} & \mathbf{0} & \mathbf{0} & \mathbf{0} \\ \mathbf{0} & \mathbf{0} & \mathbf{0} & \mathbf{0} \end{bmatrix} \tag{IV.13}$$

where proportional damping is assumed, i.e. $\mathbf{C_r}(\mathbf{p}) = \alpha \mathbf{K_r}(\mathbf{p})$. The DCB model shows a nonlinear degradation behavior at the interface, thus the extended formulation of the KF should be employed. The EKF needs the system linearization to propagate the state error covariance. Considering a first order explicit Euler integrator scheme, the discretized form of the equations of motion becomes:

$$\mathbf{g}(\mathbf{x}^*_{k+1}, \mathbf{x}^*_k, \mathbf{u}_{kn,k}) = \mathbf{x}^*_{k+1} - (\mathbf{I} + \Delta t \mathbf{A}^*(\mathbf{x}^*_k))\mathbf{x}^*_k - \Delta t \mathbf{B}^*_{kn}\mathbf{u}_{kn,k} = 0 \tag{IV.14}$$

where Δt is the discrete time step. The linearization of Eq. IV.14 around the states $\mathbf{x}^{*,0}_{k+1}$, $\mathbf{x}^{*,0}_k$, truncated at the first order with Taylor expansion is:

$$\begin{aligned}\mathbf{g}(\mathbf{x}^*_{k+1}, \mathbf{x}^*_k) \simeq \mathbf{g}(\mathbf{x}^{*,0}_{k+1}, \mathbf{x}^{*,0}_k) + \mathbf{I}(\mathbf{x}^*_{k+1} - \mathbf{x}^{*,0}_{k+1}) + \\ - (\mathbf{I} + \Delta t \frac{\delta \mathbf{A}^*(\mathbf{x}^*_k)}{\delta \mathbf{x}^*_k}\mathbf{x}^*_k + \Delta t \mathbf{A}^*(\mathbf{x}^*_k))(\mathbf{x}^*_k - \mathbf{x}^{*,0}_k)\end{aligned} \tag{IV.15}$$

Resulting in:

$$\mathbf{x}^*_{k+1} = (\mathbf{I} + \Delta t \frac{\delta \mathbf{A}^*(\mathbf{x}^*_k)}{\delta \mathbf{x}^*_k}\mathbf{x}^*_k + \Delta t \mathbf{A}^*(\mathbf{x}^*_k))\mathbf{x}^*_k + \mathbf{B}^*_{kn}\mathbf{u}_{kn,k} = \mathbf{F}^*_k \mathbf{x}^*_k + \mathbf{B}^*_{kn}\mathbf{u}_{kn,k} \tag{IV.16}$$

where:

$$\frac{\delta \mathbf{A}^*(x^*_k)}{\delta \mathbf{x}^*_k} = \begin{bmatrix} \mathbf{0} & \mathbf{0} & \mathbf{0} & \mathbf{0} \\ \mathbf{0} & \mathbf{0} & \mathbf{0} & -\mathbf{M}_r^{-1}(1+\alpha)\frac{\delta \mathbf{K}_r(p)}{\delta \mathbf{p}} \\ \mathbf{0} & \mathbf{0} & \mathbf{0} & \mathbf{0} \\ \mathbf{0} & \mathbf{0} & \mathbf{0} & \mathbf{0} \end{bmatrix} \tag{IV.17}$$

Finally, the time-discrete formulation of the equations of motion is:

$$\begin{cases} \mathbf{g}(\mathbf{x}^*_{k+1}, \mathbf{x}^*_k) = \mathbf{w}_k \\ \mathbf{y}_{k+1} = \mathbf{H}\mathbf{x}^*_{k+1} + \mathbf{v}_k \end{cases} \tag{IV.18}$$

Vectors $\mathbf{w}$ and $\mathbf{v}$ are mutually uncorrelated Gaussian variables, and represent process and measurement noise, respectively. They are included in the equations of motion to take into account model and measurement uncertainties with the associated covariance matrices $\mathbf{Q}$ and $\mathbf{R}$, respectively. Both covariance matrices are diagonal and their values drive the estimation performances [52, 39]. Within this work, the highest uncertainty is attributed to the parameters $\mathbf{p}$ and the unknown loads $\mathbf{u}_{ukn}$. The AEKF for joint state-input-parameter estimation is explained in Algorithm 3, where: $\mathbf{x}^{*-}_k$ is the a-priori state estimation at time

step k which is obtained from the numerical model of the system, $\mathbf{F}^*$ is the transition matrix of Eq. IV.16, $\mathbf{K}_k$ is the Kalman gain, $\mathbf{c}_k$ is the correction step and $\mathbf{P}_k^-$, $\mathbf{P}_k^+$ are the prior and posterior state covariance.

Algorithm 3 AEKF, state-input-parameter estimation algorithm

Initialization $\mathbf{x}_0^{*-}$, $\mathbf{P}_0^+$, $\mathbf{Q}$, $\mathbf{R}$
for $k = 1 : N_t$ **do**
Prediction
  $\mathbf{g}(\mathbf{x}_k^{*-}, \mathbf{x}_{k-1}^{*+}) = \mathbf{0}$
  $\mathbf{P}_k^- = \mathbf{F}_k^* \mathbf{P}_{k-1}^+ \mathbf{F}_k^{*T} + \mathbf{Q}$
Correction
  $\mathbf{K}_k = \mathbf{P}_k^- \mathbf{H}^T (\mathbf{H}\mathbf{P}_k^- \mathbf{H}^T)^{-1} + \mathbf{R}$
  $\mathbf{P}_k^+ = (\mathbf{I} - \mathbf{K}_k \mathbf{H}) \mathbf{P}_k^-$
  $\mathbf{c}_k = \mathbf{K}_k (\mathbf{y}_k - \mathbf{H}\mathbf{x}_k^{*-})$
  $\mathbf{x}_k^{*+} = \mathbf{x}_k^{*-} + \mathbf{c}_k$
end

A modified version of the AEKF is proposed in this contribution with Algorithm 4 for delamination growth monitoring, by including:

- a correction step with constrained parameter values;
- recursive estimation assuming embedded distribution of parameter values.

These two points are further explained in the following sections.

Modelling limitations in the correction term

The delamination growth monitoring consists of the estimation of stiffness degradation at the interface. The FE model of the DCB is initialized with very high stiffness $p_0 = k_s$ values associated with the interface spring elements (Fig. IV.3). During the estimation, each element p^l of the stiffness parameter vector $\mathbf{p}$ is constrained within the correction steps as follows:

- $|p_k^{l,-} + c_k^{p^l}| \leq |\bar{p}|$: at each time step, the predicted parameter value should not exceed the threshold parameter $\bar{p} = -p_0$ value imposed by the baseline FE model
- $(p_k^{l,-} + c_k^{p^l}) \leq 0$: the estimation always returns stiffness degradation. This means that a negative value is always added to the system. A positive value would mean an increase of stiffness with respect to the baseline model, which is a non-physical solution.

Recursive parameter estimation

The number of parameters n_p estimated for a DCB model is equal to the number of elements modelled at the interface. The simultaneous estimation of a high number of states is computationally expensive and requires a high number of sensors to fulfill the system observability requirements [52, 129, 175]. For this reason, a recursive estimation approach is proposed in this contribution which effectively relaxes, and therefore reduces, the required number of sensors. This means that the model parametrization itself is dynamic: depending on the crack propagation, a different set of interface stiffness elements is updated. At time step $k = 0$, only $p^{l=1}$ is estimated. Once $p^{l=1}$ reaches the threshold value $\bar{p}$, the stiffness matrix is updated. At a generic time step k:

$$\mathbf{K}(\mathbf{p}_k) = \mathbf{K}(p_k^{l=i}, p_k^{l=[1:i-1]} = \bar{p}, p_k^{l=i+1,..n_s} = p_0) \tag{IV.19}$$

When the l-th elemental interface stiffness is zero, i.e. $p_k^l = p_0 + \bar{p}$, the delamination is propagating.
This recursive approach assumes that the stiffness degradation in each spring element occurs gradually as a ramp function (Fig. IV.5) until reaching the target value. The velocity at which the elements are degrading is driven by the parametric dependency adopted in the estimation. This assumption does not allow stiffness distribution at the interface, that is the case for materials with very low fracture toughness G_{IC}. In a more generic condition, the delamination involves a process zone with its stiffness distribution. To guarantee a more physical workflow, a distribution function is thus proposed among the n_{pz} elements modelled in the process zone length. By considering the l-th element $p^l = p^m$, i.e. the master parameter, and the vector of parameters $\mathbf{p}_{pz} \in \mathbb{R}^{n_{pz}}$ along the beam span, the following relation exists:

$$\mathbf{p}_{pz} = \mathbf{B}_p p^m \tag{IV.20}$$

where $\mathbf{B}_p \in \mathbb{R}^{n_{pz}}$ is a vector with weight coefficients β^l, which allows to distribute the master parameter value to the slave nodes in the process zone. Fig. IV.5 shows an example of estimation by considering a recursive distributed estimation over $n_{pz} = 3$ elements. The estimation is still recursive on the master parameter but the estimated value is distributed over the next n_{pz} parameters via the weights. Line 20 of Algorithm 4 indicates that the switch from l-th to $(l+1)$-th parameter is possible when $|p^l|$ falls in the range $[0.9 - 1]\bar{p}$. The lower limit could require tuning, because it could happen that the filter will not reach a 'perfect' estimated value, i.e. $|p_k^{l,+}| = |\bar{p}|$.

System observability

One of the requirements of the KF estimation is to have a set of measurements which guarantees the observability of the system. Extensive explanation has

Algorithm 4 EKF for recursive estimation

Initialization $\mathbf{x}_0^{*-}$, $\mathbf{P}_0^{+}$, $\mathbf{Q}$, $\mathbf{R}$ with $n_p = 1$, $l = 1$
for $k = 1 : N_t$ **do**
Prediction
$\mathbf{K}_k = \mathbf{K}_{el}^0 + \sum_{i=l-1, l\neq 1}^{l} \bar{p}\bar{\mathbf{K}}_i + \sum_{i=1}^{n_{pz}} \beta_i p_{l_{k-1}} \bar{\mathbf{K}}_{l+i-1}$
$\frac{\delta \mathbf{A}^*(\mathbf{x}_{k-1}^*)}{\delta \mathbf{x}_{k-1}^*} = \begin{bmatrix} \mathbf{0} & \mathbf{0} & \mathbf{0} & \mathbf{0} \\ \mathbf{0} & \mathbf{0} & \mathbf{0} & -\mathbf{M}_r^{-1}(1+\alpha)\sum_{i=1}^{n_{pz}} \beta_i \bar{\mathbf{K}}_{l+i-1} \\ \mathbf{0} & \mathbf{0} & \mathbf{0} & \mathbf{0} \\ \mathbf{0} & \mathbf{0} & \mathbf{0} & \mathbf{0} \end{bmatrix}$
Update $\mathbf{A}^*(x_{k-1}^*)$, $\mathbf{F}_k^*$
$\mathbf{g}(\mathbf{x}_k^{*-}, \mathbf{x}_{k-1}^{*+}) = \mathbf{0}$
$\mathbf{P}_k^- = \mathbf{F}_k^* \mathbf{P}_{k-1}^+ \mathbf{F}_k^{*T} + \mathbf{Q}$
Correction
$\mathbf{K}_k = \mathbf{P}_k^- \mathbf{H}^T (\mathbf{H}\mathbf{P}_k^- \mathbf{H}^T)^{-1} + \mathbf{R}$
$\mathbf{P}_k^+ = (\mathbf{I} - \mathbf{K}_k \mathbf{H})\mathbf{P}_k^-$
$\mathbf{c}_k = \mathbf{K}_k(\mathbf{y}_k - \mathbf{H}\mathbf{x}_k^{*-})$
for $\mathbf{q}_k^-, \dot{\mathbf{q}}_k^-, \mathbf{u}_{ukn_k}^-$ **in** $\mathbf{x}_k^{*-}$ **do**
$\mathbf{q}_k^+ = \mathbf{q}_k^- + \mathbf{c}_{q_k}$
$\dot{\mathbf{q}}_k^+ = \dot{\mathbf{q}}_k^- + \mathbf{c}_{\dot{q}_k}$
$\mathbf{u}_{ukn_k}^+ = \mathbf{u}_{ukn_k}^- + \mathbf{c}_{q_k}$
for $p_k^{l,-}$ **in** $\mathbf{x}_k^{*-}$ **do**
if $|p_k^{l,-} + c_k^{p_l}| \leq |\bar{p}|$ **and** $(p_k^- + c_k^{p_l}) \leq 0$ **do**
$p_k^+ = p_k^- + c_k^{p_l}$
else do
$p_k^+ = p_{k-1}^+$
if $|p_k^{l,+}| \leq |\bar{p}|$ **and** $|p_k^{l,+}| \geq 0.9|\bar{p}|$ **do**
$l = l + 1$
end

been presented in [39] for parametric systems. Considering only position-level measurements and the stiffness parametrization of Eq. IV.3, the following major conclusions are summarized here:

- Stiffness parameters can not be estimated in a static condition if no known loads are applied;
- The system is unobservable in static conditions as well for the joint, i.e. concurrent, parameter and input estimation if no known loads are applied.

These considerations are further addressed in the numerical/experimental validation sections below.

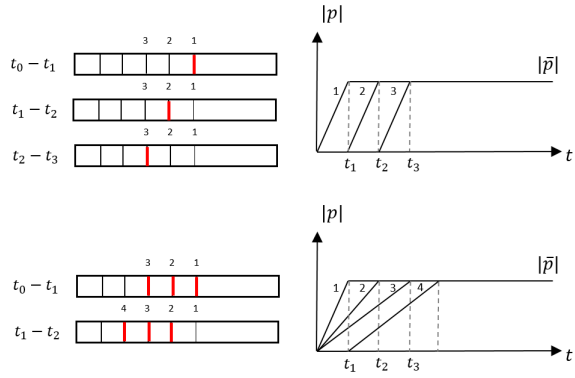

Figure IV.5: Recursive parameter estimation without (top) and with (bottom) distribution.

Estimation of delamination growth in a DCB model: numerical validation

A numerical validation is presented in this section in order to validate the proposed recursive parameter estimation approach. In particular, the following studies are addressed:

- Performances of crack propagation estimation via AEKF parameter and joint parameter/input schemes with respect to the number of measurements;
- Effect of prior knowledge of process zone length included in the distributed estimation of parameters.

Two DCB models are considered: the nonlinear FE model for reference simulated data and its linear counterpart (Fig. IV.6). Both models are 25 mm wide, 120 mm long, 3 mm thick and the pre-crack length is 38 mm. The two arms are zero degree unidirectional laminates whose material properties are summarized in Table IV.1. Two sets of cohesive properties have been considered and are listed in Table IV.2. The lower value of Mode I interlaminar fracture toughness G_{IC} is representative of a brittle interface that promotes a quick crack propagation with limited process zone. Contrarily, a high G_{IC} value means that high loading is required to propagate damage and a longer process zone is involved. The different process zone lengths resulting from the nonlinear analysis are used to identify the number of physical parameters involved in the distributed estimation.

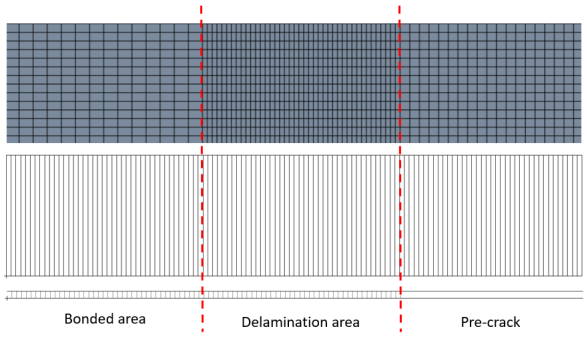

Figure IV.6: Nonlinear (top) and linear (bottom) meshes with node-to-node spring interface.

Table IV.1: Orthotropic material parameters.

E_{xx}	157000.0 MPa
E_{yy}	8500.0 MPa
E_{zz}	8500.0 MPa
ν_{xy}	0.35
ν_{yz}	0.35
ν_{xz}	0.53
G_{xy}	4200.0 MPa
G_{yz}	2700.0 MPa
G_{xz}	4200.0 MPa

The nonlinear model consists of hexahedral elements, connected with zero-thickness interface cohesive elements. The minimum cohesive element length is 1 mm. The bi-linear cohesive law is defined at the interface. The model is solved using an implicit integrator. The obtained reaction force versus opening displacement is shown in Fig. IV.7 for the two cohesive models.

The linear model employed in the KF scheme (Fig. IV.6) consists of shell elements. The span-wise mesh size is 1 mm, in accordance with the element length in the delamination area used in the nonlinear simulation. The two beams are connected through node-to-node spring elements connecting the z DoFs, as shown in Fig. IV.4. The number of DoFs in the linear model is $n_d = 2880$. Despite the advantages of using a simplified FE model with shell elements, some modelling issues could arise:

1. *Boundary conditions at the crack tip*: the two arms ahead the crack can deform in the axial direction and allow small rotations. Shell elements do

Table IV.2: Cohesive parameters.

Model A	
G_{IC}	$1.8\ kJ/m^2$
σ_n	$6.0MPa$
δ_n	$0.6mm$
n_{pz}	$7(7mm)$
Model B	
G_{IC}	$0.36\ kJ/m^2$
σ_n	$6.0MPa$
δ_n	$0.12mm$
n_{pz}	$4(4mm)$

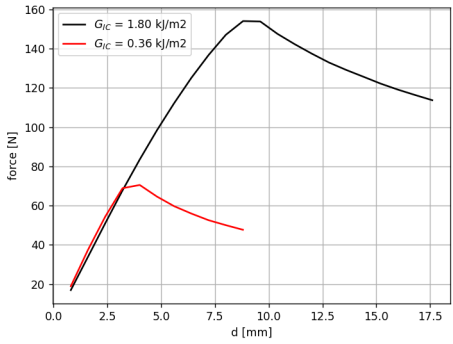

Figure IV.7: Force versus displacement curve for the two values of G_{IC}.

not capture this effect, which is however allowed in a FE model that has been meshed through the thickness, i.e. beam cross section. The effect of boundary conditions has been presented in [124] where different nodal constraints are investigated. The model with shell elements connected with node-to-node springs results to be the most accurate to predict delamination and it is considered in this work for the computation of the pROM.

2. *Rotational bending effects and shear deformations*: in [166], the delamination growth in a DCB specimen has been investigated analytically with Euler Bernoulli (EB) and Timoshenko theories. The work highlights that a loss of accuracy is observed for brittle materials if no rotational bending effects and shear deformations are considered. The employed model takes into account these effects.

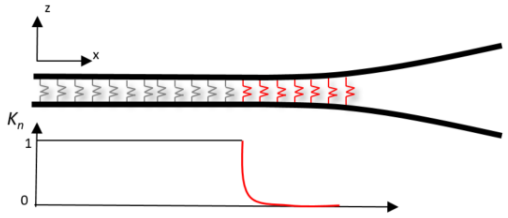

Figure IV.8: Interface stiffness law in the process zone. K_n normalized spring stiffness.

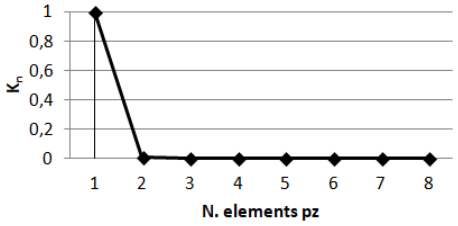

Figure IV.9: Normalized stiffness distribution in the process zone of the nonlinear model with cohesive elements.

Fig. IV.10 shows the crack propagation for model A and model B and compares the data obtained from the nonlinear simulation with data retrieved from the EB theory for each pair of force - displacement values. The comparison shows that the EB theory diverges from the nonlinear curve when the linear behavior is not followed anymore (Fig. IV.7) and it under-estimates the final crack length value of 20%. This effect appears earlier during the simulation for model A since a longer process zone is involved and thus the boundary conditions at the crack tip have a greater impact on the bending arm behavior. A static analysis has been performed by applying the maximum reaction force on the linear shell model in the following situations (Fig. IV.8):

- Node-to-node springs applied at the interface elements connecting the z-direction. The interface stiffness distribution in the process zone resulting from the nonlinear simulation with cohesive elements has been applied (Fig. IV.9);
- Constrained r_y DoF, i.e. bending, of first undamaged nodes (point B in the Fig. IV.3) at the interface, in addition to conditions specified in the previous point.

Table IV.3 compares the tip displacement of the upper arm obtained with the

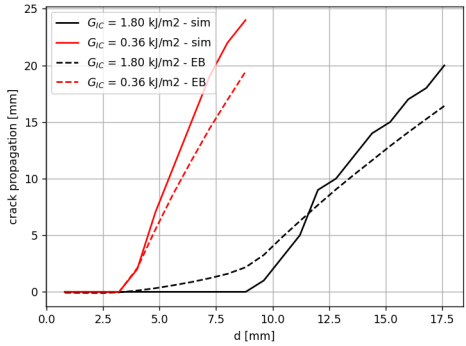

Figure IV.10: Crack propagation of model A and model B. Comparison between simulated curves and data retrieved from EB theory.

different boundary conditions. The node-to-node spring model without any local rotational constraints results to be more flexible, as also validated in [124]. Constraining r_y DoF would require more laborious modelling during estimation. Indeed, a recursive approach regarding the constraints of the undamaged nodes should be elaborated, considering that those nodes change during delamination propagation. For this reason, a simpler model, i.e. node-to-node springs, is considered in this contribution and the effect of modelling errors on the estimation are further investigated.

Table IV.3: Tip displacement. Effect of boundary conditions.

	$d[mm]$	$\%err$
Cohesive model	4.78	
Springs	5.40	13.0
Springs + $(r_y = 0)$	4.66	2.5

Parameter space

As explained in Sec. *Reduction basis*, the parametric space characterized by a set of linear models, by means of sequentially removing a sectional spring. The number of models to be included in the PROM scheme is defined by the crack propagation length in the nonlinear simulation analysis (Fig. IV.10). A total of $n = 25$ models is chosen. For each model, the local reduction basis is defined by the first bending mode and 4 static modes, i.e. residual attachment modes [46]. These modes allow to have an exact representation of the static response of the structure for a given input location. In this case, each of the

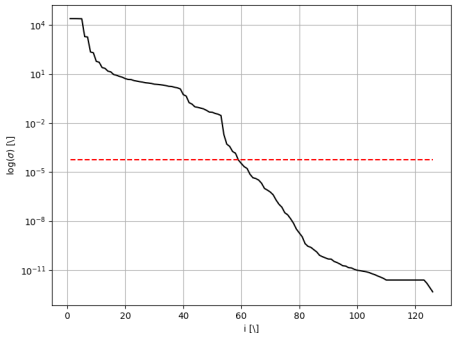

Figure IV.11: Singular Value Decomposition of parametric png basis. Red line: threshold value.

static modes corresponds to the vertical DoF of the 4 nodes at the tip of the two arms, where the forces are applied to pull both arms. Only 1 normal mode is considered as only quasi-static analyses are investigated in this work. For fatigue analysis, more normal modes should be considered within the frequency range of interest. Ideally, a more refined study on the parametric space should be performed by sampling the local distribution at the interface as in Fig. IV.5. However, this study is out of the scope of this work and the chosen parameter samples are considered adequate to allow sufficient accuracy of the interpolation over the full parameter space. The SVs of the concatenated basis are shown in Fig. IV.11 as well as the adopted threshold value. The final global reduction basis has dimension $r = 59$.

Results

The current section aims to validate the recursive estimation algorithm for crack growth monitoring in composite materials. As a first step, displacement sensor data has been generated from the linear FE model by applying constant pull-forces at the tip of the two arms and artificially removing 3 springs at the interface after a fixed time window. The results of the estimation are shown in Fig. IV.12 with $n_{pz} = 3$ and $\mathbf{B}_{pz} = [111]^T$. Furthermore, 22 displacement measurements are considered, equally distributed between the top and bottom laminae. The results show a perfect estimation of the parameter degradation and reconstruction of displacement field, which therefore appears to validate the proposed recursive estimation approach. Good levels of accuracy are also obtained locally at the boundary conditions of the beam after sequential removal of springs. In the following, the estimation results on the two DCB models with interface properties in Table IV.2 are shown.

Sensors networks

A brief study about the optimal sensor network is proposed in this section to guarantee the system observability as described in Sec. *System observability*. Model A is considered in this section, but the obtained results also be generalized to model B. The loads are assumed to be known, thus the reaction forces obtained by the nonlinear DCB simulation are applied to the linear model. The parameter n_{pz} has been fixed equal to the number of elements in the process zone of the nonlinear analysis (Table IV.2). Fig. IV.13 shows the interface stiffness, i.e. $\bar{K}_c = (1-D)K_c = \tau/\delta$, in the span-wise direction. The process zone of model A involves approximately 7 mesh elements, thus $n_{pz} = 7$, and a linear distribution of parameters is assumed. Different sensor networks have been tested within this section. The scope is to start from a distributed map of sensors, equally spaced along the span of the top arm and symmetrically applied to the bottom one, and to gradually remove some sensors to evaluate the resulting loss of accuracy. The considered number of displacement sensors on the top lamina are 14, 7 and 3, distributed between $0.6L$ and $1.0L$, starting from the root of the arms. Another analysis has been performed by considering only a tip displacement sensor on the top and bottom arms. Fig. IV.14 shows the crack length estimation and the shape reconstruction corresponding to a generic crack a greater than the critical value a_c. Fig.IV.15 shows the estimation error on the displacement field computed as:

$$\mathbf{err}(a) = \sum_{i=1}^{N_m} |\mathbf{y}(a)_{sim} - \mathbf{y}(a)_{est}| \tag{IV.21}$$

where $\mathbf{y}(a)_{sim} \in \mathbb{R}^{N_m}$ and $\mathbf{y}(a)_{est} \in \mathbb{R}^{N_m}$ are the full-field N_m simulated and estimated displacements in vertical direction. The estimated crack starts to propagate earlier compared to what is expected from the EB solution in Fig. IV.10. This can be partially explained by the initial noise on the estimation process as well as the modelling errors, i.e. lack of rotational constraints in the translational $z-$DoF springs and linear stiffness distribution assumed at the interface. As discussed in previous works [52, 150, 39], the estimator compensates here for the modelling errors in order to match the measurements. This error compensation can be explained by looking at the crack length obtained with 1 sensor: once the model reaches the critical reaction force, the stiffness distributions in the process zone of the reference and the linear models are as shown in Fig. IV.14. The reference model is shown to be much more flexible as the stiffness within the process zone is very low when compared to the assumed linear distribution where the crack tip is assumed to be at the same element. Thus, the filter estimates the same trend of crack propagation of the reference model but with a crack tip shifted towards the root, in order to match the measured tip displacement. Even if the stiffness in the first element of the

estimated process zone, i.e. $n = 7$ in Fig. IV.16, is lower than the limit value assumed in the model, i.e. $K = 10^6 N/mm$, its value is still sufficiently high to converge to a quasi-fixed boundary condition on the translational DoF. The reason why the estimation with 7 sensors returns lower accuracy is because the estimator is constrained to behave more similarly to the inverse solution of EB theory, as shown in Fig. IV.10, as it needs to match more distributed measurements. Indeed, the trend is the same as observed in Fig. IV.10, but shifted by about 3mm. The effect of a different stiffness distribution law in the process zone is quantified for the joint input/parameter estimation case by comparing the linear distribution with the one shown in Fig. IV.9.

Unknown loads: joint input/parameter estimation

The analyses performed so far consider the external loads to be known. The critical loads leading damage propagation are often unmeasurable during operation. The joint input/parameter estimation is tested here on the DCB model using the proposed recursive approach. Given the symmetry of the model, a single load is estimated and equally, i.e. symmetrically, distributed between top and bottom laminae as follows:

$$\mathbf{B}_{ukn}\mathbf{u}_{ukn}(t) = \begin{bmatrix} 0 & \dots & 1 & \dots & -1 & \dots & 0 \end{bmatrix}^T u_{top}(t) \tag{IV.22}$$

where $u_{top}(t)$ is the estimated load. $\mathbf{B}_{ukn}$ is a vector with non-zero elements at the vertical DoFs of the two tip nodes, where the loads are applied. A constant load with low amplitude of $1N$ is also applied during the estimation in order to guarantee system observability as explained in the dedicated section. Fig. IV.17 shows the estimation of reaction force, crack propagation and shape reconstruction while Fig. IV.18 show the estimation error on displacement data obtained on model A, with 14 and 1 displacement sensors on the top lamina and $n_{pz} = 7$. The crack length starts to propagate earlier and the estimated force diverges from the reference values in agreement with the simplified model behavior (Fig. IV.10). As in [124], the reaction force is under estimated by approximately 6% when the damage propagates. Similar behavior can be observed for model B (Fig. IV.19) with 14 displacement sensors and $n_{pz} = 4$.

The following conclusions can be drawn on the joint input/parameter estimation of a DCB model:

- When the load is unknown, the system parameters become unobservable if no collocated measurements are considered. Indeed a loss of accuracy is observed if only one tip measurement is used, because of lack of information regarding the interface behavior;
- The critical load is under-estimated for both models, as well as the reaction force. This is caused by the boundary conditions, i.e. modelling error,

in the simplified model employed in the KF, which has unconstrained rotations at the crack tip. The estimation therefore compensates for these modelling errors, leading to a loss of accuracy of the estimated quantities, i.e. parameters and loads. In this case, the loads exhibit a decreasing of accuracy because higher uncertainty has been assumed, i.e. $Q_u >> Q_p$.

As further analysis, the effect of the imposed stiffness distribution in the process zone embedded in the AEKF scheme is shown in Fig. IV.20. The linear and the reference cohesive distributions are tested for model A, by using 14 displacement measurements on the top arm. The results do not add significant changes to the previous conclusions. Indeed, a different distribution leads to a different estimation of the crack propagation. The estimated reaction force obtained with the cohesive law results to be different from the one obtained with linear distribution because it compensates somehow for the different distribution of forces observed at the crack tip (Fig. IV.21). As a main conclusion of this contribution, the crack propagation can thus be monitored with acceptable accuracy even when using a less-correlated numerical model, if loads and parameters are jointly estimated. Indeed, the modelling errors are compensated within the estimation, resulting in a lower force amplitude with 6% of error.

Experimental validation

Within this section, the test case shown in Fig. IV.2 is presented and the recursive estimation is validated using experimental strain data. In compliance with the EN 6033 standard [161], a $L = 250mm$ long and $w = 25mm$ wide prismatic coupon with a thickness $t = 3.3mm$ is extracted from a $[0, 90]_{4s}$ woven laminate that presents on its mid-plane a teflon film such that the initial delamination is approximately $a_0 = 26mm$. Plane hinges have been installed at the tip of the coupon on the teflon insert side to apply the mechanical load. Four strain gauges have been installed on the external layer of the coupon along its mid-line starting from $46mm$ from the tip with a spacing of $20mm$. The elastic properties of the material are validated using both static data as well as a modal analysis. Fig. IV.22 shows the setup of a cantilever beam with same stacking sequence and same geometry of the DCB specimen. The modal parameters have been acquired through impact modal analysis by installing 2 accelerometers as in Fig. IV.22. The elastic parameters $E_{xx} = E_{yy}$ of the FE model have been tuned in order to match the first and second bending normal modes. The other elastic properties, coming from previous material calibration analysis are considered constant during model validation since their influence on bending modes is negligible[1]. The static response in terms of strains is also considered as target of the FE model optimization. In particular, the linear

[1]Data can be made available on request.

elastic DCB model is simulated for static analysis by applying the latest value of the measured reaction force and the corresponding strain values and tip displacement are compared. The location of sensors installed on the top lamina is reported in Table IV.4. Results of the FE model validation are shown in Table IV.5.

Table IV.4: Location of strain gauges on top lamina of the DCB.

$\mathbf{a_0}$	**SG1**	**SG2**	**SG3**	**SG4**	$\mathbf{a_f}$
$0.89L$	$0.81L$	$0.73L$	$0.65L$	$0.57L$	$0.53L$

Table IV.5: FE model validation - % errors with respect to experimental values

	$\mathbf{f_1}$**[Hz]**	$\mathbf{f_2}$**[Hz]**	**SG1**$_T[\mu E]$	$\mathbf{d}_T[mm]$
exp	50.3	322.7	-1765.1	24.0
% err	4.0	4.7	4.8	7.0

Crack propagation

The crack length propagation has been retrieved from experimental data. From EB theory, the maximum deflection of a cantilever beam, i.e. $\delta = \frac{Pa^3}{3EI}$, is first used, where δ and P are respectively the tip displacement and the reaction force. The crack length a is shown in Fig. IV.23: the last value is about 3.6% below the target, i.e. last measured value during the test. An alternative approach is to retrieve a from the mode I interlaminar fracture toughness [30, 194] as follows:

$$G_{IC} = \frac{mP\delta}{2wa}\frac{F}{N} \tag{IV.23}$$

where F and N are correction factors taking into account the effects of large displacements and the stiffening of the specimen due to the loading hinges. The influence of these factors is however negligible for the DCB specimen investigated in this contribution. Furthermore, m is a parameter obtained from the specimen compliance, i.e. $C = \delta/P$, defined as [3]:

$$m = \frac{log(\frac{C}{N})_i - log(\frac{C}{N})_{i-1}}{log(a)_i - log(a)_{i-1}} \tag{IV.24}$$

where i indicates the i-th time sample. By solving Eq. IV.23, the crack length a can be retrieved. G_{IC} should be considered function of a as the energy increases with the crack propagation. Because of the lack of data availability,

the value corresponding to the last measured crack length $a_f = 118mm$ is used, i.e. $G_{IC} = 0.692kJ/m^2$. Eq. IV.23 is then solved by "back-propagating" a_f and the trend of a is shown in Fig. IV.23. In contrast with the EB approach, this procedure tends to overestimate the initial crack length. This is due to the fact that the assumption of a constant G_{IC} measured for a fully propagated crack causes implies an excess of fracture energy in the crack initiation region.

Results

The crack length estimation is performed in this section by considering 4 strain measurements on the upper arm (Table IV.4). Further 4 strain 'dummy' strain measurements have been considered for the lower arm given the symmetry of the system. The pROM was computed as described in Sec. *Reduction basis* and the size of the reduced model is set to $r = 67$. Contrarily to the numerical case study presented above, the local bases are computed by sub-sampling the interface every 3 springs. This means that the process zone is intrinsically $n_{pz} = 3$ with a constant parameter distribution law, i.e. $\mathbf{p}_{pz} = [111]^T p^l$. This choice allows to reduce the size of the pROM and thus its computational cost. For future validation, the knowledge of the process zone is needed and e.g. Digital Image Correlation (DIC) techniques can be employed to this end. Fig. IV.25a, Fig. IV.25b and Fig. IV.25e show respectively the estimation of measured data, strain field and crack length obtained by assuming known loads being applied to the FE model. Fig. IV.25c, Fig. IV.25d and Fig. IV.25e show measured data, strain field and crack length when the loads are unknown and estimated (Fig. IV.24). As before, constant loads with very low amplitude of $1N$ are applied during the estimation in order to guarantee the system observability. The estimated force shows some peaks corresponding to the jumps observed on the measured strain data, which is a typical behavior of woven fabric materials [61]. At those points, some additional modelling errors, e.g. boundary conditions, occur and the linear FE model cannot match the measurements. As shown in the numerical validation section, the modelling errors are therefore compensated by the KF in the force estimation since higher covariance values have been assumed for the augmented states corresponding with the unknown loads as compared with the parameters, i.e. $Q_u >> Q_p$. In conclusion, the joint input/parameter estimation accurately predict the critical load and provide full-field reconstruction even when employing a less-correlated, i.e. less accurate, linear model. The joint estimation is more advantageous with respect to parameter-only estimation, i.e. the scenario with known loads, since the modelling errors are then compensated by both the estimated loads and parameters and not fully and only by parameter degradation, and both quantities (loads and parameters) show good levels of estimation accuracy.

Conclusions

This work addresses the delamination growth monitoring in composite materials by employing the Extended Augmented Kalman Filter (EAKF). The proposed methodology is validated on simulated and experimental data for a composite Double Cantilever Beam (DCB) specimen. A simplified linear Finite Element Model (FEM) is employed in the estimator. This provides a great advantage from modelling point of view and computational costs. However, the usage of shell elements connected with node-to-node springs does not constrain rotations at the crack tip and this leads to an under-prediction of the reaction force when the damage initiates and propagates. The estimation error observed on the force is $< 6\%$ for both analyzed numerical models. The simplified model reaches a good level of accuracy also when using experimental data. A recursive parameter estimation scheme for interface stiffness degradation is proposed to reduce the number of sensors needed for the system observability. The stiffness parameter distribution embedded in the estimator allows to consider the effect of the process zone developing during the delamination propagation. The study of sensors networks shows that a single position-level measurement is enough to monitor the crack propagation when the loads are known. During operation, the critical loads causing the damage are however typically unknown and thus the joint input/parameter estimation is also addressed in this contribution, showing that the estimation accuracy increases with the number of collocated measurements. The implementation of this methodology on a real test case needs thus to sensorize the critical area of interest to monitor the damage growth and estimate the critical loads. Future investigation aims to evaluate a more accurate and advanced study on the stiffness distribution within the process zone and to explore a possible improvement of the estimation by employing embedded sensors, such as e.g. Fiber Bragg Gratings (FBGs). Implementation on a more complex test-case will be also addressed.

Acknowledgments

The authors acknowledge R&D team of Leonardo Aerostructure Division for its support in the experimental validation.

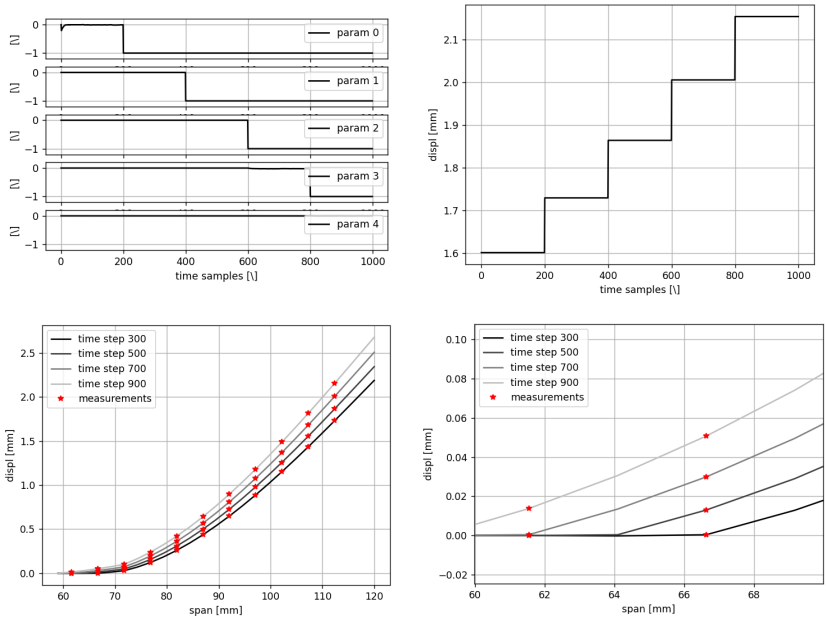

Figure IV.12: Estimated parameters (top left), samples of measurements (top right), estimated displacement field distribution at different time samples (bottom left) and corresponding estimation of boundary conditions (bottom right).

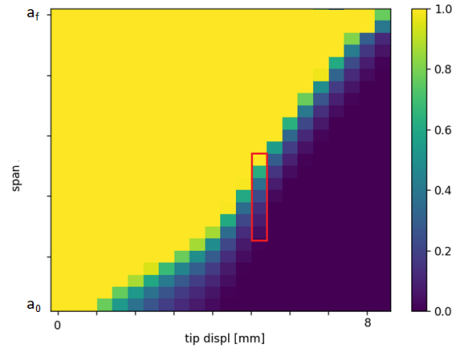

Figure IV.13: Normalized stiffness at each time step in the delaminated area. The span is from the initial delamination $a_0 = 38mm$ to a_f, i.e. delamination at the end of the simulation. The red box indicates a generic evaluation of process zone.

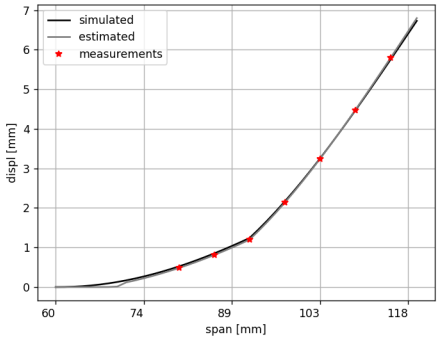

(a) 7 displacement sensors on the top lamina. $a > a_c$

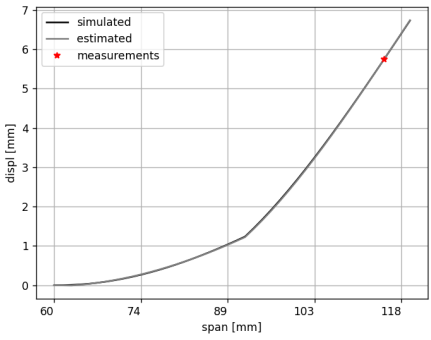

(b) 1 displacement sensors on the top lamina. $a > a_c$

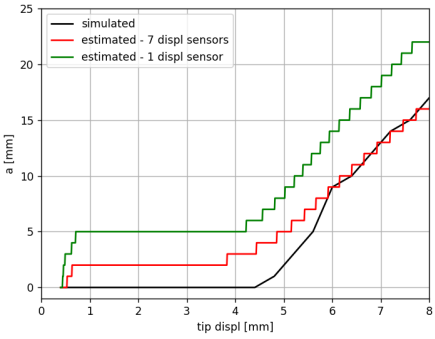

(c) Estimated crack length

Figure IV.14: Shape reconstruction and crack length estimation on model A with different sensor networks. $n_{pz} = 7$

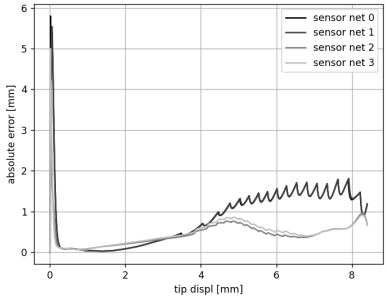

Figure IV.15: Absolute error of the simulated vs measured vertical displacements of model A, known loads. Sensor net 0,1,2,3 correspond to 14, 7, 3, 1 measurements on the top lamina employed in the estimator respectively.

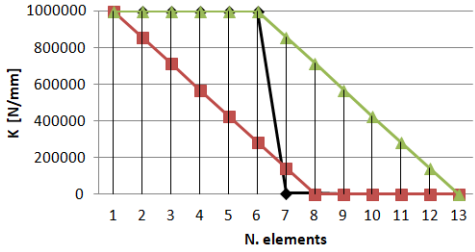

Figure IV.16: Stiffness distribution: cohesive law (black, pz: 7-13) vs estimated linear (red, pz: 1-8) vs expected linear (green, pz: 6-13).

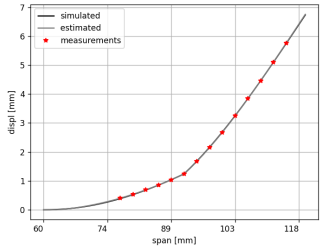

(a) 14 displacement sensors on the top lamina. Shape reconstruction at $a > a_c$

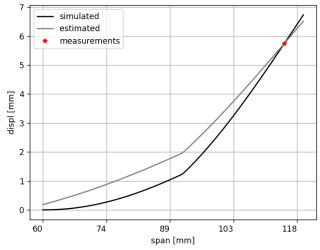

(b) 1 displacement sensor on the top lamina. Shape reconstruction at $a > a_c$

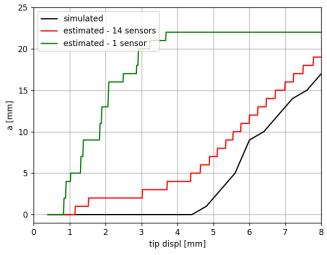

(c) Estimated crack length

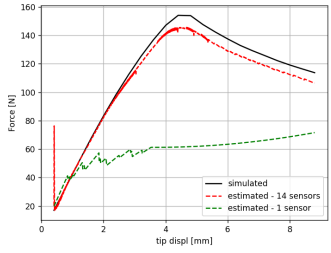

(d) Estimated reaction force

Figure IV.17: Joint input/parameter estimation results using model A. $n_{pz} = 7$

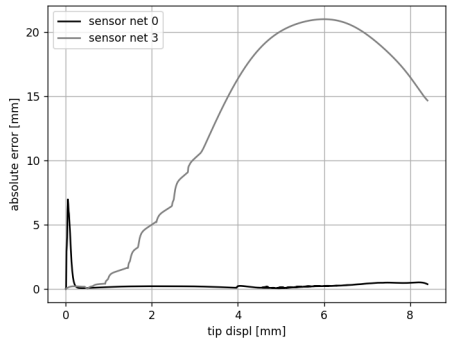

Figure IV.18: Absolute error of the simulated vs measured vertical displacements of model A, unknown loads. Sensor net 0, 3 correspond to 14, 1 measurements on the top lamina employed in the estimator.

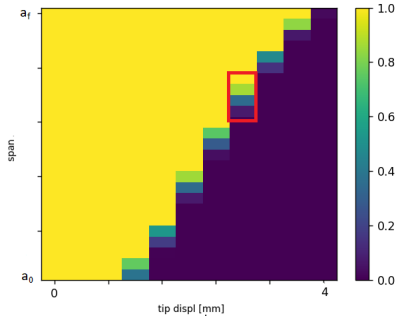

(a) Normalized stiffness with process zone length (red box) from simulated model.

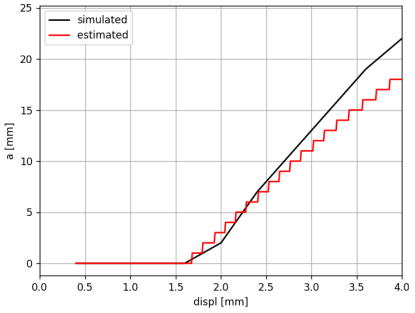

(b) Estimated crack length - 14 displacement sensors

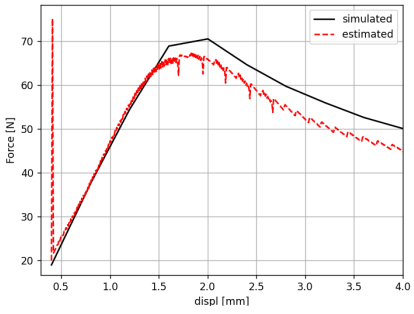

(c) Estimated reaction force - 14 displacement sensors

Figure IV.19: Joint input/parameter estimation results using model B. $n_{pz} = 4$

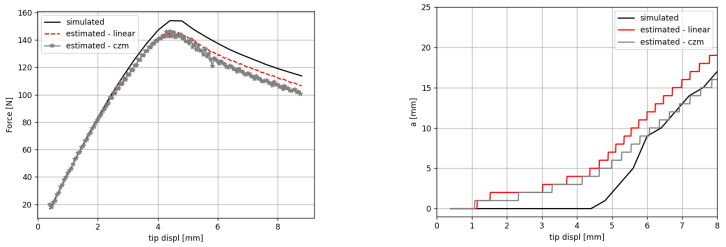

(a) Estimated reaction force (b) Estimated crack length

Figure IV.20: Joint input/parameter estimation results on model A. $n_{pz} = 7, 14$ displacement sensors. Comparison between different imposed interface stiffness distributions.

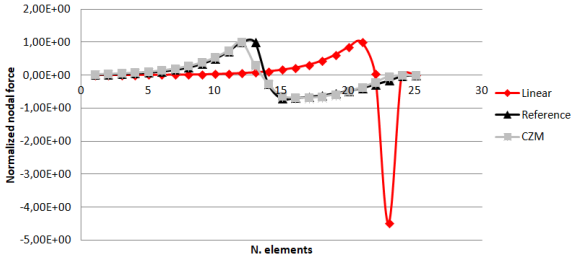

Figure IV.21: Normalized nodal forces at the interface with respect to the value at the first undamaged element. *Linear* and *CZM* are retrieved from the forward simulation using the linear shell model with imposed stiffness distributions in the process zone.

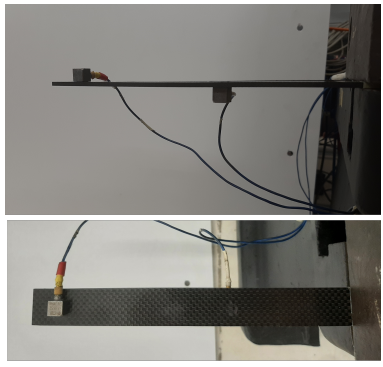

Figure IV.22: Test setup for experimental modal analysis.

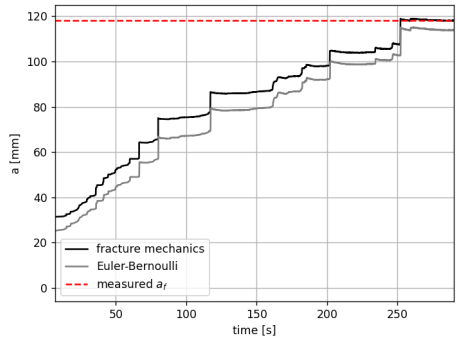

Figure IV.23: Crack propagation retrieved from experimental data.

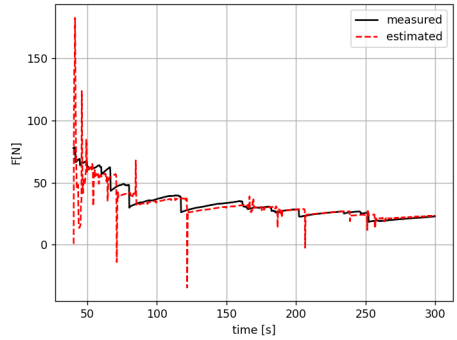

Figure IV.24: Estimation of reaction force for the experimental DCB.

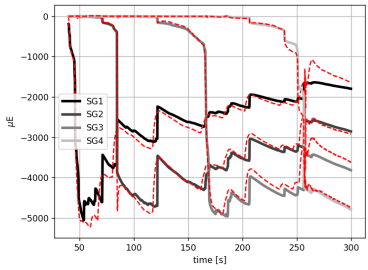

(a) Known loads: measured (red) vs estimated (black) strain (upper lamina).

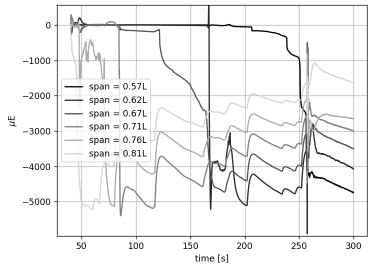

(b) Known loads: estimated (unmeasured) strain.

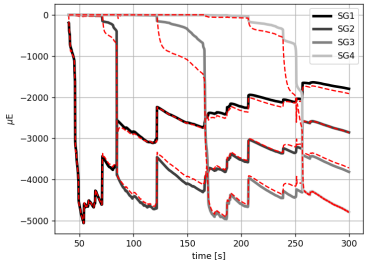

(c) Unknown loads: measured (red) vs estimated (black) strain (upper lamina).

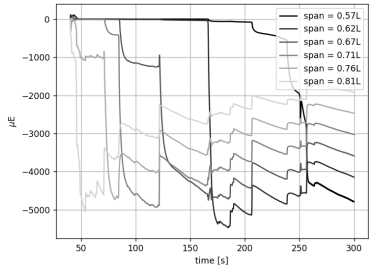

(d) Unknown loads: estimated (unmeasured) strain.

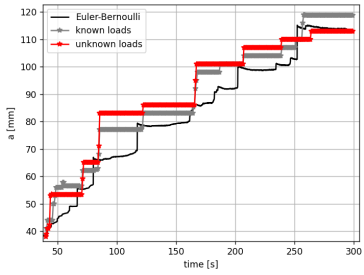

(e) Estimated crack length.

Figure IV.25: AEKF recursive estimation results on experimental DCB.

Bibliography

[1] Python. https://www.python.org/ [Accessed: 06 Feb 2024].

[2] *ASTM E2533-17. Standard Guide for Nondestructive Testing of Polymer Matrix Composites Used in Aerospace Applications.* -, 2017.

[3] *ASTM D5528/D5528M-21. Standard Test Method for Mode I Interlaminar Fracture Toughness of Unidirectional Fiber-Reinforced Polymer Matrix Composites.* -, 2022.

[4] Aabid, A., Parveez, B., Raheman, M. A., Ibrahim, Y. E., Anjum, A., Hrairi, M., Parveen, N., and Mohammed Zayan, J. A review of piezoelectric material-based structural control and health monitoring techniques for engineering structures: Challenges and opportunities. In *Actuators* (2021), vol. 10(5), MDPI, p. 101.

[5] Abhishek, A. *Analysis, validation, prediction and fundamental understanding of rotor blade loads in an unsteady maneuver.* University of Maryland, College Park, 2010.

[6] Adams, R., and Doyle, J. F. Multiple force identification for complex structures. *Experimental Mechanics 42* (2002), 25–36.

[7] Administration, F. A. Boeing 737-200, aloha airlines flight 243, n73711, 1988. https://www.faa.gov/lessons_learned/transport_airplane/accidents/N73711 [Accessed: 29 Mar 2024].

[8] Administration, F. A. Mcdonnell douglas d-10, united airlines flight 232, n1819u, 1989. https://www.faa.gov/lessons_learned/transport_airplane/accidents/N1819U [Accessed: 29 Mar 2024].

[9] Ahmed, Z., and Woolsey, C. A. The invariant extended kalman filter for wind estimation using a small fixed-wing uav in horizontal-plane flight. In *AIAA SCITECH 2024 Forum* (2024), p. 2656.

[10] Alcalay, G., Seren, C., Hardier, G., Delporte, M., and Goupil, P. An adaptive extended kalman filter for monitoring and estimating key aircraft flight parameters. *IFAC-PapersOnLine 51*, 24 (2018), 620–627.

[11] Alkahe, J., Rand, O., and Oshman, Y. Helicopter health monitoring using an adaptive estimator. *Journal of the American Helicopter Society 48*, 3 (2003), 199–210.

[12] Alshawi, A., De Pinto, S., Stano, P., van Aalst, S., Praet, K., Boulay, E., Ivone, D., Gruber, P., and Sorniotti, A. An adaptive unscented kalman filter for the estimation of the vehicle velocity components, slip angles, and slip ratios in extreme driving manoeuvres. *Sensors 24*, 2 (2024), 436.

[13] Amsallem, D., and Farhat, C. An online method for interpolating linear parametric reduced-order models. *SIAM Journal on Scientific Computing 33*, 5 (2011), 2169–2198.

[14] ANSYS, I. Ansys twin builder, 2024. `https://www.ansys.com/products/digital-twin/ansys-twin-builder` [Accessed: 31 Jan 2024].

[15] Antonov, S., Fehn, A., and Kugi, A. Unscented kalman filter for vehicle state estimation. *Vehicle System Dynamics 49*, 9 (2011), 1497–1520.

[16] Ascher, U. M., and Petzold, L. R. *Computer methods for ordinary differential equations and differential-algebraic equations*, vol. 61. Siam, 1998.

[17] Au, S.-K., Zhang, F.-L., and Ni, Y.-C. Bayesian operational modal analysis: theory, computation, practice. *Computers & Structures 126* (2013), 3–14.

[18] Authority, N. S. I. Report on the air accident near turoy, oygarden municipality, hordaland county, norway 29 april 2016 with airbus helicopters ec 225 lp, ln-ojf, operated by chc helikopter service as, 2018. `https://www.nsia.no/Aviation/Published-reports/2018-04` [Accessed: 29 Mar 2024].

[19] Azam, S. E., Chatzi, E., and Papadimitriou, C. A dual kalman filter approach for state estimation via output-only acceleration measurements. *Mechanical systems and signal processing 60* (2015), 866–886.

[20] Azam, S. E., Chatzi, E., Papadimitriou, C., and Smyth, A. Experimental validation of the kalman-type filters for online and real-time state and input estimation. *Journal of vibration and control 23*, 15 (2017), 2494–2519.

[21] Azimi, M., Eslamlou, A. D., and Pekcan, G. Data-driven structural health monitoring and damage detection through deep learning: State-of-the-art review. *Sensors 20*, 10 (2020), 2778.

[22] Bagherzadeh, S. A. Nonlinear aircraft system identification using artificial neural networks enhanced by empirical mode decomposition. *Aerospace Science and Technology 75* (2018), 155–171.

[23] Bai, W., Jia, R., Yu, P., and Xue, W. On extended state kalman filter-based identification algorithm for aerodynamic parameters. *Control Theory and Technology* (2024), 1–9.

[24] Baur, U., Benner, P., and Feng, L. Model order reduction for linear and nonlinear systems: a system-theoretic perspective. *Archives of Computational Methods in Engineering 21*, 4 (2014), 331–358.

[25] Bay, J. Fundamentals of linear state space systems.

[26] Benner, P., Gugercin, S., and Willcox, K. A survey of projection-based model reduction methods for parametric dynamical systems. *SIAM review 57*, 4 (2015), 483–531.

[27] Benner, P., Laub, A. J., and Mehrmann, V. A collection of benchmark examples for the numerical solution of algebraic riccati equations i: Continuous-time case.

[28] Bernal, D., and Ussia, A. Sequential deconvolution input reconstruction. *Mechanical Systems and Signal Processing 50* (2015), 41–55.

[29] Bernardini, G., Porcelli, R., Serafini, J., and Masarati, P. Rotor blade shape reconstruction from strain measurements. *Aerospace Science and Technology 79* (2018), 580–587.

[30] Berry, J. Determination of fracture surface energies by the cleavage technique. *Journal of applied physics 34*, 1 (1963), 62–68.

[31] Bersani, M., Vignati, M., Mentasti, S., Arrigoni, S., and Cheli, F. Vehicle state estimation based on kalman filters. In *2019 AEIT International Conference of Electrical and Electronic Technologies for Automotive (AEIT AUTOMOTIVE)* (2019), IEEE, pp. 1–6.

[32] Bhatnagar, S., Afshar, Y., Pan, S., Duraisamy, K., and Kaushik, S. Prediction of aerodynamic flow fields using convolutional neural networks. *Computational Mechanics 64* (2019), 525–545.

[33] Blau, M. Indirect measurement of multiple excitation force spectra by frf matrix inversion: influence of errors in statistical estimates of frfs

and response spectra. *Acta Acustica united with Acustica 85*, 4 (1999), 464–479.

[34] Bogert, P., Haugse, E., and Gehrki, R. Structural shape identification from experimental strains using a modal transformation technique. In *44th AIAA/ASME/ASCE/AHS/ASC Structures, Structural Dynamics, and Materials Conference* (2003), p. 1626.

[35] Bramwell, A. R. S., Balmford, D., and Done, G. *Bramwell's helicopter dynamics*. Elsevier, 2001.

[36] Branch, A. A. I. Aircraft accident report 2/2011 - aerospatiale (eurocopter) as332 l2 super puma, g-redl, 1 april 2009, 2014. https://www.gov.uk/aaib-reports/2-2011-aerospatiale-eurocopter-as332-l2-super-puma-g-redl-1-april-2009 [Accessed: 29 Mar 2024].

[37] Brenner, S. C. *The mathematical theory of finite element methods*. Springer, 2008.

[38] Brincker, R., and Ventura, C. *Introduction to operational modal analysis*. John Wiley & Sons, 2015.

[39] Capalbo, C. E., De Gregoriis, D., Tamarozzi, T., Devriendt, H., Naets, F., Carbone, G., and Mundo, D. Parameter, input and state estimation for linear structural dynamics using parametric model order reduction and augmented kalman filtering. *Mechanical Systems and Signal Processing 185* (2023), 109799.

[40] Center, F. A. A. W. J. H. T. The national aging aircraft research program. https://www.tc.faa.gov/its/cmd/visitors/data/aar-430/national.pdf [Accessed: 29 Mar 2024].

[41] Chaturantabut, S., and Sorensen, D. C. Nonlinear model reduction via discrete empirical interpolation. *SIAM Journal on Scientific Computing 32*, 5 (2010), 2737–2764.

[42] Chen, S. Kalman filter for robot vision: a survey. *IEEE Transactions on industrial electronics 59*, 11 (2011), 4409–4420.

[43] Chowdhary, G., and Jategaonkar, R. Aerodynamic parameter estimation from flight data applying extended and unscented kalman filter. *Aerospace science and technology 14*, 2 (2010), 106–117.

[44] Connelly, J., and Huston, R. The dynamics of flexible multibody systems: A finite segment approach—i. theoretical aspects. *Computers & structures 50*, 2 (1994), 255–258.

[45] Cosco, F., Naets, F., and Desmet, W. Use of concept modelling for online input force estimation. *ISMA proceedings* (2014), 1639–1651.

[46] Craig Jr, R. R. A review of time-domain and frequency-domain component mode synthesis method.

[47] Cristiani, D., Falcetelli, F., Yue, N., Sbarufatti, C., Di Sante, R., Zarouchas, D., and Giglio, M. Strain-based delamination prediction in fatigue loaded cfrp coupon specimens by deep learning and static loading data. *Composites Part B: Engineering 241* (2022), 110020.

[48] Crocker, M. J. *Handbook of noise and vibration control*. John Wiley & Sons, 2007.

[49] Cumbo, R., De Gregoriis, D., Danzi, F., Kumar, A., and Naets, F. Recursive parameter estimation for the on-line monitoring of delamination growth in composite structures. *Structural Health Monitoring* (2024), 14759217241299057.

[50] Cumbo, R., Mazzanti, L., Tamarozzi, T., Jiranek, P., Desmet, W., and Naets, F. Advanced optimal sensor placement for kalman-based multiple-input estimation. *Mechanical Systems and Signal Processing 160* (2021), 107830.

[51] Cumbo, R., Tamarozzi, T., Janssens, K., and Desmet, W. Investigation of virtual sensing techniques on a rear twistbeam suspension by performing multiple-input/state estimation. In *PROCEEDINGS OF INTERNATIONAL CONFERENCE ON NOISE AND VIBRATION ENGINEERING (ISMA2018)/INTERNATIONAL CONFERENCE ON UNCERTAINTY IN STRUCTURAL DYNAMICS (USD2018)* (2018), KATHOLIEKE UNIV LEUVEN, DEPT WERKTUIGKUNDE, pp. 2181–2195.

[52] Cumbo, R., Tamarozzi, T., Janssens, K., and Desmet, W. Kalman-based load identification and full-field estimation analysis on industrial test case. *Mechanical Systems and Signal Processing 117* (2019), 771–785.

[53] Cumbo, R., Tamarozzi, T., Jiranek, P., Desmet, W., and Masarati, P. State and force estimation on a rotating helicopter blade through a kalman-based approach. *Sensors 20*, 15 (2020), 4196.

[54] Dimitri, R., Cornetti, P., Mantič, V., Trullo, M., and De Lorenzis, L. Mode-i debonding of a double cantilever beam: a comparison between cohesive crack modeling and finite fracture mechanics. *International Journal of Solids and Structures 124* (2017), 57–72.

[55] Dipartimento di Scienze e Tecnologie Aerospaziali, P. d. M. Multibody dynamics mbdyn. `https://www.mbdyn.org/` [Accessed: 06 Feb 2024].

[56] Dobson, B., and Rider, E. A review of the indirect calculation of excitation forces from measured structural response data. *Proceedings of the Institution of Mechanical Engineers, Part C: Mechanical Engineering Science 204*, 2 (1990), 69–75.

[57] Doumiati, M., Victorino, A. C., Charara, A., and Lechner, D. Onboard real-time estimation of vehicle lateral tire–road forces and sideslip angle. *IEEE/ASME Transactions on Mechatronics 16*, 4 (2010), 601–614.

[58] Ebrahimian, H., Astroza, R., Conte, J. P., and Papadimitriou, C. Bayesian optimal estimation for output-only nonlinear system and damage identification of civil structures. *Structural Control and Health Monitoring 25*, 4 (2018), e2128.

[59] Entezami, A., Arslan, A. N., De Michele, C., and Behkamal, B. Online hybrid learning methods for real-time structural health monitoring using remote sensing and small displacement data. *Remote Sensing 14*, 14 (2022), 3357.

[60] Esposito, M., and Gherlone, M. Material and strain sensing uncertainties quantification for the shape sensing of a composite wing box. *Mechanical Systems and Signal Processing 160* (2021), 107875.

[61] Fanteria, D., Lazzeri, L., Panettieri, E., Mariani, U., and Rigamonti, M. Experimental characterization of the interlaminar fracture toughness of a woven and a unidirectional carbon/epoxy composite. *Composites Science and Technology 142* (2017), 20–29.

[62] Flynn, E. B., and Todd, M. D. A bayesian approach to optimal sensor placement for structural health monitoring with application to active sensing. *Mechanical Systems and Signal Processing 24*, 4 (2010), 891–903.

[63] Friswell, M. I., and Mottershead, J. *Finite element model updating in structural dynamics*. Kluwer Academic Publishers, 1995.

[64] Gajdatsy, P., Janssens, K., Desmet, W., and Van Der Auweraer, H. Application of the transmissibility concept in transfer path analysis. *Mechanical Systems and Signal Processing 24*, 7 (2010), 1963–1976.

[65] Gajdátsy, P. Á. Advanced transfer path analysis methods (geavanceerde transfer pad analysemethodes).

[66] Ganguli, R., Chopra, I., and Haas, D. J. Formulation of a helicopter rotor system damage detection methodology. *Journal of the American Helicopter Society 41*, 4 (1996), 302–312.

[67] Ganguli, R., Chopra, I., and Haas, D. J. Detection of helicopter rotor system simulated faults using neural networks. *Journal of the american helicopter society 42*, 2 (1997), 161–171.

[68] Ganguli, R., Chopra, I., and Haas, D. J. Helicopter rotor system fault detection using physics-based model and neural networks. *AIAA journal 36*, 6 (1998), 1078–1086.

[69] Ganguli, R., Chopra, I., and Haas, D. J. Simulation of helicopter rotor-system structural damage, blade mistracking, friction, and freeplay. *Journal of aircraft 35*, 4 (1998), 591–597.

[70] Garcia-Velo, J., and Walker, B. K. Aerodynamic parameter estimation for high-performance aircraft using extended kalman filtering. *Journal of Guidance, Control, and Dynamics 20*, 6 (1997), 1257–1260.

[71] Gear, C. W., Leimkuhler, B., and Gupta, G. K. Automatic integration of euler-lagrange equations with constraints. *Journal of Computational and Applied Mathematics 12* (1985), 77–90.

[72] Ghajari, M., Sharif-Khodaei, Z., Aliabadi, M., and Apicella, A. Identification of impact force for smart composite stiffened panels. *Smart Materials and Structures 22*, 8 (2013), 085014.

[73] Ghiringhelli, G. L., Masarati, P., and Mantegazza, P. Multibody implementation of finite volume c beams. *AIAA journal 38*, 1 (2000), 131–138.

[74] Gholizadeh, S. A review of non-destructive testing methods of composite materials. *Procedia structural integrity 1* (2016), 50–57.

[75] Ghosh, B. K., and Rosenthal, J. A generalized popov-belevitch-hautus test of observability. *IEEE transactions on automatic control 40*, 1 (1995), 176–180.

[76] Gillijns, S., and De Moor, B. System inversion with application to filtering and smoothing in the presence of unknown inputs. *Submitted for publication, KULeuven* (2007).

[77] Gillijns, S., and De Moor, B. Unbiased minimum-variance input and state estimation for linear discrete-time systems with direct feedthrough. *Automatica 43*, 5 (2007), 934–937.

[78] Glaser, R., Caccese, V., and Shahinpoor, M. Shape monitoring of a beam structure from measured strain or curvature. *Experimental mechanics 52* (2012), 591–606.

[79] Glauert, H. *Airplane Propellers*. Springer Berlin Heidelberg, Berlin, Heidelberg, 1935, pp. 169–360.

[80] Gui, G., Pan, H., Lin, Z., Li, Y., and Yuan, Z. Data-driven support vector machine with optimization techniques for structural health monitoring and damage detection. *KSCE Journal of Civil Engineering 21* (2017), 523–534.

[81] Haas, D. J., Flitter, L., and Milano, J. Helicopter flight data feature extraction or component load monitoring. *Journal of Aircraft 33*, 1 (1996), 37–45.

[82] Haghighat, E., Raissi, M., Moure, A., Gomez, H., and Juanes, R. A physics-informed deep learning framework for inversion and surrogate modeling in solid mechanics. *Computer Methods in Applied Mechanics and Engineering 379* (2021), 113741.

[83] Hansen, P. C., and O'Leary, D. P. The use of the l-curve in the regularization of discrete ill-posed problems. *SIAM journal on scientific computing 14*, 6 (1993), 1487–1503.

[84] Hart, G. C., and Yao, J. T. System identification in structural dynamics. *Journal of the Engineering Mechanics Division 103*, 6 (1977), 1089–1104.

[85] Haug, E. J. *Computer aided analysis and optimization of mechanical system dynamics*, vol. 9. Springer Science & Business Media, 2013.

[86] He, M., Ramakrishnan, K. R., Wang, Y., Zhang, Z., and Fu, J. A combined global-local approach for delamination assessment of composites using vibrational frequencies and fbgs. *Mechanical Systems and Signal Processing 167* (2022), 108577.

[87] He, M., Wang, Y., Ram Ramakrishnan, K., and Zhang, Z. A comparison of machine learning algorithms for assessment of delamination in fiber-reinforced polymer composite beams. *Structural Health Monitoring 20*, 4 (2021), 1997–2012.

[88] Heredia, G., and Ollero, A. Sensor fault detection in small autonomous helicopters using observer/kalman filter identification. In *2009 IEEE International Conference on Mechatronics* (2009), IEEE, pp. 1–6.

[89] Hong, S.-K., Epureanu, B. I., and Castanier, M. P. Next-generation parametric reduced-order models. *Mechanical Systems and Signal Processing 37*, 1-2 (2013), 403–421.

[90] Hossain, M. S., Ong, Z. C., Ismail, Z., Noroozi, S., and Khoo, S. Y. Artificial neural networks for vibration based inverse parametric identifications: A review. *Applied Soft Computing 52* (2017), 203–219.

[91] Janssens, K., Mas, P., Gajdatsy, P., Gielen, L., and Van der Auweraer, H. A novel path contribution analysis method for test-based nvh troubleshooting. In *PROCEEDINGS OF ISMA 2008: INTERNATIONAL CONFERENCE ON NOISE AND VIBRATION ENGINEERING, VOLS. 1-8* (2008), vol. 6, KATHOLIEKE UNIV LEUVEN, DEPT WERKTUIGKUNDE, pp. 3673–3683.

[92] Johnson, W. *Helicopter theory*. Courier Corporation, 2012.

[93] Ju, M., Dou, Z., Li, J.-W., Qiu, X., Shen, B., Zhang, D., Yao, F.-Z., Gong, W., and Wang, K. Piezoelectric materials and sensors for structural health monitoring: Fundamental aspects, current status, and future perspectives. *Sensors 23*, 1 (2023), 543.

[94] Jung, S., Kim, T.-Y., and Yoo, W.-S. Advanced slip ratio for ensuring numerical stability of low-speed driving simulation. part i: Longitudinal slip ratio. *Proceedings of the Institution of Mechanical Engineers, Part D: Journal of Automobile Engineering 233*, 8 (2019), 2000–2006.

[95] Kalman, R. E. A new approach to linear filtering and prediction problems. *Transactions of the ASME–Journal of Basic Engineering 82*, Series D (1960), 35–45.

[96] Kalman, R. E., and Bucy, R. S. New results in linear filtering and prediction theory.

[97] Kammer, D. C., and Steltzner, A. D. Structural identification using inverse system dynamics. *Journal of Guidance, Control, and Dynamics 23*, 5 (2000), 819–825.

[98] Karbhari, V. M. *Non-destructive evaluation (NDE) of polymer matrix composites*. Elsevier, 2013.

[99] Karniadakis, G. E., Kevrekidis, I. G., Lu, L., Perdikaris, P., Wang, S., and Yang, L. Physics-informed machine learning. *Nature Reviews Physics 3*, 6 (2021), 422–440.

[100] Kefal, A., Tabrizi, I., Tansan, M., Kisa, E., and Yildiz, M. An experimental implementation of inverse finite element method for real-time

shape and strain sensing of composite and sandwich structures. *Composite Structures 258* (2021), 113431.

[101] Khalil, M., Kouroudis, I., Wüchner, R., and Bletzinger, K.-U. Optimal sensor configuration for fatigue life prediction in structural applications. In *Dynamic Systems and Control Conference* (2019), vol. 59148, American Society of Mechanical Engineers, p. V001T06A001.

[102] Klein, V. Estimation of aircraft aerodynamic parameters from flight data. *Progress in Aerospace Sciences 26*, 1 (1989), 1–77.

[103] Kralovec, C., and Schagerl, M. Review of structural health monitoring methods regarding a multi-sensor approach for damage assessment of metal and composite structures. *Sensors 20*, 3 (2020), 826.

[104] Kuang and, K., and Cantwell, W. Use of conventional optical fibers and fiber bragg gratings for damage detection in advanced composite structures: a review. *Appl. Mech. Rev. 56*, 5 (2003), 493–513.

[105] Lai, Z., Liu, W., Jian, X., Bacsa, K., Sun, L., and Chatzi, E. Neural modal ordinary differential equations: Integrating physics-based modeling with neural ordinary differential equations for modeling high-dimensional monitored structures. *Data-Centric Engineering 3* (2022), e34.

[106] Lai, Z., Mylonas, C., Nagarajaiah, S., and Chatzi, E. Structural identification with physics-informed neural ordinary differential equations. *Journal of Sound and Vibration 508* (2021), 116196.

[107] Leishman, G. J. *Principles of helicopter aerodynamics with CD extra*. Cambridge university press, 2006.

[108] Li, L., Jia, G., Ran, X., Song, J., and Wu, K. A variable structure extended kalman filter for vehicle sideslip angle estimation on a low friction road. *Vehicle System Dynamics 52*, 2 (2014), 280–308.

[109] Liao, Y.-W., and Borrelli, F. An adaptive approach to real-time estimation of vehicle sideslip, road bank angles, and sensor bias. *IEEE Transactions on Vehicular Technology 68*, 8 (2019), 7443–7454.

[110] Liu, R., Liu, M., Duan, G., and Cao, X. Robust adaptive smooth variable structure kalman filter for spacecraft attitude estimation. *Aerospace Science and Technology 144* (2024), 108784.

[111] Liu, W., Lai, Z., Bacsa, K., and Chatzi, E. Neural extended kalman filters for learning and predicting dynamics of structural systems. *Structural Health Monitoring* (2022), 14759217231179912.

[112] Liu, X., Tian, S., Tao, F., and Yu, W. A review of artificial neural networks in the constitutive modeling of composite materials. *Composites Part B: Engineering 224* (2021), 109152.

[113] Lourens, E., and Fallais, D. Full-field response monitoring in structural systems driven by a set of identified equivalent forces. *Mechanical Systems and Signal Processing 114* (2019), 106–119.

[114] Lourens, E., Papadimitriou, C., Gillijns, S., Reynders, E., De Roeck, G., and Lombaert, G. Joint input-response estimation for structural systems based on reduced-order models and vibration data from a limited number of sensors. *Mechanical Systems and Signal Processing 29* (2012), 310–327.

[115] Lourens, E., Reynders, E., De Roeck, G., Degrande, G., and Lombaert, G. An augmented kalman filter for force identification in structural dynamics. *Mechanical systems and signal processing 27* (2012), 446–460.

[116] Luppold, R., Roman, J., Gallops, G., and Kerr, L. Estimating in-flight engine performance variations using kalman filter concepts. In *25th Joint Propulsion Conference* (1989), p. 2584.

[117] Lynch, J. P., and Loh, K. J. A summary review of wireless sensors and sensor networks for structural health monitoring. *Shock and vibration digest 38*, 2 (2006), 91–130.

[118] Maes, K. Filtering techniques for force identification and response estimation in structural dynamics.

[119] Maes, K., Lourens, E., Van Nimmen, K., Reynders, E., De Roeck, G., and Lombaert, G. Design of sensor networks for instantaneous inversion of modally reduced order models in structural dynamics. *Mechanical Systems and Signal Processing 52* (2015), 628–644.

[120] Maes, K., Van Nimmen, K., Lourens, E., Rezayat, A., Guillaume, P., De Roeck, G., and Lombaert, G. Verification of joint input-state estimation for force identification by means of in situ measurements on a footbridge. *Mechanical Systems and Signal Processing 75* (2016), 245–260.

[121] Majeed, M., and Narayan Kar, I. Aerodynamic parameter estimation using adaptive unscented kalman filter. *Aircraft Engineering and Aerospace Technology 85*, 4 (2013), 267–279.

[122] Mas, P., Sas, P., and Wyckaert, K. Indirect force determination based upon matrix inversion: A study on statistical and deterministic

accuracy. In *Proceedings of the International Conference on Noise and Vibration Engineering* (1994), pp. 1049–1065.

[123] MathWorks. Matlab care, 2023. `https://mathworks.com/help/control/ref/care.html` [Accessed: 31 Jan 2024].

[124] McElroy, M. An enriched shell element for delamination simulation in composite laminates. In *American Society for Composites Technical Conference* (2015), no. NF1676L, p. 20621.

[125] McNeill, Q., Hancock, P., and Kellaway, K. V. Report on the accident to boeing vertol 234 lr, g-bwfc 2.5 miles east of sumburgh, shetland isles on 6 novemer 1986. *London Her Majesty's Stationery Office, AAIB* (1988/9).

[126] Meng, L., Li, L., and Veres, S. Aerodynamic parameter estimation of an unmanned aerial vehicle based on extended kalman filter and its higher order approach. In *2010 2nd International Conference on Advanced Computer Control* (2010), vol. 5, IEEE, pp. 526–531.

[127] Moheimani, S. R., Savkin, A. V., and Petersen, I. R. Robust filtering, prediction, smoothing, and observability of uncertain systems. *IEEE Transactions on Circuits and Systems I: Fundamental Theory and Applications 45*, 4 (1998), 446–457.

[128] Moorthy, V., and Marappan, K. Experimental study on delamination identification in tapered laminated composite plates using damage detection models. *Composite Structures 323* (2023), 117494.

[129] Naets, F., Croes, J., and Desmet, W. An online coupled state/input/parameter estimation approach for structural dynamics. *Computer methods in applied mechanics and engineering 283* (2015), 1167–1188.

[130] Naets, F., Cuadrado, J., and Desmet, W. Stable force identification in structural dynamics using kalman filtering and dummy-measurements. *Mechanical Systems and Signal Processing 50* (2015), 235–248.

[131] NASA. Technology readiness levels, 2023. `https://www.nasa.gov/directorates/somd/space-communications-navigation-program/technology-readiness-levels/` [Accessed: 12 Apr 2024].

[132] Nemhauser, G. L., Wolsey, L. A., and Fisher, M. L. An analysis of approximations for maximizing submodular set functions—i. *Mathematical programming 14* (1978), 265–294.

[133] Noppe, N., Tatsis, K., Chatzi, E., Devrient, C., and Weijtjens, W. Fatigue stress estimation of offshore wind turbine using a

kalman filter in combination with accelerometers. In *Proceedings of International Conference on Noise and Vibration Engineering (ISMA 2018), International Conference on Uncertainty in Structural Dynamics (USD 2018)* (2018), KU Leuven, Department of Mechanical Engineering, pp. 4693–6701.

[134] Nordstrom, L. J., and Nordberg, T. P. A critical comparison of time domain load identification methods. In *The Proceedings of the International Conference on Motion and Vibration Control 6.2* (2002), The Japan Society of Mechanical Engineers, pp. 1151–1156.

[135] Nordström, L. J., and Nordberg, T. P. A time delay method to solve non-collocated input estimation problems. *Mechanical Systems and Signal Processing 18*, 6 (2004), 1469–1483.

[136] Oboe, D., Colombo, L., Sbarufatti, C., and Giglio, M. Comparison of strain pre-extrapolation techniques for shape and strain sensing by ifem of a composite plate subjected to compression buckling. *Composite Structures 262* (2021), 113587.

[137] Oboe, D., Colombo, L., Sbarufatti, C., and Giglio, M. Shape sensing of a complex aeronautical structure with inverse finite element method. *Sensors 21*, 4 (2021), 1388.

[138] Oboe, D., Poloni, D., Sbarufatti, C., and Giglio, M. Crack size estimation with an inverse finite element model. In *European Workshop on Structural Health Monitoring* (2022), Springer, pp. 443–453.

[139] Ostachowicz, W., Soman, R., and Malinowski, P. Optimization of sensor placement for structural health monitoring: A review. *Structural health monitoring 18*, 3 (2019), 963–988.

[140] Palanisamy, R. P., Cho, S., Kim, H., and Sim, S.-H. Experimental validation of kalman filter-based strain estimation in structures subjected to non-zero mean input. *Smart Structures and Systems 15*, 2 (2015), 489–503.

[141] Panopoulou, A., Loutas, T., Roulias, D., Fransen, S., and Kostopoulos, V. Dynamic fiber bragg gratings based health monitoring system of composite aerospace structures. *Acta Astronautica 69*, 7-8 (2011), 445–457.

[142] Papadimitriou, C. Optimal sensor placement methodology for parametric identification of structural systems. *Journal of sound and vibration 278*, 4-5 (2004), 923–947.

[143] Park, K., and Paulino, G. H. Cohesive zone models: a critical review of traction-separation relationships across fracture surfaces. *Applied Mechanics Reviews 64*, 6 (2011), 060802.

[144] Pawar, P., and Ganguli, R. Helicopter rotor health monitoring-a review. *proceedings of the institution of mechanical engineers, part G: Journal of Aerospace Engineering 221*, 5 (2007), 631–647.

[145] Peters, D. A. Hingeless rotor frequency response with unsteady inflow. *NASA. Ames Res. Center Rotorcraft Dyn.* (1974).

[146] Petersen, Ø. W., Øiseth, O., Nord, T. S., and Lourens, E. Estimation of the full-field dynamic response of a floating bridge using kalman-type filtering algorithms. *Mechanical Systems and Signal Processing 107* (2018), 12–28.

[147] Przemieniecki, J. S. *Theory of matrix structural analysis*. Courier Corporation, 1985.

[148] Ribeiro, M. I. Kalman and extended kalman filters: Concept, derivation and properties. *Institute for Systems and Robotics 43*, 46 (2004), 3736–3741.

[149] Risaliti, E., Cornelis, B., Tamarozzi, T., and Desmet, W. A state-input estimation approach for force identification on an automotive suspension component. In *Model Validation and Uncertainty Quantification, Volume 3: Proceedings of the 34th IMAC, A Conference and Exposition on Structural Dynamics 2016* (2016), Springer, pp. 359–369.

[150] Risaliti, E., Tamarozzi, T., Vermaut, M., Cornelis, B., and Desmet, W. Multibody model based estimation of multiple loads and strain field on a vehicle suspension system. *Mechanical Systems and Signal Processing 123* (2019), 1–25.

[151] Risaliti, E., Van Cauteren, J., Tamarozzi, T., Cornelis, B., and Desmet, W. Virtual sensing of wheel center forces by means of a linear state estimator. In *International Conference on Noise and Vibration Engineering (ISMA2016), Leuven, Belgium* (2016).

[152] Rojas, A. J. On the continuous-time algebraic riccati equation and its closed-form solution. In *49th IEEE Conference on Decision and Control (CDC)* (2010), IEEE, pp. 1330–1335.

[153] Rosafalco, L., Eftekhar Azam, S., Mariani, S., and Corigliano, A. System identification via unscented kalman filtering and model class

selection. *ASCE-ASME Journal of Risk and Uncertainty in Engineering Systems, Part A: Civil Engineering 10*, 1 (2024), 04023063.

[154] Rottiers, W. *Development of virtual measurements on a mechatronic drivetrain.* PhD thesis, Master thesis, KU Leuven, 2015.

[155] Sachse, D., Geluk, T., and Van Wayenberge, T. Accuracy of inverse load identification techniques for transfer path analysis. In *Automotive Acoustics Conference* (2013).

[156] Salau, N. P., Trierweiler, J. O., and Secchi, A. R. Observability analysis and model formulation for nonlinear state estimation. *Applied Mathematical Modelling 38*, 23 (2014), 5407–5420.

[157] Salgado, M., Middleton, R., and Goodwin, G. C. Connection between continuous and discrete riccati equations with applications to kalman filtering. In *IEE Proceedings D (Control Theory and Applications)* (1988), vol. 135-1, IET, pp. 28–34.

[158] Sarego, G., Zaccariotto, M., and Galvanetto, U. Artificial neural networks for impact force reconstruction on composite plates and relevant uncertainty propagation. *IEEE Aerospace and Electronic Systems Magazine 33*, 8 (2018), 38–47.

[159] SciPy. Scipy care, 2023. `https://docs.scipy.org/doc/scipy/reference/generated/scipy.linalg.solve_continuous_are.html` [Accessed: 31 Jan 2024].

[160] Serafini, J., Bernardini, G., Porcelli, R., and Masarati, P. In-flight health monitoring of helicopter blades via differential analysis. *Aerospace Science and Technology 88* (2019), 436–443.

[161] Series, A. *CSN EN 6033. Carbon Fibre Reinforced Plastics - Test method - Determination of interlaminar fracture toughness energy - Mode I - GIC.* -, 2015.

[162] Shabana, A. A. *Dynamics of multibody systems.* Cambridge university press, 2020.

[163] Simeon, B. Computational flexible multibody dynamics. In *A Differential-Algebraic Approach. Differential-Algebraic Equations Forum. Springer, Heidelberg* (2013), Springer.

[164] Simon, D. *Optimal state estimation: Kalman, H infinity, and nonlinear approaches.* John Wiley & Sons, 2006.

[165] Simonian, S. S. Inverse problems in structural dynamics—i. theory. *International Journal for Numerical Methods in Engineering 17*, 3 (1981), 357–365.

[166] Škec, L., Alfano, G., and Jelenić, G. Complete analytical solutions for double cantilever beam specimens with bi-linear quasi-brittle and brittle interfaces. *International journal of fracture 215* (2019), 1–37.

[167] Software, S. D. I. Executable digital twin, 2024. `https://www.siemens.com/global/en/company/stories/research-technologies/digitaltwin/x-digital-twin.html` [Accessed: 31 Jan 2024].

[168] Software, S. D. I. Simcenter 3d smart virtual sensing, 2024. `https://blogs.sw.siemens.com/simcenter/simcenter-3d-smart-virtual-sensing-unveiling-the-magic/` [Accessed: 12 Apr 2024].

[169] Sony, S., Laventure, S., and Sadhu, A. A literature review of next-generation smart sensing technology in structural health monitoring. *Structural Control and Health Monitoring 26*, 3 (2019), e2321.

[170] Starkey, J., Merrill, G., et al. On the ill-conditioned nature of indirect force measurement techniques. *Journal of Modal Analysis 4*, 3 (1989), 103–108.

[171] Sun, H., and Büyüköztürk, O. Optimal sensor placement in structural health monitoring using discrete optimization. *Smart Materials and Structures 24*, 12 (2015), 125034.

[172] System, A. D. Procam, 2018. `http://aicon3d.com/products/vehicle-testing/procam` [Accessed: Apr 2018].

[173] Takeda, S., Minakuchi, S., Okabe, Y., and Takeda, N. Delamination monitoring of laminated composites subjected to low-velocity impact using small-diameter fbg sensors. *Composites Part A: Applied Science and Manufacturing 36*, 7 (2005), 903–908.

[174] Talamo, C., Bettini, P., Rigamonti, D., Masarati, P., Cumbo, R., and De Gregoriis, D. Blade load reconstruction from embedded strain measurements. In *Proceedings of the 78th Annual Forum The Vertical Flight Society Fort Worth, Texas, May 10–12, 2022* (2022), Curran Associates, Inc.

[175] Tamarozzi, T., Risaliti, E., Rottiers, W., Desmet, W., et al. Noise, ill-conditioning and sensor placement analysis for force estimation through virtual sensing. In *In International Conference on Noise and*

Vibration Engineering (ISMA2016), (2016), Katholieke Univ Leuven, Dept Werktuigkunde, pp. 1741–1756.

[176] Tatsis, K., Dertimanis, V., Abdallah, I., and Chatzi, E. A substructure approach for fatigue assessment on wind turbine support structures using output-only measurements. *Procedia engineering 199* (2017), 1044–1049.

[177] Tatsis, K., Dertimanis, V. K., Papadimitriou, C., Lourens, E., and Chatzi, E. A general substructure-based framework for input-state estimation using limited output measurements. *Mechanical Systems and Signal Processing 150* (2021), 107223.

[178] Tatsis, K., and Lourens, E. A comparison of two kalman-type filters for robust extrapolation of offshore wind turbine support structure response. In *Fifth International Symposium on Life-Cycle Civil Engineering (IALCCE 2016), Proceedings of the Fifth International Symposium on Life-Cycle Civil Engineering (IALCCE 2016), Delft, The Netherlands* (2016), pp. 209–216.

[179] Tatsis, K., Wu, L., Tiso, P., and Chatzi, E. State estimation of geometrically non-linear systems using reduced-order models. *Life Cycle Analysis and Assessment in Civil Engineering: Towards an Integrated Vision* (2018), 219–227.

[180] Tessler, A. *A variational principle for reconstruction of elastic deformations in shear deformable plates and shells.* National Aeronautics and Space Administration, Langley Research Center, 2003.

[181] Tidriri, K., Chatti, N., Verron, S., and Tiplica, T. Bridging data-driven and model-based approaches for process fault diagnosis and health monitoring: A review of researches and future challenges. *Annual reviews in control 42* (2016), 63–81.

[182] Trivailo, P. M., Dulikravich, G. S., Sgarioto, D., and Gilbert, T. Inverse problem of aircraft structural parameter estimation: application of neural networks. *Inverse Problems in Science and Engineering 14*, 4 (2006), 351–363.

[183] Tuloup, C., Harizi, W., Aboura, Z., Meyer, Y., Khellil, K., and Lachat, R. On the use of in-situ piezoelectric sensors for the manufacturing and structural health monitoring of polymer-matrix composites: A literature review. *Composite Structures 215* (2019), 127–149.

[184] Uhl, T. The inverse identification problem and its technical application. *Archive of Applied Mechanics 77* (2007), 325–337.

[185] Van der Linden, P., and Floetke, H. Comparing inverse force identification and the mount stiffness force identification methods for noise contribution analysis. *The Shock and Vibration Digest 38*, 4 (2006), 359–360.

[186] Van Der Merwe, R. *Sigma-point Kalman filters for probabilistic inference in dynamic state-space models*. Oregon Health & Science University, 2004.

[187] van der Seijs, M. V., De Klerk, D., and Rixen, D. J. General framework for transfer path analysis: History, theory and classification of techniques. *Mechanical Systems and Signal Processing 68* (2016), 217–244.

[188] Van Loan, C. Computing integrals involving the matrix exponential. *IEEE transactions on automatic control 23*, 3 (1978), 395–404.

[189] Van Tonder, J. D., Venter, M. P., and Venter, G. A new method for improving inverse finite element method material characterization for the mooney–rivlin material model through constrained optimization. *Mathematical and Computational Applications 28*, 4 (2023), 78.

[190] Vettori, S., Di Lorenzo, E., Peeters, B., Luczak, M., and Chatzi, E. An adaptive-noise augmented kalman filter approach for input-state estimation in structural dynamics. *Mechanical Systems and Signal Processing 184* (2023), 109654.

[191] Wang, S., and Lei, Y. An unscented kalman filter under unknown input without direct feedthrough for joint input and system identification of structural systems. *Mechanical Systems and Signal Processing 208* (2024), 110951.

[192] Welch, G., Bishop, G., et al. An introduction to the kalman filter.

[193] Wielitzka, M., Busch, A., Dagen, M., Ortmaier, T., and Serra, G. Unscented kalman filter for state and parameter estimation in vehicle dynamics. In *Kalman Filters-Theory for Advanced Applications*. InTech Rijeka, 2018, pp. 56–75.

[194] Williams, J. The fracture mechanics of delamination tests. *The Journal of strain analysis for engineering design 24*, 4 (1989), 207–214.

[195] Wonham, W. M. On a matrix riccati equation of stochastic control. *SIAM Journal on Control 6*, 4 (1968), 681–697.

[196] Xie, L., Soh, Y. C., and De Souza, C. E. Robust kalman filtering for uncertain discrete-time systems. *IEEE Transactions on automatic control 39*, 6 (1994), 1310–1314.

[197] Xu, H.-g., and Lu, L.-z. Properties of a quadratic matrix equation and the solution of the continuous-time algebraic riccati equation. *Linear algebra and its applications 222* (1995), 127–145.

[198] Yang, G.-H., and Wang, J. L. Robust nonfragile kalman filtering for uncertain linear systems with estimator gain uncertainty. *IEEE Transactions on Automatic Control 46*, 2 (2001), 343–348.

[199] Zahr, M. J., and Farhat, C. Progressive construction of a parametric reduced-order model for pde-constrained optimization. *International Journal for Numerical Methods in Engineering 102*, 5 (2015), 1111–1135.

[200] Zhang, R., Xue, S., Ban, X., Zhang, R., Xie, L., et al. System identification of a structure equipped with a cable-bracing inerter system using adaptive extended kalman filter. *Structural Control and Health Monitoring 2024* (2024).

[201] Zhang, X., He, J., Hua, X., and Chen, Z. Identification of time-varying stiffness with unknown mass distribution based on extended kalman filter. *Mechanical Systems and Signal Processing 211* (2024), 111218.

[202] Zienkiewicz, O. C., and Taylor, R. L. *The finite element method: solid mechanics*, vol. 2. Butterworth-heinemann, 2000.

[203] Zou, Y., Tong, L., and Steven, G. P. Vibration-based model-dependent damage (delamination) identification and health monitoring for composite structures—a review. *Journal of Sound and vibration 230*, 2 (2000), 357–378.

Curriculum Vitae

Personal Data

Roberta Cumbo
Born 15 December 1992, Rome, Italy

Professional Experience

2024/04 – Now — **Senior Engineer, Collins Aerospace, Rome, Italy**
Hybrid Digital Twin for Predictive Maintenance

2021/04 – 2024/04 — **Research Fellow, Leonardo Labs, Rome, Italy**
Physics-informed AI for Structural Health Monitoring and data-driven solutions for the prediction of composite material properties

2019/01 – 2021/04 — **Research Engineer Associate, Siemens Digital Industries Software, Leuven, Belgium & PhD Fellow at KU Leuven, VLAIO Baekeland Mandate**
Kalman-based methods for load identification on rotating blades involving Flexible Multibody Models

2017/02 – 2019/01 — **Research Engineer Associate, Siemens Digital Industries Software, Leuven, Belgium**
Multiple load estimation via Kalman Filter on linear systems and Optimal Sensor Placement strategies

2016/07 – 2016/12 — **Internship Student, Siemens Digital Industries Software, Leuven, Belgium**
Master thesis on Dynamic Substructuring within Test Division

Education

2020/11 – **2021/11** **Master in Project Management**, Rome Business School, Rome, Italy

2014/09 – **2017/01** **Master of Science in Aeronautical Engineering**, University of Rome La Sapienza, Rome, Italy

2011/09 – **2014/07** **Bachelor of Science in Aerospace Engineering**, University of Rome La Sapienza, Rome, Italy

List of publications

Articles in international journals

[1] Cumbo, R., De Gregoriis, D., Danzi, F., Kumar, A., & Naets, F. (2024). Recursive parameter estimation for the on-line monitoring of delamination growth in composite structures. Structural Health Monitoring, 0(0), 1-20.

[2] Cumbo, R., Mazzanti, L., Tamarozzi, T., Jiranek, P., Desmet, W., & Naets, F. (2021). Advanced optimal sensor placement for Kalman-based multiple-input estimation. Mechanical Systems and Signal Processing, 160, 107830.

[3] Cumbo, R., Tamarozzi, T., Jiranek, P., Desmet, W., & Masarati, P. (2020). State and force estimation on a rotating helicopter blade through a Kalman-based approach. Sensors, 20(15), 4196.

[4] Cumbo, R., Tamarozzi, T., Janssens, K., & Desmet, W. (2019). Kalman-based load identification and full-field estimation analysis on industrial test case. Mechanical Systems and Signal Processing, 117, 771-785.

Articles in international conference proceedings

[5] Talamo, C., Bettini, P., Rigamonti, D., Masarati, P., Cumbo, R., & De Gregoriis, D. (2022, May). Blade Load Reconstruction from Embedded Strain Measurements. In Proceedings of the 78th Annual Forum The Vertical Flight Society Fort Worth, Texas, May 10–12, 2022. Curran Associates, Inc.

[6] Janssens, K., Forrier, B., Cumbo, R., Risaliti, E., Cornelis, B., Tamarozzi, T., & Desmet, W. (2021). Virtual Sensing Application Cases Exploiting Various Degrees of Model Complexity. In Vibration Engineering for a

Sustainable Future: Active and Passive Noise and Vibration Control, Vol. 1 (pp. 161-167). Springer International Publishing.

[7] Cornelis, B., Forrier, B., Cumbo, R., Risaliti, E., Janssens, K., Tamarozzi, T., & Desmet, W. (2021). Virtual sensing strategies utilizing various model complexities: Industrial applications. In Commercial Vehicle Technology 2020/2021: Proceedings of the 6th Commercial Vehicle Technology Symposium (pp. 512-523). Springer Fachmedien Wiesbaden.

[8] Vettori, S., Lorenzo, E. D., Cumbo, R., Musella, U., Tamarozzi, T., Peeters, B., & Chatzi, E. (2020). Kalman-Based virtual sensing for improvement of service response replication in environmental tests. In Model Validation and Uncertainty Quantification, Volume 3: Proceedings of the 38th IMAC, A Conference and Exposition on Structural Dynamics 2020 (pp. 93-106). Springer International Publishing.

[9] Cumbo, R., Tamarozzi, T., Desmet, W., & Masarati, P. (2020). A Kalman-based identification approach for distributed aerodynamic loads on a rotating blade. In 46th European Rotorcraft Forum (ERF 2020) (pp. 24-33). Russian Helicopters.

[10] Cumbo, R., Tamarozzi, T., Janssens, K., & Desmet, W. (2018). Investigation of virtual sensing techniques on a rear twistbeam suspension by performing multiple-input/state estimation. In Proceedings of International Conference on Noise and Vibration Engineering (ISMA2018). pp. 2181-2195. Katholieke Univ Leuven, Dept. Werktuigkunde.

Abstracts in international conference proceedings

[11] Mazzanti, L., Cumbo, R., Desmet, W., Naets, F., & Tamarozzi, T. (2020). An improved optimal sensor placement strategy for Kalman-based multiple-input estimation. In Model Validation and Uncertainty Quantification, Volume 3: Proceedings of the 38th IMAC, A Conference and Exposition on Structural Dynamics 2020 (pp. 181-185). Springer International Publishing.

Other publications

[12] Cumbo, R., Morelli, R., Nicolosi, A., & Kumar, A. (2023). System Identification Via Auto-Encoders: A Comparison Between Data-Driven and Physics-Informed Solutions. In Proceedings of European Workshop of Structural Health Monitoring 2023.

[13] Cumbo, R., Morelli, R., Kumar, A., & Nicolosi, A. (2022). Structural shape reconstruction of non-linear systems via Variational Autoencoders. Ital-IA 2023: 3rd National Conference on Artificial Intelligence.

[14] Cumbo, R., Baroni, A., Ricciardi, A., & Corvaglia, S. (2022). Design allowables of composite laminates: A review. Journal of Composite Materials, 56(23), 3617-3634.

[15] Cumbo, R., Baroni, A., Kumar, A., Nicolosi, A., & Corvaglia, S. G. (2022). Bayesian Machine Learning for faster design of composite structures. In Proceedings of 73rd International Astronautical Congress (IAC).

[16] Cumbo, R., Baroni, A., Ricciardi, A., Nicolosi, A., & Corvaglia, S. G. (2022). Gaussian Process Regression for the prediction of material allowables. In Proceedings of 20th European Conference on Composite Materials, ECCM20.

[17] Cumbo, R., & Baroni, A. (2022, June). Experimental Investigation on Fracture Toughness of Open Hole Coupons Under Tension Load. In International Symposium on Dynamic Response and Failure of Composite Materials (pp. 343-350). Cham: Springer International Publishing.

[18] Cumbo, R., Manzato, S., Coppotelli, G., Fregolent, A., & D'Ambrogio, W. (2017). A Recursive Coupling-Decoupling Approach to Improve Experimental Frequency Based Substructuring Results. In Dynamics of Coupled Structures, Volume 4: Proceedings of the 35th IMAC, A Conference and Exposition on Structural Dynamics 2017 (pp. 239-253). Springer International Publishing.

FACULTY OF ENGINEERING SCIENCE
DEPARTMENT OF MECHANICAL ENGINEERING
XXXXX
Celestijnenlaan 200A box 2402
B-3001 Leuven
first.last@cs.kuleuven.be
http://www.XXXXX.cs.kuleuven.be